



## Doctoral Thesis

# Measurement and analysis of rainfall gradients along a hillslope transect in the Swiss Alps

**Author(s):**

Schäppi, Bettina

**Publication Date:**

2013

**Permanent Link:**

<https://doi.org/10.3929/ethz-a-009913260> →

**Rights / License:**

[In Copyright - Non-Commercial Use Permitted](#) →

This page was generated automatically upon download from the [ETH Zurich Research Collection](#). For more information please consult the [Terms of use](#).

Diss. ETH No. 21084

# **Measurement and analysis of rainfall gradients along a hillslope transect in the Swiss Alps**

A dissertation submitted to  
ETH ZURICH

for the degree of  
Doctor of sciences

presented by  
BETTINA SCHÄPPI  
Dipl. Umwelt-Natw. ETH Zurich  
born May 6, 1982  
citizen of Oberrieden ZH and Zurich

accepted on the recommendation of

Prof. Dr. P. Burlando, examiner  
Prof. Dr. A. Bárdossy, co-examiner  
Dr. P. Molnar, co-examiner

2013



# Contents

List of Tables . . . . .	vii
List of Figures . . . . .	xi
List of Symbols . . . . .	xix
<b>1 Preface</b>	<b>xxiii</b>
1.1 Acknowledgement . . . . .	xxv
1.2 Summary . . . . .	xxvii
1.3 Zusammenfassung . . . . .	xxix
<b>2 Introduction</b>	<b>1</b>
2.1 Goal and motivation . . . . .	2
2.2 State of the art . . . . .	6
2.2.1 Ground observation of rainfall . . . . .	6
2.2.2 Orographic effects on precipitation . . . . .	8
2.2.3 Experimental design and working hypotheses . . . . .	13
2.3 Outline . . . . .	16
<b>3 Field experiment</b>	<b>17</b>
3.1 Weather station setup . . . . .	17
3.1.1 Reference stations . . . . .	19
3.1.2 Mobile stations . . . . .	21
3.2 Event documentation . . . . .	24
3.3 Post-processing . . . . .	29
3.3.1 Post-processing methods . . . . .	29



3.3.2	Post-processing results . . . . .	40
3.3.3	Uncertainty analysis . . . . .	46
<b>4</b>	<b>Results</b>	<b>53</b>
4.1	Spatial and temporal correlation . . . . .	53
4.1.1	Cross correlation . . . . .	54
4.1.2	Autocorrelation . . . . .	63
4.1.3	Oscillation coefficients . . . . .	65
4.2	Gradient analysis of cumulative rainfall and altitude . . . . .	70
4.2.1	Event gradients . . . . .	70
4.2.2	Effect of temporal scale . . . . .	82
4.2.3	Effect of terrain scale on gradients . . . . .	85
4.3	Weather type control on gradients . . . . .	93
4.3.1	Lightning activity during observed events . . . . .	94
4.3.2	Temperature gradient . . . . .	95
4.3.3	Wind observations on the ground . . . . .	95
4.3.4	Wind direction estimation from radar images . . . . .	105
4.3.5	Large scale weather type . . . . .	110
4.4	Modelling of orographic precipitation . . . . .	114
4.4.1	Model description . . . . .	114
4.4.2	Simulated gradients depending on wind direction . . . . .	116
4.4.3	Model calibration . . . . .	118
4.4.4	Results . . . . .	121
4.4.5	Comparison of simulated and observed gradients . . . . .	126
4.5	Cluster analysis of gradients . . . . .	129
4.5.1	Clustering methods . . . . .	129
4.5.2	Summarized event data . . . . .	131
4.5.3	Results . . . . .	132
<b>5</b>	<b>Discussion and conclusions</b>	<b>137</b>
5.1	Discussion . . . . .	137

---

5.1.1	Effect of elevation on event rainfall variability and cumulative amount . . . . .	137
5.1.2	Effects of data post-processing . . . . .	138
5.1.3	Comparison of simulated and observed rainfall distribution . . . . .	138
5.1.4	Influence of terrain scale . . . . .	139
5.1.5	Influence of meteorological conditions . . . . .	139
5.2	Conclusions . . . . .	144
5.2.1	Summary of conclusions . . . . .	148
<b>References</b>		<b>150</b>
<b>A Appendix</b>		<b>161</b>
A.1	Sensors . . . . .	161
A.2	Maps and station setup . . . . .	164
A.3	Post-processing . . . . .	167
A.4	Gradient analysis of cumulative event rainfall . . . . .	171
A.5	Weather type . . . . .	177
A.6	Modelling of orographic precipitation . . . . .	183
<b>Acronyms</b>		<b>188</b>
<b>Curriculum Vitae</b>		<b>189</b>



# List of Tables

3.1	Event dates and times in UTC: D denotes the entire event duration, $D_p$ is the duration of the wet spell within each event and P denotes the cumulative event rainfall amount. . . . .	26
3.2	Correction applied to TBR data due to device specific underestimation. All measured tip amounts were corrected according to these calibration factors. . .	33
3.3	Dynamic calibration of measured rainfall intensities for different types of rain-gauges . . . . .	38
3.4	Post-processing summary of all stations and events combined in relative and absolute amounts with respect to the previous processing step . . . . .	40
3.5	Post-processing summary of all stations and events in relative and absolute rainfall amounts. . . . .	41
3.6	Parameters of uncertainty analysis. Because the calibration factors are different for each pluviometer, the uncertainty is different for each of the mobile stations.	52
4.1	Symbols and definition of oscillation coefficients . . . . .	66
4.2	Difference between radar data products in 2010 and 2011 . . . . .	105
4.3	Mode of wind direction, $\alpha_R$ , (rounded to $10^\circ$ ) estimated from rain cell tracking in radar images for different intensity thresholds . . . . .	109
4.4	Parameters used for the event calibration: The wind direction was based on the tracking of rain cells using the intensity threshold, $I_1$ , the environmental lapse rate was estimated by averaging the lapse rates of the individual events and as reference temperature, $T_{ref}$ , the average for each event was used. . . .	119
4.5	Cumulative sum, P, and mean intensity, I, obtained from the model and observations. For each event the station average is shown. $\overline{P_O P_M > 0}$ indicates the average taken over all observations where the model simulations show a rainfall intensity $> 0$ . . . . .	122

4.6	Comparison of cluster analysis with different methods and variability in the cluster assignment by different methods. . . . .	133
5.1	Comparison of wind direction obtained from radar images at different intensity thresholds ( $I_1, I_2, I_3$ ), wind direction measured on the ground, low level wind (LLW) classification and weather type (WT) and average and maximum lightning rate, $R_L$ and $(R_{L,max})$ , within a distance of 30 km. . . . .	142
A.1	Wind sensors deployed at mobile and reference stations . . . . .	161
A.2	Rainfall sensors deployed at mobile and reference stations . . . . .	162
A.3	Temperature sensors deployed at mobile and reference stations . . . . .	162
A.4	Coordinates and id of mobile stations 2010: the letters in the last column indicate the stations that were at the same location in 2011 . . . . .	165
A.5	Coordinates and id of mobile stations 2011: the letters in the last column indicate the stations that were at the same location in 2010 . . . . .	165
A.6	Stations used in the analysis. 0 indicates a station which was not used in the event analysis due to gaps in the time series. . . . .	168
A.7	Uncertainty [%] . . . . .	169
A.8	Uncorrected event rainfall amounts [mm] . . . . .	170
A.9	Gradients of post-processed data with $0.5 < R^2 < 1$ and standard deviation . . . . .	171
A.10	Gradients of observed data with $0.5 < R^2 < 1$ and standard deviation . . . . .	172
A.11	Explained variance of DEMs filtered in the fourier domain at different frequencies $w$ and resulting length scale. $N=1000, f_s=0.01m^{-1}$ . . . . .	175
A.12	Frequency of weather types with and without conditioning on rainfall occurrence ( $f_{WT}$ and $f_{WT,P}$ respectively) on the annual time scale and on a seasonal time scale ( $f_{WT,S}$ and $f_{WT,P,S}$ respectively) and frequency of weather types associated with observed events during the field experiment, $f_{WT,E}$ . . . . .	177
A.13	Cluster reassignment from agglomerative hierarchical clustering to K-means clustering . . . . .	178
A.14	Meteorological conditions in different wind field clusters based on hourly averages of weather station data. The abbreviation shows the prevailing wind direction and its association with rainfall intensity $I$ or cumulative amount $P$ . Classes with identical properties are distinguished with letters. . . . .	179
A.15	Wind class occurrence during observed events in 2011. . . . .	180

---

A.16	Weather classification on days with events during the field experiment in 2010 and 2011 . . . . .	181
A.17	Event data used in cluster analysis and corresponding gradients. The unit of the gradients is mm/100m. . . . .	182
A.18	Calibrated parameters of linear orographic model and resulting gradients along the transects in 2010. A: Calibration based on RMSE, B: Calibration based on MAE, C: Calibration based on correlation coefficient . . . . .	183
A.19	Error statistics of the calibrated model of orographic precipitation. The relative error is estimated by dividing the error by the mean of the observed rainfall amounts. . . . .	184
A.20	Correlation between modelled and observed precipitation for the selected events based on different calibration methods . . . . .	185
A.21	Parameter values used in model simulations . . . . .	185



# List of Figures

3.1	Location and altitude of weather stations within the area surrounding the study site. Crosses indicate the existing raingauge network and circles indicate the weather stations installed permanently within the field experiment. . . . .	18
3.2	Location of the field site and location of the reference weather stations and transects of mobile stations. The green rectangle shows the location of the transects of weather stations in summer 2010 and 2011. The blue rectangle in the upper left panel indicates extent of radar data used in the analysis. . . . .	19
3.3	Overview and profile of reference station locations. The square indicates the area of the hillslope transects that were investigated . . . . .	20
3.4	Overview and profile of transects during the intensive observation periods in 2010 and 2011. In 2010 the stations number 5 and 10 were set up as master stations and T1 consists of stations 1-7 and ZE, and T2 consists of stations 8-13 and TR. In 2011 T1 consists of stations 1-9 and ZE, and T2 consists of stations 10-13 and TR. . . . .	23
3.5	Cumulative rainfall based on the original data (without post-processing) of the intensive observation periods in 2010 and 2011. The numbers indicate the day and time of the beginning and end of the events in UTC. . . . .	25
3.6	Cumulative event rainfall: The lower transect of mobile stations consists of stations 1 to 8 in 2010 and 1 to 9 in 2011. The remaining stations belong to transect 2. . . . .	27
3.7	Summary of weather station data: $I_{max}$ denotes the maximum rainfall intensity, $U$ denotes the wind speed, $P$ the cumulative rainfall amount, $D_p$ the duration of the wet spell and $cv$ denotes the coefficient of variation. The red line indicates the location of the median, the blue box denotes the interquartile range and the whiskers have a length of the 1.5 times the interquartile range. The red crosses indicate outliers. . . . .	28



3.8	Flowchart of post-processing steps applied to mobile station raingauge data. For the reference station data the calibration step and the interpolation step were excluded. . . . .	29
3.9	Evaluation of interpolation method for missing values. Number of missing values per event and station (top left); Difference in observed and interpolated intensity (top right); Ratio between interpolated and observed intensity (bottom left); Ratio between interpolated and observed cumulative precipitation (bottom right). . . . .	31
3.10	Static calibration of tipping bucket raingauges . . . . .	32
3.11	Illustration of the tipping bucket (TBR) mechanism as compared to the weighing raingauge (WR) observations for devices with the same temporal resolution. The upper panel shows the cumulative precipitation recorded by the TBR and the WR. The difference between the rainfall amount measured by the WR and the TBR is indicated in red ( $V_e$ ). The lower panel shows the corresponding rainfall intensities. . . . .	34
3.12	Distribution of intensities at the reference stations for different tip accumulation intervals, $\Delta t_{tip}$ , in comparison with tip average and average of intensities observed at the reference stations. The red line indicates the location of the median, the blue box denotes the interquartile range and the whiskers have a length of the 1.5 times the interquartile range. The red crosses indicate outliers. . . . .	35
3.13	Occurrence of tip accumulation intervals, $\Delta t_{tip}$ , for the references stations TR and ZE and cumulative amount, P, recorded during each interval. . . . .	36
3.14	Dynamic calibration of measured rainfall intensities . . . . .	37
3.15	Wind correction factor depending on rainfall intensity depending on wind speed. . . . .	39
3.16	Histogram of absolute and relative correction for each event and each station in 2010 and 2011. . . . .	41
3.17	Absolute and relative correction for each station in 2010 and 2011. The green cross indicates the sum of all corrections. In the lower part of the figure the contribution of the different components of the correction is documented and the mean cumulative precipitation, P, observed during all the events observed during the corresponding season is shown for the corrected (x) and uncorrected data (o). . . . .	43

3.18	Absolute and relative correction for each event in 2010 and 2011. The green cross indicates the sum of all corrections. In the lower part of the figure the contribution of the different components of the correction is documented and the mean cumulative precipitation, $P$ , observed during all the events observed during the corresponding season is shown for the corrected (x) and uncorrected data (o).	44
3.19	Absolute uncertainty at each post-processing step depending on the measured rainfall intensity is shown for the mobile weather station nr. 6 (the different stations only vary in terms of their static calibration factor)	49
3.20	Relative uncertainty at each post-processing step depending on the measured rainfall intensity	50
3.21	Relative uncertainty depending on wind speed $U$ and rainfall intensity $I$ for station 6	51
4.1	Cross correlation in rainfall time series between neighbouring weather stations shown for the 27 different events ( $\rho_1$ ). The red line indicates the location of the median, the blue box denotes the interquartile range and the whiskers have a length of the 1.5 times the interquartile range. The red crosses indicate outliers.	56
4.2	Cross correlation in rainfall time series between neighbouring weather stations shown for the 14 pairs of neighbouring stations ( $\rho_1$ ). Station pairs are numbered from 1 to 14 and are ordered according to increasing elevation. The red line indicates the location of the median, the blue box denotes the interquartile range and the whiskers have a length of the 1.5 times the interquartile range. The red crosses indicate outliers.	57
4.3	Decrease in spatial correlation for different combinations of $d_0$ and $s_0$	58
4.4	Correlation distance $d_0$ and shape parameter $s_0$ of different events estimated at different aggregation intervals for the original and post-processed rainfall time series.	59
4.5	Comparison of the shape parameter, $s_0$ , among different events estimated at different aggregation intervals for the original and post-processed rainfall time series.	60
4.6	Comparison of the correlation distance, $d_0$ , among different events estimated at different aggregation intervals for the original and post-processed rainfall time series. For clarification the values larger than 25 km were cut off.	61

- 4.7 Comparison of the shape parameter  $s_0$  with the correlation distance  $d_0$  among different events estimated at different aggregation intervals for the original and post-processed data. For clarification the values larger than 35 km were cut off. 62
- 4.8 Autocorrelation length,  $L_a$ , estimated from the original and post-processed rainfall time series at 1 min resolution. The numbers indicate the median of the autocorrelation length at each event and station. The red line indicates the location of the median, the blue box denotes the interquartile range and the whiskers have a length of the 1.5 times the interquartile range. The red crosses indicate outliers. . . . . 64
- 4.9 Oscillation coefficient depending on aggregation interval for different stages of data post-processing for the rainfall time series of all events combined. The coefficient  $C_{\downarrow}$  in the post-processed tipping bucket gauges is influenced by very small fluctuations due to the wind correction. . . . . 67
- 4.10 Oscillation coefficients,  $C_{\downarrow}$ , for post-processed rainfall time series without wind correction for events 7, 9, 10, 16, 17, 25 and 27 at aggregation intervals of 30, 60 and 90 min. The numbers in the legend denote the estimated gradient in terms of  $C_{\downarrow}$  for the corresponding event. . . . . 69
- 4.11 Gradient of  $C_{\downarrow}$  for post-processed rainfall time series without wind correction. The colorbar indicates the  $R^2$  of the linear regression of  $C_{\downarrow}$  and elevation. . . 69
- 4.12 Gradients in cumulative rainfall and altitude observed on T0 ( $g$ ) on T1 ( $g_1$ ) and T2 ( $g_2$ ) on the event time scale during IOP 2010 and 2011. In the lower part only the gradients with an  $R^2$  larger than 0.5 are shown. . . . . 71
- 4.13 Standard deviation of the estimated gradients based on original and post-processed cumulative event rainfall. . . . . 72
- 4.14 Relative difference between  $g_p$  and  $g_o$  vs. gradients based on original data ( $g_o$ ). Only gradients with  $R^2 > 0.5$  are shown. The horizontal errorbars indicated the absolute standard deviation of  $g_o$  and the vertical errorbars indicate the relative standard deviation of  $g_p$  . . . . . 74
- 4.15 Gradients  $g_1$  and  $g_2$  on T1 and T2 respectively based on **post-processed** data. The confidence interval of the regression is indicated by  $ci_1$  and  $ci_2$  for T1 and T2 respectively. The confidence interval based on the combined uncertainty in the data and the fitting method is indicated by  $ci_{1,m}$  and  $ci_{2,m}$  for T1 and T2 respectively. . . . . 75
- 4.16 Gradients,  $g$ , on T0 based on **post-processed** data. The confidence interval of the regression is indicated by  $ci$ . The confidence interval based on the combined uncertainty in the data and the fitting method is indicated by  $ci_m$ . . . . . 76

4.17	Gradient of intensity and gradient of duration vs. gradient in terms of cumulative precipitation for the post-processed data. The numbers indicate the events with an $R^2 > 0.5$ for the gradient in cumulative precipitation. . . . .	77
4.18	Gradient of intensity vs. gradient of duration for the post-processed data. The numbers indicate the events with an $R^2 > 0.5$ for the gradient in cumulative precipitation. . . . .	78
4.19	Comparison of gradients and gradient of quantiles. The data points are scaled according to the $R^2$ value in terms of cumulative rainfall. . . . .	79
4.20	Gradient of $P(I > q_{75})$ ( $g_{p75}$ ) and ( $g_p$ ) in comparison with gradient in rainfall duration for post-processed data on T0, T1 and T2. The numbers indicate the events with an $R^2 > 0.5$ for the gradient in cumulative precipitation. . . . .	80
4.21	Gradient evolution at different moving average aggregation intervals in comparison to $g_p$ . Large dots indicate gradients with $R^2$ values larger than 0.5. On the Y-axis on the left the corresponding rainfall intensities are shown. . . . .	83
4.22	Gradient evolution at different moving average aggregation intervals in comparison to $g_p$ indicated in green. The numbers at the top indicate the percentage of gradients with $R^2 > 0.5$ and the numbers at the bottom indicate the event duration $D$ . The red line indicates the location of the median, the box denotes the interquartile range and the whiskers have a length of the 1.5 times the interquartile range. . . . .	84
4.23	Comparison of filters applied in the digital terrain model filtering shown in 1d. . . . .	87
4.24	Elevation obtained from a filtered DEM with a symmetrical Butterworth filter ( $n=5$ ) with the elevation obtained from a DEM of 25 m resolution for the station setup in 2011 . . . . .	88
4.25	$R^2$ value for gradients on the entire transect obtained from different filtered DEMs and the original DEM at 100 and 25 m resolution. The shaded area denotes gradients with $R^2 < 0.5$ . The fraction of explained variance which maximizes $R^2$ is denoted as $f_{\sigma^2, max}$ . . . . .	89
4.26	$R^2$ value for gradients on the different transects obtained from original and filtered DEMs. As filters the ideal low pass filter (ilp), the symmetrical Butterworth filter (bw) and the directional Butterworth filter (bw $\alpha$ ) were applied. . . . .	90
4.27	Explained variance of the filtered DEM resulting in the highest $R^2$ value, $f_{\sigma^2, max}$ , for gradients on the different transects obtained for the ideal low pass filter (ilp), for the symmetrical Butterworth filter (bw) and for the directional Butterworth filter in the prevailing wind direction (bw $\alpha$ ). For events where $f_{\sigma^2, max}$ equals 1 the original DEM resulted in the highest $R^2$ value. . . . .	91

4.28	Bw-filtered and original DEM in modelled area and in the area of the transect. The filtered DEM explains around 97% of the variance of the original DEM. . . . .	92
4.29	Maximum and mean of hourly lightning strikes occurring in a distance of 30 km from the weather station in Zermatt. The numbers indicated the maximum lightning rate that occurred during each event, $R_{L,max}$ , and the total number of lightning strikes during the event, $N_L$ . . . . .	94
4.30	Hourly temperature gradient observed during each event. The numbers indicate the fraction of the duration with temperature gradients that have an $R^2$ value larger than 0.9. The red line indicates the location of the median, the blue box denotes the interquartile range and the whiskers have a length of the 1.5 times the interquartile range. The red crosses indicate outliers. . . . .	96
4.31	Hourly temperature gradient for each time of the day during the analysed events. The black line indicates the number of hours for which a temperature gradient was observed. The red line indicates the location of the median, the blue box denotes the interquartile range and the whiskers have a length of the 1.5 times the interquartile range. The red crosses indicate outliers. . . . .	96
4.32	Wind direction measured at the different weather stations during the observed events for time steps with wind velocities $> 1.5$ m/s. . . . .	97
4.33	Distance of merged clusters depending on cluster number for identification of number of clusters. . . . .	100
4.34	Station average of meteorological conditions as observed by the weather stations for each low level wind field class (LLW). . . . .	101
4.35	Probability of rainfall occurrence depending on LLW class in comparison with unconditional probability of rainfall occurrence for two intensity thresholds. . . . .	102
4.36	Diurnal pattern of LLW classes and frequency of occurrence during IOP 2011. . . . .	103
4.37	Low level wind field clustering . . . . .	104
4.38	Wind direction obtained from cell tracking in radar images at different intensity thresholds. $n_{c,i}$ indicates the average number of rain cells per hour excluding dry periods at different intensity thresholds, $i$ . . . . .	108
4.39	CAP9: Occurrence of precipitation and weather type frequency on a seasonal and annual basis within the time period of 1957-2011 and frequency of event occurrence for the field experiments in 2010 and 2011. . . . .	113
4.40	GWTWS: Occurrence of precipitation and weather type frequency on a seasonal and annual basis within the time period of 1957-2011 and frequency of event occurrence for the field experiments in 2010 and 2011. . . . .	113

4.41	Comparison of modelled gradient in rainfall intensity along transect T0, T1 and T2 depending on wind direction for different parameter sets. . . . .	116
4.42	Gradient on T1 and T2 depending on wind direction, $\alpha$ , time constants, $\tau$ , wind speed, U, and temperature lapse rate, $\Gamma$ . . . . .	117
4.43	Elevation distribution of DEM at 100 m resolution and elevation distribution of the raingauges in the surrounding area. . . . .	118
4.44	Cumulative rainfall amount observed at the raingauges for the 9 events . . . .	120
4.45	Contours of the simulated rainfall amount in comparison with the station data used in the calibration of the model for 9 selected events. The model results are based on calibration by maximizing the correlation coefficient. . . . .	124
4.46	Comparison of simulated rainfall intensity in basin area for the 9 events. . . .	125
4.47	Comparison of simulated and observed rainfall gradients for the 9 events. The calibration based on the RMSE is shown in blue, the calibration based on the MAE is shown in red and the calibration based on the correlation coefficient is shown in green. . . . .	126
4.48	Comparison of simulated gradient in rainfall intensity along the transects for the 9 events. . . . .	127
4.49	Observations and variables in the coordinate system of the first two principal components. The numbers indicate the events and they are coloured according to the cluster they belong to. . . . .	134
4.50	Gradients with $R^2 > 0.5$ depending on weather station class (WSC) for 3 and 4 clusters. The red line indicates the location of the median, the blue box denotes the interquartile range and the whiskers have a length of the 1.5 times the interquartile range. The red crosses indicate outliers. . . . .	135
5.1	Boxplot of event data within each WSC. The red line indicates the location of the median, the box denotes the interquartile range and the whiskers have a length of the 1.5 times the interquartile range. . . . .	143
A.1	Reference Stations: from left to right, top to bottom: Zermatt, Trockener Steg, St. Niklaus, Saas Balen, Randa, Stalden . . . . .	163
A.2	Setup of mobile stations . . . . .	163
A.3	Topography of the hillslopes. DEM ©2011 swisstopo (JD100042). Source: Bundesamt für Landestopografie swisstopo (Art. 30 GeoIV): 5704 000 000 . .	164

A.4	Map of weather stations in 2010 and 2011. ©2011 swisstopo (JD100042). Source: Bundesamt für Landestopografie swisstopo (Art. 30 GeoIV): 5704 000 000 . . . . .	166
A.5	Distribution of intensities at MPS station for different tip durations. . . . .	167
A.6	Gradients on T1 and T2 based on the <b>original</b> data. The confidence interval of the regression is indicated by $ci_1$ and $ci_2$ for T1 and T2 respectively. The confidence interval based on the combined uncertainty in the data and the fitting method is indicated by $ci_{1,m}$ and $ci_{2,m}$ for T1 and T2 respectively. . . .	173
A.7	Gradients on T0 based on the <b>original</b> data. The confidence interval of the regression is indicated by $ci$ . The confidence interval based on the combined uncertainty in the data and the fitting method is indicated by $ci_m$ . . . . .	174
A.8	25, 50 and 75 % quantiles of rainfall intensity depending on the station altitude for the observed events. . . . .	176

## List of Symbols

Symbol	Description	Unit
A,B	cluster index	-
$C$	cluster	-
$C_c$	centroid of rain cell $c$	-
$C_{\uparrow}$	$= Pr[I_t < I_{t+1}]$	-
$C_{\downarrow}$	$= Pr[I_t > I_{t+1}]$	-
$C_{\updownarrow}$	$\equiv C_{\downarrow\uparrow} + C_{\uparrow\downarrow}$ (oscillation coefficient)	-
$C_{\updownarrow}$	fraction of triplets with increasing and decreasing $I$	-
$C_{\downarrow\uparrow}$	fraction of triplets with decreasing and increasing $I$	-
$C_{\downarrow\downarrow}$	fraction of triplets with decreasing and decreasing $I$	-
$C_{\uparrow\uparrow}$	fraction of triplets with increasing and increasing $I$	-
$C_r$	unit conversion factor	$3.6 \cdot 10^6 \text{ mm/h}$
$D$	duration	h
$D_{a,b}$	distance between cluster centres	-
$D_a$	autocorrelation length	h
$D_p$	duration of rainfall time steps	h
$D_D$	Drop size distribution	-
$\Delta t_{tip}$	tip accumulation interval	min
$\Delta t_{tip}^*$	$\Delta t_{tip} - 1$	min
$\Delta t$	aggregation interval	min
$\Delta z$	elevation difference	m
E	event	-
H	filter mask	-
$I$	precipitation intensity	mm/h
$I_{max}$	maximum intensity	mm/h
$I_m$	measured intensity	mm/h
$I_{dc}$	dynamically corrected intensity	mm/h
$I_p$	post-processed intensity	mm/h
$I_{wc}$	wind corrected intensity	mm/h
$M_j$	number of observations	-
$N_t$	number of stations	-



$R^2$	coefficient of determination	-
$R_L$	lightning rate	$h^{-1}$
$R_{L,m}$	maximum lightning rate	$h^{-1}$
P	cumulative precipitation	mm
S	rate of cloud water generation by moist adiabatic uplift	
$S_R$	solar radiation	W/m <sup>2</sup>
T	temperature	°C
<b>U</b>	wind vector	m/s
U	wind speed	m/s
$V_d$	drop volume	
$V_e$	excess precipitation amount	mm
$V_0$	water volume used in tipping bucket static calibration	l
$V_{obs,i}$	recorded volume in static calibration by gauge $i=1,\dots,$ $n_p$	l
$\Gamma$	temperature lapse rate	K/100m
$\Gamma_m$	moist adiabatic lapse rate	K/100m
$\Gamma_d$	adiabatic lapse rate	K/100m
a,b	cluster elements	-
$\alpha_S$	wind direction estimated from weather stations	°
$\alpha_R$	wind direction estimated from radar data	°
$c, c^*$	rain cell index	-
$ci$	regression confidence interval of T0	
$ci_m$	confidence interval of T0 accounting for uncertainty in the data	
$ci_j$	regression confidence interval of Tj, j=1,2	
$ci_{j,m}$	confidence interval of Tj (j=1,2) accounting for uncertainty in the data	
$d_{ac}$	autocorrelation length	h
$d_{a,b}$	distance between cluster elements	-
d	distance	m
$e_p$	partial wind-induced error	-
f	fraction	-
$f_I$	fraction of high intensity time steps	-
$f_{c,i}$	calibration factor of pluviometer $i=1, \dots, n_p$	-
$f_w$	wind correction factor	-
$f_{WT}$	frequency of weather types	-
$f_{WT}$	frequency of weather types with event occurrence	-
$f_{WT,P}$	frequency of weather types with precipitation occurrence	-
$f_{WT,S}$	seasonal frequency of weather types	-
$f_{WT,P,S}$	seasonal frequency of weather types with precipitation occurrence	-
g	gradient	mm/100m
$g_1$	gradient T1	mm/100m
$g_2$	gradient T2	mm/100m
$g_o$	gradient of original data	mm/100m

Symbol	Description	Unit
$g_p$	gradient of post-processed data	mm/100m
$g_{qp}$	gradient in p-th quantile	mm/h*100m
$h$	intercept	mm
$i, j$	index	-
$\mu_{r, Pi}$	mean catch efficiency in each group of tipping bucket raingaugesi=1,2	-
$n_k$	number of clusters	-
$n_e$	number of cluster elements	-
$n_c, n_{c^3}$	number of rain cells	-
$n_p$	number of pluviometers	-
$n_d$	number of drops per unit volume of air and unit drop size interval	-
$p$	percentile	%
$p_a, p_b$	parameters of dynamic calibration	-
$q_p$	p-th quantile	
$q_c$	vertically integrated cloud water density	
$q_s$	vertically integrated hydrometeor density	
$r_{c,i}$	calibration factor of pluviometer $i=1, \dots, n_p$	-
$\rho$	correlation coefficient	-
$t$	time	h
$\tau_c$	time constant for cloud water conversion	s
$\tau_f$	time constant for hydrometeor fallout	s
$t_i$	time step i	min
$u, v$	wind vector components	m/s
$u_{t,j}, v_{t,j}$	wind vector components at time step t and station j	m/s
$u_T$	terminal velocity	m/s
$w$	frequency	$(100m)^{-1}$
$w_0$	cut-off frequency	$(100m)^{-1}$
$w_u, w_v$	frequency components	$(100m)^{-1}$
$x$	easting in Swiss coordinates CH1903	m
$y$	northing in Swiss coordinates CH1903	m
$z$	elevation	m
	Constants	
$c_1$	parameter in clausius-clapeyron approximation	17.67
$c_2$	parameter in clausius-clapeyron approximation	243.5°C
$L$	latent heat of vaporization	$2.25 \cdot 10^6 \text{ J/kg}$
$R_v$	gas constant	461 J/kgK



# Preface



## 1.1 Acknowledgement

I would like to thank my advisor, Professor Paolo Burlando, for giving me the opportunity to conduct this experimental investigation of orographic rainfall in the context of this Ph.D. project. I highly appreciated his input on my scientific work, and I am thankful that I could profit from his expertise in the field of rainfall research.

I am also very grateful for the numerous scientific discussions with my supervisor, Dr. Peter Molnar, which helped me in the development of my research, and for his ideas and inputs on how to approach scientific questions. I also thank my external supervisor, Professor András Bárdossy, for agreeing to revise and examine my thesis and for his scientific input on the data analysis.

The field experiment was possible only thanks to the help of several people. First I would like to thank Maurizio Savina, who was a Ph.D. student working within the same research project, for his collaboration in the organization of the fieldwork and also for all the discussions we had during this time. I especially thank Thomy Keller and Coni Senn, who helped me in numerous ways in the preparation of the weather stations and their installation in the field and whose creative ideas helped to address the technical challenges of fieldwork in an alpine environment.

I would like to thank the community of Zermatt for allowing me to set up the weather stations and for their support with the organization and logistics of the field work. I greatly appreciated the help from ZBAG, who allowed the use of their infrastructure during the field experiment. Furthermore, I thank MeteoSwiss and the communities of Saas Balen, Randa, St. Niklaus and Stalden for agreeing on the installation of the reference weather stations and to all the people who kindly provided a suitable location. In addition, I acknowledge MeteoSwiss, ARPA Piemonte, ARPA Valle d'Aosta and Meteomedia for providing data for this study.

I am also grateful for everyone who helped in the deployment of the weather stations during the intensive observation periods. These were fellow PhD students and the scientific assistants in our group, whom I also thank for the great time we spent during these years. We had many interesting discussions on science and other topics during lunch and coffee breaks. Special thanks also to Georgie Bennett for being a great office mate and for reviewing part of this document. Last but not least I also thank my family for their support and encouragement during this time.



## 1.2 Summary

Mountain ranges strongly affect meteorological processes and lead to enhanced rainfall occurrence, which makes those areas prone to natural hazards, such as landslides, debris flow and flash floods. Therefore, a better understanding of the effect of topography on precipitation amount and intensity is of great importance. In this study, the event rainfall patterns with respect to terrain elevation were experimentally investigated, with focus on liquid precipitation during the summer season. The effect of altitude was analysed in terms of gradient patterns and linked to the prevailing weather type. This analysis provides experimental evidence of the variability in the spatial rainfall distribution in complex terrain and how it is controlled by the rainfall regime, the atmospheric conditions and the surrounding terrain.

Field experiments were carried out in the Swiss Alps in the area of Zermatt (Canton Wallis) where 15 automatic weather stations were installed along two hillslope transects for two summer seasons. The two intensive observation periods provided a high resolution rainfall time series for 27 events. Their analysis provides insight into how rainfall is affected by topography at small temporal and spatial scales and how the formation of gradients is controlled by differences in rainfall intensity and duration among the different weather stations.

For the observed events, the effect of altitude is analysed by means of linear regression of cumulative event rainfall and terrain elevation, which is a commonly applied method in the generation of distributed rainfall maps for hydrological modelling applications. The results show a high variability in rainfall gradients at the event time scale. For about half of the observed events, either positive or, especially at higher elevations, also negative gradients are observed. In the other events, elevation accounts for less than 50% of the observed variance in the cumulative rainfall, indicating that the assumption of a linear increase in rainfall with altitude at the event time scale is not generally valid.

Analysis of the different controlling factors on the observed gradient patterns and comparison with idealized model simulations highlights that the rainfall regime is predominantly responsible for the observed variability. A strong gradient in rainfall duration is found for stratiform events whereas in the case of convective weather situations the gradients in cumulative rainfall are mostly due to a gradient in rainfall intensity.

By means of cluster analysis techniques, the observed events are classified according to prevailing wind speed and rainfall characteristics, such as rainfall intensity, duration and amount. The resulting groups of events show different gradient patterns and enable long lasting, stratiform events to be distinguished from short duration convective events. This classification is in good agreement with the distinction of the rainfall regime based on lightning data.

To further relate the observed gradient patterns to meteorological conditions the events were characterized according to their large scale weather type and the prevailing wind field on the ground and in the atmosphere. Analysis of the prevailing wind direction in the atmosphere by means of centroid tracking in rainfall cells obtained from radar images demonstrates the



strong relation of rainfall occurrence and south-westerly flow conditions. Weather type classes show some relation to rainfall occurrence in the area under investigation, but they are not able to distinguish among different types of events. On the other hand, the wind field observed on the ground shows distinct patterns for intense rainfall as compared to low intensity rainfall, with the latter being characterized by lower wind speeds.

An analytical model of upslope condensation with downstream advection under the assumption of steady state atmospheric conditions is calibrated for selected events, with the aim to illustrate the variability in the rainfall pattern that can be expected at the basin scale due to complex terrain. It highlights the strong variability in the rainfall distribution depending on the prevailing wind direction. Comparison of the simulated and observed rainfall distribution shows gradients of similar magnitude under stratiform rainfall regimes, indicating that the model accounts for the most relevant meteorological processes in those situations and can provide qualitative information about the rainfall distribution at the basin scale. However, the stronger deviation of the observed gradients from the simulated ones in situations with convective activity suggests the presence of additional rainfall generating mechanisms, not accounted for in the model.

The effect of spatial scale on the gradients is assessed by analysing the  $R^2$  value of the regression analysis of cumulative precipitation and terrain elevation obtained from filtered digital terrain models. The results indicate that terrain features at a scale of 3 km explain the highest fraction of variance in the cumulative event rainfall. However, the results also show a strong dependence on the applied filter and a strong variability among different events. This indicates that rainfall gradients are also strongly affected by the small scale terrain structure.

Since precipitation measurements are affected by multiple errors, several corrections are applied to the measured data in the form of post-processing. The measurement errors and their propagation in the different post-processing steps are analysed in order to quantify the uncertainty in the data. To which extent the selected sensors are suitable for investigation of precipitation processes is demonstrated in the analysis of temporal and spatial correlation. The results show that post-processing can lead to strong artefacts in those commonly applied methods. Furthermore, they demonstrate the limited ability of tipping bucket gauges to resolve the spatial rainfall pattern at low intensities. However, the post-processing was successful in reproducing the cumulative rainfall amount and the temporal correlation structure in the rainfall time series. In particular, the results show that the strength of a rainfall gradient is likely to be underestimated if data are not corrected for wind-induced errors and undercatch of high intensities.

## 1.3 Zusammenfassung

Gebirgszüge haben einen starken Einfluss auf meteorologische Prozesse und führen zu erhöhter Niederschlagshäufigkeit, was diese Gebiete anfällig macht gegenüber Naturgefahren, wie zum Beispiel Erdbeben, Murgängen und Überschwemmungen. Deshalb ist ein besseres Verständnis des Effekts der Topographie auf die Niederschlagsmenge und -intensität von grosser Bedeutung. In dieser Studie wird das Verhalten des Niederschlags in Abhängigkeit von der Terrainhöhe experimentell untersucht, wobei der Fokus auf Ereignissen in der Sommersaison liegt. Der Einfluss der Höhe wird anhand von Niederschlagsgradienten untersucht, welche mit der vorherrschenden Wettersituation in Verbindung gebracht werden. Diese Studie erbringt einen experimentellen Nachweis für die Variabilität der räumlichen Verteilung des Niederschlags im Gebirge und zeigt, wie diese Variabilität durch das Niederschlagsregime, die atmosphärischen Bedingungen und das umgebende Terrain beeinflusst wird.

Die experimentelle Untersuchung wurde in den Schweizer Alpen im Gebiet von Zermatt (Kanton Wallis) durchgeführt, wo während der Sommermonate in den Jahren 2010 und 2011 15 automatische Wetterstationen in der Falllinie von zwei Hängen installiert wurden. Diese Feldexperimente lieferten eine hochaufgelöste Messreihe von 27 Niederschlagsereignissen. Deren Analyse zeigt auf, wie der Niederschlag auf kleiner räumlicher und zeitlicher Skala durch die Terrainhöhe beeinflusst wird und wie die Bildung von Niederschlagsgradienten durch Unterschiede in der Niederschlagsintensität und -dauer erklärt werden kann.

Für die beobachteten Niederschlagsereignisse wird der Effekt der Höhe anhand von linearer Regression der kumulativen Niederschlagsmenge in Abhängigkeit von der Terrainhöhe analysiert. Dies ist eine weit verbreitete Methode, um die räumliche Verteilung des Niederschlags für Anwendungen in der hydrologischen Modellierung abzuschätzen. Die Resultate zeigen eine hohe Variabilität in den Niederschlagsgradienten auf der Zeitskala von einzelnen Ereignissen. Für etwa die Hälfte der beobachteten Ereignisse werden entweder positive oder negative Niederschlagsgradienten beobachtet, wobei die negativen vermehrt am höher gelegenen Hang auftreten. In den anderen Fällen erklärt die Terrainhöhe weniger als 50 % der beobachteten Varianz im kumulativen Niederschlag. Dies ist ein Hinweis, dass die Annahme eines linearen Anstiegs mit der Höhe auf der Zeitskala von einzelnen Ereignissen nicht allgemein gültig ist. Die Analyse der Faktoren, welche zu den beobachteten Gradientenmustern führen, und ein Vergleich mit idealisierten Modellsimulationen zeigen, dass hauptsächlich das Niederschlagsregime verantwortlich ist für die beobachtete Variabilität. Für Ereignisse mit Frontregen wird ein ausgeprägter Gradient in der Dauer des Niederschlags beobachtet, während für Gewitter die Gradienten im kumulativen Niederschlag mehrheitlich auf Unterschiede in der Intensität zurückzuführen sind.

Durch die Anwendung verschiedener Cluster-Analysetechniken werden die beobachteten Ereignisse gemäss der vorherrschenden Windgeschwindigkeit und Niederschlagseigenschaften, wie zum Beispiel Dauer, Menge und Intensität, klassifiziert. Die resultierenden Klassen von Ereignissen

nissen zeigen unterschiedliche Gradientenmuster und ermöglichen die Unterscheidung zwischen lang andauernden stratiformen Ereignissen und kurzen konvektiven Ereignissen. Diese Klassifikation stimmt gut überein mit der Unterscheidung des Niederschlagsregimes, die auf der Analyse von Blitzdaten basiert.

Um die beobachteten Gradientenmuster weiter mit den meteorologischen Bedingungen zu verknüpfen, wurden die Ereignisse in Bezug auf die allgemeine Wetterlage und das vorherrschende Windfeld über dem Boden und in der Atmosphäre charakterisiert. Die Windrichtung in der Atmosphäre wurde anhand von „Centroid-Tracking“ von Niederschlagszellen aus Radarbildern abgeschätzt. Das Resultat zeigt, dass Niederschlagsereignisse vor allem bei Wetterlagen mit südwestlicher Windrichtung auftreten. Die Klassifizierung der allgemeinen Wetterlage zeigt nur einen schwachen Zusammenhang mit dem Auftreten von Niederschlagsereignissen in diesem Gebiet. Insbesondere kann sie die beobachteten Unterschiede in den Ereignissen nicht erklären. Das Windfeld über dem Boden zeigt andere Muster für intensive Niederschlagsereignisse im Vergleich zu solchen mit geringer Niederschlagsintensität, wobei letztere mit schwachen Windgeschwindigkeiten in Verbindung stehen.

Ein analytisches Modell der Kondensation aufgrund des Höhenanstiegs und anschliessender Advektion unter der Annahme eines Gleichgewichtszustandes wird für ausgesuchte Ereignisse kalibriert. Das Ziel ist, die Variabilität im Niederschlagsmuster aufzuzeigen, welche im Einzugsgebiet aufgrund der Topographie zu erwarten ist. Die Modellresultate illustrieren die grosse Variabilität in der Niederschlagsverteilung in Abhängigkeit von der Windrichtung. Der Vergleich von simulierten und beobachteten Niederschlagsverteilungen zeigt Niederschlagsgradienten von ähnlicher Grössenordnung für stratiforme Ereignisse, was darauf hinweist, dass das Modell in diesem Fall die relevanten Prozesse berücksichtigt und deshalb qualitative Aussagen über die Niederschlagsverteilung im Einzugsgebiet ermöglicht. Für konvektive Ereignisse zeigt das Modell jedoch grössere Abweichungen von den beobachteten Niederschlagsgradienten, was auf das Vorhandensein weiterer Mechanismen der Niederschlagsbildung hinweist, welche im Modell nicht berücksichtigt werden.

Der Einfluss der räumlichen Auflösung auf die Niederschlagsgradienten wird anhand des  $R^2$ -Werts der Regressionsanalyse von kumulativem Niederschlag und Terrainhöhe für verschiedene gefilterte digitale Höhenmodelle untersucht. Die Resultate zeigen, dass die Terrainstrukturen bei einer Auflösung von etwa 3 km den grössten Teil der Varianz im kumulativen Niederschlag erklären. Jedoch sind die Resultate abhängig von der verwendeten Filter-Methode und zeigen eine grosse Variabilität zwischen den verschiedenen Ereignissen. Dies ist ein Indiz, dass die Niederschlagsgradienten auch durch kleinskalige Terrainstrukturen beeinflusst werden.

Da Niederschlagsmessungen mit unterschiedlichen Messfehlern behaftet sind, müssen die gemessenen Daten nachträglich korrigiert werden. Die Messfehler und deren Fortpflanzung in der Korrektur der Daten werden analysiert, um die Unsicherheit in den Daten zu quantifizieren. Inwieweit die gewählten Messinstrumente für die Analyse des Niederschlagsprozesses geeignet sind, wird anhand einer Analyse der zeitlichen und räumlichen Korrelation aufgezeigt.

Die Resultate zeigen, dass die Messmethoden die statistischen Analysen beeinflussen, so dass nur bedingt Rückschlüsse auf den Niederschlagsprozess möglich sind. Weiter belegen sie, dass Pluviometer, welche den Niederschlag mit Wippen registrieren, das räumliche Niederschlagsmuster nur ungenau auflösen können. Die angewendeten Korrekturen ermöglichen jedoch eine gute Reproduktion der kumulativen Niederschlagsmenge und der zeitlichen Korrelationsstruktur in der Niederschlagszeitreihe. Die Resultate zeigen vor allem, dass der Niederschlagsgradient unterschätzt wird, wenn die Daten nicht einerseits um den windinduzierten Fehler und andererseits wegen der allgemeinen Unterschätzung der hohen Intensitäten korrigiert werden.



## Chapter 2

# Introduction

In mountain basins, which are characterized by fast hydrological response time, accurate forecasts of precipitation are very important. Spatially distributed rainfall data are required for many practical and scientific applications such as input for hydrological simulations and evaluation of weather forecasts (Colle et al., 2000; Clark and Slater, 2006). Accurate estimations of the spatial distribution of rainfall are also required in the risk assessment of landslides, which are often triggered by intense rainfall (D'Odorico et al., 2005; Guzzetti et al., 2008). Since rainfall input data are responsible for a large part of the uncertainty in hydrological model outputs such as runoff or streamflow (Fekete et al., 2004; Bronstert and Bardossy, 2003), more accurate description of the spatial and temporal distribution of precipitation is required to better model streamflow and runoff response in mountain watersheds (Mandapaka et al., 2009; Obled et al., 1994; Arnaud et al., 2002).

Estimation of the spatial distribution of rainfall is commonly based on either ground observations from rain gauges or remote sensing by satellite or weather radar. Point measurements on the ground are of particular importance since they are also used in the calibration and evaluation of rainfall maps obtained by remote sensing techniques (Joss and Lee, 1995; Dinku et al., 2008). Quantitative precipitation estimation in mountain areas is a particularly challenging task since both observations and the meteorological processes themselves are affected by the complex orography in numerous ways.

Terrain causes modification of the air mass flow such as blocking or forced lifting (Roe, 2005; Rotunno and Ferretti, 2001), and this induces strong differences in precipitation distribution on the lee side as compared to the windward slope (e.g. Neiman et al., 2002; Sinclair et al., 1997). These modulating effects of the terrain result in a strong signature of orography in the temporal and spatial rainfall structure (Savina et al., 2011; Nykanen and Harris, 2003; Harris et al., 1996), which can be observed across a wide range of spatial and temporal scales and which shows a strong dependence on the prevailing wind direction of the rain storms (Hill, 1983). In addition to the inherent complexity of the meteorological processes in mountain areas, their monitoring presents various technical difficulties. The number of ground obser-

variations is generally low, especially at high altitudes (Weisse and Bois, 2001), due to limited accessibility and power supply. Furthermore, the measurements are affected by wind-induced errors. Radar data also suffer from large uncertainties due to ground clutter and beam shielding by surrounding mountains (Germann et al., 2006; Joss and Germann, 2000; Dinku et al., 2002). Due to the difficulties in radar measurements in mountain terrain, a dense network of ground observations at high spatial and temporal resolution is crucial for the analysis of the precipitation distribution.

Spatially distributed precipitation maps are often generated either by merging of radar and rain gauge data (e.g. Krajewski, 1987) or by interpolation of point observations (e.g. Kyriakidis et al., 2001), and therefore they strongly depend on availability of ground based data. Furthermore, generation of realistic maps by interpolation of point measurements needs to account for the effect of the terrain on precipitation distribution (Daly et al., 1994; Hutchinson, 1995; Schiemann and Frei, 2010), which requires a detailed knowledge of the involved processes and their interaction with the underlying topography.

So, on one side there is a lack of rainfall data at high spatial and temporal resolution in mountain environments and a limited knowledge about how the involved meteorological processes are affected by terrain. On the other hand, there is a strong need for accurate information about the spatial and temporal distribution of precipitation. Therefore, this work aims at improving the knowledge about the spatial distribution of rainfall in mountain areas by experimental investigation of the rainfall processes on the ground. It also provides insight into the driving mechanisms which form rainfall gradients with altitude by analysing how orography affects the precipitation processes and how the effect of altitude is related to the prevailing meteorological conditions.

The following section describes the goals and motivation of this study, and it ends with a summary of the research questions (Section 2.1). The main findings regarding these research questions are listed in Section 5.2.1. Section 2.2 summarizes the state of the art in the field of point rainfall measurements, i.e. their errors and necessary corrections (Section 2.2.1), and in the field of orographic effects on spatial rainfall distribution and its control by terrain and weather characteristics (Section 2.2.2). Based on this, the experimental design and working hypotheses of this study are presented in Section 2.2.3. The introduction finishes with an outline of this document (Section 2.3).

## 2.1 Goal and motivation

Spatial variability in rainfall affects the peak flow of small mountain catchments mostly because there is less attenuation than in river networks of large basins (Mandapaka et al., 2009). The lack of smoothing of the peak discharge in small catchments, along with fast hydrological response and related short lead time for forecasts, puts small basins at particular risk of

rainfall related natural hazards, such as flash floods. In the last decades the southern alpine region of Switzerland has experienced an increase in severe weather situations, which have led to fatalities and large economic losses due to landslides, debris flow and flood events (Hegg et al., 2002; Röthlisberger, 1988; Zeller and Röthlisberger, 1994).

Against the background of increases in weather related natural hazards, a more detailed knowledge of the involved meteorological processes and their interaction with orography is crucial in alpine areas. This requires accurate precipitation measurements on the ground, which can then be used for the generation of precipitation maps by spatial interpolation (Hutchinson, 1995; Daly et al., 1994), as ground truth for the calibration of remote sensing based precipitation maps such as satellite images or weather radar maps (Ciach and Krajewski, 1999a,b) or for spatial merging of radar and gauge data (Krajewski, 1987). A dense network of raingauges is of particular importance in mountain areas, where radar measurements are highly affected by errors due to ground clutter, beam blocking and attenuation (Germann et al., 2006; Joss and Germann, 2000; Dinku et al., 2002). Under those circumstances the estimation of spatially distributed precipitation strongly relies on point measurements on the ground.

However, installation and maintenance of rain gauges at high altitudes is challenging and therefore most operational networks have a higher density of stations at low elevations, which leads to an undersampling of the rainfall process at high altitudes (Briggs and Cogley, 1996; Weisse and Bois, 2001). This is in particular true for gauges operating at high temporal resolution, which require more maintenance and are more difficult to install than simple cumulative precipitation gauges. Additionally, because stations at high elevations experience strong winds, point measurements of rainfall at high altitudes are more susceptible to various errors such as wind-induced losses (Sevruk, 1982).

To gain further insight into the rainfall process at high elevations, this work describes an experimental investigation of rainfall along two hillslope transects in an alpine valley in Switzerland (Zermatt, Canton Wallis). Because the effect of altitude on meteorological processes is a very localized phenomenon that cannot be extrapolated to other areas, gathering of data at high spatial and temporal resolution is particularly important. Given the difficulties related to precipitation measurement, in particular at high altitudes, the study focuses in a first part on a detailed analysis of different error sources with the aim of developing a detailed correction procedure for rainfall data and an estimate of their uncertainty for different types of raingauges.

Mountains cause a modification of the flow of air masses by orographic lifting and blocking (Roe, 2005), which leads to strong spatial variability in the rainfall distribution over a wide range of spatial scales. The modulating effects of orography are numerous, and their occurrence depends on weather type as well as topographic features. Globally, precipitation tends to increase in areas with high mountains but also at the catchment scale rainfall can exhibit strong spatial variability due to local orographic blocking or enhancement effects (Sevruk, 1997; Weingartner and Pearson, 2001; Singh and Kumar, 1997). In addition, the influence



of the terrain is not constant in time but it depends on weather type, climatic conditions and temporal scale of the processes under investigation. On seasonal and annual time scales, precipitation amounts often tend to increase with elevation (Hill, 1983; Minder et al., 2008; Sevruk, 1997; Wastl and Zangl, 2010). However, depending on the climatic conditions, a decrease may also be observed (Dinku et al., 2008). The pattern at the event timescale can deviate substantially from that observed over the long term and tends to be more variable (Loukas and Quick, 1996, 1993; Sevruk and Miegilitz, 2002). As a result of the various effects of terrain on rainfall processes, mountain catchments are characterized by high spatial rainfall variability (Savina et al., 2011).

Many techniques for the generation of precipitation maps that account for orographic effects have been developed. One line of research has approached the task of estimating orographic effects by modelling of the underlying physical processes (e.g. Zangl, 2007). Due to the complexity of the involved meteorological processes, such models tend to be computationally intensive and are often confined to simplified terrain geometry, which limits their use in real time applications such as early warning systems of rainfall related natural hazards. However, under the simplified assumption of steady state atmospheric conditions and assuming linearity in the physical processes, orographic precipitation can be modelled even in the case of complex topography (Smith, 2003b). This approach suffers from the strong simplification of the meteorological processes, but nevertheless it can provide a general indication of the effect of orography on rainfall patterns. Furthermore, it serves as a benchmark against which observations can be compared in order to identify other relevant processes.

Another line of research is to estimate the precipitation distribution solely on the basis of interpolation of scarcely scattered point measurements. Since in most raingauge networks the high altitudes are generally under-represented, many techniques have been developed to account for the effects of local topographic features, such as elevation, slope and exposition. Common techniques are kriging with external drift (Kyriakidis et al., 2001) or multiple linear regression (Daly et al., 1994), and in hydrological models often a constant elevation gradient of precipitation is applied (Finger et al., 2011). These techniques, however, are not able to capture the observed spatial rainfall variability in the catchment at the event time scale. This is mainly due to the fact that the orographic effect strongly depends on the local interaction between terrain and meteorological processes.

For example, Hill (1983) found rainfall enhancement due to altitude to be related to low level wind speed and direction. Classification of wind patterns across Switzerland showed a connection between certain wind fields and particular patterns of rainfall distribution at the regional scale (Weber and Furger, 2001) and several studies have demonstrated a relation between atmospheric circulation types and rainfall and flood occurrence (Schiemann and Frei, 2010; Bardossy and Filiz, 2005; Sevruk and Miegilitz, 2002). Furthermore, the relationship between terrain elevation and rainfall has been found to be dependent on the spatial resolution at which the terrain is represented (Sharples et al., 2005; Hutchinson, 1998; Daly et al., 2007).

The need for more knowledge about the orographic effects on rainfall distribution and its dependence on the meteorological conditions was addressed in the present study by a thorough investigation of the rainfall variability along an alpine hillslope. By focusing on how event rainfall amount, intensity and duration are controlled by terrain characteristics and atmospheric conditions, this work aims to provide experimental evidence on the type and magnitude of orographic effects and their dependence on the general weather situation. This study provides insight into how different weather types are related to rainfall occurrence in this particular area with a focus on the effect of the wind direction on the ground and in the atmosphere as estimated from weather stations and radar images respectively. Additionally, the dependence of the observed orographic effects on the terrain resolution was investigated in order to improve the understanding of the scale dependence of the topographic effects on rainfall processes. By comparing the observed rainfall patterns at the hillslope scale with the pattern obtained by assuming a constant gradient and with the pattern obtained by assuming steady state atmospheric conditions, this work provides guidance as to which techniques of generating spatially distributed rainfall are appropriate, and it demonstrates their limitations. Furthermore, this study highlights under which circumstances and at which spatial scale those methods can be used for realistic estimation of the rainfall distribution at the event time scale. In particular the following questions were addressed:

- i. Based on an experimental investigation of rainfall in a mountain area, to which extent can the variability in rainfall cumulative amount, intensity and duration be explained by the terrain elevation at the time scale of individual rain storms, focusing on summer events with liquid precipitation?
- ii. How do errors in rainfall measurements affect the estimation of cumulative event rainfall and the temporal and spatial correlation structure of the rainfall time series?
- iii. How do the observed spatial rainfall patterns compare to the simulated spatial distribution of rainfall obtained by applying a steady state model of orographic rainfall, which accounts for upslope condensation and subsequent downslope advection?
- iv. At which spatial scale does the local terrain show the highest correlation with the ground observations of event rainfall amounts?
- v. How are the orographic effects observed in the spatial rainfall distribution on the ground related to atmospheric conditions such as wind direction, large scale weather type and rainfall regime?

## 2.2 State of the art

### 2.2.1 Ground observation of rainfall

Rainfall measurements at the point scale are highly affected by measurement errors, which need to be considered in the data analysis (Sieck et al., 2007; Villarini et al., 2008). This section gives an overview of the state of the art in point measurement of rainfall on the ground focusing on the widely used electronic weighing gauges and tipping bucket gauges, which were used in the experimental investigation of the orographic effect on event rainfall. In particular their advantages and disadvantages with respect to installation in mountain areas are discussed as well as their measurement errors and possible corrections.

#### 2.2.1 - i Experimental investigations of rainfall at small spatial scales

The effect of altitude on precipitation patterns has been experimentally investigated by the deployment of raingauge networks in different mountain areas. Blumer (1994) investigated several hillslopes at hourly resolution over a period of 2 years. Looking at annual and seasonal cumulative precipitation no general pattern was observed. Some of the study sites showed increasing precipitation with elevation and others a decrease or no differences in the vertical profile. Classification according to prevailing weather types showed a stronger effect of elevation for cyclonic events as compared to convective events. Additionally, cyclonic events with airflow parallel to the mountain range were found to have lower gradients as compared to those with airflow perpendicular to the mountain range.

In recent years the use of wireless sensor networks for hydrological applications has been tested in several studies (e.g. Simoni et al., 2011; Trubilowicz et al., 2009; Ingelrest et al., 2010). Given the need for data at high spatial and temporal resolution, the concept of weather stations which are easy to deploy and which are independent of an external power source seems promising, especially in basins with complex topography. Simoni et al. (2011) deployed a dense network of wireless weather stations in a mountain catchment in the Alps to investigate spatial variability in rainfall and temperature. Trubilowicz et al. (2009) investigated a forested catchment in British Columbia (Canada) with a focus on the technical aspect of the deployment, such as hardware reliability and power consumption. Despite various technical issues that still have to be resolved, the use of wireless stations has potential for collecting hydrological data at high spatial and temporal resolution in mountain areas where easy and flexible deployment is important.

### 2.2.1 - ii Errors in point rainfall measurements

The widely used tipping bucket raingauge (TBR) can be deployed within networks of wireless weather stations (Ingelrest et al., 2010) allowing a high spatial coverage at affordable costs. Its main disadvantage is the sensitivity to various sources of systematic and random errors.

Random errors may occur when the tipping mechanism is obstructed or the funnel outlet is blocked by leaves or insects. Those errors are difficult to detect since the device might still record precipitation but a much lower intensity is registered. One way to detect them is to use a dual gauge system in order to have redundancy in the raingauge network (Krajewski et al., 2003). The raingauges themselves may also be affected by random local errors, resulting from the time-sampling effect due to the discretization and hydrodynamic water flow instabilities in the funnel (Ciach, 2003).

Systematic errors are due to water loss at high intensity rainfall during the movement of the tips, wind-induced losses caused by the disturbance of the wind field around the gauge, evaporation and wetting losses of water in the funnel before it is being measured, and splashing of rain drops upon impact (Sevruk, 1982; Duchon and Essenberg, 2001). Wind-induced errors are of particular importance in mountain areas as weather stations at high altitudes are generally exposed to higher wind speeds compared to stations in the valley for the reason that air masses flowing over mountain tops are less affected by friction due to terrain (Barry, 2008). Since wind-induced losses tend to be altitude dependent, their correction is of particular importance when analysing the effect of altitude on the rainfall distribution from raingauge observations. Another important source of error is the sampling mechanism of tipping bucket gauges, which is designed to measure the time needed for the accumulation of one tip volume rather than an actual intensity. Low intensity rainfall is therefore poorly resolved by the gauge and depends on tip volume and sampling time (Habib et al., 2001). Even though this does not introduce an error in the cumulative precipitation amount, it strongly affects the measured rainfall intensities and the intermittency of the rainfall process. This effect is particularly important at the start and end of a storm, which tend to be characterized by low intensities. The timing of the storm estimated by a TBR is therefore also affected by high uncertainty.

As a consequence of these various sources of errors in the observations, the resulting uncertainty in commonly used statistics, such as the estimation of return periods, can be significant (La Barbera et al., 2002; Molini et al., 2005). For electronic weighing gauges the sampling error is negligible in comparison to TBRs, however it is also affected by wind-induced losses and underestimation of high intensities with the latter being less pronounced as compared to TBRs. While providing the advantage of more accurate rainfall measurements, the installation of a weighing raingauge is more complicated due to the requirement of a nearby power source. In addition, because of its considerably higher cost, it is not suitable for dense raingauge networks in mountain areas.

### 2.2.1 - iii Correction of point rainfall measurements

In order to overcome the errors mentioned above, many corrections have been suggested in the literature. The most important errors are wind-induced losses, which can be in the order of up to 10% for liquid rainfall, and underestimation of high intensities, which can be as high as 10-15% for intensities  $>200$  mm/h (La Barbera et al., 2002; Marsalek, 1981). The underestimation of high intensity rainfall can be addressed by dynamic calibration, which provides an intensity dependent correction. In dynamic calibration a known range of intensities is recorded by the gauge and the observations are compared to the theoretically expected one. By fitting of a power law function a calibration function is estimated (Vasvari, 2005; Niemczynowicz, 1986). Due to the nonlinearity in the underestimation of the rainfall intensities a dynamic calibration is generally recommended. Based on an extensive field intercomparison, the World Meteorological Organization (WMO) provides empirical formulas for dynamic calibration of a wide variety of instruments (Vuerich et al., 2009). In the case of TBR also a static calibration is required. It corrects for the constant device specific bias in the recorded intensities, which is, unlike dynamic calibration, independent of the rainfall intensity.

The sampling error in TBRs has been investigated by applying different disaggregation techniques to the time series in order to reconstruct a realistic distribution of rainfall intensities (e.g. Molini et al., 2005; Wang et al., 2008; Fiser and Wilfert, 2009). Wind-induced losses have been investigated either by means of an empirical comparison of unshielded gauges with wind shielded gauges and ground level gauges (Sevruk, 1982) or by numerical studies of the wind field around the gauge and its effect on the trajectory of falling raindrops (Habib et al., 1999; Nespov and Sevruk, 1999).

Given the various sources of errors and their effect on the recorded data, the choice of instruments strongly depends on what the data will be used for. Application of correction procedures helps to minimize the error in the time series and can thereby improve the performance of rainfall runoff models. For example Habib et al. (2008) showed that dynamic calibration of TBR data and wind correction introduced 5 to 15% difference in the runoff peak and volume simulated by a distributed hydrological model.

### 2.2.2 Orographic effects on precipitation

Rainfall generation processes are strongly affected by orography, which leads to a strong signature of the underlying terrain in the spatial distribution of precipitation. Estimation of spatially distributed rainfall is commonly based either on statistical interpolation of precipitation measurements or on numerical or analytical modelling of the physical processes involved in the generation of precipitation. Commonly used rainfall interpolation techniques, which incorporate the dependence on topographic properties, are linear regression (Daly et al., 1994; Basist et al., 1994), geostatistical techniques (Hevesi et al., 1992) and thin plate smoothing

splines (Hutchinson, 1998). However, their ability to account for the complex interaction of meteorological processes with the underlying terrain is limited. Tobin et al. (2011) used terrain elevation in combination with weather forecasts as covariates in kriging with external drift, which resulted in an improvement in a hydrological model application. These results demonstrate the importance of improved interpolation techniques that account for the effect of topography in the rainfall distribution depending on the meteorological conditions. A prerequisite for improvement in the estimation of spatially distributed rainfall estimation are detailed observations and analysis of their connection to different weather situations.

### **2.2.2 - i Orographic effects on spatial distribution of precipitation as observed by raingauges**

The effect of altitude on precipitation amount observed by raingauges has been investigated in numerous studies for different mountain areas around the world focusing on the precipitation amount accumulated on monthly and annual time scales (Glazirin, 1997; Hill, 1983; Minder et al., 2008; Sevruk, 1997; Wastl and Zangl, 2010; Basist et al., 1994). Under those circumstances the observed rainfall amounts frequently show a linear increase with elevation, however, some studies reported a threshold elevation at which the gradient decreases and can even be negative (Loukas and Quick, 1996). On the other hand, Sevruk (1997) observed an increase in the gradients above 1500 m a.s.l. as compared to lower elevations. These examples suggest that the effect of the terrain on cumulative precipitation strongly depends on the climatic region, on the local topographic features, the temporal scale of rainfall aggregation and prevailing weather type. Additionally, in many cases, the assumption of linear increase with elevation is not confirmed by rainfall observations on the ground.

For example, innermountain valleys can be shaded from precipitation and therefore may exhibit different altitude effects than similar areas in close proximity (Singh and Kumar, 1997; Sevruk and Miegitz, 2002). Also depending on the temporal scale of aggregation, orography plays a different role in the distribution of the accumulated precipitation. At annual or seasonal time scales many studies have found linearly increasing precipitation amounts with altitude. However, at the time scale of single rainfall storms, the cumulative event precipitation can show a very different spatial distribution. For example Loukas and Quick (1993) analysed precipitation gradients at the event time scale in a catchment in British Columbia. They found gradients in the order of 1mm/100m and a stronger correlation was observed for large events as compared to smaller ones. Apart from the temporal aggregation, strong differences in the altitude effects on cumulative precipitation were also observed when comparing the lee side of the mountain range with hillslopes on the windward side (Singh and Kumar, 1997).

Since gradients are formed by a combination of differences in rainfall duration and differences in terms of rainfall intensity, several studies have investigated the relative importance of those processes in the formation of the gradient in cumulative precipitation at a given time interval

and found strong differences depending on the meteorological processes involved (Loukas and Quick, 1996).

In the past, several studies and experiments have investigated the effect of altitude on the spatial distribution of precipitation in different areas of the Swiss Alps. Sevruck and Mieglistz (2002) investigated the effect of topography on daily precipitation amounts at different locations in the alpine area and its relation to different factors such as region, weather type, wind direction and topographic characteristics. The mean gradients in summer were mostly positive. However, the results show considerable variability among different valleys and especially in the southern part of the Swiss Alps low gradients with low  $R^2$  values were detected. The dependency on the direction of airflow at 500 hPa is most pronounced in the summer months, when positive gradients predominate and are mostly related to SW and W conditions. Observed negative gradients can be artificial if the upper stations experience high wind speeds causing underestimation of the true rainfall amount. Havlik (1969) investigated annual and seasonal cumulative precipitation along horizontal north-south profiles across the Alps in order to detect locations of maximum precipitation. In this case, precipitation was generally found to increase with elevation up to the highest stations at around 3500 m a.s.l..

### **2.2.2 - ii Effect of terrain scale on orographic precipitation**

The strength of the correlation between altitude and precipitation amount was also found to be dependent on the scale of the morphological features. Several studies have addressed the scale dependence of the orographic effect by analysing the effect of filtering and resizing of Digital Elevation Model (DEM)s on different rainfall processes in the context of rainfall interpolation. Boni et al. (2008) studied the effect of different DEMs in the mapping of annual rainfall maxima by applying multivariate linear regression of rainfall and descriptors of terrain and climate. The descriptors of the orography were selected from DEMs filtered in the frequency domain in order to identify the scale at which the topography provides the best description of the spatial rainfall distribution. The regression analysis with the highest  $R^2$  was obtained by using orographic descriptors based on the DEM, which explained only 90% of the original spatial variability. This corresponds to a filtering of wavelengths smaller than  $100 \text{ km}^{-1}$ .

Sharples et al. (2005) interpolated monthly rainfall amounts by fitting trivariate thin-plate spline models using elevations derived from different DEMs as independent variables. DEM resolutions from about 250 m to 90 km were investigated and the averaged DEMs were smoothed by applying biquadratic spline interpolation. The subsequent generalized cross-validation analysis showed a minimum in the difference between measured and interpolated rainfall for resolutions of 4-11 km. The effect of DEM resolution was also investigated in the PRISM (Precipitation Regression on Independent Slopes Model) framework (Daly et al., 1994). They found that elevations obtained from a 6x9 km DEM were best able to explain the observed orographic effects in monthly and annual precipitation totals. Similarly the

interpolation of daily precipitation by Hutchinson (1998) showed best performance when using a DEM of 10 km resolution. Other work suggests a strong influence of the topography also at smaller scales (Cosma et al., 2002).

All of these findings do not only indicate a strong dependence of the gradients on the scale of the terrain features, but also a strong dependence on the process and area of investigation.

### 2.2.2 - iii Weather type control on orographic precipitation

The high variability in observed gradients at different spatial and temporal scales is largely due to the differences in the meteorological processes involved. Therefore, the dependence of observed orographic effects on weather type and meteorological conditions at different spatial and temporal scales needs to be considered. Atmospheric processes at a larger scale are to a certain extent linked to the local weather pattern. Many studies have therefore investigated the relationship between weather type and precipitation occurrence (Sevruk and Mieglistz, 2002; Schiemann and Frei, 2010; Havlik, 1969). However, their predictive ability for rainfall occurrence is generally small, especially in mountain areas, where the local topography strongly modulates the mesoscale airflow dynamics, and the relationship is seasonally dependent (Schiemann and Frei, 2010).

The comparison of precipitation amount and weather type by Havlik (1969) showed that 70% of the annual precipitation was falling during anticyclonic weather conditions. The strongest differences between mountain and valley stations were also observed in those conditions. The differences could be explained as a combination of higher intensity and longer duration rainfall at high altitude stations. Negative gradients were explained with the presence of convective weather conditions, where the magnitude of the horizontal water vapour transport is less relevant as compared to the moisture content in the air column above a station, which is larger in low land stations as compared to mountain stations. Since advective weather situations occur more frequently than convective ones, the precipitation gradients at annual time scales are generally positive.

The most important weather characteristic affecting mechanisms of orographic precipitation is the wind direction, since it determines how the air masses interact with topography. For example, large differences in the observed rainfall distribution occur when comparing situations with flow direction parallel to a mountain range with those with winds perpendicular to the slopes (Neiman et al., 2002). Sevruk and Mieglistz (2002) compared the frequency of rainfall gradient occurrence and weather classification based on the airflow direction at 500hPa and found a high frequency of positive gradients for westerly and south-westerly flow conditions for the summer months. Also the evaluation of a numerical model of orographic precipitation by Zangl (2007) showed highest sensitivity to modification of the wind direction, which substantially altered the small scale precipitation pattern, whereas the sensitivity with respect to wind speed was lower and resulted in changes in rainfall amount rather than changes in the



rainfall distribution.

Since wind patterns on the ground are strongly affected by local topographic features, they are not necessarily representative of the flow direction of the overlying air masses (Steiner et al., 2003; Whiteman and Doran, 1993). However, even though single observations on the ground are sometimes poorly correlated to the general storm direction, the wind field on the ground estimated from several point measurements can be linked to precipitation occurrence as was shown by Weber and Furger (2001) in a classification of wind patterns based on surface wind observations across Switzerland. In this case, wind patterns originating from the west accounted for around 70% of the annual precipitation over Switzerland.

The estimation of storm direction may also be done on the basis of weather radar data. To estimate a direction from a time series of radar images, techniques which are based on either cross correlation between consecutive radar images or cell identification and subsequent centroid tracking are often used. The latter method was found to perform better in the case of convective weather situations (Pierce et al., 2004). These studies indicate that observed rainfall patterns at the hillslope scale show a weak relation to the large scale weather type but are quite strongly related to the local wind field.

### 2.2.3 Experimental design and working hypotheses

#### 2.2.3 - i Experimental design

The experimental setup of the rainfall observations along the hillslopes was designed as a combination of tipping bucket and weighing raingauges, since the experimental investigation of orographic rainfall along hillslopes at the event time scale requires both high spatial and temporal resolution. The use of electronic weighing gauges provides high quality rainfall data at locations with access to a power supply, which can be used as a reference, and the deployment of a dense network of mobile tipping bucket gauges ensures that the rainfall variability is captured also at small spatial scales. In order to have a flexible setup, allowing continuous adaptation of the network, and to have data access in real time, wireless weather stations equipped with a General Packet Radio Service (GPRS) modem were chosen for the experiment.

Given the large errors in point rainfall measurements (Section 2.2.1 - ii), the data recorded in the field experiments of this study were corrected for wind-induced errors, and both a static and a dynamic calibration were performed (Section 2.2.1 - iii). Since strong winds and intense rainfall occur often at high altitudes, higher corrections are expected at those locations. This implies that the effect of altitude cannot be captured fully based on uncorrected data. Therefore, correction of measurement errors is of particular importance at high altitudes and was given special consideration in the present study. Since this post-processing can lead to artefacts in the data analysis (e.g. Paschalis et al., 2012), a particular focus of this work was set on careful investigation of the effect of applying corrections on the results and their uncertainty.

#### 2.2.3 - ii Working hypotheses

This section describes how, based on the state of the art (Section 2.2), the working hypotheses are elaborated and how they are approached within this study. They are developed with regards to the five research questions described in Section 2.1.

**Effect of elevation on event rainfall variability and cumulative amount** Since in many applications a linear relation between precipitation amount and altitude is assumed but experimental evidence indicates that this assumption is frequently violated (Section 2.2.2 - i), this study investigates under which circumstances this assumption is justified by estimating gradients for observed rainfall events at different spatial and temporal scales. We test the hypothesis that by comparison of rainfall gradients at the event time scale with the prevailing weather situation, meteorological conditions can be identified under which the assumption of a constant rainfall gradient is justified .

In order to highlight the driving mechanisms in the gradient formation as observed during this experiment, the gradients in terms of cumulative event rainfall are compared with the observed gradients in rainfall intensity and duration. This line of investigation addresses the hypothesis that the relative importance of rainfall intensity and duration in the formation of gradients in cumulative rainfall varies among events with different rainfall regimes. Additionally, we test the hypothesis that the event rainfall variability in terms of temporal and spatial correlation is affected by altitude and that this effect is also dependent on the predominant rainfall regime.

**Effects of data post-processing** Since correction of rainfall measurements is expected to increase with altitude, a strong effect on the resulting gradient is expected. We test the hypothesis that if rainfall measurements are corrected for wind-induced losses and underestimation of high rainfall intensities, the estimated gradients will be larger than in the case of uncorrected data.

Due to the limited ability of TBR to resolve low intensity rainfall, analysis of the spatial and temporal correlation structure is expected to be affected by the measurement errors. We therefore test the hypothesis that corrected rainfall data provide a more accurate estimate of the spatial and temporal event rainfall structure.

**Comparison of simulated and observed rainfall distribution** To further investigate the relevant rainfall generating mechanisms in complex terrain, an analytical model of upslope condensation and downstream advection is applied to the observed events. It is expected that, based on differences in the observed and simulated rainfall distribution, the presence of additional rainfall generating processes, not accounted for by the model, can be identified. Thereby, this analysis is expected to further highlight the meteorological conditions affecting rainfall distribution and to provide qualitative information on the rainfall distribution at the basin scale. We test the hypothesis that by comparison of observed and simulated rainfall gradients, this model is able to provide qualitative information about the rainfall processes relevant in the gradient formation.

**Influence of terrain scale** Several studies suggest that there exists a threshold scale of terrain features below which terrain has no influence on the rainfall generating mechanisms. Since gradients along a hillslope transect are strongly dependent on the altitude difference between the stations, changes in resolution of the underlying terrain model are expected to have an influence on them, both qualitatively and quantitatively (Section 2.2.2 - ii). We test the hypothesis that the spatial scale which maximizes the correlation between altitude and rainfall amounts is lower than the real terrain scale.

**Influence of meteorological conditions** The analysis of weather type control on gradients focuses on the prevailing wind patterns and the rainfall regime, since they were identified in many studies as the main factors controlling the rainfall gradient patterns on the ground (Section 2.2.2 - i and 2.2.2 - iii). Even though the literature does not suggest a strong relation between large scale weather types and variability in local orographic effects, in the present study weather type classifications and radar based wind direction estimates are compared to the observed gradient patterns in order to gain insight into how the general weather situation related to the local meteorological conditions. We test the hypothesis that events with different rainfall gradient patterns also exhibit distinct patterns in the local wind field as well as differences in the predominant rainfall regime.

## 2.3 Outline

In Chapter 3, the field experiment is documented. The setup of the weather stations and their locations are described, and a brief summary of the observed data is given. Furthermore, the different corrections applied to the measured data and the resulting uncertainty is analysed. Chapter 4 presents the results of the data analysis and it consists of five sections, each one illustrating the outcome of the line of investigations described in Section 2.2.3.

Section 4.1 shows the results of the correlation structure in the rainfall data based on analysis of autocorrelation, spatial cross correlation and oscillation coefficients of the rainfall time series at the event time scale. Section 4.2 deals with the analysis of the rainfall gradients with elevation for the different events and their dependence on intensity and duration. In addition, the effect of temporal aggregation is addressed by investigating gradients at the sub-event time scale and the dependence on the terrain resolution is analysed by estimating gradients based on filtered DEMs. In Section 4.3 the observed events are characterized by weather type based on analysis of weather radar data and wind measurements on the ground. From the weather radar data the prevailing wind direction is estimated by tracking the centroid of the rain cells in the radar maps and a cluster analysis of the ground observations of wind speed and direction identifies characteristic wind patterns, which are then linked to precipitation occurrence. Furthermore, the events are compared to different large scale weather type classifications. In Section 4.4 the linear steady state model of orographic precipitation is introduced and calibrated to the observed events. The results are then compared to the observed events and the weather characteristics described in the previous section. In Section 4.5 a cluster analysis of the gradients based on different event characteristics is shown.

The discussion shows a comparison between the classification of the ground observations and the related weather type characteristics (Section 5.1). In addition, the effects of instrumental errors on the correlation structure and on the gradients are presented, which illustrates to which extent the results can be interpreted as effects of altitude and how much they are affected by artefacts of the applied corrections. The discussion ends with a summary of how the observed gradient patterns are linked to specific meteorological conditions. The conclusions are summarized in Section 5.2.

## Chapter 3

# Field experiment

This section describes the field experiment that was carried out in order to investigate rainfall processes at the hillslope scale. In Section 3.1 the field site is presented and the sensors used in this study are described. Next, a brief summary of the observed rainfall events is presented (Section 3.2). The last section of this chapter describes the correction of the rainfall data. In particular, the correction methods (Section 3.3.1), their application to the measured data (Section 3.3.2) and the resulting uncertainty (Section 3.3.3) are addressed.

### 3.1 Weather station setup

The field investigations were carried out in the Swiss Alps in the catchment of the river Vispa, which is surrounded by high mountain ranges with peaks above 4000 m a.s.l.. Its location being protected from rainfall makes it one of the driest areas in Switzerland (Weingartner and Pearson, 2001). It is characterized by steep slopes, and its aspect is mostly east and west, since it is oriented in north-south direction. Due to the steepness, rainfall events can lead to a rapid response of the river levels, which allows only little lead time for flood forecasting. The watershed is shown in Figures 3.1 and 3.2. In the past, this area was affected by several severe storms, which led to landslides, debris flow and flooding (Zeller and Röthlisberger, 1994; Hegg et al., 2002). Events leading to natural disasters are often characterized by long lasting rain storms coming from the south. In the context of early warning systems of rainfall related natural hazards a better understanding of the spatial distribution of rainfall at this particular location is therefore crucial.

In order to obtain a detailed picture of the spatial rainfall patterns a dense network of observations is therefore necessary. The area surrounding the catchment is covered by a high number of weather stations recording precipitation at a temporal resolution of at least 1 hour operated by the different national meteorological services. However, there is a lack of stations in the north west of the basin. Within the catchment there are few raingauges operating at 10 min

resolution (Figure 3.1). In this study, the existing network of raingauges in the catchment area was complemented with additional weather stations aiming at a more detailed investigation of the spatial and temporal rainfall structure. In order to cover also the very small spatial scale and to explore the effect of terrain elevation, some of the raingauges were set up along a transect of one particular hillslope in the southern part of the basin (Figure 3.2). Additional stations were set up throughout the valley in order to obtain a more dense network within the catchment.

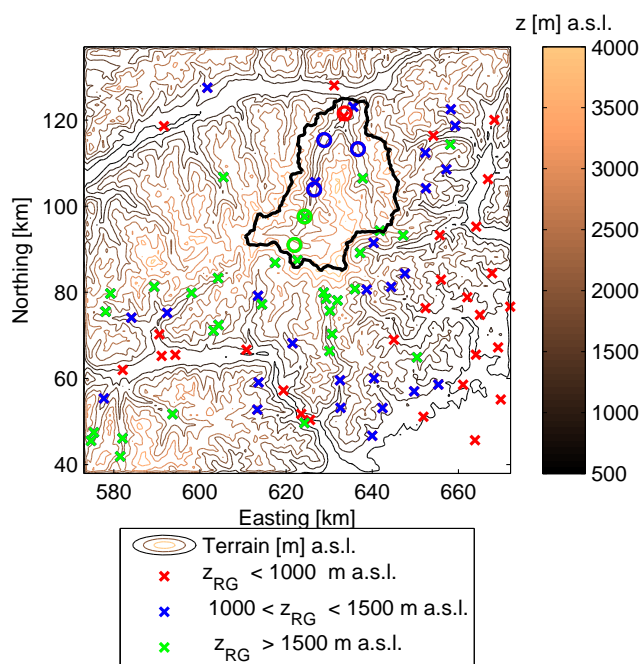


**Figure 3.1:** Location and altitude of weather stations within the area surrounding the study site. Crosses indicate the existing raingauge network and circles indicate the weather stations installed permanently within the field experiment.

In order to observe precipitation at the small spatial scale of single hillslopes, high quality measurements are necessary that are able to resolve the small scale temporal structure of rainfall events. In addition, a high number of stations is required in order to capture the small scale spatial variability. Furthermore, a flexible adjustment of the stations is required in order to adapt the setup according to the finding of the experiment in order to continuously optimize the network. Electronic weighing raingauges provide accurate measurements at high resolutions, however they require an external power source and are therefore not suitable in a mobile setup of weather stations. On the other hand, tipping bucket raingauges are easy to deploy and can therefore be used in a mobile station network (Simoni et al., 2011). However, due to the coarse volumetric resolution, the small scale temporal rainfall structure is captured only to a limited extent, especially in the case of low intensity rainfall.

In order to benefit from both the high quality data provided by electronic weighing gauges and the flexibility in the deployment of tipping bucket gauges, the raingauge network was designed as a combination of mobile and reference stations. The latter were equipped with a weighing raingauge and they were installed permanently within the valley, between 5 and 10 km apart at locations with external power supply. The mobile stations were deployed only during intensive observation period (IOP)s in summer for the investigation of the small scale variability of rainfall along two hillslopes above the village of Zermatt (Figure 3.2). They were equipped with tipping bucket raingauges and were set up independently of external power supply allowing a flexible deployment of the stations.

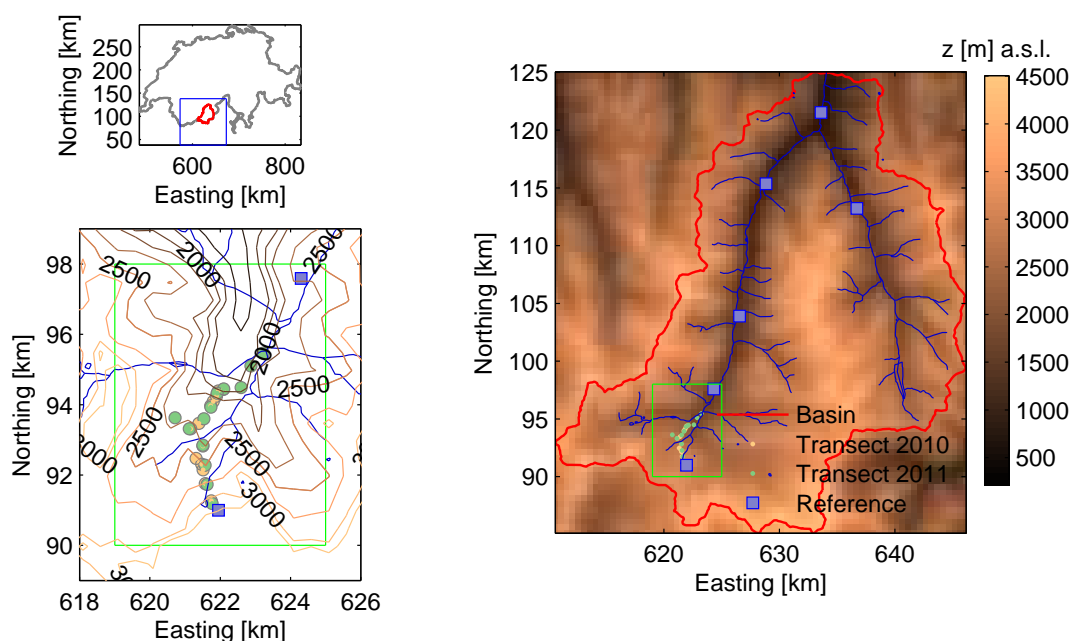


**Figure 3.2:** Location of the field site and location of the reference weather stations and transects of mobile stations. The green rectangle shows the location of the transects of weather stations in summer 2010 and 2011. The blue rectangle in the upper left panel indicates extent of radar data used in the analysis.

### 3.1.1 Reference stations

In the Vispa valley six reference stations were installed (Figure A.1). Since the sensors require an external power source, the possible locations were confined to settlement areas which are mostly in the valley or infrastructure such as cable car stations for the stations at higher elevations. Some of the stations were set up close to existing raingauges for the purpose of data quality control, i.e. the reference station Zermatt (ZE) (Savina et al., 2012). Furthermore, the transects of mobile stations were complemented by two reference stations at the bottom and at the top (reference station Trockener Steg (TR) and ZE) allowing comparison of mobile



and reference station data.

The stations were equipped with a wind sensor, a weighing rain gauge and a thermometer measuring at 1 min temporal resolution. The volumetric resolution of the weighing rain gauge is 0.001 mm and it has an orifice area of 200 cm<sup>2</sup> (Table A.2). The locations selected for the permanent installation of the reference stations are shown in Figure 3.3. The station elevations were retrieved from a 25 m DEM (Bundesamt für Landestopografie swisstopo) and they are covering a range between 700 and 2900 m a.s.l..

The highest reference station was installed on the roof of a cable car station (TR). Even though such a location is not ideal for precipitation measurement, it was chosen because of easy access to power supply and because it did not have to be moved vertically in winter since the snow height remains relatively low. In order to protect the gauge from wind-induced losses at such an exposed position it was equipped with a wind shield. All the other locations were not shielded but the data were corrected for wind-induced losses (Section 3.3.1).

Since the primary focus of this work is the analysis of storm rainfall events, permanent monitoring and maintenance of the network was necessary, and therefore the stations were equipped with a GPRS modem, which allows automatic transfer of the data and access in real time.

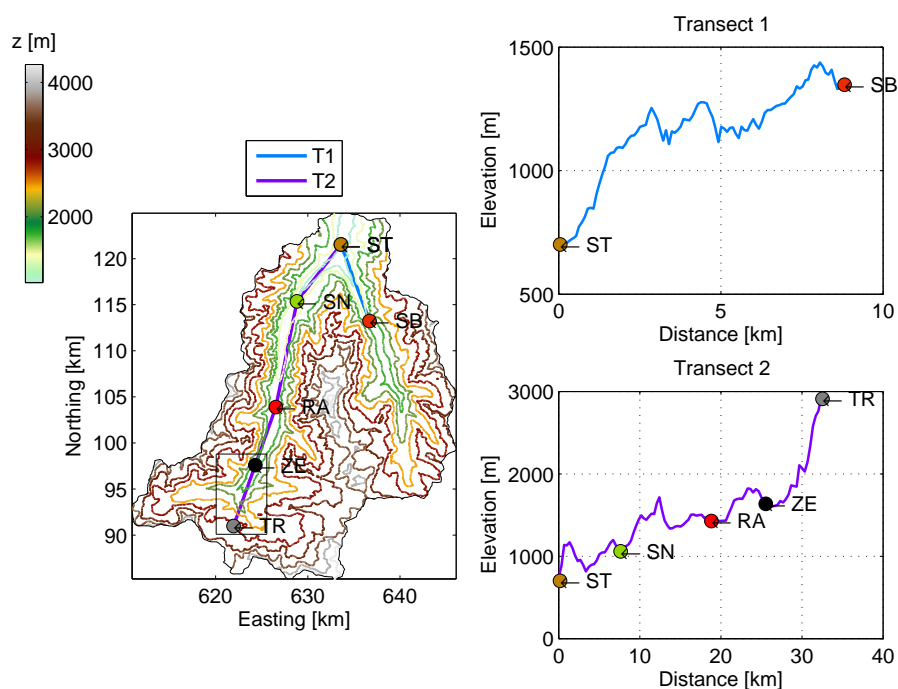


**Figure 3.3:** Overview and profile of reference station locations. The square indicates the area of the hillslope transects that were investigated

### 3.1.2 Mobile stations

The IOPs investigating the effect of terrain elevation along a particular hillslope required a dense network of weather stations that are easily deployable and able to operate independently of an external power source. Recently developed wireless stations were chosen for this task since they fulfill the before mentioned requirements, and they allow automatic data transfer and access in real time as in the case of the reference stations. This allows continuous monitoring of the stations, which increases the reliability of the network. A network of wireless stations was set up as a combination of master and slave stations (Ingelrest et al., 2010). Master stations are able to collect data from slave stations and are equipped with a GPRS modem. Slave stations on the other hand, are not able to send data directly but are designed to transmit the collected data to the master station by using a low-power radio chip. This is possible either by direct connectivity to a master station or by serial connectivity through different slave stations. In flat terrain connection among stations is possible for distances up to 2 km, in steep terrain however this distance decreases rapidly to a few hundred meters. In the first field experiment 2 out of 13 stations were designed as master stations. The positioning of the 11 slave stations was therefore constrained by the need for establishing a reliable radio communication with the master station. This was achieved by maximising the visibility among the different stations along the transect and at the same time covering as much of the elevation range as possible. The mobile stations were set up along a transect which consists of two hillslopes with slightly different orientation, which will be referred to hereafter as lower transect (T1) and upper transect (T2). T1 is oriented towards northeast and T2 is oriented more towards north. The entire transect (T0) consists of one reference station at the top and one at the bottom, which were installed permanently, and in between the mobile stations were set up during two IOP in 2010 and 2011. During the first IOP in summer 2010 the stations were set up as shown in Figure 3.4. The station elevations were retrieved from a 25 m DEM and they are covering an altitude range between 2000 m and 2900 m in 2010 and between 1600 m and 2900 m in 2011. The mean vertical distance between the stations was 84 m and the horizontal distance was about 320 m (Table A.4). The minimum distance was rather small (vertical 40 m, horizontal 150 m) in order to ensure communication between adjacent stations at locations with steep slopes. The stations number 5 and 10 were set up as master stations.

The results of the first field campaign have shown some limitations in the operation of a wireless network in steep terrain. Some areas of the hillslope could not be covered by the stations due to insufficient connectivity among neighbouring stations and they had to be moved closer. However, the placement of stations in close proximity of each other leads to redundancy in the observations and lack of measurements in other areas. In order to optimize the coverage of the area, all mobile stations were equipped with a GPRS modem allowing a setup independent from each other for the second IOP in summer 2011. Therefore, the stations could be positioned further apart as shown in Figure 3.4 allowing a full coverage of

the transect. The mean vertical distance was about 100 m and the mean horizontal distance was about 545 m (Table A.5). A comparison of the setup in 2010 and 2011 is shown in Figure A.3.

The mobile stations were equipped with an anemometer, two tipping bucket rain gauges and a relative humidity and air temperature sensor. The anemometer was installed at 2 m above ground, the raingauge at 1.8 m and the relative humidity and air temperature sensor at around 1.5 m above ground (Figure A.2). The air temperature sensors were protected with a radiation shield. In order to achieve a more precise point rainfall estimate, 2 rain gauges were installed at each station, which will be referred to as first set of tipping bucket raingauges (P1) and second set of tipping bucket raingauges (P2) hereafter. The volumetric resolution of the tipping bucket raingauge is 0.254 mm and the orifice area is 213 cm<sup>2</sup>. As in the case of the reference stations (except TR) no wind shield was used, but the data were corrected for wind-induced losses, and the static calibration of the data obtained from the tipping bucket gauges was applied in the post-processing of the data (Section 3.3.1).

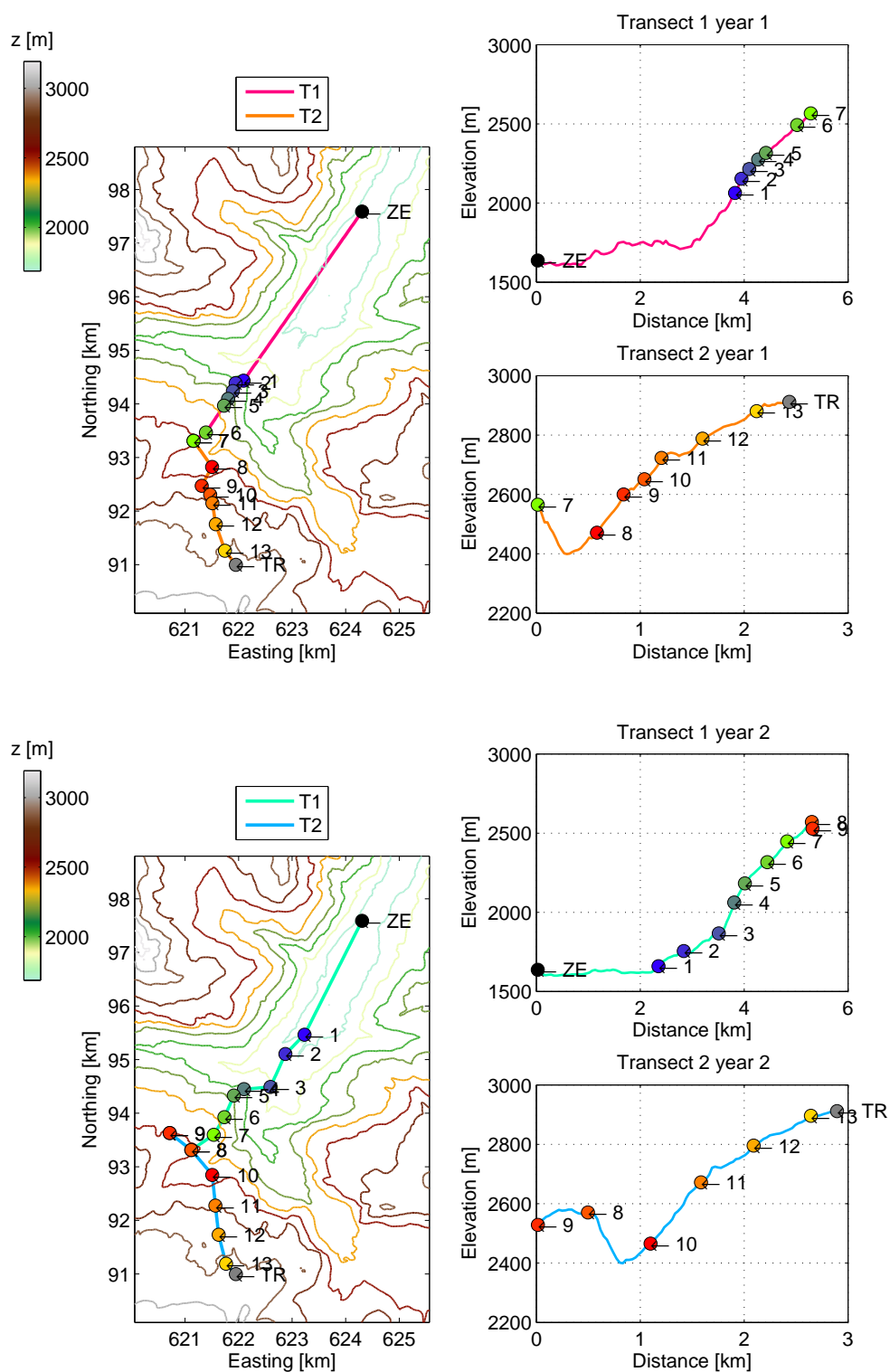


**Figure 3.4:** Overview and profile of transects during the intensive observation periods in 2010 and 2011. In 2010 the stations number 5 and 10 were set up as master stations and T1 consists of stations 1-7 and ZE, and T2 consists of stations 8-13 and TR. In 2011 T1 consists of stations 1-9 and ZE, and T2 consists of stations 10-13 and TR.

## 3.2 Event documentation

Since this analysis focuses on storm rainfall at short durations of few hours to several days, the recorded rainfall data were used to extract such events and the subsequent analysis was then confined to the time periods of those events. Another reason for restricting the data analysis were technical problems such as insufficient connectivity among the stations in the first IOP, which led to gaps in the time series of single stations. Additionally, during events with strong wind some of the stations fell on the ground and therefore they have to be excluded from the analysis. Detection of rainfall events and stations measuring reliably during those time periods were selected based on analysis of cumulative rainfall. Figure 3.5 shows the cumulative rainfall measured during the two field experiments. In 2010 a cumulative amount of around 100 to 250 mm was recorded at the different stations (except station nr. 2, which had connectivity problems) and in 2011 the amount ranged between 150 and 450 mm.

During the second field experiment the reference stations ZE and TR were recording all the events and therefore the cumulative rainfall can be compared on a seasonal basis. In this case, the station in the valley (ZE) recorded 155 mm and the one at the top (TR) about twice as much (320 mm), which results in a gradient of about 12 mm/100m given the elevation difference of 1300 m. Some of the mobile stations located at the top of T1 observed a considerably higher rainfall amount, which indicates that the seasonal gradient could even be higher. However, since some of the mobile weather stations were not recording all the events, the cumulative rainfall recorded by the mobile stations can only be analysed on the event time scale. The events were selected from the time series according to the duration and according to the cumulative rainfall. In the literature different definitions of rainfall events have been suggested. For example, Fiener and Auerswald (2009) defined rainfall events as time periods with more than 5 mm of rainfall separated by at least 6 h of dry duration. Wang et al. (2008) define events solely based on the dry duration and illustrate the sensitivity of the rainrate estimated from TBRs on the criterion used for the event definition. These examples show that the definitions of what is considered a rainfall event are variable and depend on the climatic regime of the area and on the temporal and spatial scale at which the data are analysed.

In this study, based on analysis of the recorded rainfall data, an event was defined as a time period in which at least one station measured more than 5 mm of rainfall and during which the dry duration did not exceed 12 h. Applying these criteria resulted in 27 events (Table 3.1). For each event selected from the time series the stations with gaps in the data were excluded from the analysis. Temperature data were used to detect stations that were recording snowfall. Since the tipping bucket gauges at the mobile station are not able to record solid precipitation, stations that recorded temperatures below 0°C were excluded from the analysis. Table A.6 shows which stations were discarded from the analysis. Except for event 7, where only 7 stations measured the entire event, at least 10 stations were recording during the entire time.

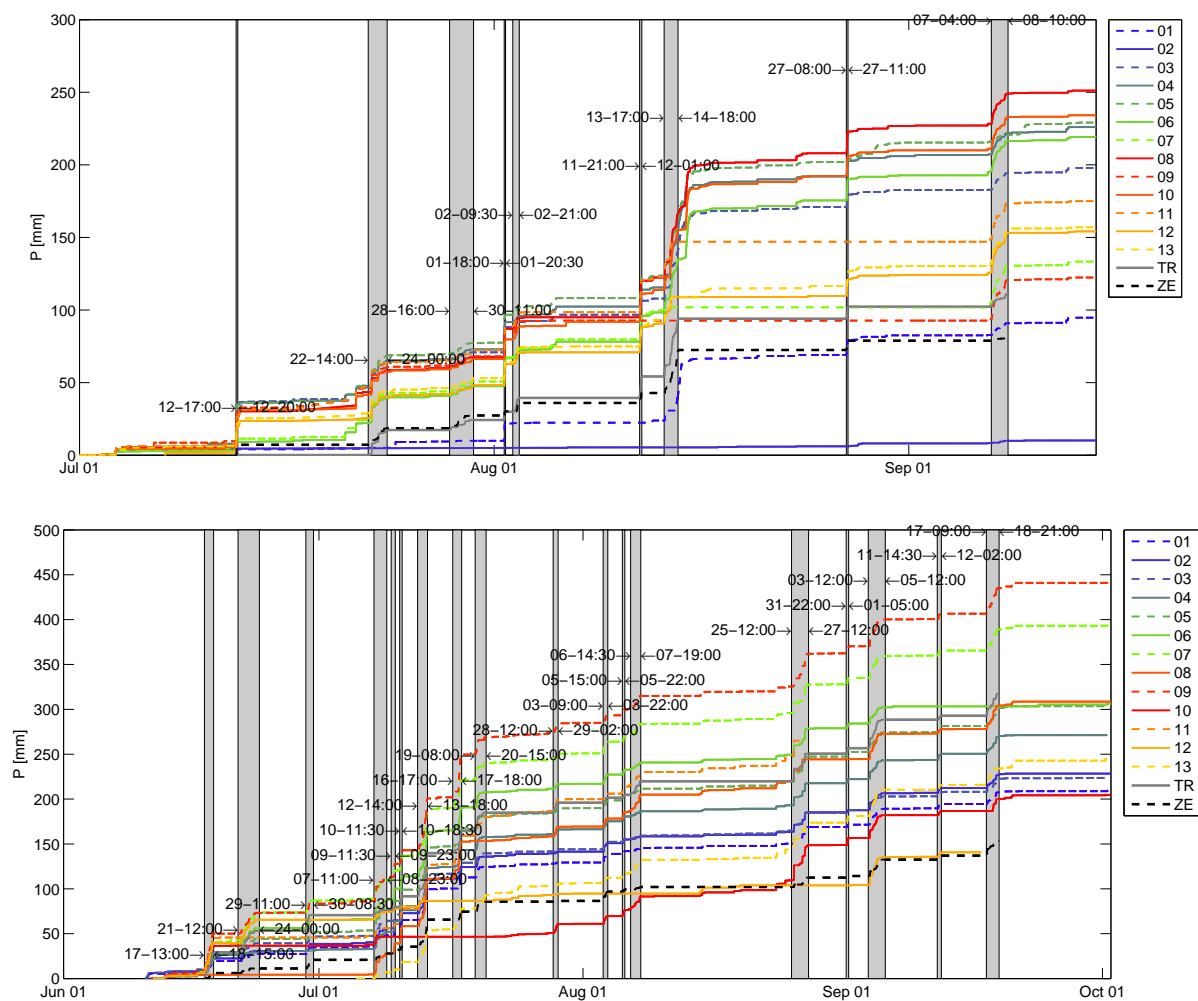


**Figure 3.5:** Cumulative rainfall based on the original data (without post-processing) of the intensive observation periods in 2010 and 2011. The numbers indicate the day and time of the beginning and end of the events in UTC.

Due to connectivity problems in the first IOP the events were on average recorded by about 12 stations whereas in the second one an average of 13 stations was reached. Connectivity problems affected mostly stations along the lower transect, which is much steeper, and they were solved in the second IOP. Still remaining is the problem of falling of stations in situations of strong winds, which occurs more frequently in the upper part. This explains why in the second IOP stations with missing data are almost exclusively located in the upper transect. The duration of the selected events ranges from a few hours to as much as 2.5 days (Table 3.1). However, each event contained also dry intervals, which are referred to as dry duration. The effective rainfall duration,  $D_p$ , is therefore considerably shorter, ranging between 1.5 and 14 h. In most events  $D_p$  corresponds to about 20% of the total event duration. The cumulative rainfall of the selected events is shown in Figure 3.6. The long duration events generally consist of several wet spells that are separated by dry periods. The data show elevation

**Table 3.1:** Event dates and times in UTC:  $D$  denotes the entire event duration,  $D_p$  is the duration of the wet spell within each event and  $P$  denotes the cumulative event rainfall amount.

Event	Date start	time start	Date end	time end	$D$ [h]	$D_p$ [h]	$D_p$ [%]	$P$ [mm]
1	2010-Jul-12	17:00	2010-Jul-12	20:00	3.0	1.8	60	24.64
2	2010-Jul-22	14:00	2010-Jul-24	00:00	34.0	5.4	16	17.86
3	2010-Jul-28	16:00	2010-Jul-30	11:00	43.0	5.6	13	6.56
4	2010-Aug-01	18:00	2010-Aug-01	20:30	2.5	1.4	56	17.26
5	2010-Aug-02	09:30	2010-Aug-02	21:00	11.5	3.2	28	7.03
6	2010-Aug-11	21:00	2010-Aug-12	01:00	4.0	2.6	65	16.59
7	2010-Aug-13	17:00	2010-Aug-14	18:00	25.0	12.8	51	38.47
8	2010-Aug-27	08:00	2010-Aug-27	11:00	3.0	2.1	70	12.16
9	2010-Sep-07	04:00	2010-Sep-08	10:00	30.0	10.7	36	18.93
10	2011-Jun-17	13:00	2011-Jun-18	15:00	26.0	13.3	51	24.94
11	2011-Jun-21	12:00	2011-Jun-24	00:00	60.0	8.5	14	16.67
12	2011-Jun-29	11:00	2011-Jun-30	08:30	21.5	3.0	14	9.63
13	2011-Jul-07	11:00	2011-Jul-08	23:00	36.0	3.7	10	16.38
14	2011-Jul-09	11:30	2011-Jul-09	23:00	11.5	1.8	16	8.89
15	2011-Jul-10	11:30	2011-Jul-10	18:30	7.0	2.0	28	12.81
16	2011-Jul-12	14:00	2011-Jul-13	18:00	28.0	11.8	42	46.06
17	2011-Jul-16	17:00	2011-Jul-17	18:00	25.0	8.5	34	23.62
18	2011-Jul-19	08:00	2011-Jul-20	15:00	31.0	9.1	29	14.21
19	2011-Jul-28	12:00	2011-Jul-29	02:00	14.0	4.5	32	5.78
20	2011-Aug-03	09:00	2011-Aug-03	22:00	13.0	3.2	25	8.80
21	2011-Aug-05	15:00	2011-Aug-05	22:00	7.0	2.1	30	4.60
22	2011-Aug-06	14:30	2011-Aug-07	19:00	28.5	6.7	24	9.24
23	2011-Aug-25	12:00	2011-Aug-27	12:00	48.0	5.9	12	28.10
24	2011-Aug-31	22:00	2011-Sep-01	05:00	7.0	2.0	29	4.95
25	2011-Sep-03	12:00	2011-Sep-05	12:00	48.0	13.2	28	22.50
26	2011-Sep-11	14:30	2011-Sep-12	02:00	11.5	2.3	20	5.30
27	2011-Sep-17	09:00	2011-Sep-18	21:00	36.0	10.2	28	19.67

dependence in some of the events, but depending on the event, both decrease or increase in cumulative rainfall were observed, which indicates high variability in the effect of elevation at small temporal scales. For the analysis of the oscillation coefficients long events were selected according to event duration ( $D > 8$  h) and rainfall duration ( $D_p > 25\%$ ), which is the case in event nr. 7, 9, 10, 16, 17, 25 and 27.

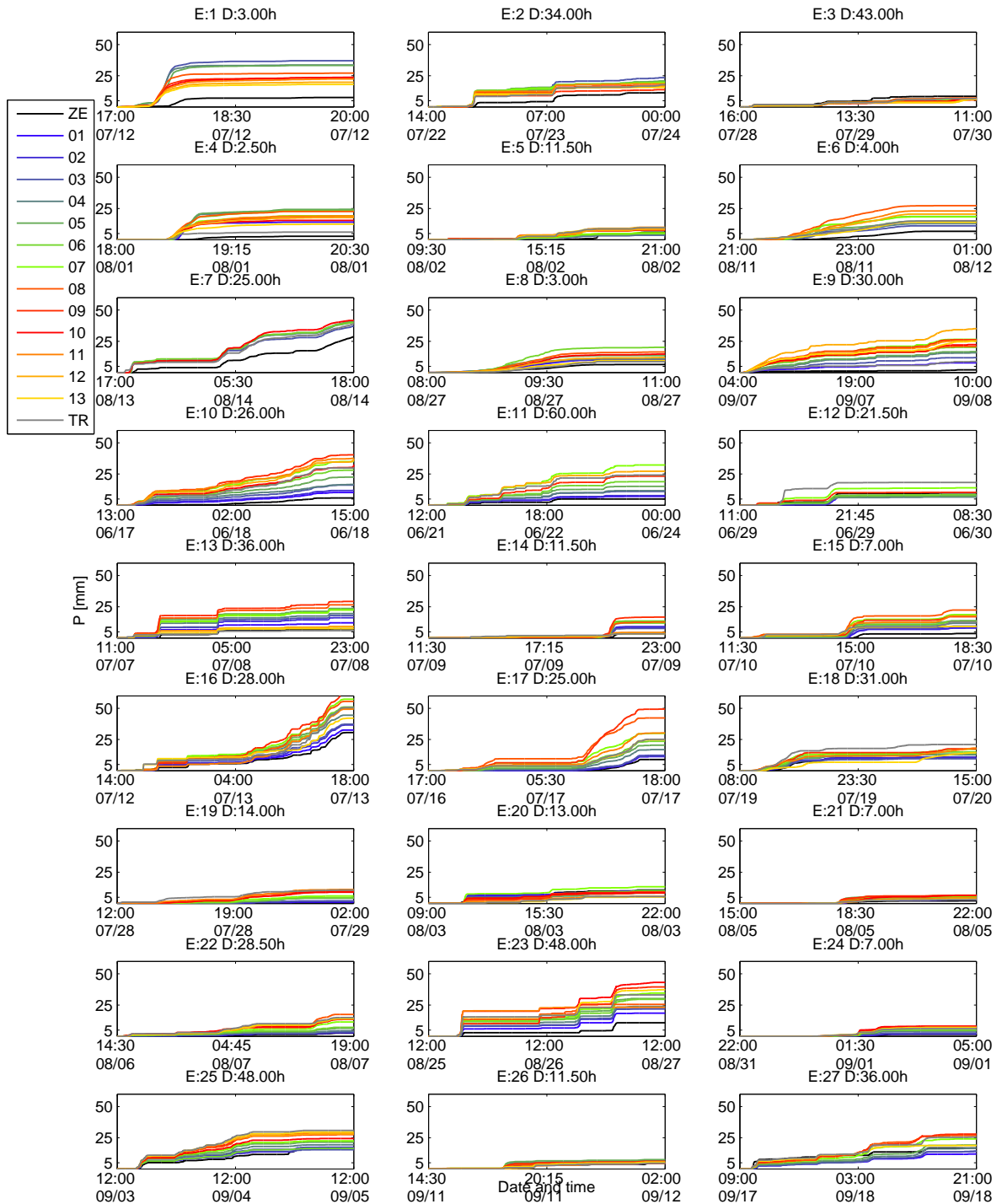
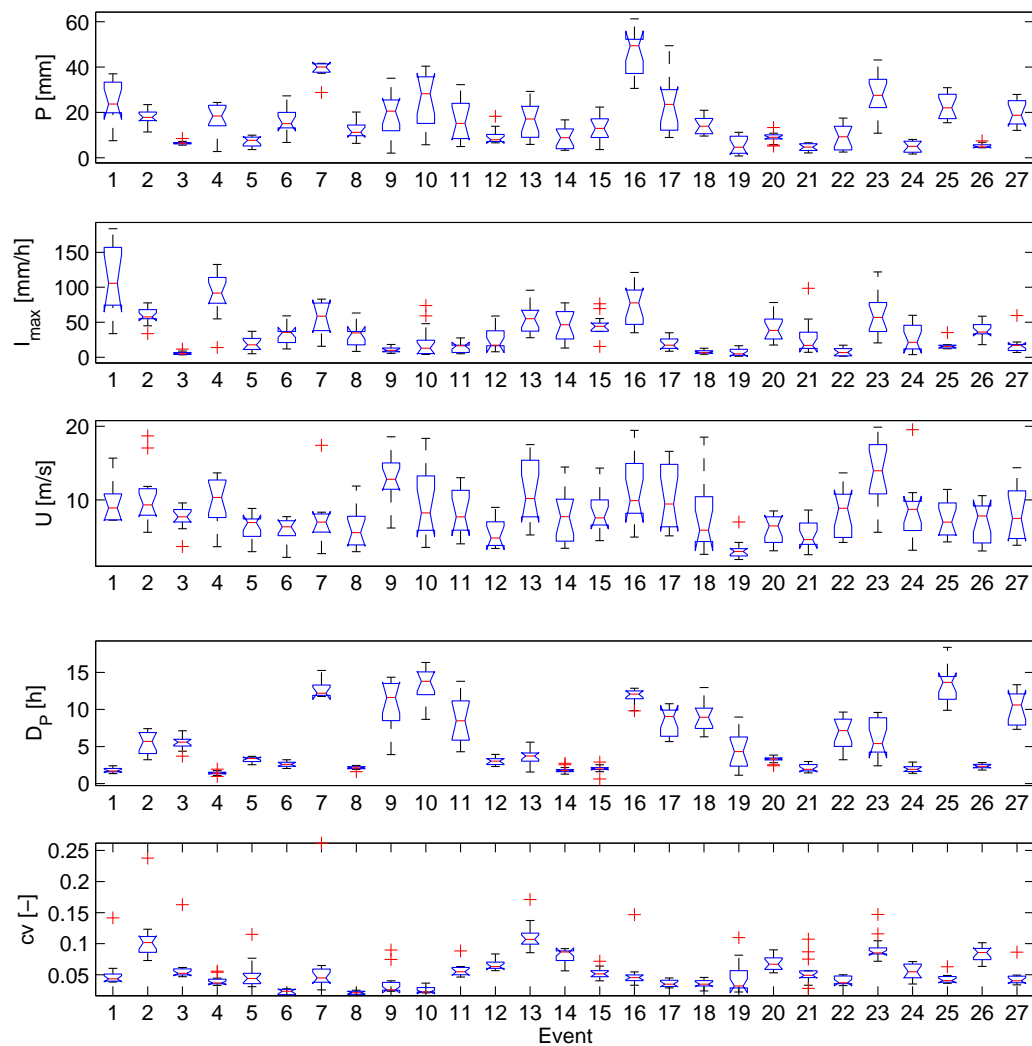


Figure 3.6: Cumulative event rainfall: The lower transect of mobile stations consists of stations 1 to 8 in 2010 and 1 to 9 in 2011. The remaining stations belong to transect 2.



An overview of several statistical properties of the different events is shown in Figure 3.7. It shows the strong variability among the different events, especially in terms of rainfall duration,  $D_p$  and intensity,  $I_{max}$ . It also shows some indications that intense rainfall events are of rather short duration, while long events are characterized by low intensity rainfall.



**Figure 3.7:** Summary of weather station data:  $I_{max}$  denotes the maximum rainfall intensity,  $U$  denotes the wind speed,  $P$  the cumulative rainfall amount,  $D_p$  the duration of the wet spell and  $cv$  denotes the coefficient of variation. The red line indicates the location of the median, the blue box denotes the interquartile range and the whiskers have a length of the 1.5 times the interquartile range. The red crosses indicate outliers.

## 3.3 Post-processing

### 3.3.1 Post-processing methods

Before the rainfall data recorded by the weather stations can be analysed, a careful quality control and error assessment are necessary. The raw data obtained from the logger contain missing values and faulty measurements and different sensor types cannot be directly compared since the measurement technique is different. Therefore, additional post-processing of the data is needed. Figure 3.8 shows a schematic summary of the post-processing steps applied to the observed rainfall data.

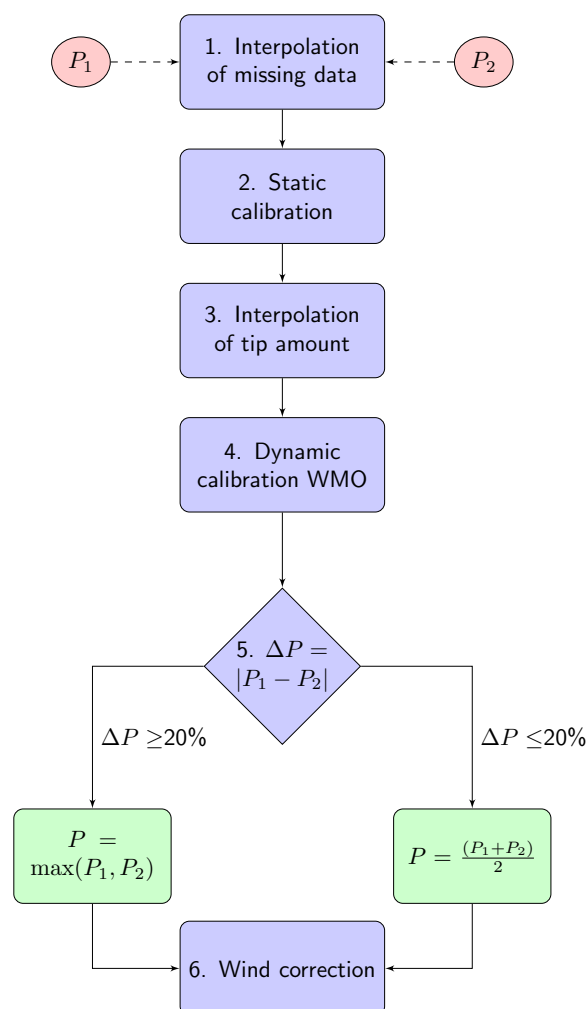


**Figure 3.8:** Flowchart of post-processing steps applied to mobile station raingauge data. For the reference station data the calibration step and the interpolation step were excluded.

### 3.3.1 - i Missing values and faulty measurements in time series

All data were corrected for missing values. The missing data were interpolated using the data measured within a time window of  $\pm 5$  min. If less than 10 values were available within this window, the average value was taken. The missing value was replaced only if the estimated value was higher than the volumetric resolution of the gauge, and it was rounded to a multiple of the volumetric resolution of the raingauge.

In order to assess the performance of this method, interpolated and observed values were compared by successively removing recorded values from the time series and replacing them with interpolated ones. This allows then the comparison of original and corrected values. When looking only at cases where the data are replaced by an interpolated value, i.e. periods with continuous rainfall, the difference between interpolated and observed intensities in absolute terms is in the order of  $-1$  to  $+0.75$  mm. In about 50% of the cases the interpolated intensity corresponds exactly to the measured ones (Figure 3.9 upper right panel). In relative terms this corresponds to about  $\pm 20\%$  (Figure 3.9 lower left panel). Even though the intensities can be reproduced quite well in situations with continuous rainfall, the difference in terms of the cumulative precipitation,  $P$ , can be substantial (Figure 3.9 lower right panel). This is due to the high frequency of tips that are separated by dry durations longer than 5 min and therefore in most cases the missing value is replaced with zero rainfall. As a result, if all values had to be replaced by interpolated ones, the interpolated rainfall amount would account for only 0-80% of the actually recorded rainfall.

In summary, this method provides an accurate estimate of missing values in situations with intense rainfall, and in situations with low rainfall intensity the missing value is assumed to correspond to a dry period and is therefore replaced by zero rainfall. The number of missing values per station is apart from one exception below 30, which corresponds to less than half an hour during which the station was not recording. Since in most events only few data points are missing and since some of them fall into dry periods, this correction is almost negligible (Figure 3.9 upper left panel).

### 3.3.1 - ii Static calibration (SC) of mobile station raingauges

Static calibration accounts for device specific bias in the recorded rainfall intensity, which is, in contrast to the dynamic calibration, constant for all rainfall intensities. As pointed out by Fankhauser (1998), static calibration (SC) is crucial for accurate estimation of the cumulative rainfall amount, since it affects all measurements. On the other hand, dynamic calibration (Vuerich et al., 2009), which accounts for under- and overestimation within the entire range of intensities, has a much more pronounced effect on high intensities and is therefore not necessarily relevant for the total precipitation amount.

The 26 tipping bucket raingauges, i.e. P1 and P2 of each of the 13 mobile weather stations,

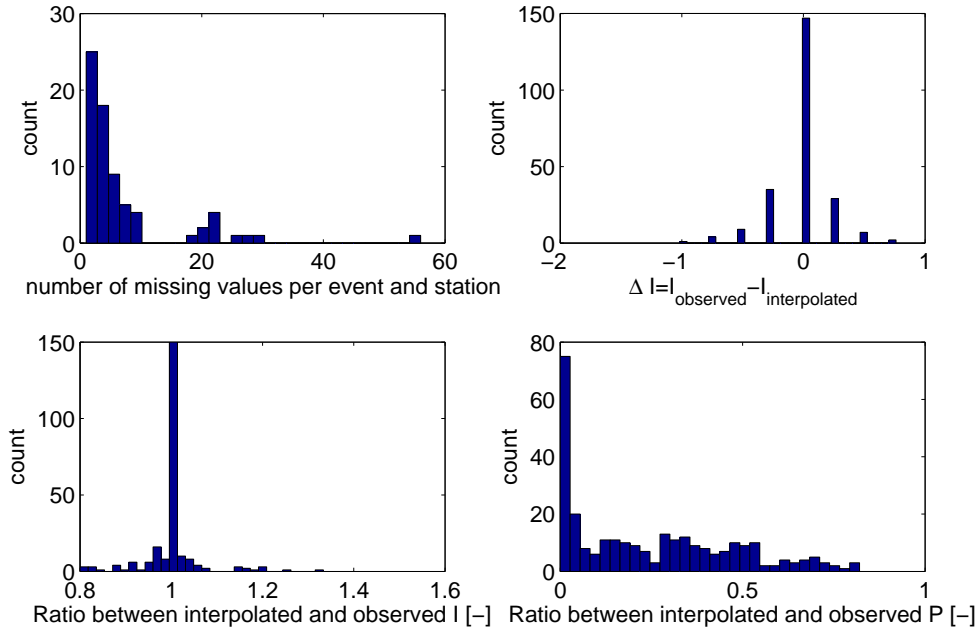


**Figure 3.9:** Evaluation of interpolation method for missing values. Number of missing values per event and station (top left); Difference in observed and interpolated intensity (top right); Ratio between interpolated and observed intensity (bottom left); Ratio between interpolated and observed cumulative precipitation (bottom right).

were calibrated in the laboratory in order to detect and remove device specific under- or overestimation. The devices are not calibrated to the true rainfall amount but to an arbitrary reference, since the only goal of this correction is to remove the device specific under- or overestimation. The correction for underestimation of the true rainfall amount (i.e. due to undercatch of intense rainfall and wind-induced losses) is accounted for by dynamic calibration and wind correction, which are described in sections 3.3.1 - iv and 3.3.1 - vi.

The gauges were calibrated by pouring a defined volume of water,  $V_{0,i}$ , into each raingauge  $i$ . For each gauge three runs were performed. By computing the ratio between the measured volume,  $V_{\text{obs},i}$ , at station  $i$  and the true volume,  $V_{0,i}$ , the catch efficiency,  $r_{c,i}$ , can be estimated for each station as the average of the three runs.

$$r_{c,i} = \frac{1}{3} \sum_{k=1}^3 \frac{V_{\text{obs},i}}{V_{0,i}}, i = 1, \dots, n_p \quad (3.1)$$

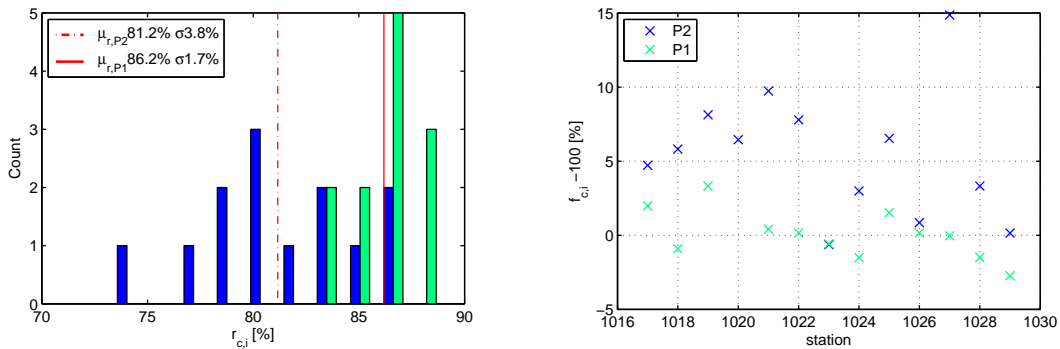
where  $n_p$  indicates the number of pluviometers.

Figure 3.10(a) shows the catch efficiency for each pluviometer. The second set of pluviometers (P2) seems to underestimate precipitation to a larger extent. In this case only 81% of the total volume was recorded by the gauge as compared to 86% in the case of the first group of pluviometers (P1). In addition, P1 shows a smaller standard deviation from the group mean. Therefore, the mean catch efficiency,  $\mu_{r,P1}$ , of this set of pluviometers was used as reference

for the calibration of all the gauges. In a next step, for each pluviometer the deviation from this reference value was computed, which results in the following expression for the calibration factors,  $f_{c,i}$ .

$$f_{c,i} = \frac{1}{1 + (r_{c,i} - \mu_{r,P1})}, i = 1, \dots, n_p \quad (3.2)$$

The resulting calibration factors (Figure 3.10(b), Table 3.2) are correcting the relative differences among the devices to the mean of the first set of pluviometers,  $\mu_{r,P1}$ , rather than adjusting the gauges to the true rainfall volume,  $V_0$ . Correction to the true rainfall amount is done by application of a dynamic calibration (Section 3.3.1 - iv). Most correction factors of the first group of pluviometers are in the range of  $\pm 5\%$  ( $f_c = 0.95 \div 1.05$ ). The second group of pluviometers shows considerably higher correction factors up to 12%, which accounts for the underestimation of those devices as compared to the average rainfall amount observed by the first group of pluviometers.



(a) Catch efficiency for pluviometer sets 1 (green) and 2 (blue). (b) Deviation of the catch efficiency from the mean catch efficiency of P1 for each pluviometer.

**Figure 3.10:** Static calibration of tipping bucket raingauges

### 3.3.1 - iii Interpolation of tipping bucket rainfall data

Since the amount of rainfall measured by a tipping bucket rain gauge did not necessarily fall within the time step in which it was measured, the rainfall amount cannot directly be converted to an intensity. The rainfall amount fell sometime between the time step of the last tip and the current time step. In order to establish a rainfall intensity, the cumulative amount measured at the time step of the tip has to be disaggregated within that interval. Figure 3.11 illustrates how a TBR and a weighing rain gauge (WR) are measuring the same rainfall event. The tipping bucket gauge is recording the rainfall only when a fixed tip volume is reached whereas the weighing gauge records rainfall at every time step. Whenever a tip is recorded, a residual water volume,  $V_e$ , is left in the tip and therefore recorded with a delay.

**Table 3.2:** Correction applied to TBR data due to device specific underestimation. All measured tip amounts were corrected according to these calibration factors.

Station ID		Underestimation		Correction Factor	
2010	2011	Underestimation P2 [%]	Underestimation P1 [%]	P2 [-]	P1 [-]
10	11	-4.51	-1.95	1.05	1.02
5	6	-5.50	0.92	1.06	0.99
13	13	-7.52	-3.22	1.08	1.03
9	3	-6.06		1.06	1.00
11	1	-8.87	-0.41	1.10	1.00
12	12	-7.23	-0.15	1.08	1.00
8	10	0.64	0.59	0.99	0.99
2	2	-2.90	1.53	1.03	0.98
3	5	-6.14	-1.51	1.07	1.02
4	9	-0.85	-0.16	1.01	1.00
6	7	-12.94	0.03	1.15	1.00
7	8	-3.22	1.51	1.03	0.99
1	4	-0.15	2.81	1.00	0.97

A very simple approach to estimate an intensity from tipping bucket data is averaging of the tip volume over the time interval since the last tip:

$$I(T_i - T_{i-1}) = \frac{\Delta V}{T_i - T_{i-1}} \quad (3.3)$$

where  $I$  denotes the estimated intensity,  $\Delta V$  the bucket volume and  $T_i$  and  $T_{i-1}$  the time of the tip at time step  $i$  and  $i-1$  respectively (Habib et al., 2001). The underlying assumption is a constant rainfall intensity between consecutive tip recordings. This assumption is problematic at low rainfall intensities when the intervals between tips are long, since this method is not able to reproduce intermittent rainfall. Because of this, an intensity threshold has to be set in order to obtain realistic intensities by the interpolation procedure (Fankhauser, 1998).

**Comparison with reference station** In order to test whether this method is appropriate for the disaggregation of the tip amount, the data from the reference stations were analysed as if they were measured by a tipping bucket raingauge with the same resolution as the mobile stations. Those artificial tips were estimated as described in Savina et al. (2012). From the time series of artificial tips all the tips with the same tip accumulation interval,  $\Delta t_{tip}$ , were selected. In a next step, the original intensities corresponding to each of those intervals were analysed. The intensity measured at the last time step is not necessarily representative for the intensities of a specific tip accumulation interval since it can happen that only a small fraction of the rainfall amount recorded at this time step was actually required for the tip to be filled. Therefore, only intensities measured during the interval  $\Delta t_{tip}^* = \Delta t_{tip} - 1$ , were considered in

the analysis. For example the filling duration of 5 minutes was analysed based only on the intensities measured within the first 4 min.

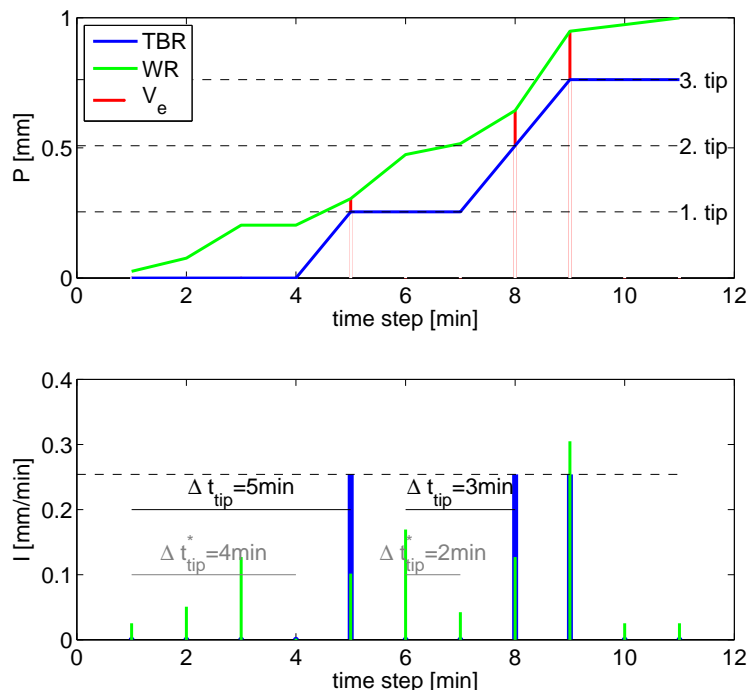


**Figure 3.11:** Illustration of the tipping bucket (TBR) mechanism as compared to the weighing raingauge (WR) observations for devices with the same temporal resolution. The upper panel shows the cumulative precipitation recorded by the TBR and the WR. The difference between the rainfall amount measured by the WR and the TBR is indicated in red ( $V_e$ ). The lower panel shows the corresponding rainfall intensities.

Figure 3.12 shows the intensities measured by the references stations for each tip interval compared to the intensity which would be obtained if the intensity were constant during each interval, which is obtained by dividing the tip amount by the interval size, as described by Fiser and Wilfert (2009).

At small intervals there is a large variability in the observed intensities and the median is higher than the average intensity. For interval lengths of 6 to 15 min the median of the observed intensities is close to the average, and for longer intervals it tends to be slightly lower than the average. A possible explanation for this is that at high intensity rainfall the last tip accounts only for a small fraction of the total tip amount, and therefore the intensities are generally higher than the average intensity which would be expected for that interval.

At long intervals, which often correspond to the beginning of an event with gradually increasing rainfall intensity, the last tip accounts for a higher fraction of the total tip amount and therefore the median of the intensities can even be lower than the average intensity. The variability in the rainfall intensity decreases with interval length, which indicates lower fluctuations in the rainfall intensity as compared to the short intervals.

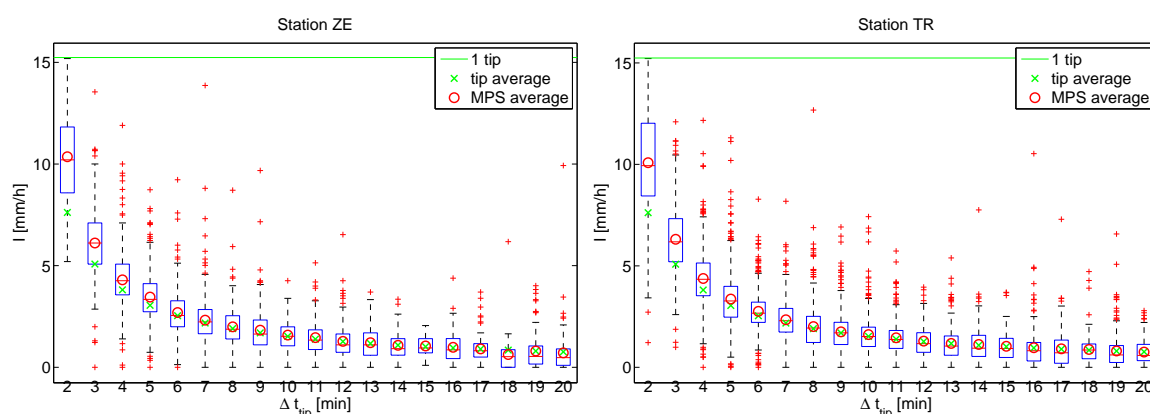


**Figure 3.12:** Distribution of intensities at the reference stations for different tip accumulation intervals,  $\Delta t_{tip}$ , in comparison with tip average and average of intensities observed at the reference stations. The red line indicates the location of the median, the blue box denotes the interquartile range and the whiskers have a length of the 1.5 times the interquartile range. The red crosses indicate outliers.

So far the analysis has shown that this interpolation technique reproduces well the median of the actually observed intensities for tip accumulation intervals of 6 to 15 min. In order to further assess the error introduced by this method, the frequency of the different tip accumulation intervals and the relative contribution of different tip accumulation intervals to the total rainfall amount was investigated (Figure 3.13). The latter was estimated by dividing the cumulative rainfall observed at a specific tip interval,  $P(\Delta t_{tip})$ , by the total cumulative rainfall,  $P$ .

Intervals of 1 to 5 min occur most frequently (i.e. 7-16% of all intervals) and the largest fraction of the total cumulative rainfall amount is recorded at those tip accumulation intervals (i.e. each interval accounts for 5 to 20% of the total rainfall amount). On the other hand, intervals above 6 min contribute always less than 5% of the total amount and the frequency of those accumulation intervals is below 5%. The higher total amount recorded at the station at the top is due to the higher frequency of short intervals, i.e. high intensity rainfall.

The analysis of the reference intensities for different tip accumulation intervals suggests that interpolation of tipping bucket data by assuming a constant average intensity is a good approximation for intervals between 6 and 15 min. For lower intervals there is an underestimation of the intensities observed by the reference gauge. This is particularly important since those short intervals occur most often and account for the largest part of cumulative precipitation. The overestimation for longer intervals is negligible since they occur very rarely and account only for a small amount of the cumulative rainfall recorded during the entire event.



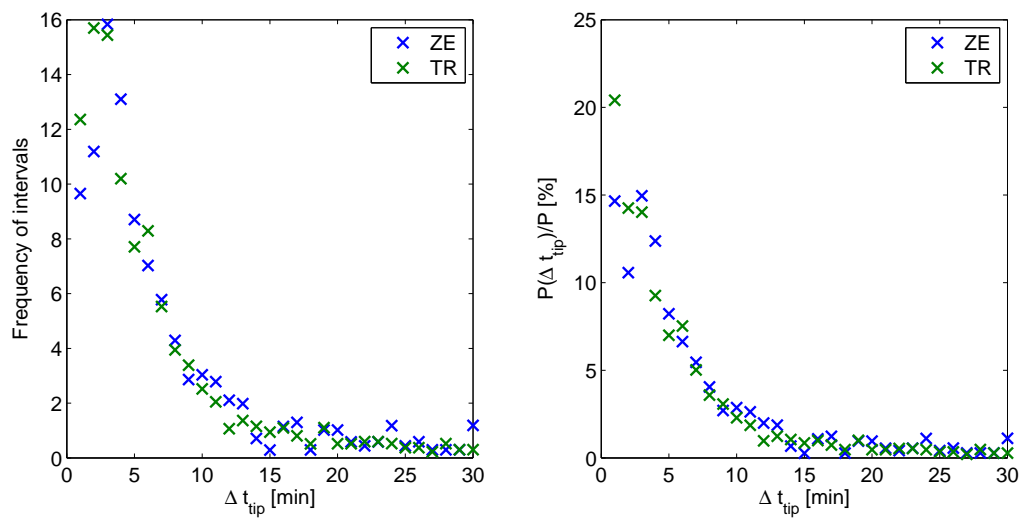


**Figure 3.13:** Occurrence of tip accumulation intervals,  $\Delta t_{tip}$ , for the reference stations TR and ZE and cumulative amount,  $P$ , recorded during each interval.

### 3.3.1 - iv Dynamic calibration (DC)

The measured intensities were corrected for systematic errors of the instruments according to the WMO field intercomparison of raingauges (Vuerich et al., 2009). It is a dynamic calibration (DC), i.e. it provides a correction factor, which is not constant but dependent on the measured rainfall intensity. In the WMO field intercomparison the measured rainfall intensities of different types of raingauges were compared to a composite reference, which consisted of an average rainfall intensity as obtained from a group of four reference raingauges. The behaviour of the gauges depending on the reference was estimated by fitting the following power law function.

$$I_m = p_a I_{dc}^{p_b} \quad (3.4)$$

where  $I_m$  denotes the measured intensity,  $I_{dc}$  the dynamically corrected intensity and  $p_a, p_b$  are parameters of the fitted power law. Consequently from the measured intensities the corrected intensity can be estimated. The parameters for the different gauges are listed in table 3.3. Due to mechanical errors in the tipping bucket mechanism, the correction of TBRs at high intensities exceeds the one of the weighing gauge. For the Davis tipping bucket gauges intensities below 5.6 mm/h result in a negative correction while for higher intensities the correction is positive. For the reference gauges the threshold intensity is 6.3 mm/h.

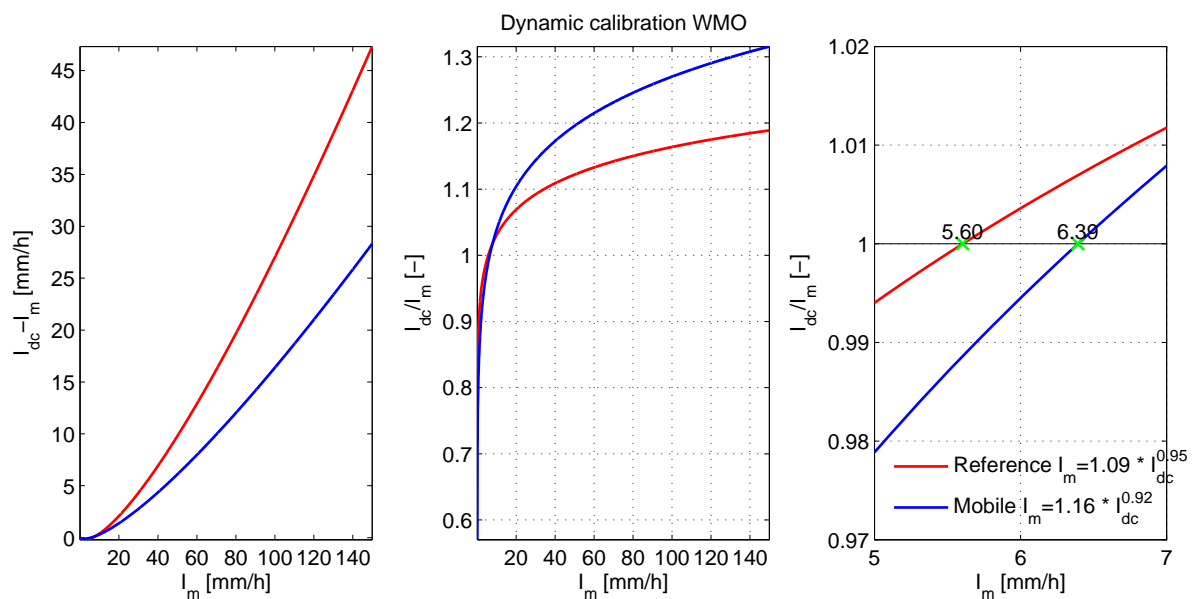


Figure 3.14: Dynamic calibration of measured rainfall intensities

### 3.3.1 - v Averaging between P1 and P2

The mobile stations were equipped with two pluviometers (P1, P2) in order to have some redundancy because the tipping bucket mechanism is rather sensitive to various sources of

**Table 3.3:** *Dynamic calibration of measured rainfall intensities for different types of raingauges*

Raingauge	$p_a$	$p_b$	$R^2$
Mobile station (Davis)	1.16	0.92	0.73
Reference station (MPS)	1.09	0.95	0.59

errors. For example obstruction of the funnel outlet by leaves and insects, or accumulation of dust in the tips can affect the tipping volume and the timing of the tips. A simple solution for detection of those mechanical problems is the installation of two devices at the same station as suggested by Krajewski et al. (2003) since a simultaneous failure of both gauges is very unlikely.

The first three post-processing steps were applied to each gauge individually. The interpolation and the wind correction were applied to the averaged values. To account for cases where one raingauge measured was not working properly (i.e. obstacles that were stuck in the funnel), the average was taken only if the difference between P1 and P2 were smaller than 20%. Otherwise the pluviometer with the higher precipitation amount was used instead of the average.

$$\bar{I} = \begin{cases} \frac{I_1 + I_2}{2} & \text{if } |I_1 - I_2| < 0.2I_1 \\ I_1 & \text{if } I_2 < 0.8I_1 \\ I_2 & \text{if } I_1 < 0.8I_2 \end{cases} \quad (3.5)$$

### 3.3.1 - vi Wind correction (WC)

Since the rain gauge disturbs the local wind field, the rainfall amount falling on the ground is underestimated by the gauge. Since none of the gauges were shielded, except the reference station TR, a wind correction wind correction (WC) was applied. The wind correction factor depends on rainfall intensity, drop size and wind speed. It is high at low intensities, for small drop sizes and high wind speeds. The correction factor was estimated based on the results of a numerical simulation of the wind field around a raingauge, from which the trajectories of the raindrops were estimated (Nespor and Sevruk, 1999). The true rainfall intensity is estimated by integrating the number of drops,  $n_D$ , per unit volume of air and unit drop size interval over the dropsize distribution  $D_D$ .

$$I = C_R \int_{D_{D,min}}^{D_{D,max}} n_D V_D u_T dD_D \quad (3.6)$$

where  $C_R$  is a unit conversion factor,  $V_D$  is the drop volume and  $u_T$  is the terminal velocity of the drop. The missing rainfall intensity,  $I^*$ , is estimated by integrating the partial wind-induced error,  $e_p$ , over the drop size distribution  $D_D$ .

$$I^* = C_R \int_{D_{D,min}}^{D_{D,max}} e_p n_D V_D u_T dD_D \quad (3.7)$$

The wind corrected intensity,  $I_{wc}$ , is calculated as follows.

$$I_{wc} = I + I^* \quad (3.8)$$

In this study the wind correction factor,  $f_w$ , is defined as follows.

$$f_w = \frac{I_{wc}}{I} \quad (3.9)$$

where  $I$  denotes the rainfall intensity obtained in the previous post-processing step and  $I_{wc}$  the intensity corrected for wind-induced losses. As shown in Figure 3.15 the wind correction is relevant for high wind speeds and for low rainfall intensities. The error is only in the order of about 5% for intensities higher than 4 mm/h and for wind speeds below 5 m/s. However, for all wind speeds there is a rapid increase in the correction factor for intensities below about 1 mm/h.

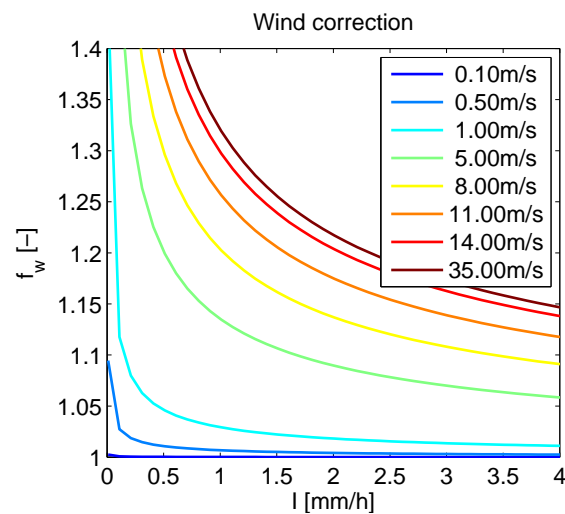


**Figure 3.15:** Wind correction factor depending on rainfall intensity depending on wind speed.

### 3.3.2 Post-processing results

This section presents the results of the data post-processing according to the procedure described in Section 3.3.1. The data analysis was concentrated on single events as shown in Figure 3.5. The absolute and relative amount of corrected rainfall was analysed for the different stations and for the different events. Since the placement of the stations was different in the two IOPs, the data were also analysed separately for the two observation periods.

#### 3.3.2 - i Corrections during entire observation period

Table 3.4 shows the absolute and relative correction in each step of the post-processing procedure. The interpolation of missing values is negligible in comparison to the other corrections. Static calibration and wind correction are of similar magnitude in terms of mean and standard deviation, however wind correction is always positive whereas the static calibration can also be negative. The dynamic calibration is the correction with the largest standard deviation and it can also be either positive or negative depending on the intensities (Figure 3.16). Its mean is slightly negative, which indicates that low intensities occur more frequently than high ones. The maximum correction is also obtained for the dynamic calibration, which shows the importance of this correction for intense rainfall.

**Table 3.4:** *Post-processing summary of all stations and events combined in relative and absolute amounts with respect to the previous processing step*

	IM	SC	DC	WC
Mean [%]	0.08	2.12	-1.49	2.42
Std [%]	0.52	3.06	6.89	1.93
Max [%]	7.88	20.51	21.37	10.52
Min [%]	0.00	-10.28	-11.78	0.00
Mean [mm]	0.02	0.34	-0.07	0.42
Std [mm]	0.11	0.62	1.19	0.52
Max [mm]	1.65	4.78	6.35	2.73
Min [mm]	0.00	-2.19	-2.21	0.00

#### 3.3.2 - ii Corrections during the two field experiments

The results were also analysed separately for the two field experiments since the location of the mobile stations was different in the two periods. In Table 3.5 the post-processing results are summarized for each event and station separated according to the measurement period. Comparison between the two measurement periods shows little differences in the interpolation

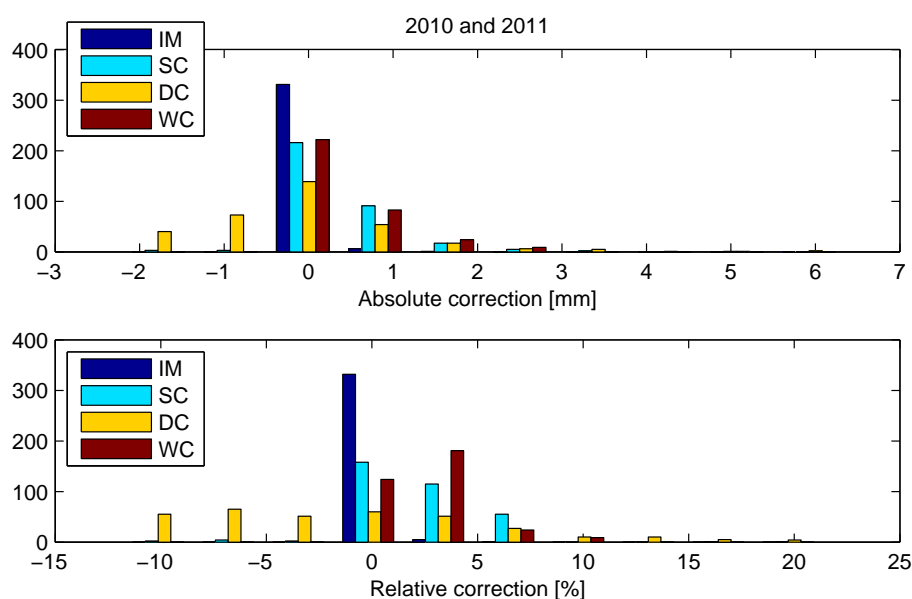


**Figure 3.16:** Histogram of absolute and relative correction for each event and each station in 2010 and 2011.

of missing values, the static calibration and the wind correction. The slightly higher WC in 2010 could be explained by the fact that more stations were placed in the upper part of the transect, where generally higher wind speeds are observed. The DC on the other hand shows considerable differences between the two measurement periods. In 2010 the average was positive, whereas in 2011 the mean correction was negative. A possible explanation is that less high intensity events were observed in 2011. Since high intensities are more frequently observed at high altitudes, the difference in the WMO correction could also be due to the change in the station location towards the lower altitudes in 2011 (Figure 3.18).

**Table 3.5:** Post-processing summary of all stations and events in relative and absolute rainfall amounts.

	2010				2011			
	IM	SC	DC	WC	IM	SC	DC	WC
Mean [%]	0.15	2.51	1.00	2.61	0.05	1.94	-2.63	2.34
Std [%]	0.49	3.52	8.77	2.33	0.53	2.81	5.50	1.72
Max [%]	2.63	20.51	21.37	10.52	7.88	7.47	11.93	7.98
Min [%]	0.00	-9.85	-11.08	0.03	0.00	-10.28	-11.78	0.00
Mean [mm]	0.03	0.40	0.39	0.42	0.01	0.31	-0.28	0.42
Std [mm]	0.09	0.71	1.58	0.55	0.11	0.58	0.88	0.51
Max [mm]	0.51	4.78	6.35	2.73	1.65	3.62	2.33	2.47
Min [mm]	0.00	-1.43	-2.16	0.01	0.00	-2.19	-2.21	0.00

### 3.3.2 - iii Comparison of corrections for different stations

The mean absolute and relative corrections of all the events in 2010 and 2011 are summarized for the different stations in Figure 3.17. The sum of all corrections is in the order of -2 to 2.2 mm which corresponds to about -3 to 9.5% of the mean event precipitation observed at each station. Negative corrections were observed mainly at the reference station ZE, but in 2011 some of the stations at low elevations showed negative corrections. The largest difference between the two observation periods is the dynamic calibration, which is generally positive in 2010 (-0.1 to 1 mm or -2 to 7 %), except for the reference stations, and mostly negative in 2011 (-1 to -0.2 mm or -5 to -1 %).

Missing values occurred more often in the first measurement period, since the data storage and transfer was dependent on the communication with the base station. A high correction was obtained for stations that had bad connectivity to the base stations number 5 and 10.

The static calibration factor can be different at the same station between the two measurement periods, because the stations were not put in the same order along the elevation profile. Another reason is that the rainfall amount is measured with two pluviometers at the mobile stations. Depending on how much each of the pluviometer measures one or the other calibration coefficient has more influence on the total correction.

The wind correction shows an increasing tendency for stations at higher elevations, especially for the field experiment of 2011. However, comparison of processed and original mean cumulative event precipitation shows that the increase does not alter the pattern substantially. For both there is an increase along the lower transect up to station number 9 in 2011 and slightly lower precipitation in the upper part.

### 3.3.2 - iv Comparison of events

Figure 3.18 shows the absolute and relative correction of the different events averaged over the different stations for the field experiments of 2010 and 2011. The interpolation of missing values is negligible compared to the other correction procedures. The static calibration in terms of relative amounts is very similar among the different events. The dynamic calibration shows the highest variability among the different events. In 2010 there were two events (nr. 1 and 4) with corrections of more than 3 mm. These two events are responsible for the positive DC correction observed at the mobile stations during that period. In 2011 there were less high intensity events and therefore the dynamic calibration was negative in 12 out of 18 events with a minimum of -2 mm or -9% resulting in a negative DC correction at all stations 3.17. The wind correction is of similar magnitude for most events.

The cumulative corrections among the events vary between -7 and +10%, which is a much stronger variability than observed among the different stations. It is mainly due to differences in the wind correction and the dynamic calibration.

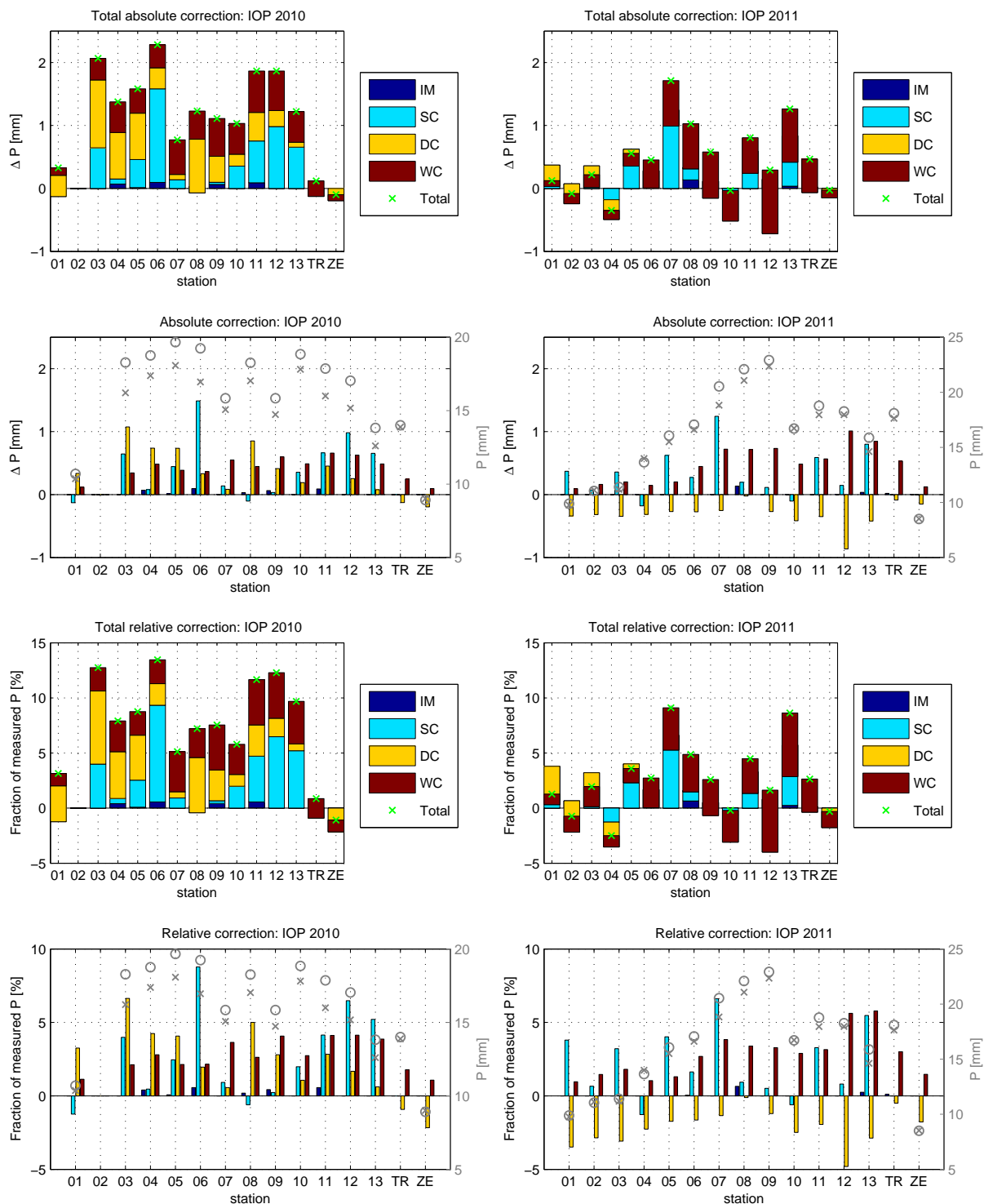


**Figure 3.17:** Absolute and relative correction for each station in 2010 and 2011. The green cross indicates the sum of all corrections. In the lower part of the figure the contribution of the different components of the correction is documented and the mean cumulative precipitation,  $P$ , observed during all the events observed during the corresponding season is shown for the corrected ( $x$ ) and uncorrected data ( $o$ ).



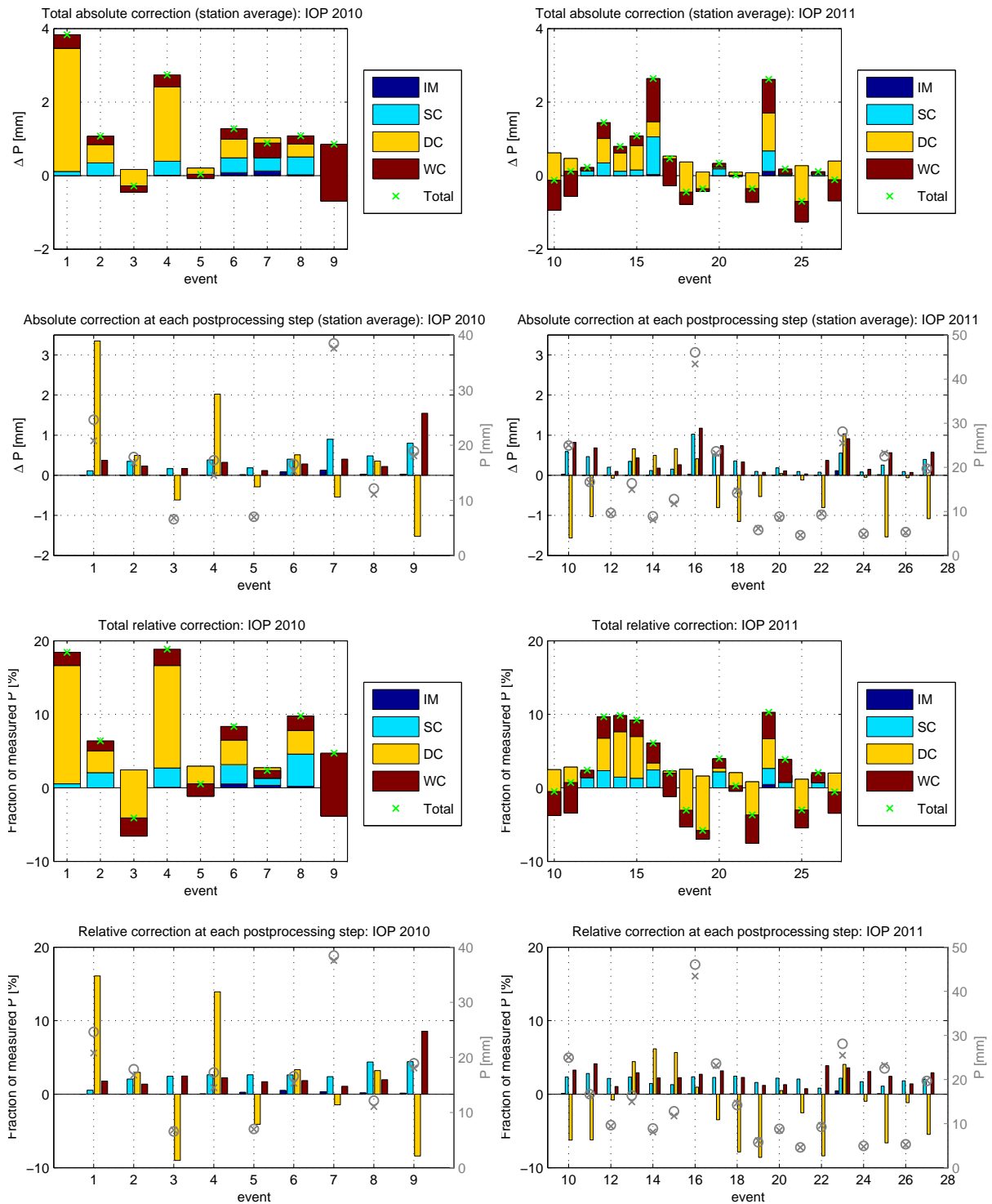


**Figure 3.18:** Absolute and relative correction for each event in 2010 and 2011. The green cross indicates the sum of all corrections. In the lower part of the figure the contribution of the different components of the correction is documented and the mean cumulative precipitation,  $P$ , observed during all the events observed during the corresponding season is shown for the corrected ( $x$ ) and uncorrected data ( $o$ ).

### 3.3.2 - v Summary of post-processing results

The rainfall data measured by different weather stations were corrected for missing data in the time series by linear interpolation of the data recorded within a time interval of 10 min. The analysis of the selected events shows that this correction has only a minor effect on the total cumulative rainfall. Device specific deviation from a reference obtained from the first set of TBRs, which were found to provide a more reliable rainfall estimate, was accounted for by static calibration. This correction consist of a constant correction factor for each station the absolute and relative importance of this correction is therefore station dependent, ranging from -5 to +10%. For different events the static calibration results in an increase of about 2%. Because the rainfall amounts measured at different locations vary among the events, the absolute and relative correction shows some variation among the different events however it is always positive.

By applying a dynamic calibration the measurements were corrected for intensity dependent errors. Comparison of the averaged correction of each event shows large differences, which are ranging between -10 and +17% depending on the intensities measured during a particular storm. In 2010 more high intensity events were observed, which leads to a positive correction for the station average. An exception are the two reference stations which have on average a negative correction since they are able to record low intensity rainfall. During IOP 2011 more low intensity events were recorded, which results in a negative correction when looking at the station average. For most of the stations and events the dynamic calibration was more important than the static one.

In addition, a wind correction based on numerical simulation of the wind field around the gauge was applied in order to account for wind-induced losses. Wind correction is always positive and results in corrections in the order of 2-5% for both station and event average. Since winds tend to be stronger in the upper part of the transect, the data show a slight increase in the wind correction with the station elevation.

The relative importance of the different corrections depends on both the specific station, its location and on the event characteristics such as rainfall intensity and wind speed. Correction of missing values is negligible compared to the other sources of errors.

### 3.3.3 Uncertainty analysis

Rainfall observations are affected by measurement errors, and application of the different post-processing steps described in Section 3.3.1 introduces additional uncertainty to data. For the interpretation of the results a detailed investigation of the uncertainty is therefore necessary. In this section, the method selected for the uncertainty analysis and its application to the data at the different post-processing steps is presented.

#### 3.3.3 - i Method

The error of any function  $q$  can be quantified by the uncertainties of the input variables (Taylor, 1997). For a function  $q$  of one variable  $x$  the absolute uncertainty,  $u_a$ , is computed by multiplying the uncertainty of variable  $x$ ,  $\delta x$ , by the derivative of  $q$  with respect to  $x$ .

$$u_a = \delta q = \left| \frac{dq}{dx} \right| \delta x \quad (3.10)$$

If  $q(x, \dots, z)$  is a function of several variables or parameters. The absolute uncertainty is computed as the sum of partial derivatives with respect to all variables.

$$u'_a = \delta q' = \left| \frac{\partial q}{\partial x} \right| \delta x + \dots + \left| \frac{\partial q}{\partial z} \right| \delta z \quad (3.11)$$

Assuming independent and random errors in the variables, the absolute uncertainty in  $q$  is reduced to the following.

$$u_a = \delta q = \sqrt{\left( \left| \frac{\partial q}{\partial x} \right| \delta x \right)^2 + \dots + \left( \left| \frac{\partial q}{\partial z} \right| \delta z \right)^2} \leq \delta q' \quad (3.12)$$

This equation was applied in the analysis of the uncertainties of the data post-processing. The fractional uncertainty,  $u_f$ , is computed by dividing the absolute uncertainty by  $q$ .

$$u_f = \frac{\delta q}{|q|} \quad (3.13)$$

In the post-processing of the tipping bucket data five corrections were applied, namely the static calibration, the averaging of the two pluviometers, the dynamic calibration, the interpolation of the TBR data and the wind correction. In this case the uncertainty associated with the intensity computed by equation 3.14 needs to be evaluated.

$$I_{p5} = 0.5 f_w \left[ p_a \left( \frac{f_{c,1} I_1}{n} \right)^{p_b} + p_a \left( \frac{f_{c,2} I_2}{n} \right)^{p_b} \right] \quad (3.14)$$

where  $I_{p5}$  denotes the rainfall intensity at post-processing step 5,  $I_i$  denotes the rainfall intensity at raingauge  $i$ ,  $f_{c,i}$  denotes the static calibration factor of raingauge  $i$ ,  $n$  is the tip interval,  $f_w$

is the wind correction factor and  $p_a, p_b$  are parameters of the dynamic calibration. Since the analysis of the post-processing has shown that the interpolation of missing values is negligible, this step was neglected in the analysis of the uncertainty. In the case of the reference stations no static calibration was applied ( $f_{c,1} = f_{c,2} = 1$ ), no averaging was necessary and the data of the weighing raingauge do not need to be interpolated ( $n = 1$ ). Therefore, equation 3.14 reduces to the following.

$$I_{p6} = f_w p_a I_1^{p_b} \quad (3.15)$$

### 3.3.3 - ii Uncertainty of different post-processing procedures

Uncertainty in the final intensity estimate results from measurement errors of the gauges but also from uncertainty in the parameter estimates of the different post-processing steps. Therefore, the uncertainty in the post-processed rainfall intensity,  $I_p$ , was estimated as the combination of measurement errors and parameter uncertainties. In the following section the uncertainty is computed for each post-processing step as described in Section 3.3.1.

The parameters and their relative uncertainty used in the uncertainty analysis are listed in Table 3.6. Since the error was not documented for all variables and parameters, they were estimated to be 5% and 2% in the case of the exponent of the dynamic calibration. Since the uncertainty due to post-processing is more important for the tipping bucket data as compared to the weighing raingauge, only the former will be described in detail. At each post-processing step the uncertainty is analysed for the average between the two pluviometers installed at one station. The second post-processing step, i.e. the static calibration, is applied to the amount of precipitation measured in 1 min. In order to apply the dynamic calibration and the wind correction, the data need to be interpolated to intensities in mm/h. In the following section the mathematical equations of the different corrections are described. The uncertainty introduced by applying the different corrections was then evaluated by applying these functions in equation 3.12.

**Measurement error and averaging** First the uncertainty was computed for case where no post-processing is applied to the data except the averaging between the two tipping bucket gauges. The measurement error of the tipping bucket gauges is 5%, which results in an absolute uncertainty of  $\delta I = 0.05I$ .

$$I_{p1} = 0.5(I_1 + I_2) \quad (3.16)$$

**Static calibration** If in addition to the measurement errors the error due to calibration is included, the following equation has to be evaluated.

$$I_{p2} = 0.5(f_{c,1}I_1 + f_{c,2}I_2) \quad (3.17)$$

**Interpolation of TBR data** Adding the interpolation step to the post-processing results in the following equation.

$$I_{p3} = \frac{(f_{c,1}I_1 + f_{c,2}I_2)}{2n} \quad (3.18)$$

**Dynamic calibration** Application of the dynamic calibration results in the following equation.

$$I_{p4} = a \left( \frac{f_{c,1}I_1}{2n} \right)^b + a \left( \frac{f_{c,2}I_2}{2n} \right)^b \quad (3.19)$$

**Wind correction** The uncertainty introduced due to the wind correction depends also on the wind speed, which has a measurement error of 5% for both the reference and the mobile weather stations. Moreover, the correction is based on multiple parameters, which characterize the geometry of the raingauge and the drop size distribution (Nespor and Sevruk, 1999). Since the uncertainty of the parameters is not known, the uncertainty is not calculated explicitly and the resulting wind correction factor,  $f_w$ , was assumed to have an uncertainty of 5%.

$$I_{p5} = f_w \left[ a \left( \frac{f_{c,1}I_1}{2n} \right)^b + a \left( \frac{f_{c,2}I_2}{2n} \right)^b \right] \quad (3.20)$$

### 3.3.3 - iii Quantification of uncertainty

Figure 3.19 shows the results of the uncertainty analysis in terms of absolute values for each post-processing step as described above. For the first two steps (averaging and calibration) the correction refers to the tip intensity,  $I_{tip}$ , which is defined as the average between the two pluviometers without interpolating the data ( $I_{tip} = \frac{1}{2}(I_1 + I_2)$ ). The other post-processing steps are based on the interpolated intensity ( $I = \frac{1}{2n}(I_1 + I_2)$ ).

For the averaging, the static calibration and the interpolation the absolute uncertainty increases linearly with increasing intensity. The fractional uncertainty is therefore independent of the intensity (Figure 3.20(a)). On the other hand, the relative uncertainties due to the dynamic calibration and due to the wind correction are dependent on the intensity. At high intensities mainly the dynamic calibration is responsible for the strong increase in the relative uncertainty. At low intensities it is less important, and the wind correction has a higher influence on the relative uncertainty. Comparison of the correction at different wind speeds shows that at high intensities the influence on the relative uncertainty is almost negligible, whereas at low intensities the wind speed is very important (Figures 3.20(a) and 3.21).

The uncertainty due to post-processing is generally smaller for the reference stations since no static calibration is applied and since it measures lower intensities (Figure 3.20(b)).

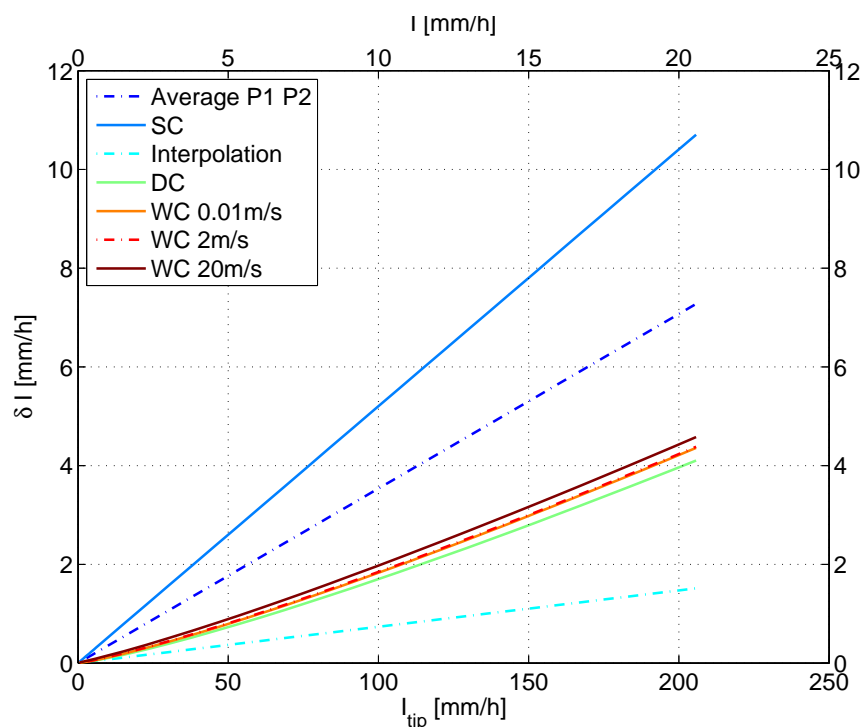
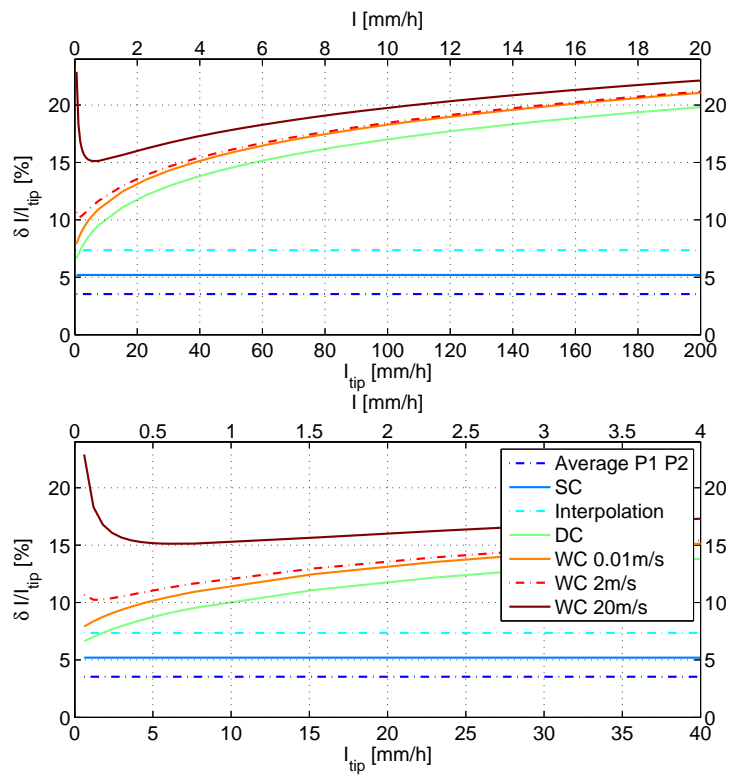
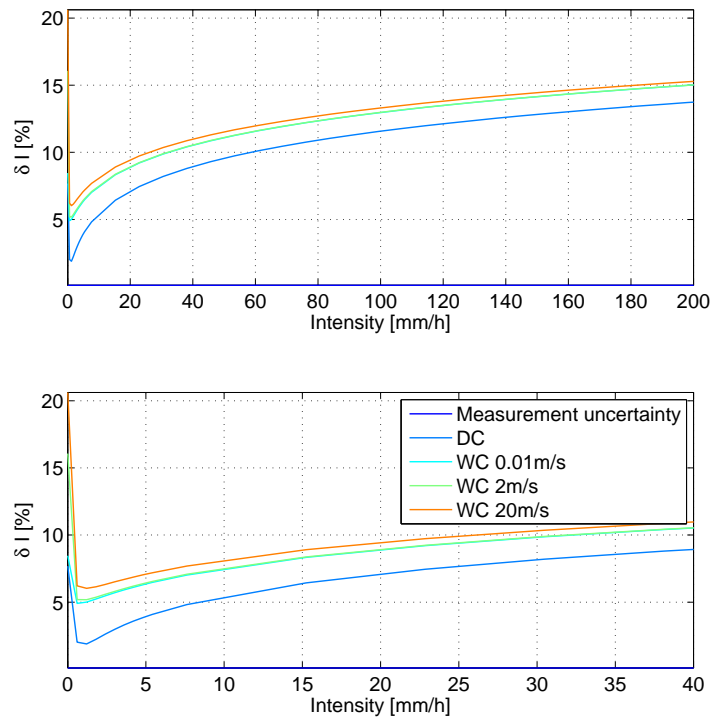


**Figure 3.19:** Absolute uncertainty at each post-processing step depending on the measured rainfall intensity is shown for the mobile weather station nr. 6 (the different stations only vary in terms of their static calibration factor)



(a) Mobile weather station 6



(b) Reference weather station TR

Figure 3.20: Relative uncertainty at each post-processing step depending on the measured rainfall intensity

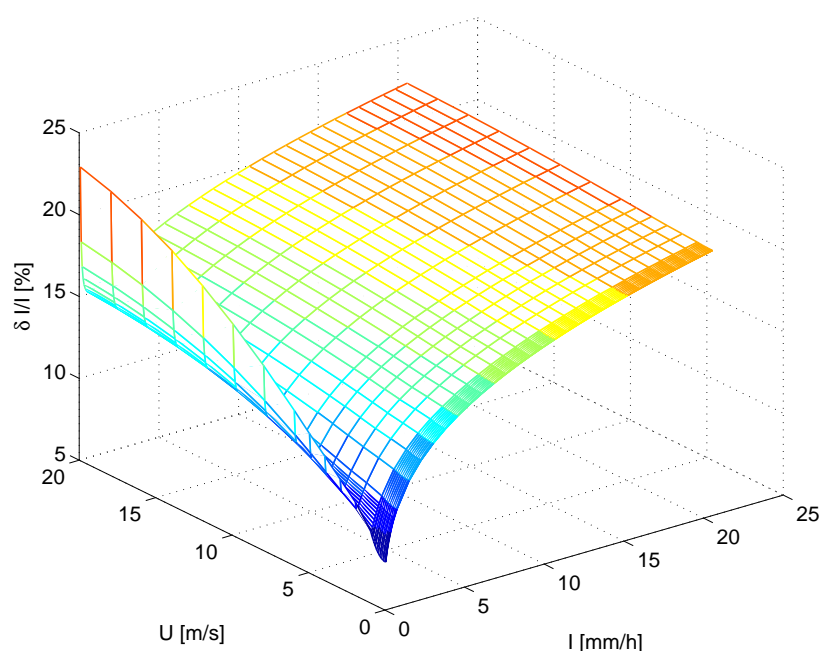


**Figure 3.21:** Relative uncertainty depending on wind speed  $U$  and rainfall intensity  $I$  for station 6

Figure 3.21 shows the fractional uncertainty relative to the measured precipitation, depending on wind speed,  $U$ , and intensity,  $I$ . The measured precipitation is assumed to be the mean of the two raingauges interpolated over a duration of  $n=10$  time steps ( $I = \frac{1}{2n}(I_1 + I_2)$ ). Since the calibration factor differs among all pluviometers, the uncertainty varies slightly between each station, since each of them consists of two different pluviometer devices. The figures above show the results for station 6 ( $f_{c,1}=0.950, f_{c,2}=1.020$ ).

**Uncertainty analysis of event precipitation** The measurement uncertainty estimated in the previous section was then applied to the measured event rainfall data. The resulting uncertainty in the cumulative event rainfall is listed in Table A.7. The reference stations have an uncertainty between 5 and 8 %, and the mobile stations have an uncertainty of 15 to 22 %. The original time series has an uncertainty of 0.1% in the case of the weighing raingauges and 5% in the case of the original TBR data. Due to the dual gauge deployment at the mobile stations the uncertainty of the TBR can be reduced to 3.5%. Due to the nonlinearity of the dynamic calibration, the absolute uncertainty is largest at high intensities, and therefore it affects intense rainfall events more than stratiform rainfall.



**Table 3.6:** Parameters of uncertainty analysis. Because the calibration factors are different for each pluviometer, the uncertainty is different for each of the mobile stations.

Parameters	unit	mobile stations		reference stations	
		value	$\delta$ [%]	value	$\delta$ [%]
$f_{c,1}$	-	station specific	5	-	-
$f_{c,2}$	-	station specific	5	-	-
a	-	0.862	2	0.917	2
b	-	1.087	2	1.053	2
$f_w$	-	f(u)	5	f(u)	5
n	min	10	5	-	-
<b>Variables</b>					
$l_1, l_2$	mm	0.01÷15 (0.1)	5	0.001÷15 (0.1)	0.1
U	m/s	1÷35 (5)	5	1÷35 (5)	5

## Chapter 4

# Results

The recorded rainfall events were analysed with respect to the small scale spatial and temporal pattern and its elevation dependence, and the influence of the terrain and weather type on the observed rainfall patterns were investigated. In Section 4.1 the rainfall time series are analysed in terms of their spatial and temporal correlation in order to assess the effect of terrain elevation on the internal structure of the events. Section 4.2 addresses the effect of elevation on cumulative event rainfall by investigation of rainfall gradients with elevation along the hillslope transects and the uncertainty of the resulting gradients due to data post-processing is presented. Furthermore, the gradient formation is analysed at the sub-event time scale and the control of the of terrain scale on the gradients is analysed. Section 4.3 investigates the control of the atmospheric conditions on gradient formation. In Section 4.4 the effect of terrain elevation on rainfall intensity is investigated within the framework of a linear model of orographic precipitation in order to analyze the effect of elevation on the spatial distribution of rainfall that can be expected due to the physical process of orographic lifting. In Section 4.5 the observed gradients are classified according to rainfall characteristics measured by the weather stations.

### 4.1 Spatial and temporal correlation

The correlation coefficient as a measure of the interdependence among random variables can be used to study the spatial and temporal structure of rainfall processes. The strength of the correlation is directly related to the rainfall regime, with convective events being characterized by low correlation coefficients and stratiform ones exhibiting higher correlations (Krajewski et al., 2003). Apart from distinguishing among different types or rainfall events, correlation coefficients are also expected to reflect the changes in the rainfall generating mechanisms due to altitude.

Therefore, in this study the spatial and temporal correlation structure were analysed. Since

the correlation coefficient is strongly affected by the absolute rainfall intensity, the correlation structure and its elevation dependence was also investigated by estimating so called oscillation coefficients, which consider only the sign of the fluctuation in the rainfall time series and are therefore a more robust measure of the correlation structure. Aside from the analysis of the spatial structure of the different correlation measures, this analysis was also used to evaluate the post-processing (Section 3.3.1) and its effect on the statistical analysis of the data.

#### 4.1.1 Cross correlation

The cross correlation in the rainfall time series at neighbouring weather stations during the observed events was estimated according to Pearson's formula for the time series at 1 min resolution. Since the 1 min rainfall intensities are expected to be strongly affected by measurement errors, also the data aggregated over 15 and 60 min were analysed. In order to investigate how post-processing is affecting the cross correlation, it was estimated for both the original and the post-processed time series. The original data consist of the average between the two tipping bucket gauges at each station without any further correction of the data. In the case of the post-processed data, the correction was applied prior to the aggregation of the data. The correlation was analysed for the time series with time steps of zero rainfall included.

$$\rho(X, Y) = \frac{\sqrt{\sum_{i=1}^n (X_i - \bar{X})(Y_i - \bar{Y})}}{\sqrt{\sum_{i=1}^n (X_i - \bar{X})} \sqrt{\sum_{i=1}^n (Y_i - \bar{Y})}} \quad (4.1)$$

where  $\rho(X, Y)$  denotes the cross correlation between rainfall time series of length  $n$  at stations  $X$  and  $Y$ .

##### 4.1.1 - i Cross correlation for different events and stations

The results of the cross correlation analysis were compared among different events to analyse the influence of the rainfall regime and among different stations to detect the possible effects of altitude. In addition, the results obtained from original and post-processed data are compared.

**Comparison of events** Among the different events there are large differences in the median values obtained for the original time series ranging between 0.1 up to 0.9 (Figure 4.1(a)). It tends to be high for events with high intensity rainfall (i.e. event 1, 4, 13-16, 23) as can be seen from Figure 3.7. This finding contradicts the expectation that convective rainfall events are characterized by low correlation. Data aggregation generally increases the median value, and it decreases the interquartile range. The fact that aggregation of the time series reduces the difference in the cross correlation coefficient among the events indicates that its variability

is confined to small temporal scales.

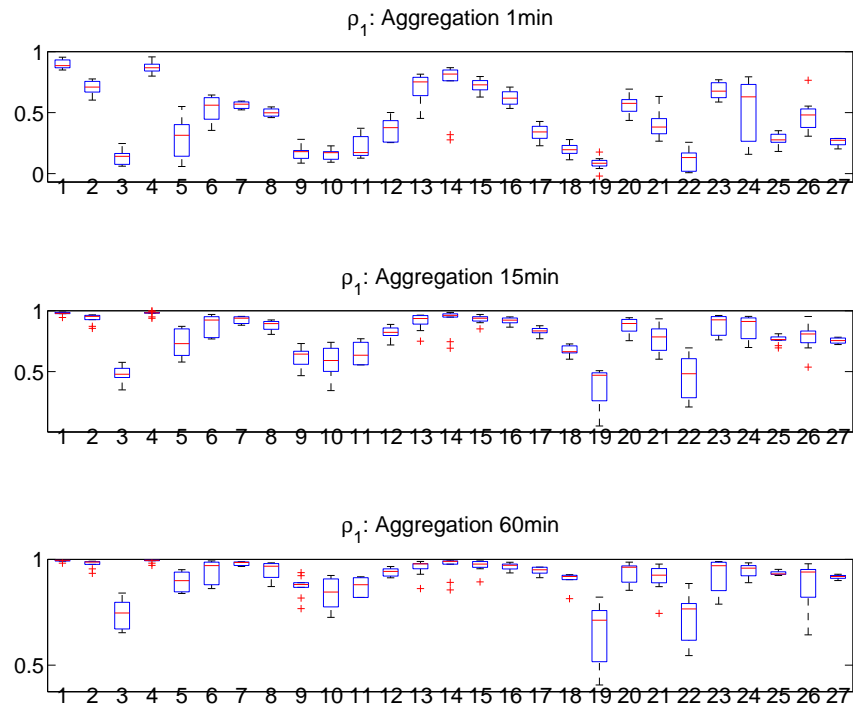
Post-processing increases the cross correlation, especially at the 1 min aggregation interval (Figure 4.1(b)). The effect is largest for events that have a low cross correlation in the original time series. Thus the post-processing causes a homogenization of the correlation structure in the different events. However, this is more likely an artefact of the post-processing rather than an actual similarity in the correlation structure of the different events.

Overall, this analysis shows the limitations of tipping bucket raingauges in capturing the small scale structure of the rainfall events. Application of post-processing results in a strong increase the correlation coefficients, especially for low intensity events, which results in a very similar correlation structure among the different events. However, this is more likely an artefact of the corrections rather than a reflection of the actual variability in the rainfall regime.

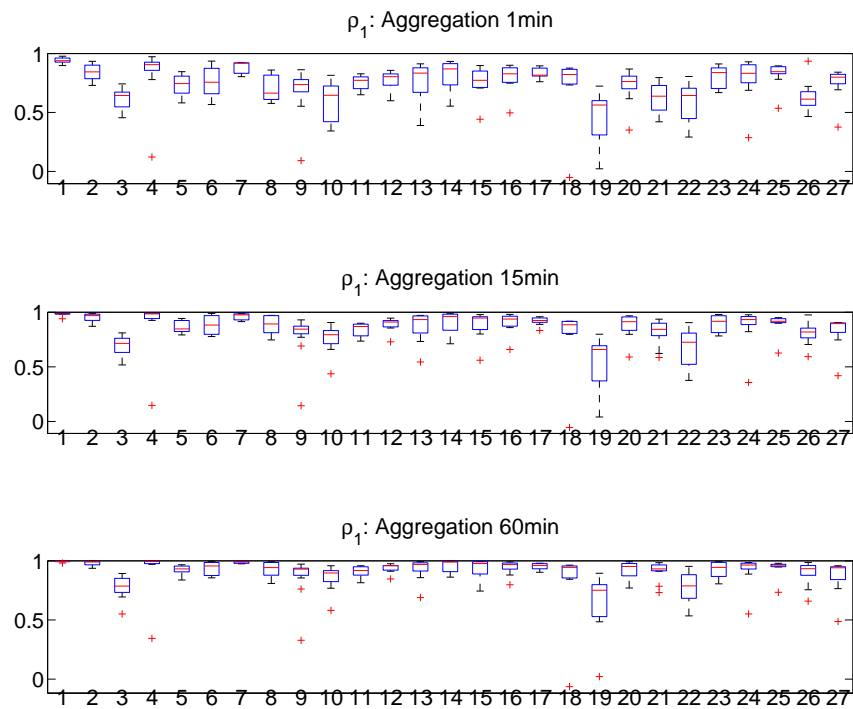
**Comparison of different stations** The cross correlation among pairs of neighbouring stations was compared among the different stations in order to detect a possible effect of elevation on the correlation structure. In the original data at 1 min resolution the cross correlation is rather low with median values below 0.5 (Figure 4.2(a)). Aggregation of the data at 15 min intervals strongly increases the median of the cross correlation up to 0.9, and at the same time the interquartile range decreases. When the aggregation interval is increased to 60 min, the cross correlation shows again a slight increase and a further decrease in variability among the different events.

After post-processing of the data the correlation tends to be higher (Figure 4.2(b)). For the time series at 1 min resolution the median of the cross correlation ranges between 0.5 and 0.9, and it is further increased as the data are aggregated at 15 and 60 min. For the 1 and 15 min aggregation the lowest cross correlation is observed between the reference station ZE and the first mobile station, which reflects the rather large distance between them, especially in the first field experiment in 2010.

Figure 4.2 shows no effect of altitude on the correlation structure, however this is most likely due to the limited ability of the tipping bucket gauges to resolve the small scale structure of the rainfall process. Therefore, it cannot be concluded that there is no effect of altitude on the correlation structure.

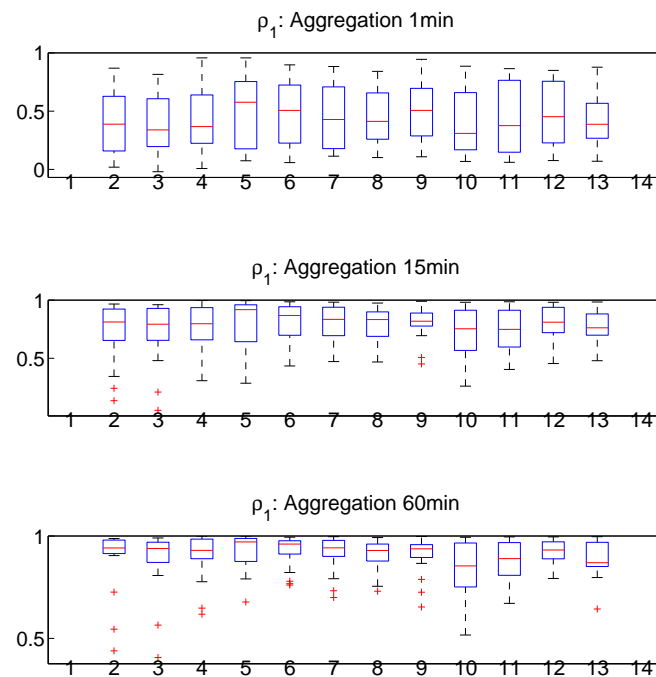


(a) Original rainfall time series

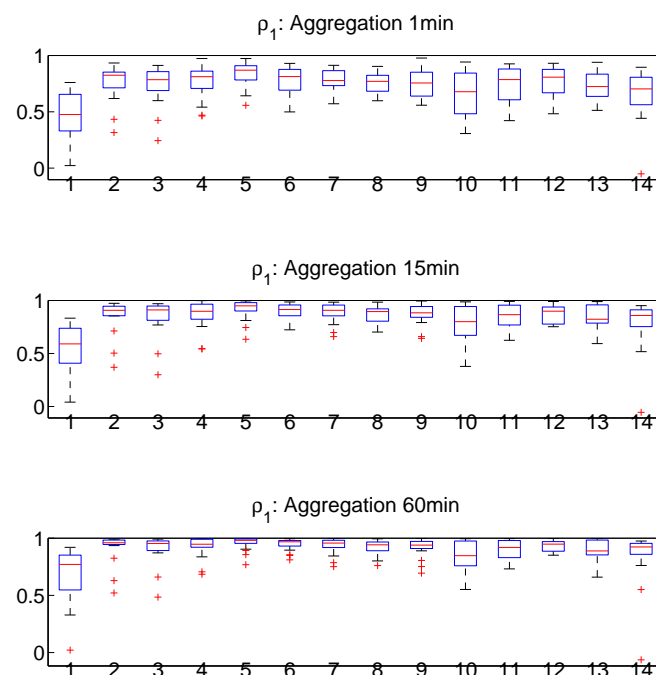


(b) Post-processed rainfall time series

**Figure 4.1:** Cross correlation in rainfall time series between neighbouring weather stations shown for the 27 different events ( $\rho_1$ ). The red line indicates the location of the median, the blue box denotes the interquartile range and the whiskers have a length of the 1.5 times the interquartile range. The red crosses indicate outliers.



(a) Original rainfall time series



(b) Post-processed rainfall time series

**Figure 4.2:** Cross correlation in rainfall time series between neighbouring weather stations shown for the 14 pairs of neighbouring stations ( $\rho_1$ ). Station pairs are numbered from 1 to 14 and are ordered according to increasing elevation. The red line indicates the location of the median, the blue box denotes the interquartile range and the whiskers have a length of the 1.5 times the interquartile range. The red crosses indicate outliers.

#### 4.1.1 - ii Decrease in spatial correlation with station distance

Since the analysis cross correlation in the rainfall time series among neighbouring pairs of weather stations shows some differences among the events (Section 4.1.1 - i), the cross correlation was also analysed for pairs of stations further apart. In particular, the decrease in cross correlation with increasing horizontal distance between station pairs was investigated. This investigation aims at detecting, whether different types of events exhibit a distinct spatial decorrelation. Decrease in cross correlation was modelled by fitting equation 4.2 to the estimated cross correlation coefficients as described in Krajewski et al. (2003), who found the spatial cross correlation structure at small distances to be strongly dependent on the climatic regime.

$$\rho = \rho_0 \exp\left(\left[-\frac{d}{d_0}\right]^{s_0}\right) \quad (4.2)$$

$\rho_0$  denotes the local decorrelation due to instrumental errors,  $d$  is the distance between station pairs and  $d_0$  is the correlation distance. A measure of the decrease in the spatial correlation is the shape parameter,  $s_0$ . For simplicity the parameter  $\rho_0$  was assumed to be equal to 1. Values of  $s_0$  equal to 1 indicate an exponential decrease in spatial correlation with increasing distance,  $s_0 < 1$  indicates a stronger decrease and for  $s_0 > 1$  the decrease is slower as compared to the exponential decrease. For the same shape parameter, a decrease in  $d_0$  causes a faster drop in correlation. Figure 4.3 shows the behaviour of equation 4.2 for different values of  $d_0$  and  $s_0$ .

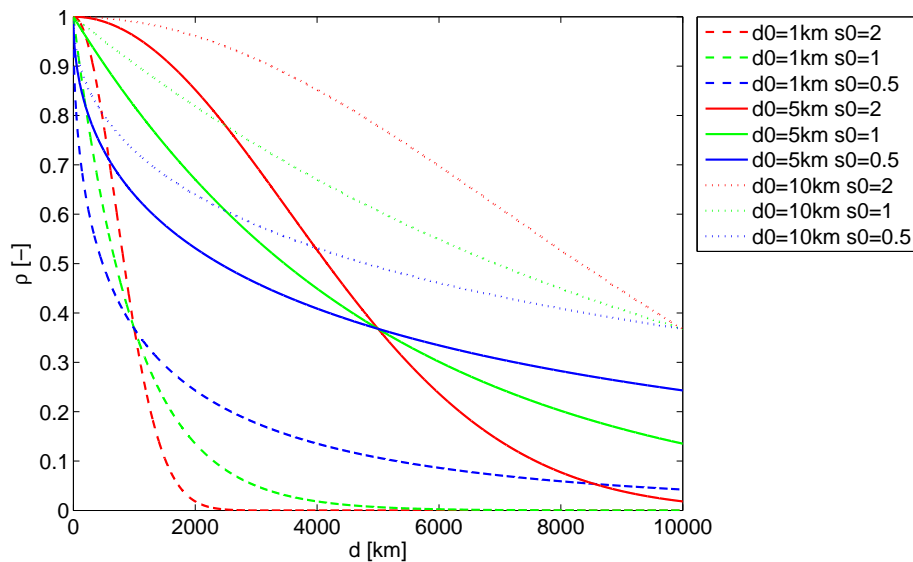
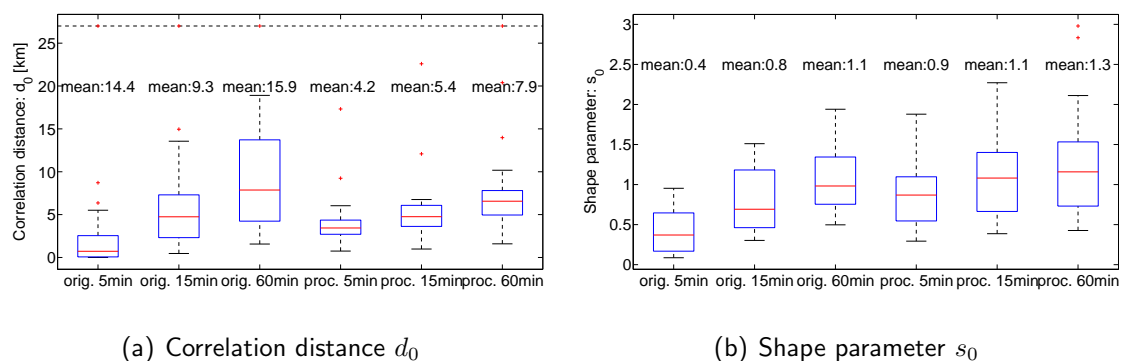


**Figure 4.3:** Decrease in spatial correlation for different combinations of  $d_0$  and  $s_0$

**Results** Figures 4.4(a) and 4.4(b) show the variability of the correlation distance and the shape parameter depending on the aggregation interval of the time series and depending on whether the data are post-processed or not. The data were analysed for different aggregation intervals, since tipping bucket gauges are not able to resolve the rainfall structure at very small temporal scales. The results show that both  $s_0$  and  $d_0$  increase with increasing aggregation interval and also with application of the post-processing.

The median of the correlation distance is increasing as the aggregation interval is increased and it slightly increases when the post-processing is applied to the 5 and 15 min data. The median of  $d_0$  ranges from 0.7 to 7.9 km for the original data and from 3.4 to 6.6 km for the post-processed data. However, application of the post-processing decreases the very large extreme values for event 2, which causes a strong decrease in the mean correlation distance as compared to the original data. The post-processing also decreases the variability in this parameter among the different events.

The shape parameter increases with increasing aggregation interval and with application of the post-processing. The aggregation causes a smoothing of the time series and shows therefore a slower decrease in cross correlation with increasing distance. The median of  $s_0$  ranges between 0.37 and 0.98 for the original data and between 0.87 and 1.16 for the post-processed data.



(a) Correlation distance  $d_0$

(b) Shape parameter  $s_0$

**Figure 4.4:** Correlation distance  $d_0$  and shape parameter  $s_0$  of different events estimated at different aggregation intervals for the original and post-processed rainfall time series.

**Effect of aggregation and post-processing** The magnitude of the increase in  $s_0$  and  $d_0$  due to data aggregation and post-processing are event dependent and so is their relative importance. Figure 4.5 shows the shape parameter for the different events and its confidence interval for the original and post-processed data at different aggregation intervals. In event 4, 5, 9-12, 23-25 and 27, for example, the aggregation causes less increase in  $s_0$  as compared to the change due to post-processing (Figure 4.5), but the opposite pattern is observed for the other events. Increasing the aggregation interval from 5 to 15 min causes a stronger increase in the shape parameter than from 15 to 60 min and in quite a few events the effect



of aggregation is stronger for the original data as compared to the post-processed ones. In a study by Krajewski et al. (2003) low values of the shape parameter were found to be associated with convective events whereas stratiform weather types resulted in values of  $s_0 > 1$ . Therefore, this parameter was compared among the different events in order to highlight differences in the rainfall regime. The fitting of the model to the original and post-processed data at different aggregation levels shows the importance of the resolution at which the data are measured and analysed. The application of the post-processing causes a smoothing of the intensities by averaging the tip amount over the time interval since the last tip recording, which results in an artificial increase in the spatial correlation among the stations. Furthermore, because the TBR are unable to capture low intensity rainfall, the original time series consist of a series of single tips that are separated by long dry durations, which results in a fast decrease in spatial cross correlation, even though there might be constant rainfall of low intensity. In this case a low value of  $s_0$  is not associated with a localized convective event, but it is an artefact of the temporal and volumetric resolution at which the gauge is operating. High correlations in the original time series can only occur for intense rainfall, where several tips can occur in a short amount of time, as can be seen for example in events 1 and 4 (Figure 4.5). However, the short duration and high rainfall intensities observed in those events (Figure 3.7), indicates convective rather than stratiform character. On the other hand, long duration events are often characterized by very low values of  $s_0$ . Both post-processing and aggregation generally cause an increase in the shape parameter but they do not lead to a substantial change in the relative position among different events.

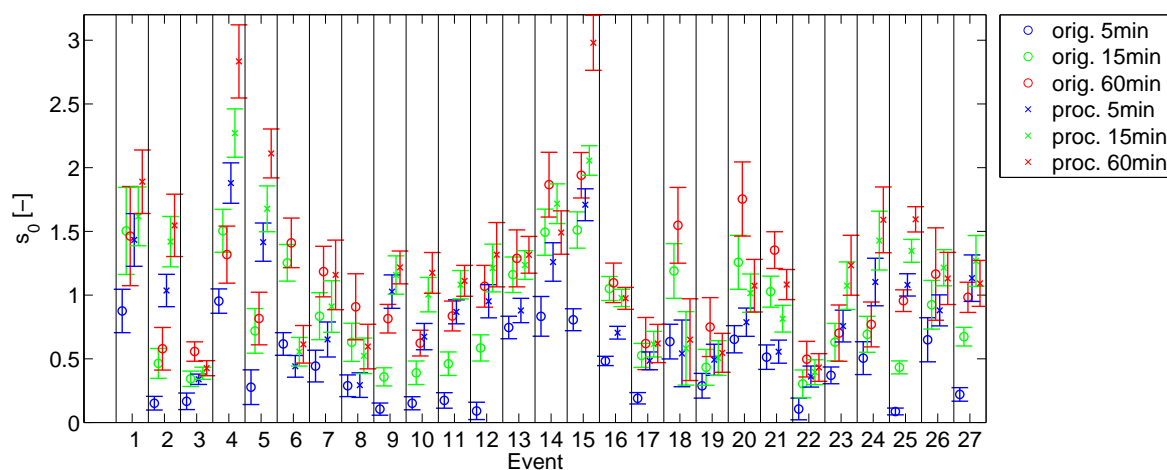


**Figure 4.5:** Comparison of the shape parameter,  $s_0$ , among different events estimated at different aggregation intervals for the original and post-processed rainfall time series.

A comparison of the correlation distance is shown in Figure 4.6. The correlation distance is affected more by the aggregation than the post-processing in most events. Exceptions are events 6, 8, 17-19, 22 and 27, where post-processed data at the 5 min aggregation show a

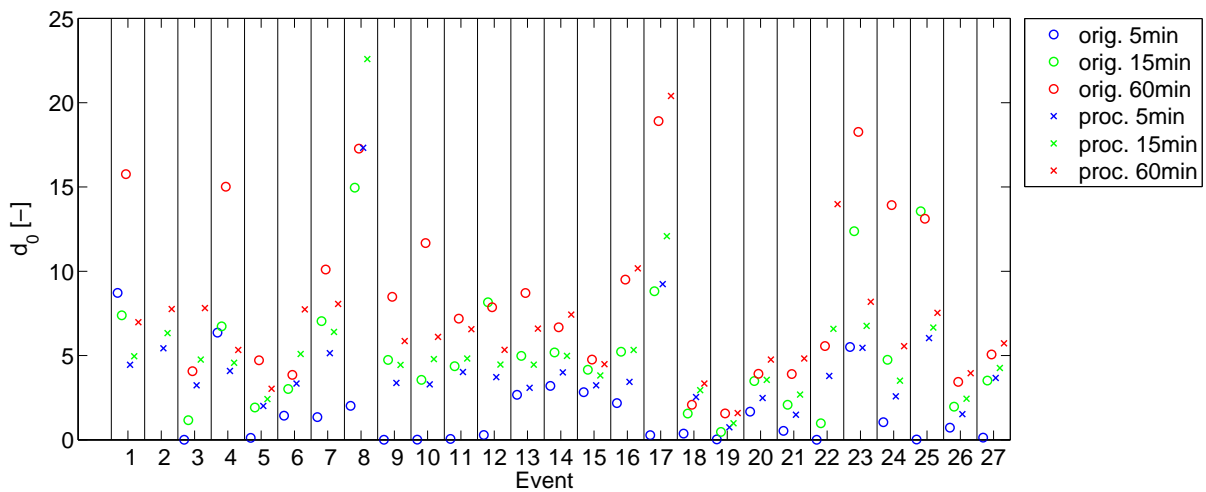


**Figure 4.6:** Comparison of the correlation distance,  $d_0$ , among different events estimated at different aggregation intervals for the original and post-processed rainfall time series. For clarification the values larger than 25 km were cut off.

stronger increase in  $d_0$  as compared to aggregation at 15 min intervals. Comparison of all events shows that both an increase from 5 to 15 and from 15 to 60 minutes can have a substantial effect on the correlation distance (Figure 4.6).

Comparison of  $d_0$  and  $s_0$  shows that for the post-processed rainfall time series, high values of  $s_0$  are observed for low values of  $d_0$  and vice versa (Figure 4.7). In the spatial decorrelation analysed from the original rainfall time series there is a higher correlation between the two parameters. An increase in the aggregation interval tends to increase both parameters, while the post-processing is often affecting one of the two parameters more than the other (e.g. event 15) or it increases one while decreasing the other as for example in event 8. As can be seen from Figure 4.3 a strong increase in  $s_0$  at low values of  $d_0$  corresponds to an increase of spatial correlation at short distances and a strong increase in  $d_0$  at low values of  $s_0$  affects mainly correlations at long distances.

In summary the analysis of the decrease in spatial correlation with increasing distance has highlighted a strong dependence of the shape parameter and the correlation distance on the post-processing of the data and on the aggregation interval and both tend to increase spatial correlation. The parameters vary among different events, however the variability reflects artefacts of the measurement technique and post-processing, rather than actual differences in the rainfall regime.

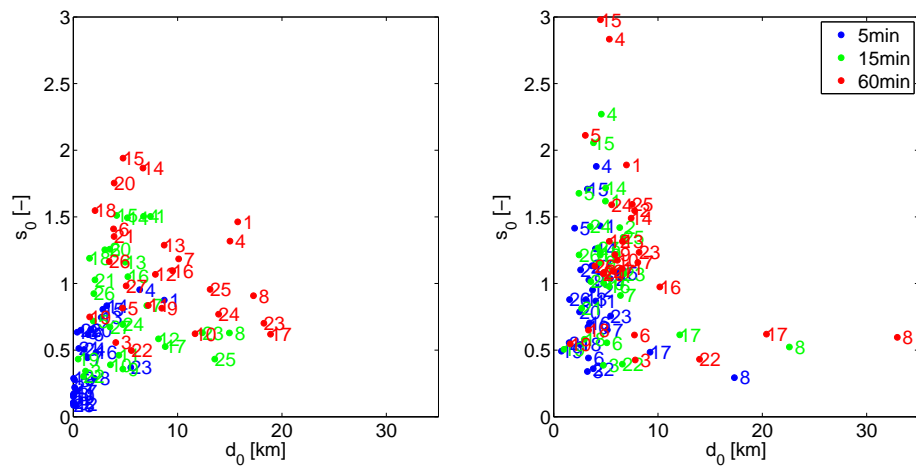


**Figure 4.7:** Comparison of the shape parameter  $s_0$  with the correlation distance  $d_0$  among different events estimated at different aggregation intervals for the original and post-processed data. For clarification the values larger than 35 km were cut off.

### 4.1.2 Autocorrelation

The autocorrelation of the rainfall time series was analysed in order to detect differences in the temporal rainfall structure among different weather stations, i.e. different altitudes, and among the observed events events, i.e. different rainfall regimes. The sample autocorrelation length,  $L_a$ , was estimated from the autocorrelation of the time series by searching the lag time at which the autocorrelation dropped below the 95% confidence interval defined as follows:

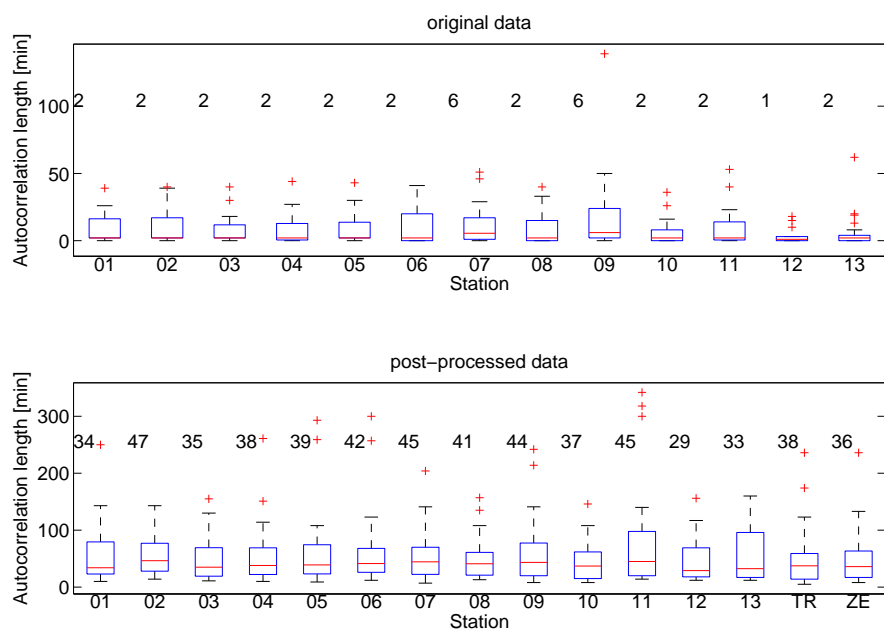
$$\pm \frac{2\sigma}{\sqrt{n}} \quad (4.3)$$

where  $n$  denotes the number of data points and  $\sigma$  the standard deviation. Comparison of autocorrelation lengths among different events and different stations for original and post-processed data at 1 min resolution is shown in Figure 4.8.

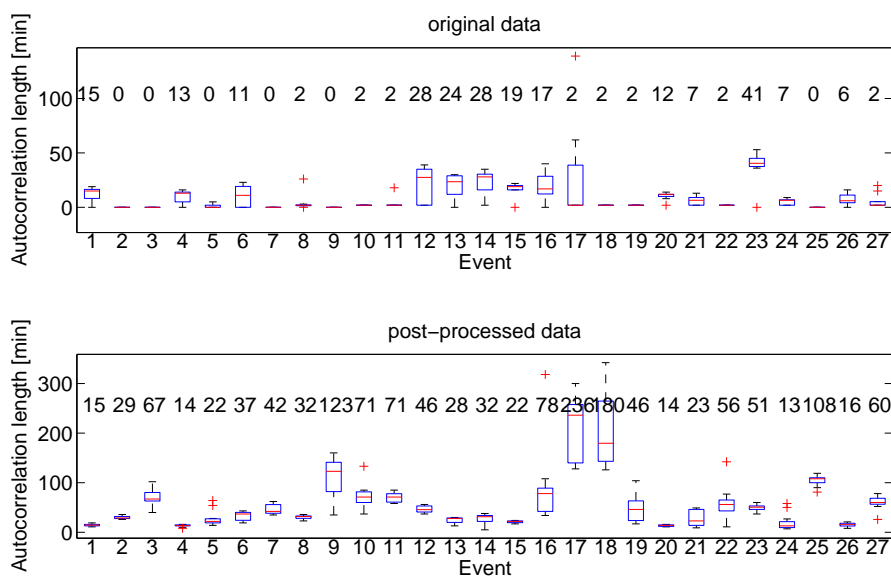
**Autocorrelation length depending on the station** The median of the autocorrelation length shows only small differences among different stations. For the original time series the autocorrelation length is in the order of 1 to 6 min (Figure 4.8(a)). An increase in autocorrelation is caused by the application of the post-processing procedure, resulting in a median of about 30 to 50 min. Also there seems to be a tendency for a stronger increase in autocorrelation for the stations at the top of T1 as compared to the stations in the valley and at the top. The reference stations show a similar range of values as the mobile stations when compared at the post-processed level, which indicates that the application of the post-processing to the rainfall time series measured by the two gauge types is successful in reconstructing a realistic decorrelation length.

**Autocorrelation length depending on the event** The median of the autocorrelation length for the different events is ranging between 0 and 30 min for the original rainfall time series (Figure 4.8(b)). Events with larger median values show also a high variability in  $L_a$ . For the post-processed data the autocorrelation length increases and it ranges between about 10 and 250 min. There is a much stronger increase in autocorrelation length for events with low values for the original data. For example in events number 17 and 18,  $L_a$  increases from 2 min to 180 and 240 min respectively, whereas in events 1, 4 and 13 - 16 only a very small increase in autocorrelation length is observed. These events are characterized by short duration with high intensity rainfall (Figure 3.7). Since in high intensity rainfall events the time intervals between the tips are smaller, less interpolation is necessary, and therefore in those events the autocorrelation of the time series is less affected by the post-processing as compared to events with long durations and low rainfall intensities.

Overall, comparison of the autocorrelation length,  $L_a$ , observed at different stations shows little effect of altitude. A stronger variation is observed among different events. In this case,



(a) Station comparison



(b) Event comparison

**Figure 4.8:** Autocorrelation length,  $L_a$ , estimated from the original and post-processed rainfall time series at 1 min resolution. The numbers indicate the median of the autocorrelation length at each event and station. The red line indicates the location of the median, the blue box denotes the interquartile range and the whiskers have a length of the 1.5 times the interquartile range. The red crosses indicate outliers.

post-processing has a substantial effect on  $L_a$ . Comparison with Figure 3.7 shows that in particularly low intensity events are strongly affected by the post-processing (e.g. events 9, 17, 18 and 25 show an increase in  $L_a$  of several hours), which results in  $L_a$  exceeding the ones

of intense rainfall events, for which the increase is generally less than 10 min (e.g. event 1, 4, 13-15, 23). The different effect of the post-processing is strongly related to differences in the rainfall regime, which will be shown later (Section 4.3.1). Events with a strong increase in  $L_a$  tend to be of stratiform nature, whereas the other events exhibit more convective activity. The fact that, in contrast to the original data set, the post-processed data show an autocorrelation length which reflects the rainfall regime (i.e. low  $L_a$  for convective events and high  $L_a$  for stratiform ones) shows that the applied corrections are successful in reconstructing the temporal correlation structure of the rainfall time series. This result highlights the importance of applying an appropriate correction to the measured rainfall data when analysing the temporal rainfall patterns.

### 4.1.3 Oscillation coefficients

Oscillation coefficients were computed as a robust nonparametric measure for analysing the correlation structure in rainfall time series as described in Carsteanu and Foufoula-Georgiou (1996), who used this measure to study the temporal dependence among weights in a multiplicative cascade model. This method was chosen to further investigate the event time series of rainfall data with a particular focus on how the device characteristics, such as temporal and volumetric resolution, affect the results.

Oscillation coefficients indicate the fraction of time steps which contain fluctuations in the intensity. They are computed by counting the sign of the fluctuations in rainfall intensity within three time steps,  $t$ . Between two time steps the intensity either increases, decreases or remains the same.  $C_{\uparrow}$  denotes the probability that the intensity at time step  $t$  is smaller than at  $t+1$  and vice versa for  $C_{\downarrow}$  (Table 4.1). There are four possible oscillation coefficients for triplets of rainfall intensity. Either the changes twice in the same direction ( $C_{\uparrow\uparrow}$  and  $C_{\downarrow\downarrow}$ ) or there is first an increase and then a decrease or vice versa ( $C_{\uparrow\downarrow}$  and  $C_{\downarrow\uparrow}$ ). The sum of the latter is abbreviated as  $C_{\uparrow\downarrow}$  and will be referred to hereafter as oscillation coefficient. The fraction of time steps with this fluctuation pattern was computed with respect to the rainfall duration,  $D_P$ , at each station in order to remove the effect of differences in  $D_P$  among the stations on  $C_{\uparrow\downarrow}$ . Therefore,  $C_{\uparrow\downarrow}$  reflects only differences in the fluctuation in the rainfall intensity and is not affected by differences in the rainfall duration among the stations.

Since oscillation coefficients are not affected by the absolute value of the intensity but only by its fluctuations, they are a robust measure of the temporal rainfall pattern. The oscillation coefficients were computed for the selected events for different aggregation intervals from 1 min to 4 h.

**Table 4.1:** Symbols and definition of oscillation coefficients

symbol	definition
$C_{\uparrow}$	$= Pr[I_t < I_{t+1}]$
$C_{\downarrow}$	$= Pr[I_t > I_{t+1}]$
$C_{\downarrow\uparrow}$	$\equiv C_{\downarrow\uparrow} + C_{\uparrow\downarrow}$
$C_{\uparrow\downarrow}$	Fraction of 1 min timestep triplets with increasing and decreasing I
$C_{\downarrow\uparrow}$	Fraction of 1 min timestep triplets with decreasing and increasing I
$C_{\downarrow\downarrow}$	Fraction of 1 min timestep triplets with decreasing and decreasing I
$C_{\uparrow\uparrow}$	Fraction of 1 min timestep triplets with increasing and increasing I

**Results for different post-processing steps** Figure 4.9 shows the oscillation coefficient,  $C_{\downarrow}$ , estimated from the rainfall time series measured at the different weather stations at different aggregation intervals for all events combined. This coefficient was computed for the time series at four different stages of post-processing, namely the original data series of P1, the interpolated time series of P1 as well as the data obtained from dynamical calibration and wind correction of the averaged data of P1 and P2. In all four cases there is a steep decrease in  $C_{\downarrow}$  as the aggregation interval is increased. However, in terms of absolute values  $C_{\downarrow}$  shows strong differences among the different stages of post-processing.

The different stations along the transects show a slightly different behaviour. A clearly distinct behaviour was observed for the reference station data, which show a considerably higher oscillation coefficient at all aggregation intervals. This indicates that oscillation coefficients are strongly affected by the measurement technique and comparison of time series obtained by different types of devices is not possible. Since both the reference station at the top, TR, and the one in the valley, ZE, show similar values, altitude does not seem to influence the oscillation coefficient.

The oscillation coefficients are strongly affected by the post-processing. The original tipping bucket data have a high  $C_{\downarrow}$  for short aggregation intervals,  $\Delta t$ , in the order of about 50 %, which indicates that almost all triplets belong to this category. Interpolation of the tipping bucket volume by averaging over the time interval since the last tip decreases the fraction of  $C_{\downarrow}$  at short  $\Delta t$  and leads to an increase at longer  $\Delta t$  resulting in coefficients ranging from 1-7 % for short  $\Delta t$  to 0.1-1 % for long  $\Delta t$ .

The rainfall data obtained after dynamic calibration and averaging of both pluviometers (P1 and P2) show an increase in  $C_{\downarrow}$  as compared to the interpolated data. Since the dynamic calibration is not affecting the sign of the fluctuations, the increase in  $C_{\downarrow}$  is solely due to the averaging between P1 and P2, which are measuring slightly different rainfall amounts. Comparison with the two reference stations shows that the oscillation coefficients estimated by simple averaging of TBR data results in a strong underestimation of the fluctuations.

Wind correction strongly increases  $C_{\downarrow}$ . Since the wind speed is highly variable, this correction introduces small variations in the rainfall intensity, which leads to an increase in the frequency

of  $C_{\downarrow}$  at  $\Delta t = 1$  min from 10 to 30 %. To a lesser extent also the  $C_{\downarrow}$  at longer  $\Delta t$  are increased by the wind correction (Figure 4.9). Since this increase in  $C_{\downarrow}$  is purely artificial, the following analysis of the effect of altitude on  $C_{\downarrow}$  was performed based on the rainfall time series corrected only up to the dynamic calibration, i.e. without applying wind correction.

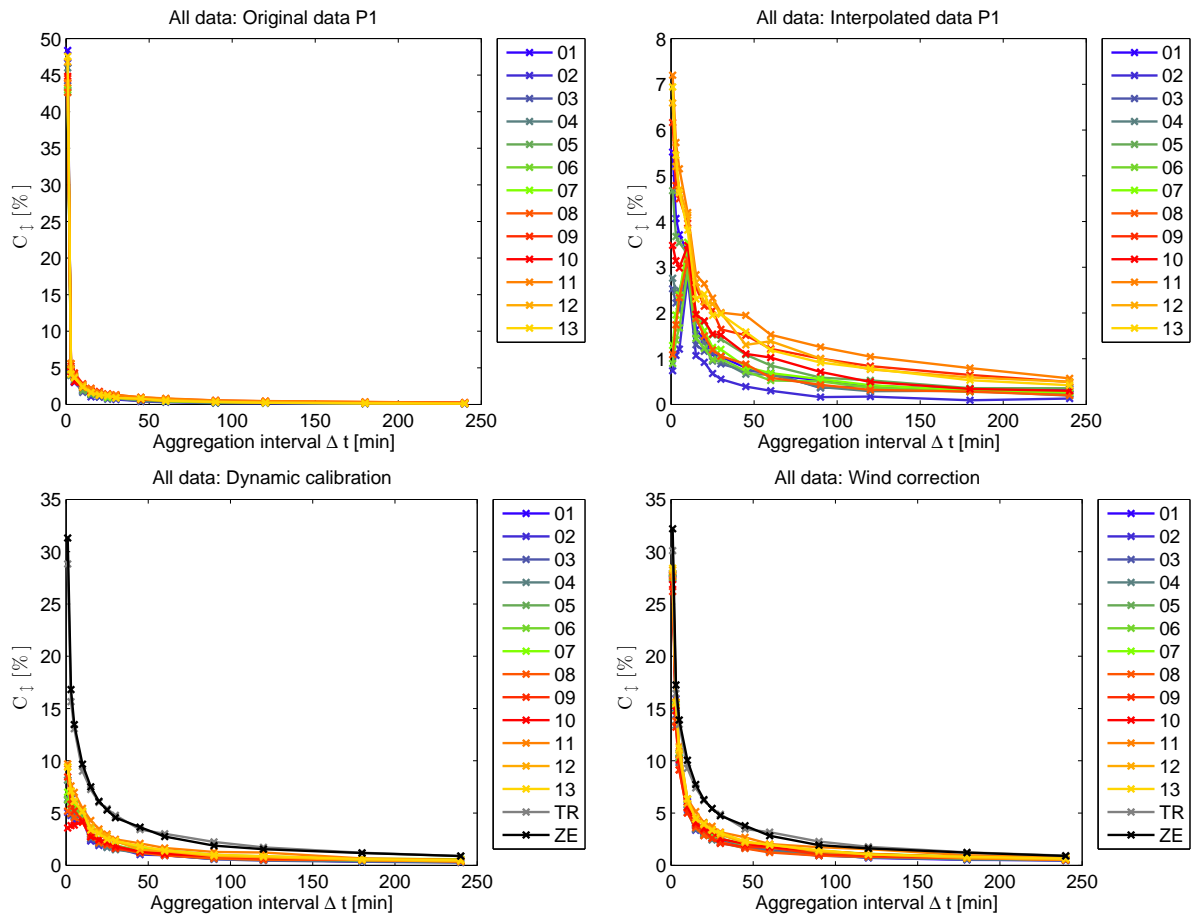


**Figure 4.9:** Oscillation coefficient depending on aggregation interval for different stages of data post-processing for the rainfall time series of all events combined. The coefficient  $C_{\downarrow}$  in the post-processed tipping bucket gauges is influenced by very small fluctuations due to the wind correction.



**Oscillation coefficients of selected events** For selected events of long event and rainfall durations the oscillation coefficients were computed individually. In order to assure a sufficient length of the time series, the oscillation coefficients were computed for events that had a mean event duration,  $D$ , of at least 8 h and a mean wet duration  $D_p$  of at least 25 % of the event duration. These criteria are fulfilled by events 7, 9, 10, 16, 17, 25 and 26. The different events were compared for three selected aggregation intervals,  $\Delta t$ . At low  $\Delta t$  there are strong fluctuations in  $C_{\downarrow}$  and at longer  $\Delta t$  there is uncertainty due to the low number of data points in the aggregated time series. Therefore, the coefficient was analysed for 0.5, 1 and 1.5 h. For those intervals the elevation dependence of  $C_{\downarrow}$  was analysed for the selected events (Figure 4.10).

$C_{\downarrow}$  tends to increase slightly with elevation in most cases. However, the slope changes with increasing aggregation interval and it can even change the sign, as can be observed for events 10, 16 and 17 at the 60 min aggregation. Events 7 and 9 show the strongest gradients in  $C_{\downarrow}$  with elevation at all three aggregation intervals. The increase in  $\Delta t$  from 30 to 60 min tends to decrease the gradient of  $C_{\downarrow}$ , but a further increase to 90 min can also cause a slight increase again.

The gradients were not significant in most cases, i.e. an  $R^2 < 0.5$  was obtained in the regression analysis (Figure 4.11). Event 7 has a significant gradient at the two lower aggregation intervals and events 9, 10 and 27 at either the 90 min or the 60 min intervals.

In conclusion, there seems to be a small effect of elevation on the  $C_{\downarrow}$  indicating a more fluctuating rainfall pattern at high altitudes for the observed events. The increase, however, is strongly dependent on the data post-processing, the type of event and the aggregation interval.

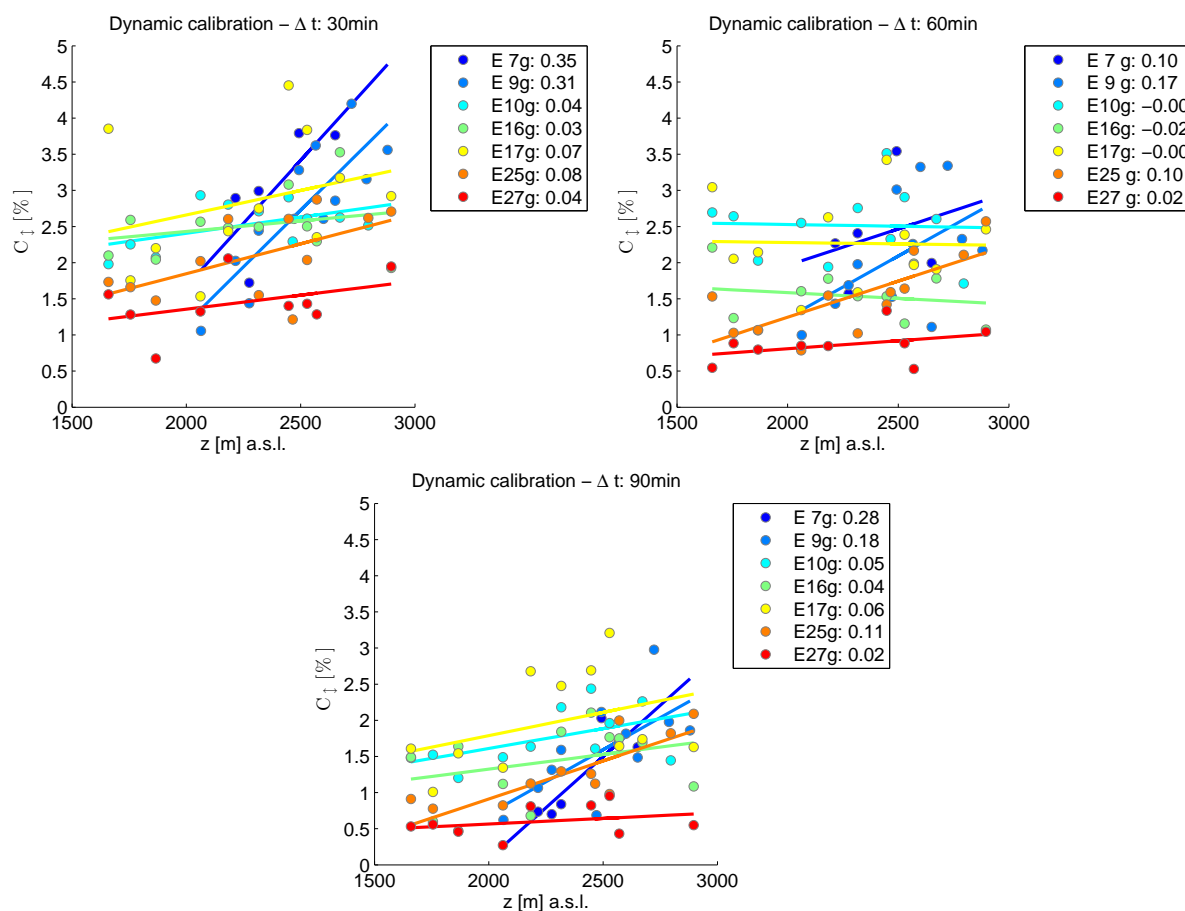


**Figure 4.10:** Oscillation coefficients,  $C_{\uparrow}$ , for post-processed rainfall time series without wind correction for events 7, 9, 10, 16, 17, 25 and 27 at aggregation intervals of 30, 60 and 90 min. The numbers in the legend denote the estimated gradient in terms of  $C_{\uparrow}$  for the corresponding event.

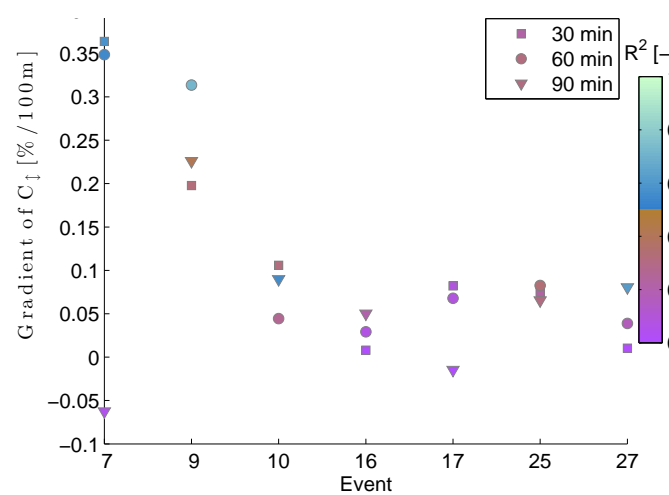


**Figure 4.11:** Gradient of  $C_{\uparrow}$  for post-processed rainfall time series without wind correction. The colorbar indicates the  $R^2$  of the linear regression of  $C_{\uparrow}$  and elevation.

## 4.2 Gradient analysis of cumulative rainfall and altitude

This section investigates the effect of altitude on the observed event rainfall by means of gradient analysis, and several controlling factors, such as rainfall intensity and duration as well as spatial and temporal scale effects are analysed for their potential to explain the differences observed in the estimated gradients.

The effect of elevation on rainfall was investigated by analysing the gradients in terms of cumulative rainfall on the time scale of single rainfall events during the IOPs in summer and early autumn of 2010 and 2011. Since the upper and lower part of the transect showed considerable differences in the gradients, the analysis was also performed for the upper and the lower part of the transect separately. Since the gradients in cumulative event rainfall are caused by differences in rainfall intensity and/or rainfall duration among the stations along the transects, also the gradients in terms of rainfall intensity and duration were analysed. The aim is to identify their relative importance in the formation of the gradient in cumulative event rainfall. In order to assess how much the gradient is affected by the post-processing of the rainfall data, the gradients were also estimated from the original data and the uncertainty due to the corrections was analysed.

Additionally, the gradients were investigated at time intervals shorter than the event time scale. For very short intervals the gradient strongly depends on the storm speed and direction. For example, a slowly moving storm of constant rainfall intensity will lead to a gradient at the beginning of the storm, when not all raingauges are collecting rainfall. However, when the rainfall is aggregated over the entire storm duration there will be no gradient. Therefore, the variability in the gradients is expected to be highest at small time intervals.

The last part of this section addresses the effect of the spatial scale of the underlying topography on the gradient estimation. Since small scale features are not expected to have a strong contribution to the gradient formation, application of a low-pass filter to the terrain data is expected to highlight the scale at which topography shows the highest influence on the distribution of cumulative rainfall amounts.

### 4.2.1 Event gradients

The gradient of cumulative event rainfall with altitude was estimated by linear regression. Due to the small number of stations a simple linear regression was performed using only the elevation,  $z$ , as independent variable.

$$P = gz + h \quad (4.4)$$

where  $z$  denotes the station elevation and  $P$  the cumulative event rainfall. The estimated parameters of the linear regression are the intercept,  $h$ , and the slope,  $g$ , which will be referred

to hereafter as gradient. The gradient of rainfall with elevation was calculated for the entire transect ( $g$ ) as well as for the upper ( $g_2$ ) and the lower part ( $g_1$ ), provided that at least 3 stations were recording rainfall during a given event on a particular transect. The gradient with elevation on the entire transect,  $g$ , was computed using data of all stations. Since some of the stations were set up at slightly different locations in the two IOPs (Section 3.1), the gradients obtained for events that occurred in different seasons are not directly comparable. In 2010 the upper transect consisted of 6 mobile stations and one reference station (8-13 and TR) and the lower one consisted of 7 mobile stations plus one reference station (1-7 and ZE). In 2011 the upper transect consisted of 4 mobile stations and one reference station (10-13 and TR) and the lower one consisted of 9 mobile stations plus one reference station (1-9 and ZE).

#### 4.2.1 - i Results

The gradients of cumulative event rainfall are summarized in Figure 4.12. Gradients with  $R^2$  values lower than 0.5 were discarded from further analysis. This leads to the exclusion of 14 events for the upper transect, 4 events for the lower transect and 12 events on the entire transect (Table A.9). Out of all the events with an  $R^2$  value above 0.5 the largest gradient was observed on the lower transect (4.45 mm/100m) and the lowest one on the upper transect (-2.98 mm/100m). The average gradient was positive on T0 (1.24 mm/100m) and T1 (1.67 mm/100m) whereas the mean gradient of T2 is negative (-1.15 mm/100m).

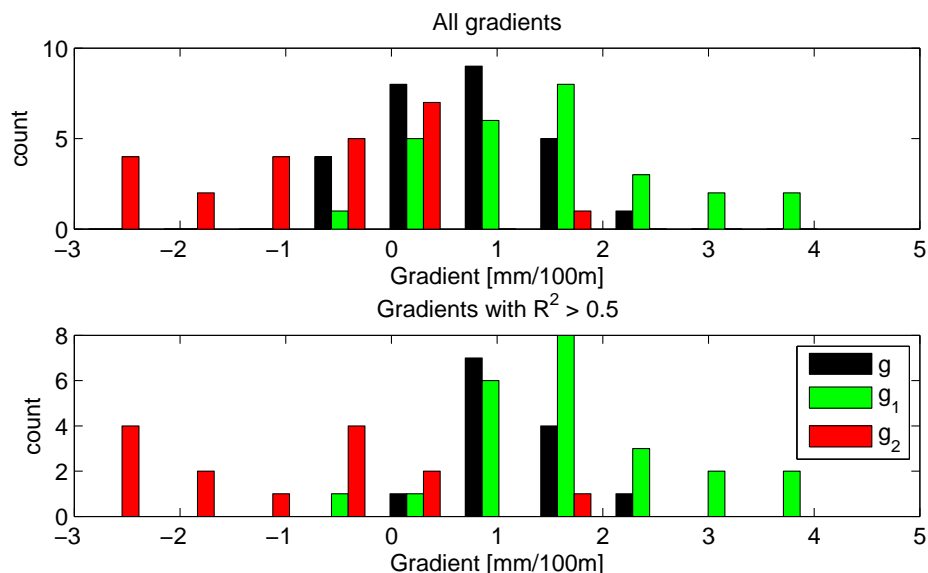


**Figure 4.12:** Gradients in cumulative rainfall and altitude observed on T0 ( $g$ ) on T1 ( $g_1$ ) and T2 ( $g_2$ ) on the event time scale during IOP 2010 and 2011. In the lower part only the gradients with an  $R^2$  larger than 0.5 are shown.

**Uncertainty** The uncertainty in the estimated gradients is due to the uncertainty in the data and due to the fitting of the regression line. The combined uncertainty was quantified by simulating different gradients by taking into account the uncertainty bounds due to the measurement errors at each station. From these simulated gradients the standard deviation was estimated.

By randomly sampling the cumulative rainfall,  $P$ , at each station from a uniform distribution within the uncertainty bounds due to the measurement errors (Section 3.3.1), 1000 simulations were performed. From the resulting gradients a mean gradient and its standard deviation were computed. The largest standard deviation is observed for the upper part of the transect (Figure 4.13). This is due to the smaller number of stations and the strong increase in the standard deviation along the upper transect due to the post-processing results from the high wind speeds and rainfall intensities, which introduce high uncertainty in the corrected data. However, even though the standard deviation is quite large, the gradients on the two transects show clearly a distinct pattern, which exceeds the uncertainty due to the measurement error and due to the fitting method.

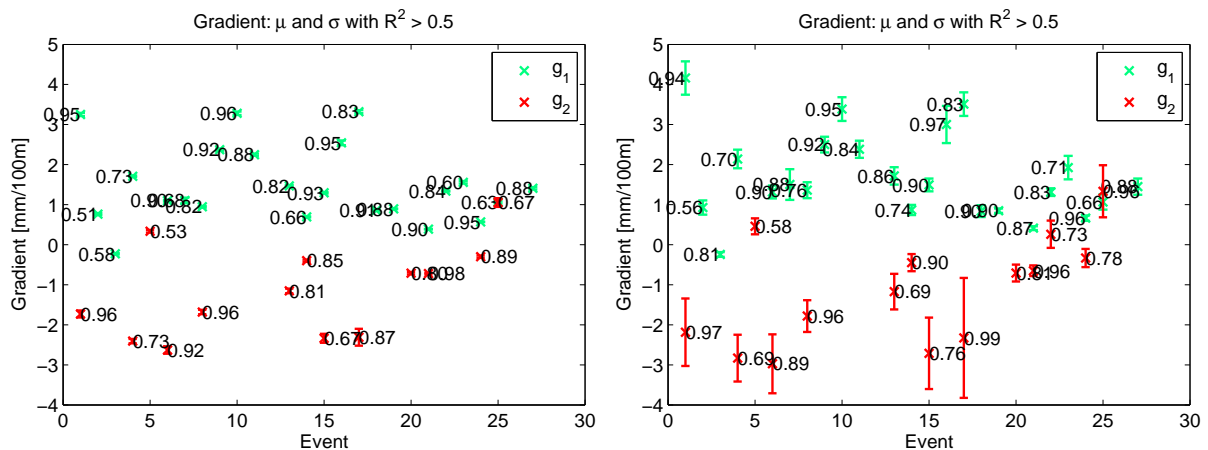


**Figure 4.13:** Standard deviation of the estimated gradients based on original and post-processed cumulative event rainfall.

**Effect of post-processing** Since the rainfall data were corrected for different measurement errors (Section 3.3.1), the gradient estimated from the post-processed data is to a certain extent affected by the post-processing applied to the data. Since generally wind speed increases with elevation and high intensities are recorded more often at high elevations, corrections are expected to be higher at high altitude, thereby causing an increase in the gradients. Therefore, the difference between the gradients of the post-processed and the original data ( $g_p - g_o$ ) relative to the original gradient was estimated and compared to the uncertainty due to the post-processing, i.e. the standard deviation in  $g_p$  (Figure 4.14). Comparison of gradients estimated from post-processed ( $g_p$ ) and original ( $g_o$ ) data shows an increase in the absolute value of the gradients in the order of up to 40%, e.g. event 5 on T2 and event 8 on T1. The post-processing increases positive gradients and it weakens the negative gradients, which confirms the expectation that the post-processing is to a certain extent elevation dependent, because wind and rainfall intensity tend to increase with altitude. However, in most cases the relative increase in the gradient due to the post-processing is smaller than the uncertainty in the gradient based on the post-processed data ( $g_p$ ). Exceptions are some events on T1, for example events 1 and 4.

Gradients on T1 and T2 are affected more strongly by the post-processing as can be seen by the larger relative differences between  $g_p$  and  $g_o$  as compared to gradients on T0. For the latter only an increase up to 20% is observed. Because of the smaller amount of data points on T1 and T2 and the fact that stronger gradients are observed on T1 and T2, the post-processing has a stronger effect on those gradients in comparison to the gradient of the entire hillslope. For the latter a large correction of the rainfall amount at single stations is more likely to be compensated by corrections at other station, whereas on T1 and T2 a single data point has more weight in the regression and therefore has a stronger influence on the resulting gradient.

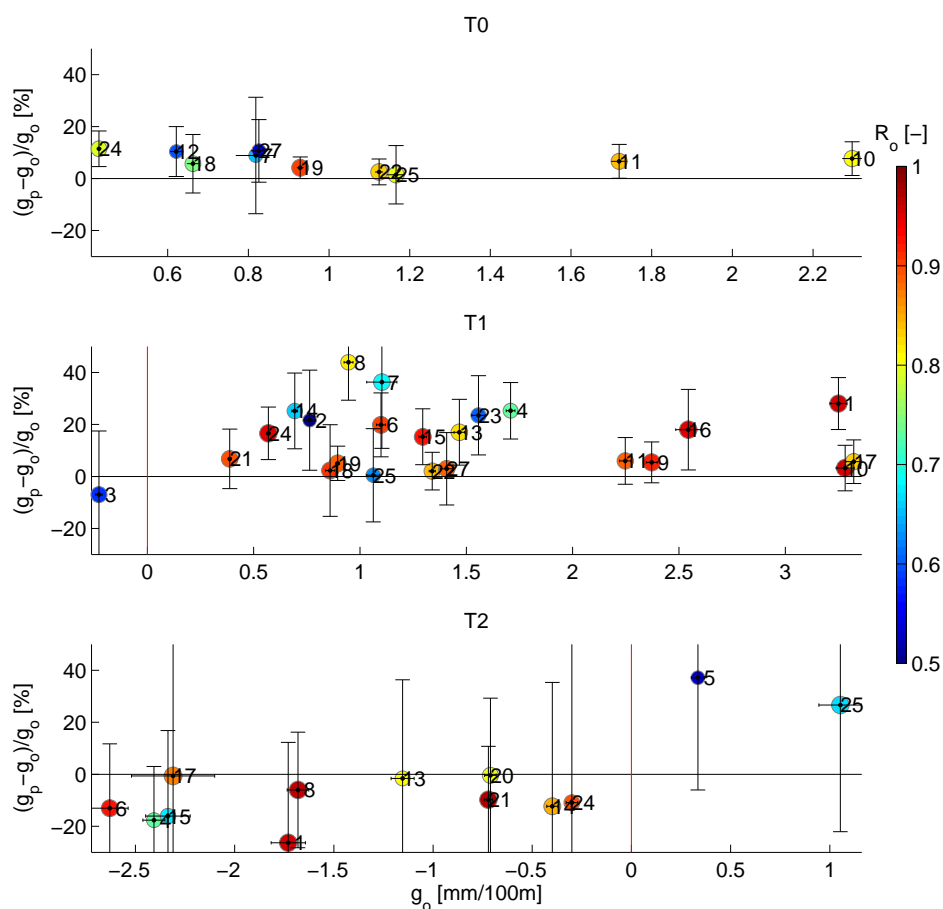


**Figure 4.14:** Relative difference between  $g_p$  and  $g_o$  vs. gradients based on original data ( $g_o$ ). Only gradients with  $R^2 > 0.5$  are shown. The horizontal errorbars indicated the absolute standard deviation of  $g_o$  and the vertical errorbars indicate the relative standard deviation of  $g_p$

**Comparison of events** The gradients on the lower transect tend to be positive, whereas the gradients in the upper part are rather small and sometimes even negative (Figures 4.15 (post-processed data) and A.6 (original data)). Often the two hillslopes show opposite gradients within the same event. Even though these events do not show a significant trend on the entire transect, the observed pattern can be explained by the station elevation when the upper and lower hillslope are considered separately. The gradients of the entire transect are mostly positive but slightly smaller than the ones observed for the lower transect due to the tendency for decreasing rainfall in the upper part (Figures 4.16 (post-processed data) and A.7 (original data)).

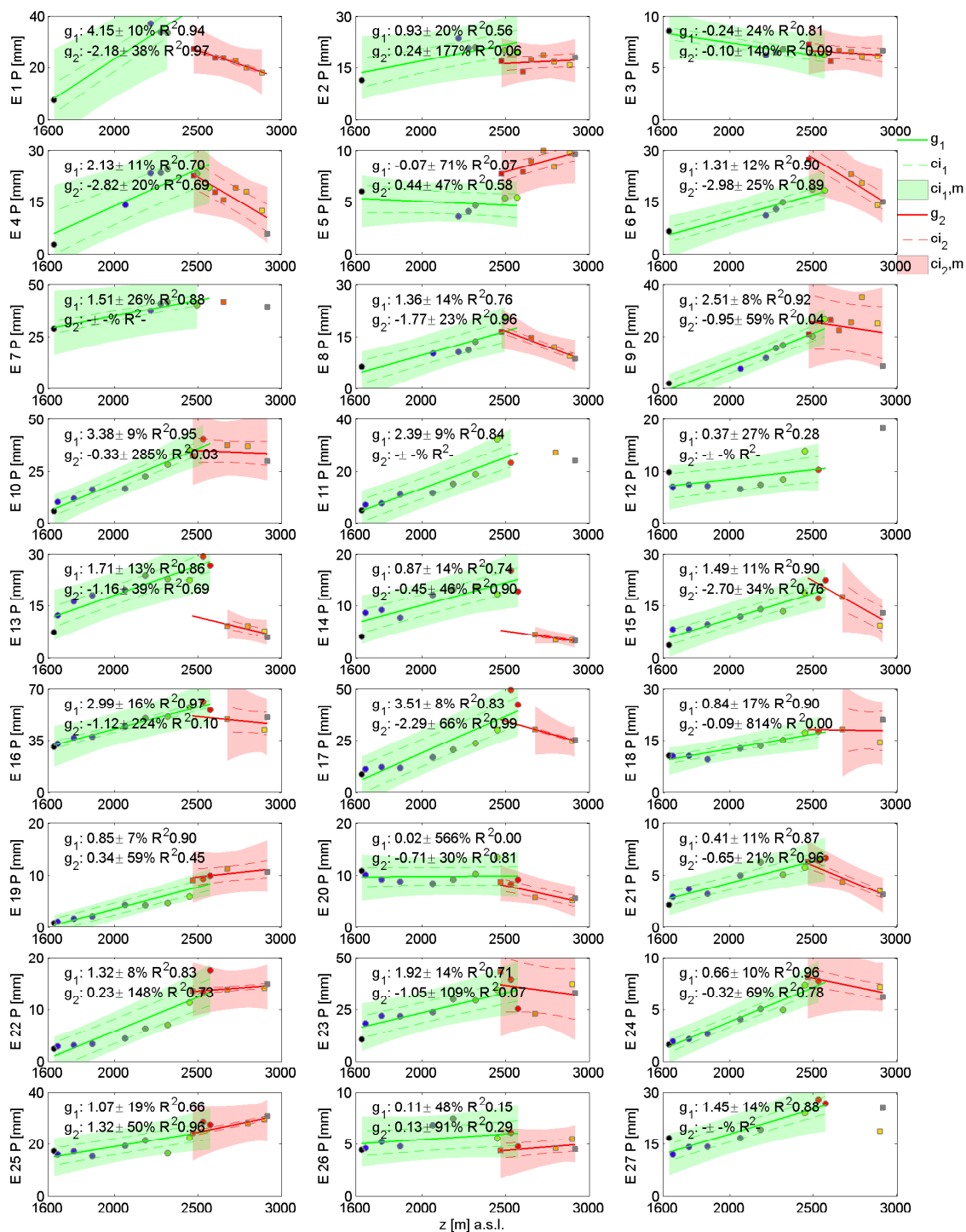
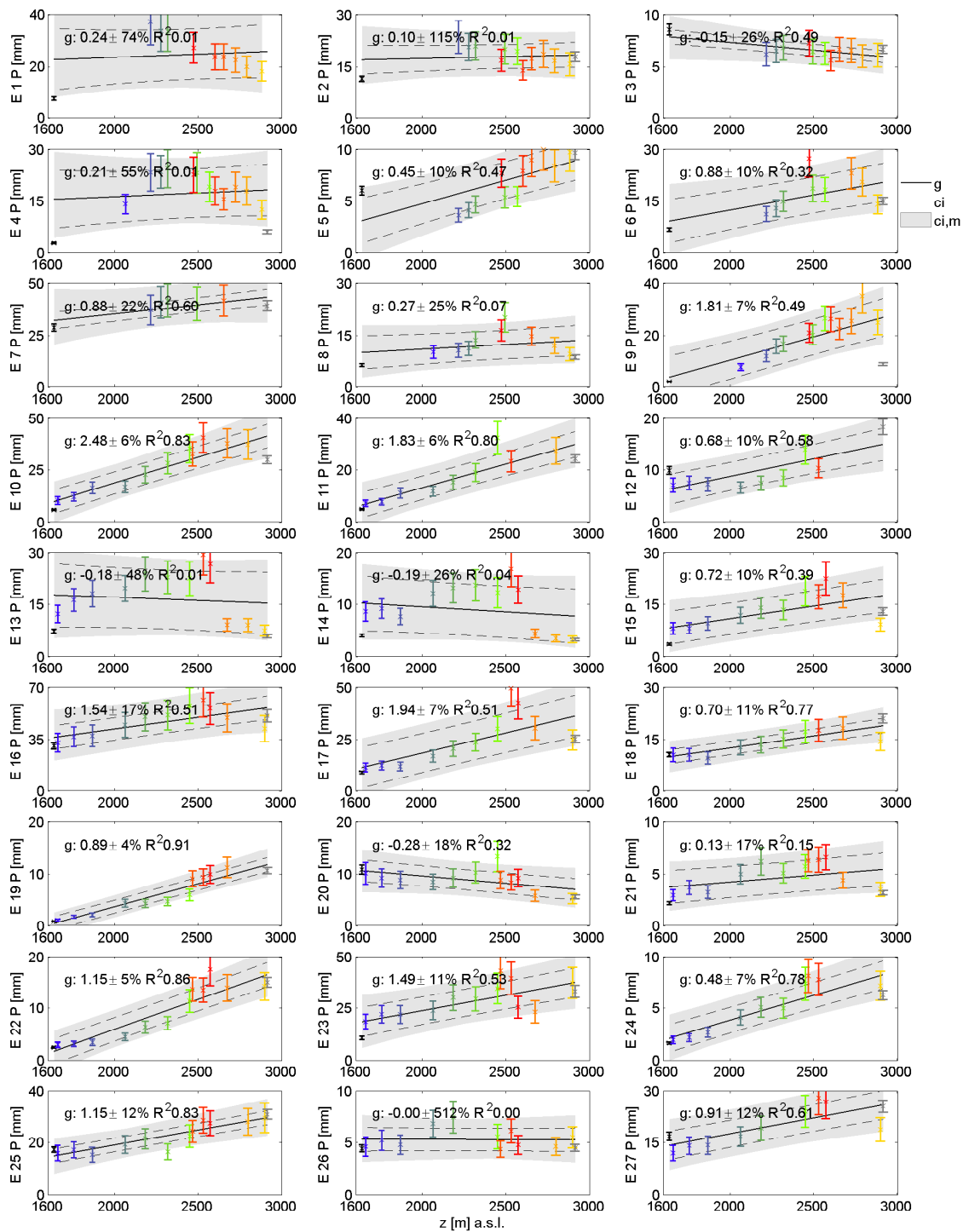


Figure 4.15: Gradients  $g_1$  and  $g_2$  on T1 and T2 respectively based on post-processed data. The confidence interval of the regression is indicated by  $ci_1$  and  $ci_2$  for T1 and T2 respectively. The confidence interval based on the combined uncertainty in the data and the fitting method is indicated by  $ci_{1,m}$  and  $ci_{2,m}$  for T1 and T2 respectively.





**Figure 4.16:** Gradients,  $g$ , on  $T0$  based on **post-processed** data. The confidence interval of the regression is indicated by  $ci$ . The confidence interval based on the combined uncertainty in the data and the fitting method is indicated by  $ci_m$ .

**Gradients depending on rainfall duration and intensity** Gradients are formed by a combination of differences in intensity and duration between stations at low elevations as compared to high altitude stations. It is expected that the relative importance of these two factors vary among the different events and can be used to distinguish differences in the rainfall regime. The dependence of the rainfall intensity and duration on the station elevation was analysed by linear regression analogous to the gradient estimation for cumulative rainfall. The mean intensity was estimated for the wet duration at each station, i.e. by excluding values of zero rainfall based on the post-processed data. Figure 4.17 shows how the gradients in terms of cumulative rainfall,  $P$ , relates to the gradient in terms of rainfall intensity,  $I$ , and duration respectively. Events with a gradient in  $P$  with  $R^2 < 0.5$  were excluded. The results show that for most events positive gradients in  $P$  are associated with positive gradients in rainfall duration and intensity, and the opposite is observed for negative gradients in  $P$ . However, some points are located in the upper left or lower right quadrant of Figure 4.17, which indicates that in some cases the gradients in intensity and duration are acting against the formation of the final gradient in  $P$ . For example, event 13 has a positive gradient in rainfall duration but the final gradient in  $P$  is negative, and events 2 and 7 have a slightly positive gradient even though the corresponding gradient in rainfall intensity is negative.

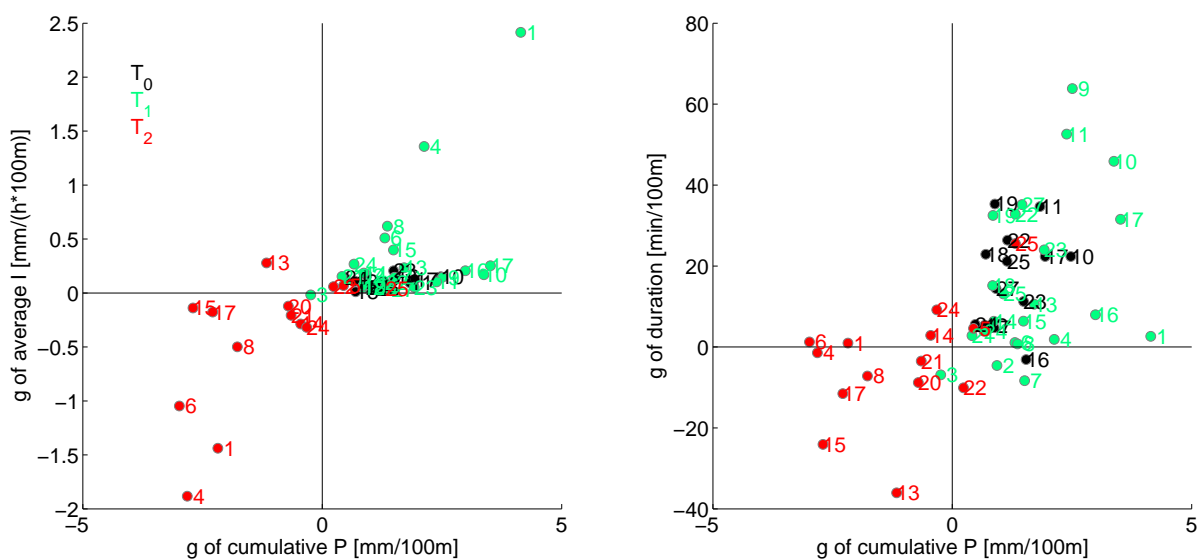


**Figure 4.17:** Gradient of intensity and gradient of duration vs. gradient in terms of cumulative precipitation for the post-processed data. The numbers indicate the events with an  $R^2 > 0.5$  for the gradient in cumulative precipitation.

The relative importance of the gradients in terms of rainfall intensity and duration for the different events is illustrated in Figure 4.18. On the entire transect gradients are mainly due to differences in the duration whereas on the upper and the lower transect gradients are more often due to differences in the rainfall intensities. In particular events with very strong gradients

(i.e. event number 1 and 4) are mainly due to the gradient in terms of intensity. The figure also shows that events with strong intensity gradients tend to have low gradients in duration and vice versa, i.e. depending on the event one or the other driving mechanism in gradient formation plays a more important role.

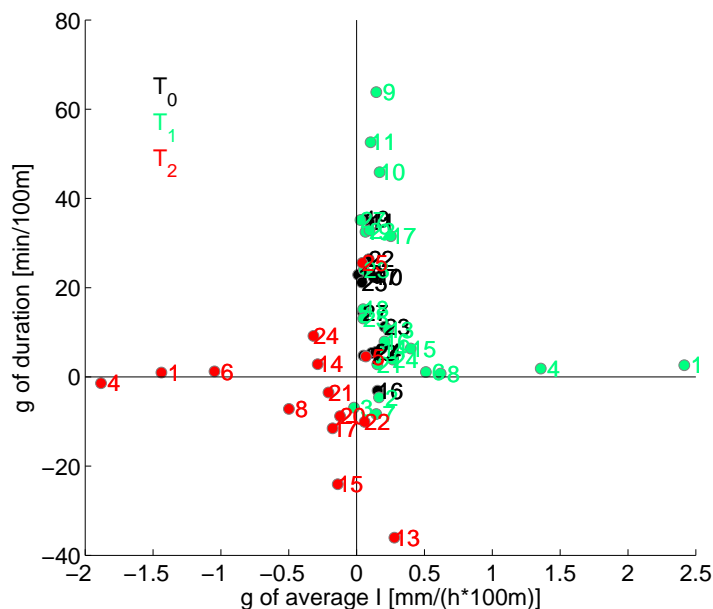


**Figure 4.18:** Gradient of intensity vs. gradient of duration for the post-processed data. The numbers indicate the events with an  $R^2 > 0.5$  for the gradient in cumulative precipitation.

**Gradients in rainfall intensity quantiles** The gradient in rainfall intensity as described above reflects only the pattern of the mean intensity. In order to investigate which intensities are mainly relevant for the gradient formation at the event time scale, also the intensity quantiles,  $q_{25}$ ,  $q_{50}$  and  $q_{75}$ , indicating the 25, 50 and 75% quantile, were analysed at each station. They were estimated for each event and each station based on the post-processed nonzero rainfall intensities.

In order to investigate the effect of elevation on the different quantiles, the gradients in terms of the different intensity quantiles was estimated as follows:

$$q_p = g_{qp}z + h \quad (4.5)$$

where  $g_{qp}$  denotes the gradient in terms of the quantile,  $q_p$ ,  $z$  denotes the station elevation and  $h$  the intercept of the linear regression.

The quantiles estimated for each station and event are shown in Figure A.8. The results show a strong variation in the quantiles among the different events, especially for the 75% quantile. It can vary from around 4 mm/h to 20 mm/h depending on the event. Only the 75% quantile

shows a slight increase with altitude in some of the events. A negative gradient in  $q_{75}$  on the entire transect was observed only for event 3 and 14. However, on the upper transect a decrease in  $q_{75}$  was observed more frequently (e.g. event 4, 6 and 21), which indicates that in those cases high intensity rainfall in particular shows an elevation dependence.

A comparison of the  $g_{qp}$  for  $p$  equal to 25, 50 and 75% on the entire transect shows however a rather weak dependence on altitude (Figure 4.19). A comparison with the gradient in terms of cumulative event precipitation,  $g$ , shows almost no correlation. The  $R^2$  value of  $g_q$  shows slightly higher values for stronger gradients,  $g$ , indicating that in those events altitude tends to have a stronger effect on the rainfall intensity than in events with weak rainfall gradients.

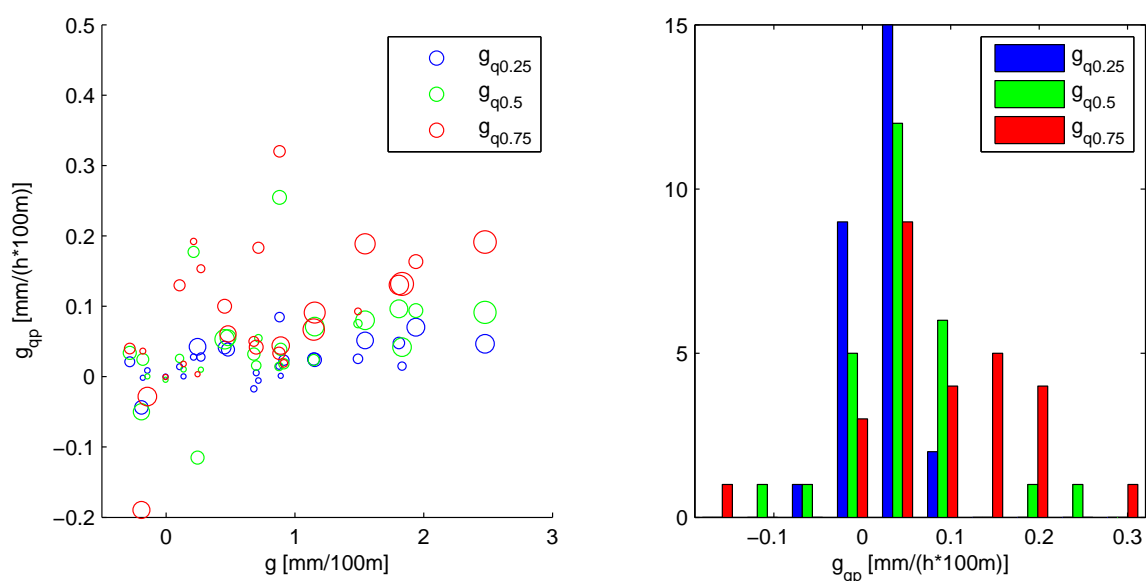


**Figure 4.19:** Comparison of gradients and gradient of quantiles. The data points are scaled according to the  $R^2$  value in terms of cumulative rainfall.

Since high intensity rainfall is expected to contribute to a large portion of the cumulative amount, the high intensities can be responsible for gradient formation even if there is no strong gradient in the quantiles. Therefore, the gradient was analysed for cumulative event rainfall amounts arising from intensities above the 75% quantile, which will be denoted as  $g(I > q_{75})$ . In most cases the gradient in cumulative rainfall due to intensities above the 75% quantile is responsible for a large part of the observed  $g$  (Figure 4.20). For a large number of events the gradients are almost equal and with a few exceptions  $g(I > q_{75})$  accounts for at least 50% of  $g$ . In some cases  $g(I > q_{75})$  is even larger than  $g$  indicating that different rainfall intensities are affected differently by altitude.

In some cases the gradient can be altered substantially also due to low intensity rainfall, as for example in event 6, where the  $g_p$  is considerably smaller (-3 mm/100m as compared to -2 mm/100m) even though almost no gradient in duration can be observed in Figure 4.17. Other examples show the importance of the gradient in duration, which can even change the

gradient from positive to negative as can be seen in event 16. However, in most cases both, the gradient in rainfall duration and the gradient of the cumulative rainfall above the 75% quantile, have the same sign, but the relative importance varies considerably among different events. In summary, the analysis of the intensity quantiles shows that the 25 and 50% quantiles show no altitude dependence and the 75% quantile shows a weak gradient in some events. However, comparison of the gradient in cumulative rainfall due to high intensities (i.e. above the 75% quantile) and the gradient in total cumulative precipitation shows that differences in high intensity rainfall makes a substantial contribution to the gradient in most cases.

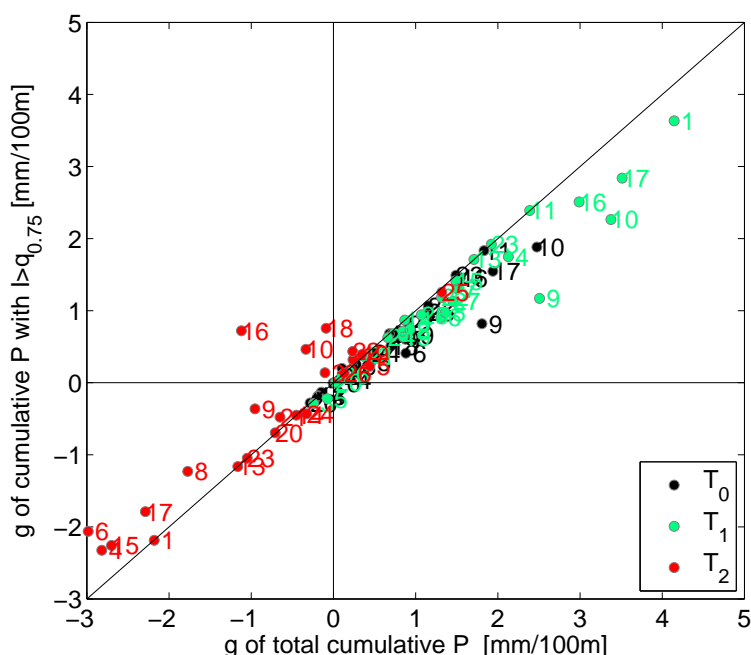


**Figure 4.20:** Gradient of  $P(I > q_{75})$  ( $g_{p75}$ ) and ( $g_p$ ) in comparison with gradient in rainfall duration for post-processed data on  $T_0$ ,  $T_1$  and  $T_2$ . The numbers indicate the events with an  $R^2 > 0.5$  for the gradient in cumulative precipitation.

#### 4.2.1 - ii Summary

The gradient analysis of cumulative event rainfall has shown a strong variability among different events and also among different transects, with positive gradients occurring more frequently on the entire transect and in the lower part whereas in the upper part frequently negative gradients were observed. The data post-processing affects the resulting gradient but the value remains within the uncertainty bounds of the gradient estimation for most events. The uncertainty in the gradients is smaller than the difference in the gradients observed for different events and transects. Therefore, it can be concluded that the differences in the estimated gradients are reflecting the differences in the rainfall processes and that the artefacts due to the post-processing are relatively small.

Analysis of the effect of altitude on of rainfall intensity and duration has shown that both positive as well as negative gradients can occur. Generally both factors are affecting rainfall gradients in the same way, however depending on the event one or the other plays a much more important role. Intensity quantiles are less affected by altitude than the average intensity, especially the 25 and 50% quantile. However, even though the 75% quantile shows only a small gradient, the intensities above this threshold have the strongest contribution to the gradient in cumulative event rainfall.

## 4.2.2 Effect of temporal scale

Because gradients are affected by the duration over which the rainfall is accumulated, comparison at the event time scale can be misleading if events with different durations are compared. Therefore, the gradients were also analysed at aggregation intervals shorter than the event duration. Those gradients are highly influenced by the storm evolution. In a hypothetical case of constant rainfall intensity, at the sub-event time scale a positive gradient can be observed if it starts raining first at the upper stations. This gradient will be compensated at the end of the storm when only the lower stations receive rainfall, which results in a negative gradient at the sub-event time scale towards the end of the storm. Analysis of rainfall gradients at short time intervals therefore illustrates how the gradient evolves and which parts of the event are mostly relevant in forming the gradient at the event time scale. The evolution of the gradient is investigated by analysing the gradients of the accumulated rainfall based on the moving average time series for different lag times.

### 4.2.2 - i Gradient depending on temporal aggregation

The gradient evolution during each event was investigated by computing the gradient at each time step for the cumulative rainfall of the original time series as well as for the moving average time series at different lag times. For each event, the gradient evolution was analysed for moving average windows between 1 and 10 h (or less if the event duration was shorter). The results show the gradient is highly variable if only short moving average windows are considered. Figure 4.21 shows two selected events which provide interesting insight into how the gradients at the event time scale are formed. Event 10 has a strong positive gradient, and all the wet spells make a positive contribution to the gradient. However, the magnitude varies between the different rainfall periods. In this particular event wet spells with intensities above 4 mm/h exhibit the strongest gradients. Event 3 has a negative gradient at the event time scale but the last wet spell of the event has a positive gradient, which considerably increases the gradient. In this case strong negative gradients are associated with rather low intensities mostly below 1 mm/h. The  $R^2$  values are rather high up to the last wet spell, which leads to an insignificant gradient on the event time scale. This example shows that the event gradient is highly affected by the criteria according to which events are separated.

The range of gradients obtained for the data at different aggregation intervals is summarized in Figure 4.22. As the aggregation interval increases, the median tends to increase whereas the variability in the gradients decreases. This is due to the fact that longer events generally exhibit positive gradients, which tend to grow with increasing durations, and the moving average accumulation causes a smoothing of the time series, which results in a decrease in the gradient variability.

The analysis of the rainfall gradients at the sub-event time scale highlights the strong influence

of the temporal scale at which the gradients are analysed. It illustrates the strong variability in the gradients at short aggregation intervals. In addition, different wet spells during one event can exhibit both qualitative and quantitative differences in the gradients, and therefore gradient analysis at the event time scale is highly sensitive to the dry duration threshold used as a criteria to separate different events.

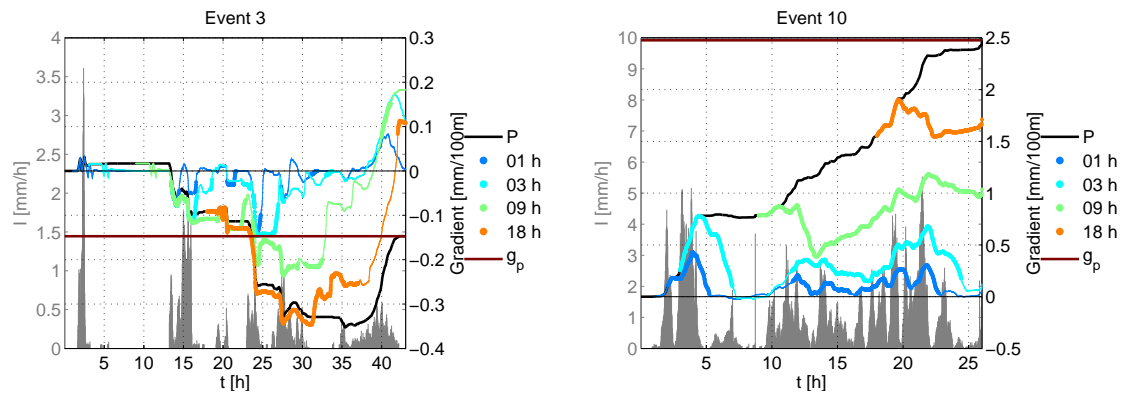


**Figure 4.21:** Gradient evolution at different moving average aggregation intervals in comparison to  $g_p$ . Large dots indicate gradients with  $R^2$  values larger than 0.5. On the Y-axis on the left the corresponding rainfall intensities are shown.



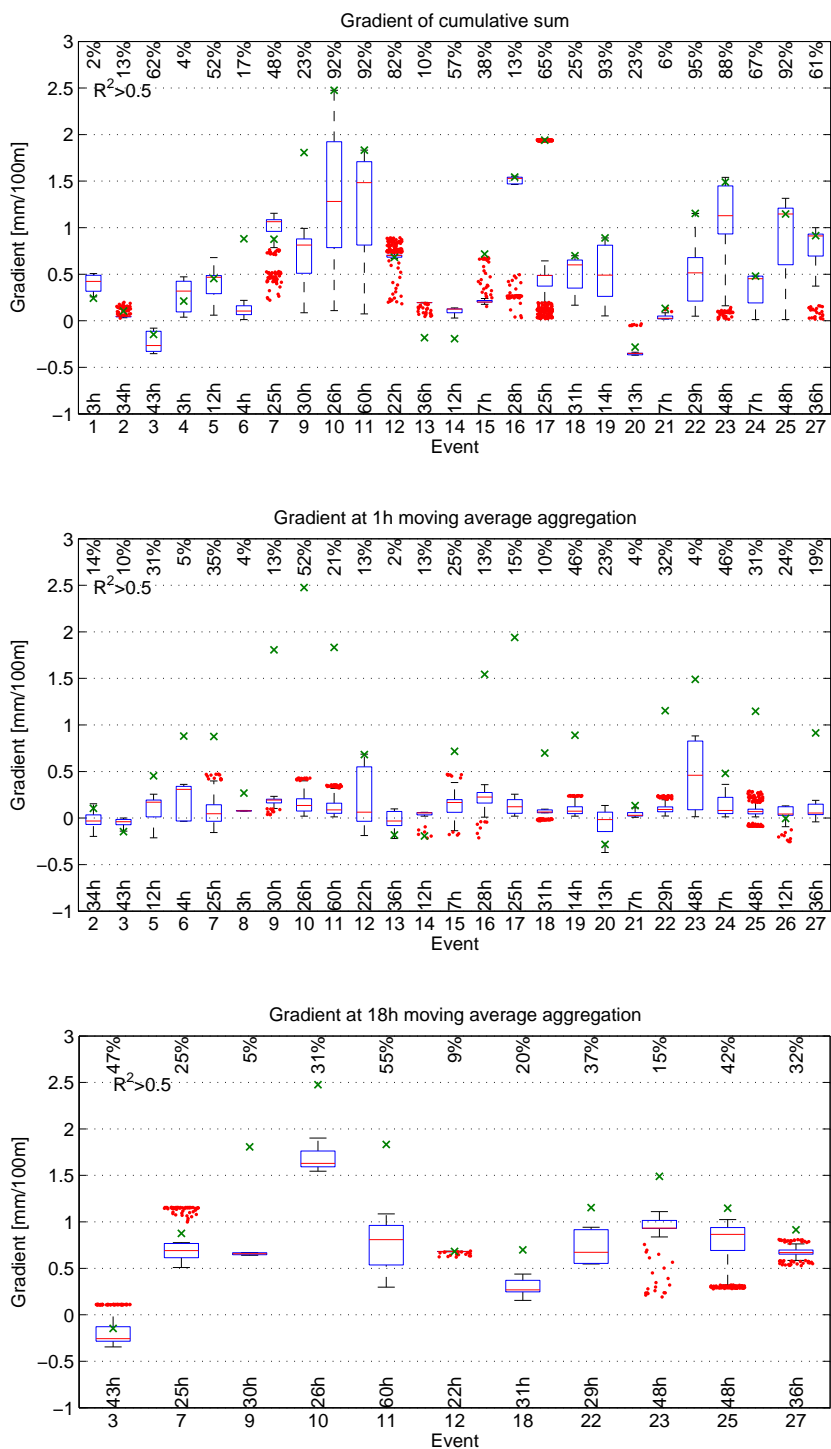


**Figure 4.22:** Gradient evolution at different moving average aggregation intervals in comparison to  $g_p$  indicated in green. The numbers at the top indicate the percentage of gradients with  $R^2 > 0.5$  and the numbers at the bottom indicate the event duration  $D$ . The red line indicates the location of the median, the box denotes the interquartile range and the whiskers have a length of the 1.5 times the interquartile range.

### 4.2.3 Effect of terrain scale on gradients

Several studies have suggested that precipitation processes are affected mainly by large scale orographic features and small structures do not have a significant effect. This hypothesis was investigated by analysing the effect of lowered terrain resolution and terrain filtering on the relationship between precipitation on altitude (Boni et al., 2008; Sharples et al., 2005; Hutchinson, 1998; Daly et al., 1994). These studies found a stronger dependence when small scale terrain features were excluded, however, depending on the scale of the rainfall process under investigation, a different degree of terrain smoothing provided best results.

These findings indicate that the rainfall pattern observed in this study is not primarily affected by the elevation of the weather station but rather by the large scale terrain, and therefore a higher correlation can be expected when rainfall gradients are estimated based on a smoothed topography. To test this hypothesis and to investigate the scale at which topography has the strongest influence on the spatial distribution of cumulative event rainfall, the DEM (Bundesamt für Landestopografie swisstopo) was subjected to filters of different strengths, and the effect of the filtering on the resulting gradients was analysed. In particular, the effect of the DEM smoothing on the  $R^2$  value of the gradient estimation was investigated.

Previous studies have analysed the effect of the topographic scale by testing DEMs at different resolutions (Sharples et al., 2005) or by filtering the terrain model (Boni et al., 2008). In this work the latter approach was chosen since the stations are located rather close to each other and for low grid resolutions different stations would be assigned identical elevations. When the terrain is smoothed by filtering, the grid resolution remains constant thereby preserving different terrain elevations also for stations that in close proximity. Therefore, rather than changing the DEM resolution, a DEM at 100 m grid size was filtered in the Fourier domain, thereby smoothing the terrain while keeping the same resolution.

#### 4.2.3 - i DEM filtering methods

The Fourier transformed DEM,  $F(u,v)$ , was filtered by a function,  $H(u,v)$ , designed to remove the high frequency components of the DEM.

$$G(u, v) = H(u, v)F(u, v) \quad (4.6)$$

The resulting in Fourier transformed DEM,  $G(u,v)$ , was transformed back to the spatial domain by inverse Fourier transformation. In order to test to which extent the effect of the filtering is due to the choice of the filter, different types of filters were tested. In particular, an ideal low pass (ilp) filter and a symmetrical and a directional Butterworth (bw) filter were applied. An ilp-filter cuts off frequencies above a certain threshold frequency number,  $w_0$ , and lets low

frequency components pass, which results in the following filter function:

$$H(u, v) = \begin{cases} 1 & \sqrt{w_v^2 + w_u^2} < w_0 \\ 0 & \text{otherwise} \end{cases} \quad (4.7)$$

where  $w_0$  is the threshold frequency number for the DEM filtering and  $w_u$  and  $w_v$  are the corresponding u and v components.  $w_u$  and  $w_v$  were set equal in order to obtain a symmetrical filter and values ranging from 10 to 100 were chosen. The resulting frequencies in  $m^{-1}$  can be derived from the frequency number,  $w_0$ , as follows:

$$f_w = w_0 \frac{f_s}{N} \quad (4.8)$$

where  $f_s$  indicates the sampling frequency, which equals  $0.01 m^{-1}$  for a grid resolution of 100 m, and N indicates the grid size, which equals 1000 in this case. The resulting DEMs account for 85 to 99% of the variance in the original DEM, and this fraction of explained variance will be denoted as  $f_{\sigma^2}$ .

$$f_{\sigma^2} = \sigma_{DEM}^2 / \sigma_{DEM_{100}}^2 \quad (4.9)$$

The fraction of explained variance,  $f_{\sigma^2}$ , depending on the strength of the ilp-filter is listed in Table A.11.

To test how the resulting gradients are affected by the filtering method, also a smoother filter was applied to the DEM. A smoother filtering can be obtained when instead of completely cutting off certain frequencies, the frequencies are weighed by a smooth function such as for example a bw-filter, which results in the following filter function:

$$H(u, v) = \frac{1}{1 + \left[ \frac{w_u^2 + w_v^2}{w_0^2} \right]^n} \quad (4.10)$$

where the exponent, n, defines the decay of the function. This function defines the weighing of each frequency component at frequency numbers  $w_u$  and  $w_v$ . In this study, the bw-filter exponent, n, was set to 5. The filtered DEM is obtained by multiplying the DEM in the frequency domain with H and applying an inverse Fourier transform as described above. A comparison of the ilp-filter and the bw-filter with different exponents is shown in Figure 4.23 for the one dimensional case.

Since it can be expected that terrain features parallel to the prevailing wind direction are affecting the rainfall processes to a smaller extent those perpendicular, also a directional filter was applied. In this case, the frequencies parallel to the event direction were smoothed more by modifying the filter mask H. Instead of a circular shape an ellipse of the same area was defined with a major axis twice as long as the minor one. This filter was applied to the 8 major wind directions and for each event the one closest to the prevailing wind direction was

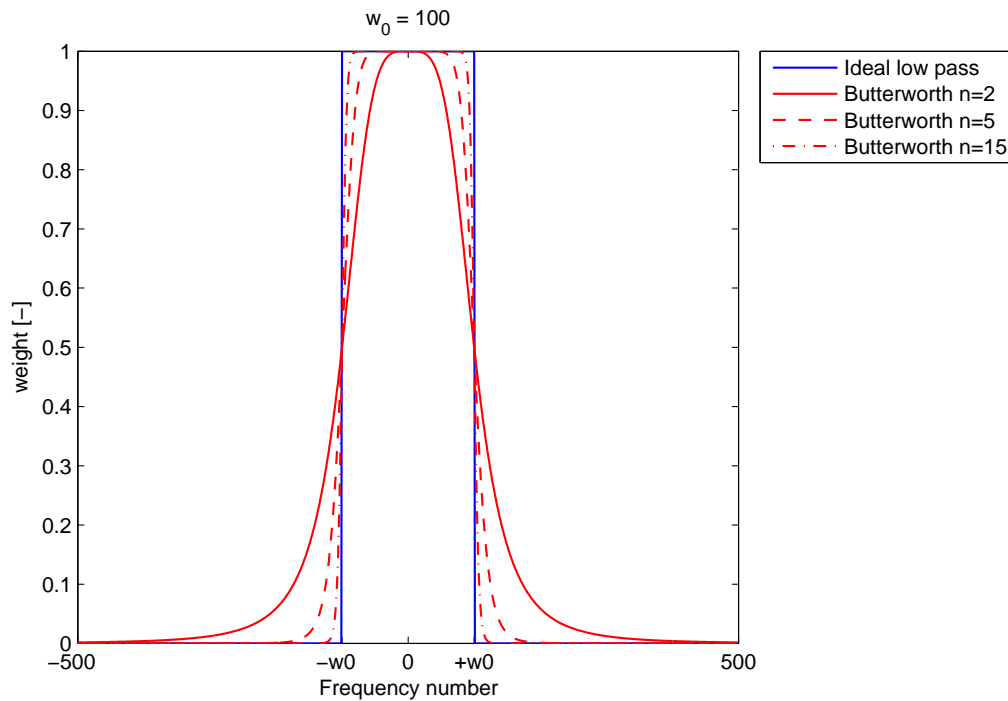
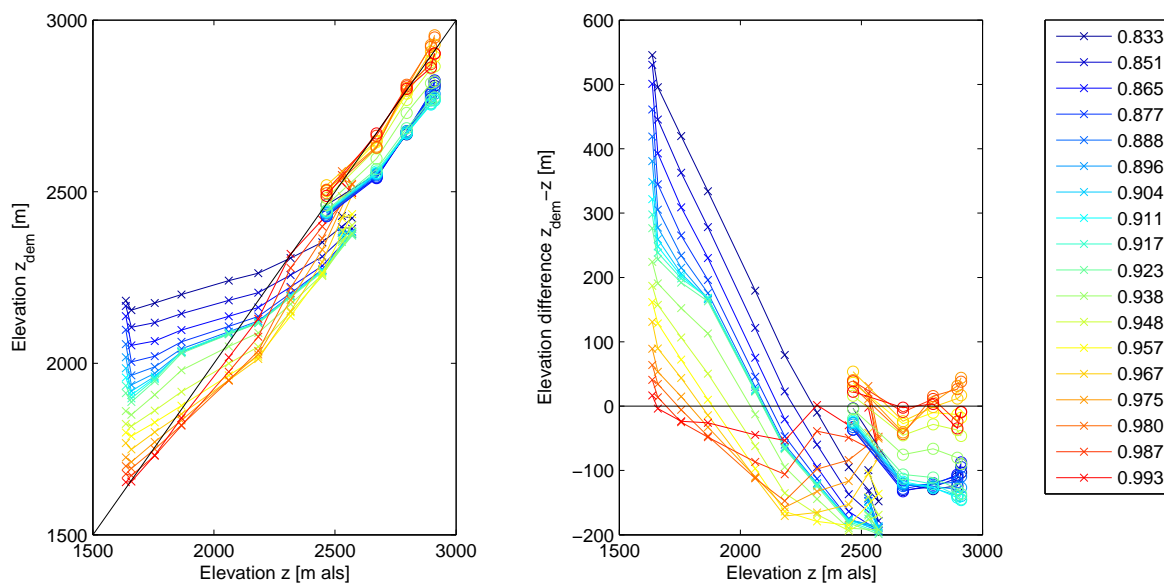


Figure 4.23: Comparison of filters applied in the digital terrain model filtering shown in 1d.

tested for its ability to improve the  $R^2$  value in the gradient estimation. This filter is referred to as bw  $\alpha$ .

$$H = \frac{1}{1 + \left[ \frac{2w_x^2 + 0.5w_y^2}{w_0^2} \right]^n} \quad (4.11)$$

**Elevation difference between filtered and original DEM** Figure 4.24 shows the filtered DEM elevations at the station locations in comparison to the station elevation obtained from a DEM at 25 m in the case of the symmetrical bw-filter. In the filtered DEMs the stations at lower elevations show positive differences and the stations at high elevations negative ones. This results in a smoothing of the terrain, however the effect varies among the stations. There is a shift towards higher  $\Delta z$  values for T1 as compared to T2. Furthermore, the shift does not only depend on the elevation of the stations but also on the horizontal location as can be seen from comparison of station ZE and the first mobile station, which have an elevation of 1630 and 1660 m respectively but have very different  $\Delta z$  values. Overall, the elevation range, which is covered by the stations, strongly decreases when a filter is applied. Since the filtering has a different effect on the upper and the lower transect, the gradients are expected to be strongly altered when the station elevations are extracted from filtered DEMs.



**Figure 4.24:** Elevation obtained from a filtered DEM with a symmetrical Butterworth filter ( $n=5$ ) with the elevation obtained from a DEM of 25 m resolution for the station setup in 2011

#### 4.2.3 - ii Results

To test the effect of different filtering methods, the gradients and their  $R^2$  value were analysed for the filtered DEMs. As an example the effect on  $R^2$  depending on the explained fraction in the DEM variance,  $f_{\sigma^2, max}$ , is shown for different degrees of bw-filtering for the gradients on the entire transect (Figure 4.25). Additionally, the gradients estimated for the original DEM at 25 and 100 m resolution are shown, in order to assess the effect of the change in resolution as compared to the effect of the filtering.

In most of the events both the gradient as well as its  $R^2$  value are very sensitive to the degree to which the DEM is filtered. The variability in the gradients exceeds the standard deviation obtained for the gradient of the 25 m DEM in most events. A change in resolution from 25 to 100 m is affecting the gradients less than the filtering. Depending on the event,  $R^2$  shows a very different dependence on the topography used for the gradient estimation. In most cases there are local maxima and minima but their location is event specific. Different strengths of the DEM filter can result in a change in  $R^2$  of up to 0.3. Since the filtering causes a decrease in the elevation range, the magnitude of the gradients tends to increase when a stronger filter is applied.

Overall, Figure 4.25 shows that the filtering has a strong effect on the  $R^2$  of the resulting gradient. However, depending on the event the maximum was observed at different terrain scales, expressed as explained fraction of the variance in the original DEM. In most cases either the strongest filter or the unfiltered DEM resulted in a maximum  $R^2$ .

However, at this point it cannot be distinguished to which extent these findings are reflecting the interaction between topography and rainfall processes and to which extent they are affected by the selected filtering method. Therefore, in the following section the maximum  $R^2$  value and the corresponding  $f_{\sigma^2, max}$  is compared to the results obtained by applying different types of filters.

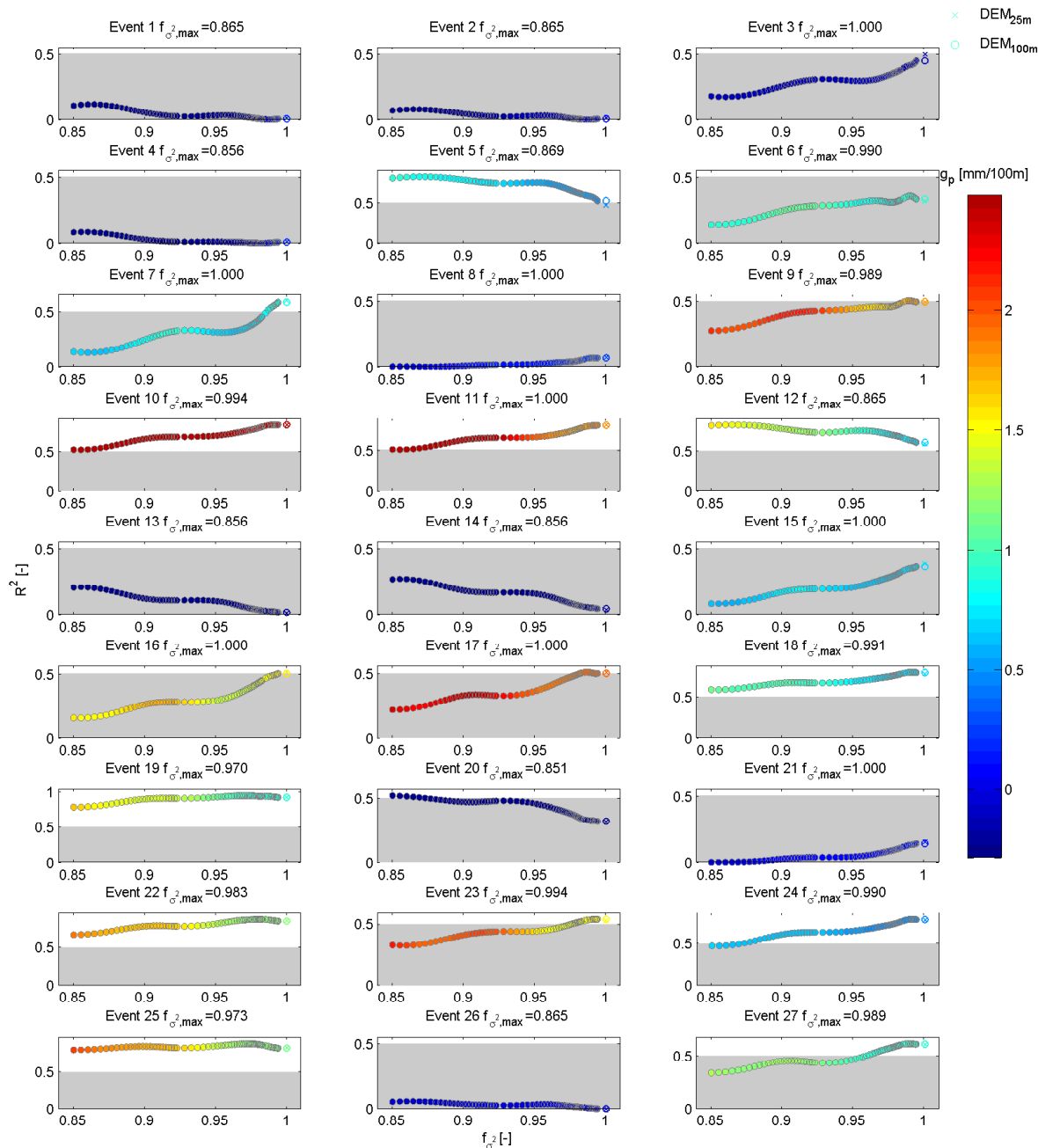


**Figure 4.25:**  $R^2$  value for gradients on the entire transect obtained from different filtered DEMs and the original DEM at 100 and 25 m resolution. The shaded area denotes gradients with  $R^2 < 0.5$ . The fraction of explained variance which maximizes  $R^2$  is denoted as  $f_{\sigma^2, max}$

**Effect of DEM filtering method** Figure 4.26 shows the maximum  $R^2$  value obtained for different filtered DEMs in comparison to the  $R^2$  value obtained for the original DEM at 25 m resolution. In some cases the filtering causes a strong increase in the  $R^2$  value especially on the entire transect and the effect is most pronounced in the case of the ilp-filter followed by the directional bw-filter and the symmetrical bw-filter. On the upper and lower transect the different filters have less effect. This is due to the more similar smoothing of the elevations on the upper and lower transect as compared to the entire one (Figure 4.24). In addition, the change in  $R^2$  is most pronounced in the case of events with  $R^2$  values below 0.5.

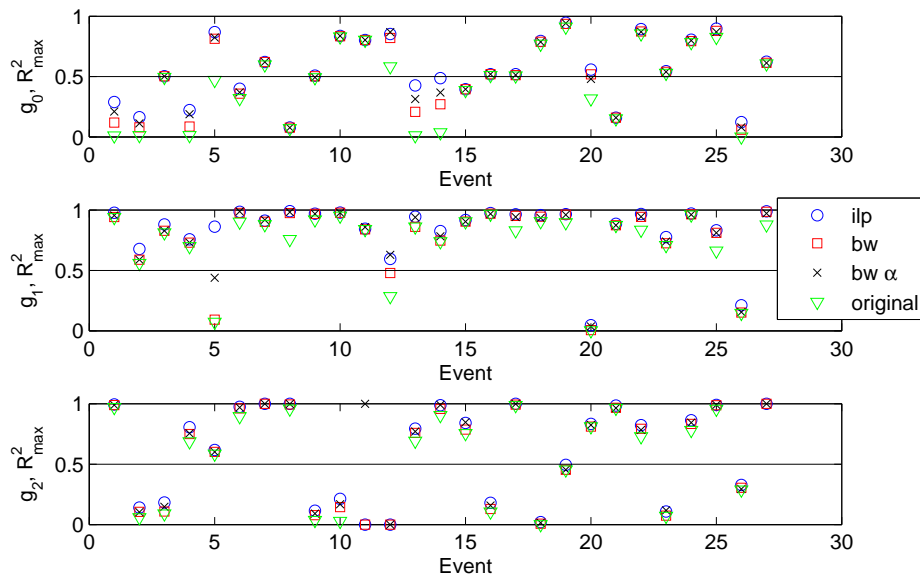


**Figure 4.26:**  $R^2$  value for gradients on the different transects obtained from original and filtered DEMs. As filters the ideal low pass filter (ilp), the symmetrical Butterworth filter (bw) and the directional Butterworth filter (bw  $\alpha$ ) were applied.

Comparison of the fraction of explained variance,  $f_{\sigma^2, max}$ , which maximizes the  $R^2$  value of the gradients for different filtered DEMs shows a strong event dependence (Figure 4.27). Especially on the entire transect,  $g_0$ , many events have a maximum  $R^2$  when the original DEM is used ( $f_{\sigma^2, max}=1$ ), whereas others reach a maximum for a filtered DEM explaining only between 80 and 90% of the DEM variance. On the upper and lower transect the difference among the events is less pronounced since  $f_{\sigma^2, max}$  is more affected by the choice of the filter. Comparison of the different filters shows that the maximum  $R^2$  value is obtained for DEMs with a similar degree of smoothing in the case of both bw-filters on T0. For the ilp-filter  $R^2$  is maximized when a less smoothed DEM is used.

Looking at the upper and lower transect separately, the type of filter has a strong effect on  $f_{\sigma^2, max}$ , and in addition the effect is event dependent. Since the difference in  $R^2_{max}$  obtained for the different filters are generally small, the effect of the filtering on the gradient estimation

seems to be less important as compared to the entire transect. The strong dependence of  $f_{\sigma^2, max}$  on the type of filter used, indicates that the degree of smoothing is not an indication for the scale at which topography influences the rainfall gradients. On the other hand, for the entire transect the different filtering methods tend to result in a more similar  $f_{\sigma^2, max}$ , which indicates that the gradients are not affected by terrain features below this specific spatial scale. On T0 comparison of the different events shows a bimodal distribution of the  $f_{\sigma^2, max}$  value. One group of events shows a maximum in  $R^2$  for the original DEM ( $f_{\sigma^2, max}=1$ ) and the other one shows a maximum for the filtered DEM which explains between 85 and 90% of the original DEM. The latter, however, consists mainly of events with low  $R^2$  values, i.e. cases with opposite gradients on the upper and lower transect.

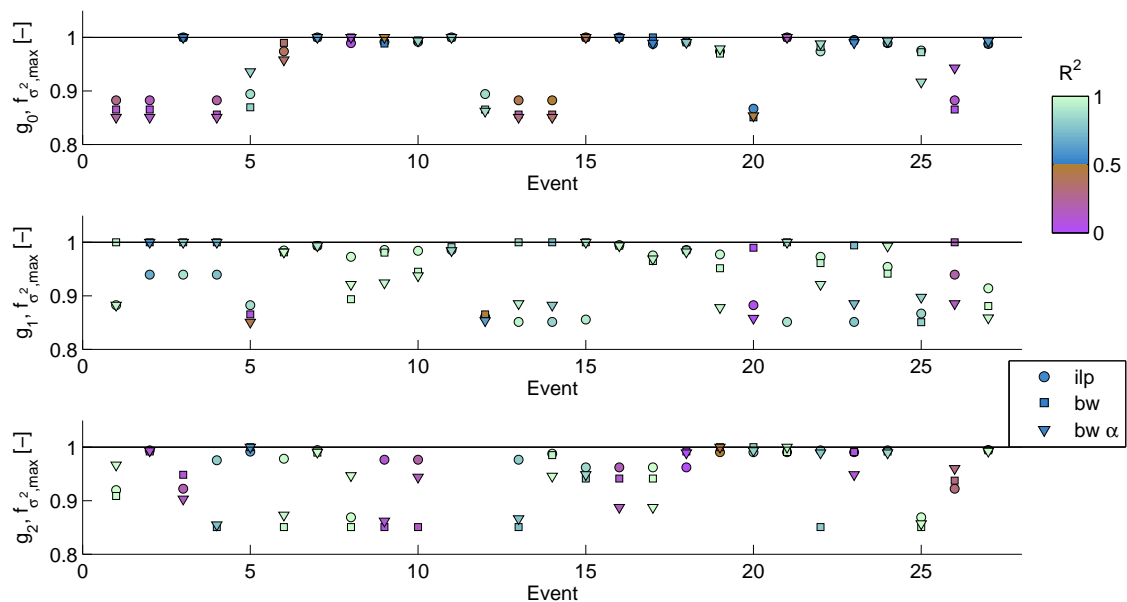


**Figure 4.27:** Explained variance of the filtered DEM resulting in the highest  $R^2$  value,  $f_{\sigma^2, max}$ , for gradients on the different transects obtained for the ideal low pass filter (ilp), for the symmetrical Butterworth filter (bw) and for the directional Butterworth filter in the prevailing wind direction ( $bw \alpha$ ). For events where  $f_{\sigma^2, max}$  equals 1 the original DEM resulted in the highest  $R^2$  value.

Since only on T0  $f_{\sigma^2, max}$  was found to be independent from the type of filter, the analysis of the topographic scales with the strongest influence on the rainfall process was confined to those gradients. Additionally, only events with  $R^2 > 0.5$  based on the original DEM were considered. Among those events on average a bw-filtered DEM which explains 97% of the variance of the original DEM yielded a maximum  $R^2$ , which corresponds to an orographic length scale of around 3 km. The standard deviation of the  $f_{\sigma^2}$  with maximum  $R^2$  among the different events is in the order of 5%.

Based on this analysis a DEM representing 97% of the variance of the original DEM seems to be describing best the orographic features relevant for the gradient formation on T0. The



original DEM and the filtered DEM explaining 97% of the variance of the original one are shown in Figure 4.28 for the area of the transect and for the entire watershed. On the upper and lower transect the effect of the smoothing on the  $R^2$  value of the gradient is strongly dependent on the filtering method, and therefore the resulting topographic scale cannot be associated with the observed gradients.

In addition, on T0 the effect is strongly event dependent, and therefore the conclusion that DEM filtering results in a higher correlation between cumulative event rainfall and elevation is not valid in general. Comparison with the observed events shows that DEM has strongest effects in the case of events with opposite gradients on T1 and T2. In summary, removal of terrain features below 3 km results in a slight improvement in the  $R^2$  value of the gradient estimation, but the effect is strongly event dependent and only along the entire transect results obtained by different filtering methods are consistent. The use of a filtered DEM for rainfall gradient analysis at this spatial scale is not supported by the results.

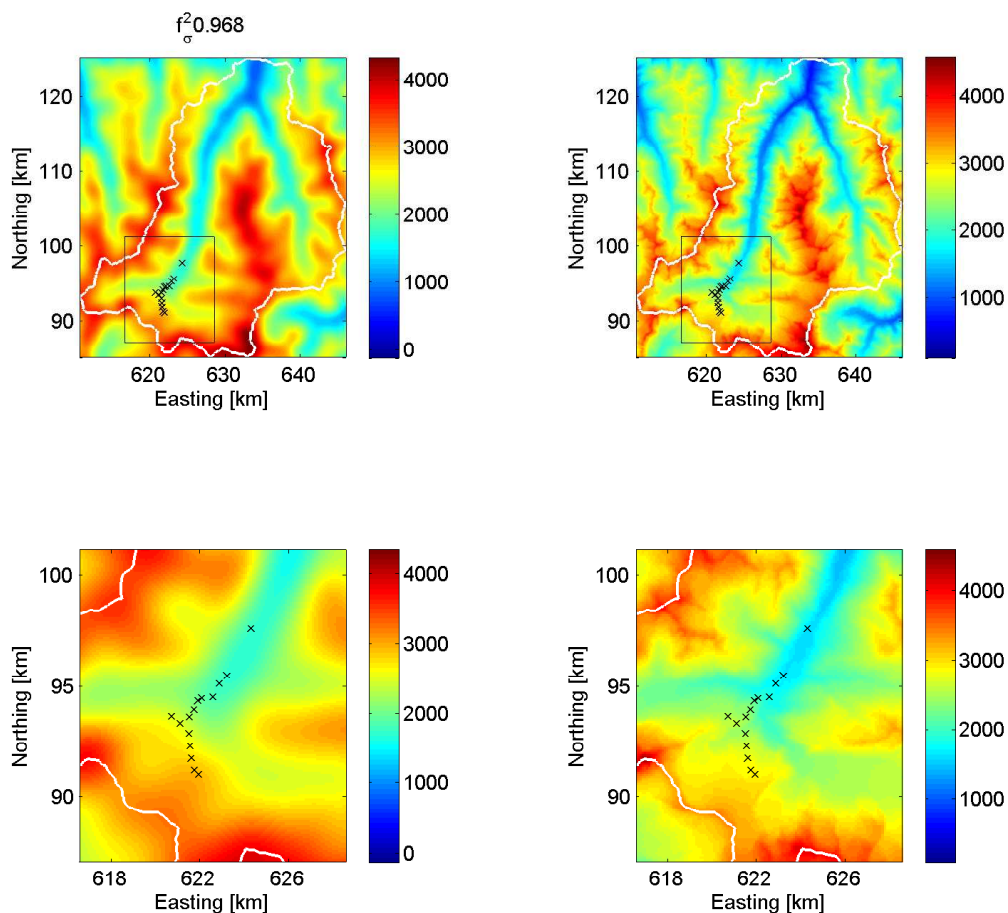


**Figure 4.28:** *Bw-filtered and original DEM in modelled area and in the area of the transect. The filtered DEM explains around 97% of the variance of the original DEM.*

### 4.3 Weather type control on gradients

The effect of topography on rainfall generation mechanism strongly depends on various meteorological conditions such as the stability and moisture content in the atmosphere and the speed and direction of the flowing airmasses. Therefore, a strong dependence of the observed gradient patterns on weather characteristics is expected, and the dependence is expected to decrease with increasing spatial scale at which the atmospheric processes are taking place. In this chapter, weather characteristics at different spatial scales are investigated with respect to their ability to classify the observed events. In the final discussion (Section 5.1) the event classification based on different weather characteristics is compared to the event classification based on the statistical properties of the event rainfall observations on the ground, which will be described in Section 4.5.

The effect of orography on the precipitation formation process is to a large extent dependent on the prevailing wind direction during an event. Wind observations on the ground however do not necessarily represent the direction of the storm because the topography modifies the local wind field. Additionally, the wind direction on the ground deviates by about 5 to 30 % from the wind direction at 500 hPa due to friction on the surface (Beck et al., 2007). Therefore, the effect of the wind direction on event rainfall gradients was analysed based on observations on the ground and in the atmosphere.

The latter was based on analysis of rain cell movement obtained from vertically aggregated radar images and weather type classification data. The tracking of rain cells is able to provide a direction for the event duration at 5 min resolution, and this direction is directly related to the storm movement. On the other hand, the direction provided by the weather type classification data are only available at a daily time scale and they are based on a specific pressure level, which does not necessarily correspond to the location of the clouds. However, the weather type data provide additional information about the atmospheric circulation, such as the distinction between high and low pressure systems, and they are available for a long time period which allows a frequency analysis of different weather patterns.

The wind pattern on the ground was analysed based on the ground observations from the weather stations, and in addition these data were used in a cluster analysis of hourly wind speed and direction in order to characterize the low level wind field (Kaufmann and Weber, 1994; Kaufmann and Whiteman, 1999). The results were then analysed with respect to the occurrence of rainfall in order to identify wind fields that are related to particular event characteristics.

In order to establish a classification of the events into convective and stratiform rain, lightning data were analysed, and the stability of the low level air mass was investigated based on the temperature gradient observed along the transects.

### 4.3.1 Lightning activity during observed events

There exists a strong correlation between lightning activity and occurrence of convective rainfall (Petersen and Rutledge, 1998; Soriano et al., 2001; Tapia et al., 1998). Therefore, in order to distinguish convective and stratiform events, lightning data in the area of the field site were analysed. Records of lightning strikes are available for the weather station located in Zermatt operated by the Swiss office of Meteorology and Climatology (MeteoSwiss). Hourly data are provided for an area of 30 km radius. For each event the hourly average and maximum rate of lightning strikes,  $R_L$  and  $R_{L,m}$  respectively, were estimated (Figure 4.29). The maximum rate of lightning strikes shows considerable differences among the observed events. Applying a classification of thunderstorms as described by Rigo et al. (2010), which considers storms with  $120 \text{ h}^{-1} < R_{L,m} < 600 \text{ h}^{-1}$  as moderate and those below as weak, indicates that events 12-16, 20, 23 and 26 are characterized by moderate convection. The average lightning rate for those events is larger than  $10 \text{ h}^{-1}$  for all of those events (Figure 4.29). In addition, also events 1, 4 and 24 have a high average lightning rate, which indicates even though the convection is not as strong, it is present during the entire event. The remaining events have either no or only low lightning activity, and therefore the rainfall is more of stratiform nature.

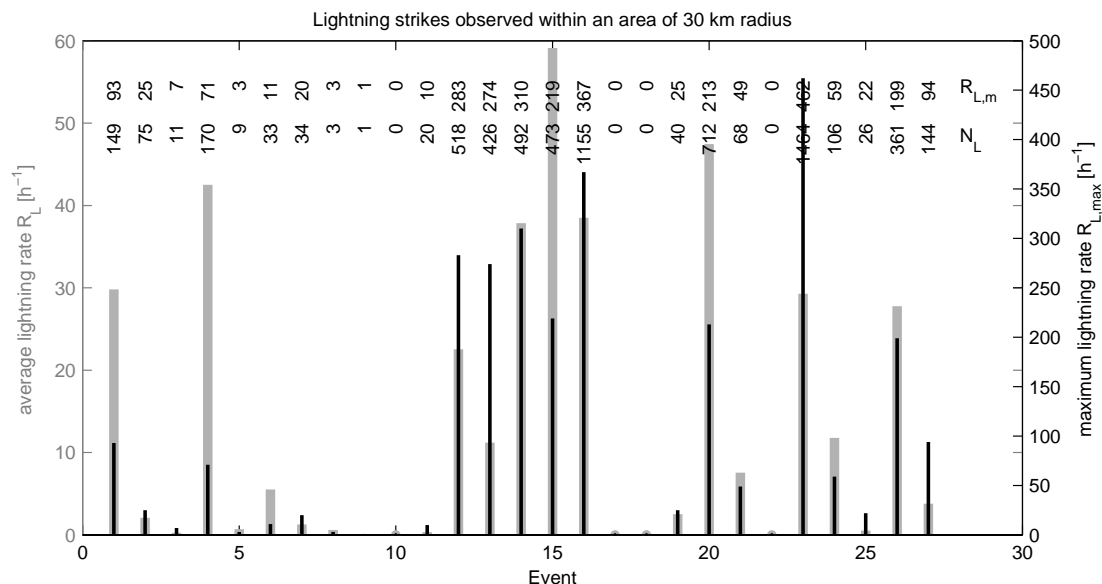


**Figure 4.29:** Maximum and mean of hourly lightning strikes occurring in a distance of 30 km from the weather station in Zermatt. The numbers indicated the maximum lightning rate that occurred during each event,  $R_{L,max}$ , and the total number of lightning strikes during the event,  $N_L$ .

### 4.3.2 Temperature gradient

Temperature data were used to characterize the stability of the near-surface air mass based on the observed temperature gradient (Figure 4.30). It was estimated by linear regression of hourly station data with elevation. Only gradients with an  $R^2$  value larger than 0.9 were selected for the analysis. As is indicated in Figure 4.30, for the majority of the events all estimated gradients fulfil this condition. For the others between around 60 and 90% of the event duration had a temperature gradient with  $R^2 > 0.9$ . The atmosphere can be characterized as very stable if the gradient is larger than -3 K/km, stable for values between -3 K/km and -6 K/km and close to neutral for values below -6 K/km (Kaufmann and Whiteman, 1999).

In most of the observed events the distribution of the hourly gradients has a median within the range of stable gradients. Some of the events exhibit near neutral gradients, in particular events that occurred in the beginning of the second IOP (Event 11, 13-15). The gradients also show a strong diurnal pattern (Figure 4.31), with gradients in the afternoon being more likely in the range of near neutral gradients whereas the rest of the day exhibits mostly stable gradients. Stronger gradients are to some extent associated with convective events as classified according to lightning activity, however the correspondence is rather weak. Due to the diurnal pattern in the temperature gradient also the timing of the event has an effect on the distribution of the resulting gradients and comparison among events that occurred at different times throughout the day is not possible.

The number of hours during which a temperature gradient was observed is also shown in Figure 4.31. It shows that the events occur preferentially during the afternoon and temperature gradients with  $R^2 > 0.9$  are more likely to occur during those hours as well. Overall, the temperature gradients show a strong variability within each event and due to the strong diurnal pattern a comparison of events that occurred at different times is not possible.

### 4.3.3 Wind observations on the ground

#### 4.3.3 - i Wind direction during rainfall events

Wind direction was measured on the ground at all of the weather stations. This allows the analysis of the prevailing wind direction on the ground during the different events and of the influence of the local topography on the wind field. The wind direction was analysed only for time steps with wind velocities larger than 1.5 m/s. This threshold corresponds to 3 knots below which according to the beaufort scale wind vanes are not moving and therefore anemometers cannot provide a reliable measurement of the wind direction for those wind speeds.

The wind directions observed during all the events at 1 min temporal resolution are shown in Figure 4.32. The two IOPs were analysed separately since the location of some of the stations

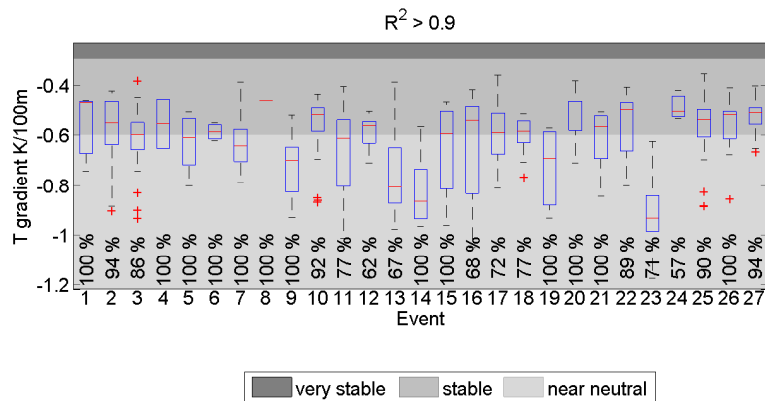


**Figure 4.30:** Hourly temperature gradient observed during each event. The numbers indicate the fraction of the duration with temperature gradients that have an  $R^2$  value larger than 0.9. The red line indicates the location of the median, the blue box denotes the interquartile range and the whiskers have a length of the 1.5 times the interquartile range. The red crosses indicate outliers.

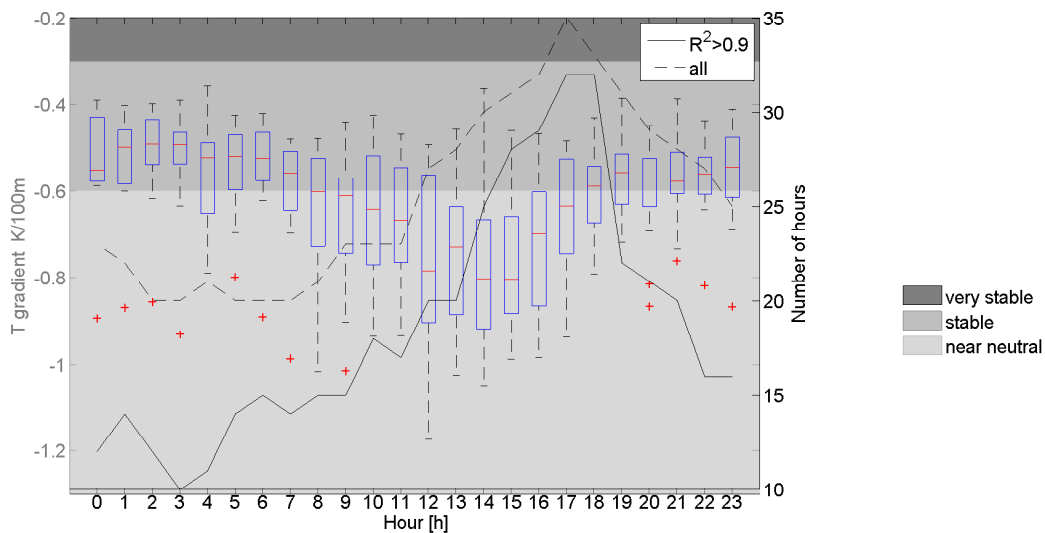


**Figure 4.31:** Hourly temperature gradient for each time of the day during the analysed events. The black line indicates the number of hours for which a temperature gradient was observed. The red line indicates the location of the median, the blue box denotes the interquartile range and the whiskers have a length of the 1.5 times the interquartile range. The red crosses indicate outliers.

was changed. The majority of the stations show most frequently winds from the southwest, the west and the south in both IOPs. An exception is the reference station ZE, which shows frequently wind from the north, in 2011 and the northeast in 2010. Also station 1 in 2011, which was rather close to ZE, showed frequently wind from the east. In 2010 in several events a high fraction of north-easterly winds was observed.

Since wind observations at single stations indicates a strong influence of the local topography on the wind direction, the ground observations were also analysed by means of cluster analysis in order to define wind patterns associated with rainfall occurrence.

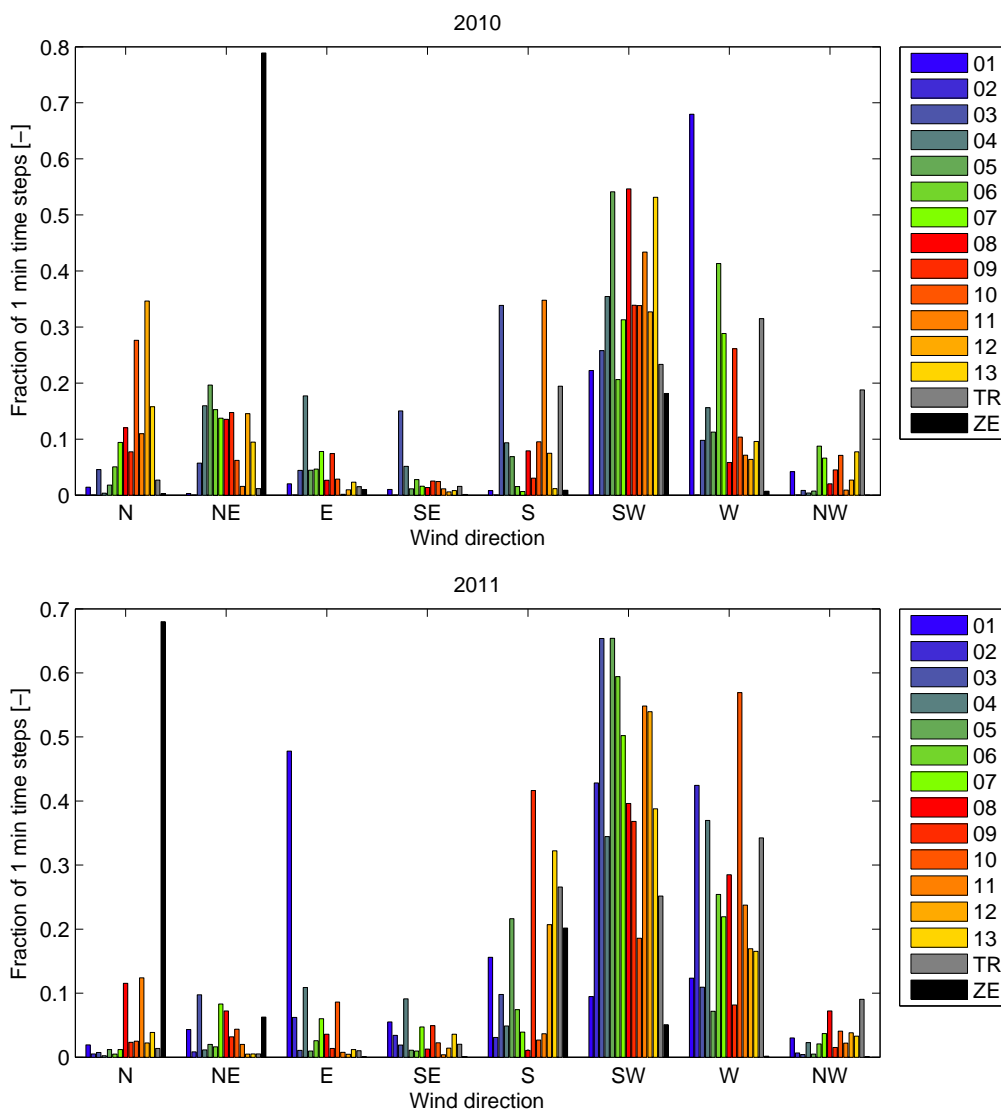


**Figure 4.32:** Wind direction measured at the different weather stations during the observed events for time steps with wind velocities > 1.5 m/s.

### 4.3.3 - ii Classification of low level wind field

The wind field in mountain areas is strongly affected by the local topography, and therefore it does not necessarily reflect the direction of the actual event. In order to highlight distinct wind patterns observed along the transects, a cluster analysis was performed in order to group similar wind fields. The resulting classification was then compared to rainfall characteristics, such as intensity and depth, in order to distinguish wind patterns associated with rainfall occurrence from those caused by differential heating of the surface topography. Since for the latter a strong diurnal pattern is expected, the frequency of occurrence of the different wind field classes throughout the day was analysed.

**Data** The classification was based on the horizontal wind observations along the transects at hourly aggregation using average wind speed and the mode of the wind direction. Since in the first field experiment there are large gaps in the time series due to connectivity problems, only the data of the second IOP were used in the wind field analysis and only those stations which were measuring without large gaps in the time series. These are 10 stations (nr. 1-7, 9, 10 and TR). The total length of the hourly wind time series is 2429 h.

**Clustering method** In order to perform a cluster analysis, a distance measure for all pairs of observations and a method according to which the data are clustered have to be defined. In order to classify the wind fields, a two stage clustering procedure as described in Whiteman and Doran (1993) and Weber and Furger (2001) was applied. In a first step, Agglomerative Hierarchical Clustering (AHC) yields an initial guess of the cluster groups, which are then used in K-means clustering. In AHC the data are clustered according to the complete linkage method (Anderberg, 1973):

$$D(A, B) = \max(d(a, b)) \quad (4.12)$$

where  $d(a,b)$  denotes the distance between cluster elements  $a$  in cluster  $A$  and  $b$  in cluster  $B$ .  $D(A,B)$  denotes the distance between two cluster centres  $A$  and  $B$ . The resulting cluster centres were then used as initial clusters in the K-means clustering method.

The distance measure is defined as in the study of Kaufmann and Whiteman (1999) based on the vector components of the wind observations. Due to variations in the mean wind speeds among the stations, the wind vector components  $u_{tj}$  and  $v_{tj}$  were normalized by the temporal average wind speed at each station,  $j$ , for each time step,  $t$ .

$$u'_{tj} = \frac{u_{tj}}{s_j}, \quad v'_{tj} = \frac{v_{tj}}{s_j} \quad (4.13)$$

where the temporally averaged wind speed,  $s_j$ , is denoted as:

$$s_j = \frac{1}{M_j} \sum_{t=1}^{M_j} \sqrt{(u_{tj}^2 + v_{tj}^2)} \quad (4.14)$$

where  $M_j$  is the number of data points at the station  $j$ . This prevents stations with high wind speeds from having too much weight in the clustering procedure.

Furthermore, the wind data were normalized in the spatial domain in order to distinguish wind fields which differ in terms of wind directions or relative wind speeds at different stations rather than by a scaling factor only.

$$\tilde{u}_{tj} = \frac{u'_{tj}}{s_j}, \quad \tilde{v}_{tj} = \frac{v'_{tj}}{s_j} \quad (4.15)$$

where the spatially averaged wind speed,  $s'_t$ , is denoted as:

$$s'_t = \frac{1}{N_t} \sum_{j=1}^{N_t} \sqrt{(u'^2_{tj} + v'^2_{tj})} \quad (4.16)$$

where  $N_t$  is the number of stations. The distance between the data points at time step  $s$  and  $t$  is defined as follows:

$$d_{st} = \frac{1}{N_{st}} \sum_{t=1}^{N_{st}} [(\tilde{u}_{sj} - \tilde{v}_{tj})^2 + (\tilde{u}_{sj} - \tilde{v}_{tj})^2]^{1/s} \quad (4.17)$$

where  $N_{st}$  is the number of sites that have valid data at time  $s$  and  $t$ . This dissimilarity matrix was then applied in the AHC according to the complete linkage method. In order to identify the number of clusters to be used, the distances at which two clusters are merged is plotted against the number of clusters (Figure 4.33). The largest jump in the distances is at 14 and 13 clusters. In order to reduce the number of clusters, the next large jump in the distance was selected, which results in 9 groups. These clusters were then used as an initial guess in the K-means clustering.

This method is based on the minimization of the total within cluster sum of squared error (twcss)

$$twcss = \sum_{k=1}^{n_k} \sum_{x_j \in C_k} \|x_j - \mu_k\|^2 \quad (4.18)$$

where  $x_j$  denotes the observations,  $n_k$  the number of clusters and  $\mu_k$  the average of the observations in cluster  $C_k$ . After assignment of each observation to one of the initially defined clusters, the cluster centres are recomputed and the observations are reassigned to the new clusters. This procedure is repeated until none of the observations are reassigned to a new cluster.



Table A.13 shows the reassignment of the observations in the AHC clustering to the K-means clusters. The agglomerative clustering results in clusters with very different sizes. The application of the K-means clustering results in a more even distribution of the observations among the different clusters. It considerably changes the assignment of the observations in comparison to the clusters obtained by AHC. The outliers, which were defined as wind fields with a minimum distance larger than 0.9, were excluded in the cluster analysis and reassigned to the nearest cluster after the final clusters have been defined.

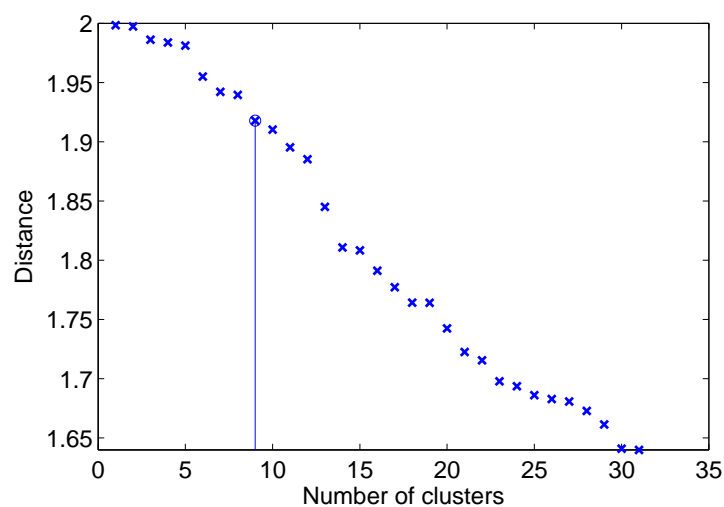


**Figure 4.33:** *Distance of merged clusters depending on cluster number for identification of number of clusters.*

### 4.3.3 - iii Results

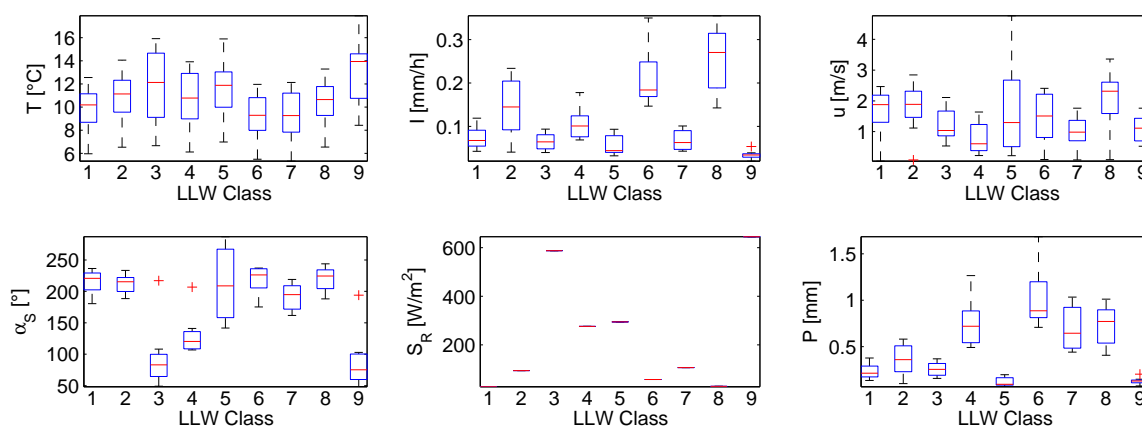
A map of the average wind field within each cluster is shown in Figure 4.37. The resulting clusters were analysed with respect the meteorological conditions observed by the weather stations. The nine low level wind (LLW) classes differ in terms of their diurnal pattern as well as their rainfall intensity and cumulative amount.

Figure 4.34 shows the mean values measured at each station. High wind speeds occur in classes LLW1, LLW2, LLW5, LLW6 and LLW8. Wind direction is mainly between south and west with the exception of groups LLW3 and LLW9 which area characterized by wind directions between east and north and group LLW4, which has no clear direction (Figure 4.37) and is characterized by low wind speed . Solar radiation is high for groups LLW3 and LLW9, which indicates that rainfall occurs only rarely under such wind conditions, medium for groups LLW4 and LLW5 and very low for the rest of them. Temperature does not show a strong difference among the groups. The mean and standard deviation of the grouped data are listed in Table A.14.

The diurnal pattern of each group is shown in Figure 4.36. Groups LLW3, LLW5 and LLW9 occur almost exclusively during the day, and they are characterized by high solar radiation, strong temperature gradients and winds from southeast or northeast. The strong diurnal

pattern observed for those classes indicates that they are linked to local thermal winds due to differential heating rather than large scale winds related to low and high pressure systems. Therefore, they are not expected to be related to precipitation occurrence. These wind fields are observed during about 15% of the time. Also the other classes show a diurnal pattern but to a lesser extent and with highest frequencies rather in the late afternoon and during the night. The most frequent cluster is characterized by winds from southwest with rather low velocity, and about 25% of the analysed wind fields are assigned to this class.

Five out of the nine groups are connected to either large rainfall depths or high intensity rainfall or both. Groups LLW2, LLW6 and LLW8, which are characterized by high wind speeds from the southwest, are related to high mean rainfall intensities. Two additional groups (LLW4 and LLW7) are associated with high rainfall amounts, but without intense rainfall. In those cases, the wind speeds are rather low, and the direction is either from the southwest (LLW7) or it is variable (LLW4).



**Figure 4.34:** Station average of meteorological conditions as observed by the weather stations for each low level wind field class (LLW).

Comparison of the rainfall occurrence in different LLW classes with the unconditional probability of rainfall occurrence during the entire season shows that rainfall occurs more frequently in classes LLW4, LLW6 and LLW8 (Figure 4.35). When selecting an threshold intensity of 1 mm/h for hourly mean precipitation averaged over all station, also for the class LLW2 the probability of rainfall occurrence is slightly higher than in average. Figure 4.35 also illustrates that even though LLW3 is not associated with high intensity rainfall or high cumulative rainfall probability of rainfall occurrence is still quite high, whereas LLW1 and LLW9 show considerably lower probability of rainfall occurrence in comparison to the average.

The wind patterns occurring during the observed events are listed in Table A.15. The most frequent LLW class within each event is summarized in Table 5.1 Each event is associated with more than one wind pattern with classes LLW4, LLW6, LLW7 and LLW8 occurring most frequently. During event 19 and 27 wind class LLW3 was observed most frequently, indicating

small low intensity rainfall events. Also classes LLW1, LLW5 and LLW9 were observed during the events, however they are never the most frequent class within an event.

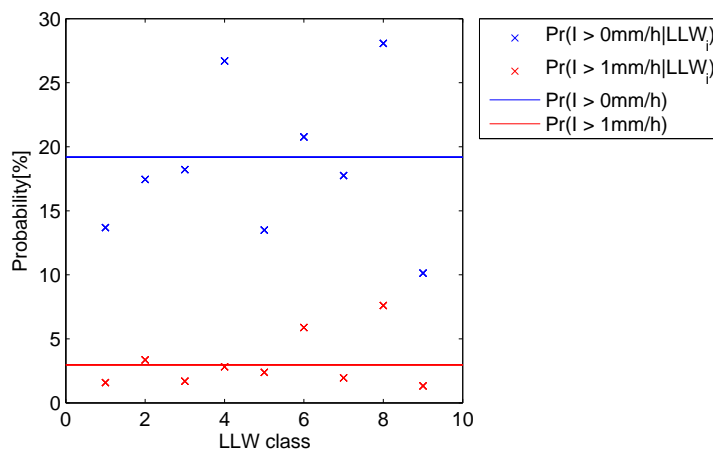


**Figure 4.35:** Probability of rainfall occurrence depending on LLW class in comparison with unconditional probability of rainfall occurrence for two intensity thresholds.

**Summary** Even though the local wind field is strongly influenced by the local terrain features, it shows distinct patterns in situations with rainfall occurrence, which reflect the type of rainfall. Classification of the low level wind field is successful in distinguishing among wind patterns occurring during a rainfall event from those driven by differential heating of the local surface, which exhibit a strong diurnal pattern. The wind fields related to rainfall occurrence are also reflecting the type of rainfall, since some of them are associated with intense rainfall while others are observed more frequently during low intensity rainfall. Therefore, this classification has the potential to point out how different gradient patterns are related to a specific wind pattern on the ground, which can provide further information about how the gradient on the ground is related to the meteorological conditions. This comparison will be shown in Section 5.1.

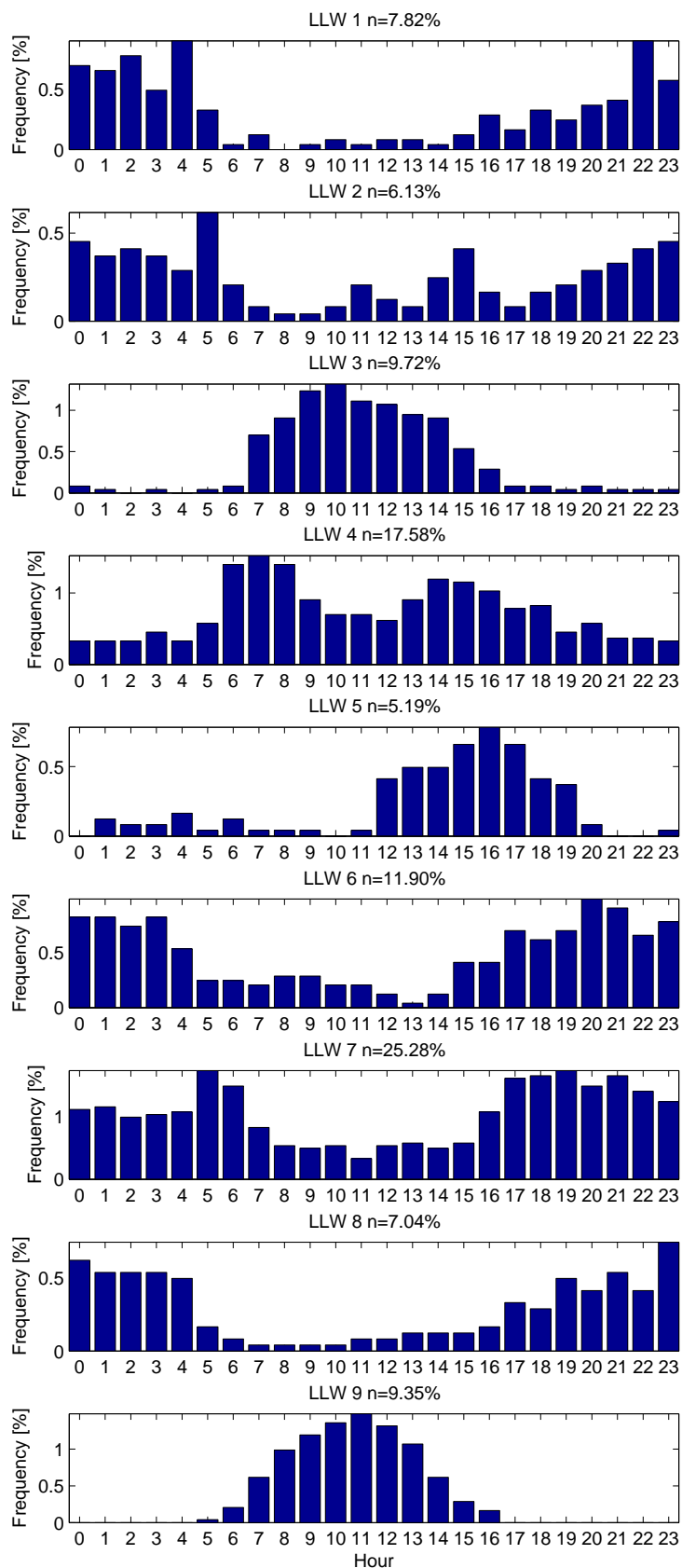


Figure 4.36: Diurnal pattern of LLW classes and frequency of occurrence during IOP 2011.

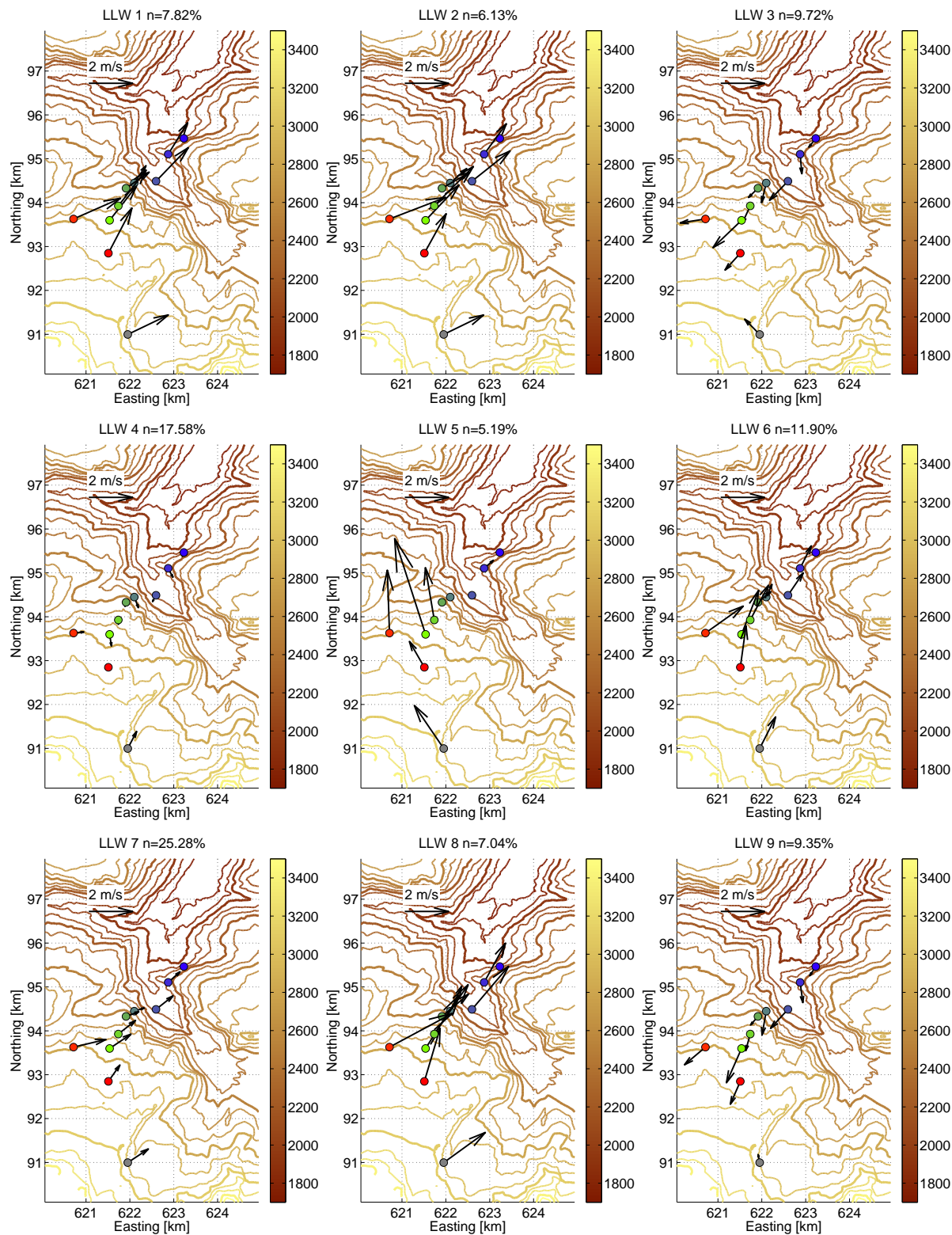


Figure 4.37: Low level wind field clustering

#### 4.3.4 Wind direction estimation from radar images

As shown above (Section 4.3.3), ground based wind observations are affected by the local topography. Therefore, also the atmospheric winds need to be analysed. However, observations are scarce and the wind direction observed at a specific pressure level does not necessarily correspond to the movement of the rain clouds. In order to obtain an estimate of the event direction which is less disturbed by the topography, wind direction was also analysed based on the displacement of rain cells derived from weather radar images. The resulting event direction is then compared to the wind direction observed on the ground in order to identify to which extent the ground level wind field is affected by the local topography.

The wind direction estimation from radar images has the advantage that it is directly related to the movement of the rain cells and therefore it gives a good estimate of the event direction. It was estimated based on the displacement of the centroids of the rainfall cells in consecutive radar images. The rain cells were analysed for an area of 120 × 120 km as indicated in Figure 3.2. To summarize the storm direction at the event time scale, the mode of the direction of all rain cells observed during the entire event was estimated.

**Data** Radar data were provided by the Swiss Federal Office of Meteorology and Climatology (MeteoSwiss). The data used in this study are a composite of the three operational C-band weather radars in Switzerland, and they consist of a vertically averaged rainfall intensity. Rainfall intensities are provided in terms of ranges and not absolute values. Two different types of radar products were used for the analysis of the storm direction due to technical modifications in the radar between 2010 and 2011. They mainly differ in terms of spatial and temporal resolution as well as number of intensity ranges (Table 4.2).

**Method** First, rain cells were selected in each radar image. A threshold area of 40 km<sup>2</sup> was defined for the selection of rain cells in order to remove possible clutter from the cell tracking. For the detected rain cells the centroid of the wet area was computed. Because of the logarithmic scale of the radar intensity classes, the centroid was computed without

year	unit	2010	2011
Cellsize	m	310	1000
Intensity classes	-	16	254
I threshold 1	mm/h	0 (class 1)	0 (class 2)
I threshold 2	mm/h	1.87 (class 28)	1.85 (class 33)
I threshold 3	mm/h	5.15 (class 6)	5.05 (class 9)
Temporal resolution	min	5	2.5

**Table 4.2:** *Difference between radar data products in 2010 and 2011*

accounting for differences in rainfall intensity within the cell, since this would always move the centroid close to the pixel with highest intensity. However, the location with highest intensity can change substantially between consecutive images, and therefore the centroid was computed assuming a constant intensity within the rain cell. In order to account for the different rainfall intensities, the selection of rain cells and the subsequent cell tracking was repeated for three different intensity thresholds, which have corresponding intensity classes in both radar products ( $I_1 = I > 0 \text{ mm/h}$ ,  $I_1 = I_2 > 1.87(1.85) \text{ mm/h}$  and  $I_1 = I_2 > 5.15(5.05) \text{ mm/h}$ ).

The detected cells were then tracked between consecutive time steps. The matching of cells between two successive images was based on the minimum distance between the cell centroids. For a given cell centroid at time step 1 the distance to all centroids at time step 2 was computed, and the cell with the minimum distance was selected as the matching cell at time step 2. Then the cell velocity and direction were computed based on the displacement of the centroid between the two images. If the minimum distance was larger than 6 km it was assumed that the rain cell disappeared and it was not included in the analysis. This distance threshold allows a maximum velocity of 72 km/h (20 m/s) for the rain cell movement. This threshold prevents the matching of rain cells which are too far apart.

- i. The radar image is searched for connected wet areas larger than  $40 \text{ km}^2$  at  $t_i$ , which will be referred to as cells,  $c$ . The number of cells is referred to as  $n_c$ .
- ii. If  $n_c > 0$  the centroids,  $C_{c,i}$ , of each cell  $c = 1, \dots, n_c$  in radar images at  $t_i$  are computed.
- iii. Step 1 and 2 are repeated for the next time step,  $t_{i+1}$ , in order to find the  $n_{c^*}$  centroids of the rain cells at the next time step (centroids ( $C_{c^*,i+1}, c^* = 1, \dots, n_{c^*}$ ) for each cell,  $c^*$ ).  $n_{c^*}$  and  $n_c$  are not necessarily identical since old cells can disappear or merge and new cells can be formed.
- iv. For each cell,  $c$ , at time step,  $t_i$ , the distance,  $d$ , between  $C_{c,i}$  and  $n_k$  centroids  $C_{c^*,i+1}$  at  $t_{i+1}$  are computed.
- v. Each cell,  $c$ , at  $t_i$  is matched to a cell  $c^*$  at  $t_{i+1}$  based on the minimum distance between  $C_{c,i}$  and all centroids  $C_{c^*,i+1}$ .
- vi. If  $d_{min}$  is smaller than 6 km ( $U=6 \text{ km}/5\text{min} = 72 \text{ km/h}$ ), the cells are assumed to match and the velocity,  $U$ , and direction,  $\alpha_R$ , between  $C_{c,i}$  and  $C_{c^*,i+1}$  are computed.
- vii. Step 1 to 6 are repeated for each image of the event and after all cells have been matched, the storm direction is estimated as the mode of the directions observed for all cells observed during the entire event.

**Results** Figure 4.38 shows the distribution of the wind direction estimated from the rain cell tracking at different intensity thresholds and the most frequent one is indicated in the legend. The mode was estimated by rounding the wind direction data to the nearest ten degrees, since in some of the short events only a small number of cells could be tracked. For most of the events the wind directions between south and west occur most frequently. Exceptions are events 7, 9 and 25 where wind from south is most frequent and event 19 which shows most frequently wind from the north. During event 21 no rainfall cells larger than  $40 \text{ km}^2$  were observed by the radar but the weather stations along the transect observed a cumulative amount of up to 7 mm. This discrepancy could be either due to limited visibility of the radar in this area or due to the area threshold used in the cell tracking algorithm.

The number of cells per hour,  $n_c$ , was computed by excluding the dry periods of the event. Comparison of the number of rain cells obtained for different intensity thresholds shows strong differences among the events. Low intensity events such as for example event 9 or 18 have a much higher number of cells when the lowest threshold is applied, whereas for high intensity events the application of a higher threshold results in a similar number of cells (e.g. event 1 and 10). Since the higher thresholds are not appropriate for low intensity events, the direction estimated at the lowest threshold is used in the further analysis. In addition, the mode of the wind direction estimated at different intensity thresholds generally differs by no more than  $30^\circ$ . The mode of the wind direction is summarized in Table 4.3 for different intensity thresholds. The high frequency of events with wind directions from the west and the southwest is in agreement with the ground observations. Comparison shows that the northerly winds, which are observed frequently at the weather stations along the upper transect 4.32, are not representative for the general circulation since they are not observed when the wind direction is derived from radar images. This shows that in particular on the upper transect the wind field is heavily influenced by the local topography, which causes a deviation from the event direction in the atmosphere. The analysis of the event direction also confirms the results obtained from the classification of the LLW field, which showed that mainly the wind fields with strong winds from the southwest are associated with occurrence of rainfall.

Overall, analysis of the wind direction estimated from radar images clearly shows that events are mostly associated with flow from the west and the southwest and that the wind direction remains fairly constant during an event. However, there are few exceptions, which have a more variable wind direction. Comparison of the wind direction estimated from the displacement of rain cells obtained from radar images with wind observations on the ground (Figure 4.32), shows that the wind direction at the cloud level is much less variable. Both show a prevailing wind direction in the quadrant between south and west. However, this comparison highlights which of the ground observations are affected by the local topography, for example the reference station in Zermatt, which shows frequently northerly winds.



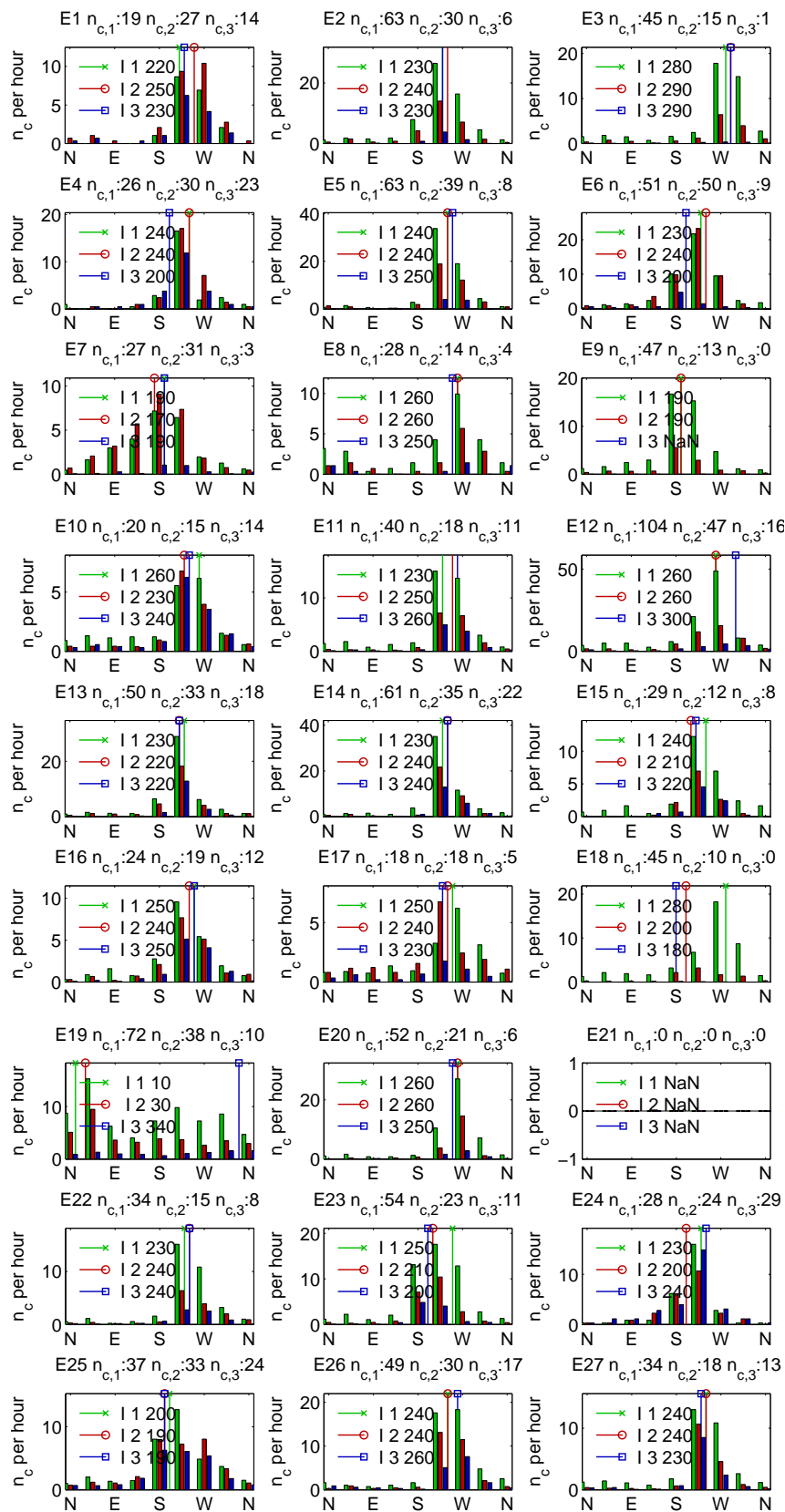


**Figure 4.38:** Wind direction obtained from cell tracking in radar images at different intensity thresholds.  $n_{c,i}$  indicates the average number of rain cells per hour excluding dry periods at different intensity thresholds,  $i$ .

**Table 4.3:** Mode of wind direction,  $\alpha_R$ , (rounded to  $10^\circ$ ) estimated from rain cell tracking in radar images for different intensity thresholds

$\alpha_R$ [ $^\circ$ ]	$I > 0$ mm/h	$I > 1.8$ mm/h	$I > 5$ mm/h
Event 1	220	250	230
Event 2	230	240	230
Event 3	280	290	290
Event 4	240	240	200
Event 5	240	240	250
Event 6	230	240	200
Event 7	190	170	190
Event 8	260	260	250
Event 9	190	190	-
Event 10	260	230	240
Event 11	230	250	260
Event 12	260	260	300
Event 13	230	220	220
Event 14	230	240	240
Event 15	240	210	220
Event 16	250	240	250
Event 17	250	240	230
Event 18	280	200	180
Event 19	10	30	340
Event 20	260	260	250
Event 21	-	-	-
Event 22	250	250	240
Event 23	230	240	240
Event 24	250	210	200
Event 25	200	190	190
Event 26	240	240	260
Event 27	240	240	230
<b>mean</b>	<b>230.4</b>	<b>225.8</b>	<b>237.2</b>
<b>min</b>	<b>10.0</b>	<b>225.8</b>	<b>237.2</b>
<b>max</b>	<b>280.0</b>	<b>290.0</b>	<b>340.0</b>

### 4.3.5 Large scale weather type

Occurrence of rainfall events is strongly related to the atmospheric circulation at a larger scale. For the alpine region, advective weather types with moist airmasses flowing from the southwest are in general more likely to be associated with rainfall occurrence than situations where airmasses originate from continental areas. Furthermore, since different weather types are mainly characterized by differences in the prevailing wind direction, a distinct interaction with the underlying topography is expected, which is associated with a specific rainfall distribution on the ground. Therefore, the large scale weather types observed during the events were compared to the corresponding gradient. However, the meteorological conditions at the local scale can deviate from the general weather situation, and many studies found only little correlation between the weather types and the local rainfall pattern (Blumer, 1994; Sevruck and Miegli, 2002). Therefore, in a first step the association between occurrence of the observed rainfall events and the corresponding weather types is investigated, and in a next step the association with a particular gradient pattern is analysed. This analysis is expected to provide insight into whether certain weather types are connected to the occurrence of rainfall events with a particular gradient pattern at the location of the field site.

Weather types used in this study are provided by MeteoSwiss and are based on the results of the project COST Action 733 "Harmonization and Applications of Weather Type Classifications for European regions". Two types of weather automatic weather classification methods are used. The method Gross Weather Type (GWT) and cluster analysis of principal components (CAP). The CAP classification is based on a two stage procedure which is based on a principal component analysis for the derivation of the dominant patterns of variability, and in a second step the time series of the principal components is classified by means of clustering. This classification is based on the mean sea level pressure (SLP) obtained from the numerical weather prediction model Integrated Forecast System (IFS) of ECMWF or from ERA-40 and ERA-interim for the reanalysis period (1957-2010).

The GWT classification method is based on the correlation between predefined types and the mean SLP field or the field of geopotential height at 500 hPa (Beck, 2000; Weusthoff, 2011). The predefined types are based on the European GWTs described by Hess and Brezowsky (1977). Initially three prototypical SLP patterns are defined, which represent idealized west-east, south-north and central low pressure isobars over the area of Europe. Next, each field is classified into one of 10 classes according to its correlation coefficient with these three idealized patterns. High and low pressure situations are based on minimum and maximum vorticity respectively and the remaining eight classes are defined according to the main direction of the isobars. These classes can be further subdivided according to the sign of the vorticity correlation coefficient into cyclonic and anticyclonic patterns (Beck, 2000; Beck et al., 2007). An additional classification GWTWS extends the GWT classification with 8 types based on the 500 hPa geopotential heights by including the mean wind speed at 500 hPa in order to

differentiate between advective and convective patterns using a threshold of 7 m/s. Above this threshold one of the 8 GWT types is assigned and below the field is classified according to the averaged mean SLP into low, high and flat pressure situations.

**Method** In a first step the frequency of the weather types were analysed and compared to the occurrence of precipitation at the weather station in Zermatt in order to test if certain weather type (WT)s are associated with precipitation occurrence in this particular area on the climatic time scale and in particular during the IOPs. Later the weather types associated with each event are investigated for their potential to classify the corresponding gradients into distinct classes (Section 5.1).

Weusthoff (2011) showed that weather types explain between 10 and 25% of the variation in daily precipitation in the Alps with lowest values being observed for the summer months. The GWT method was found to give the best results for the summer period. Among the classifications with a low number of classes GWTWS and CAP9 gave best results. Therefore, the methods GWTWS and CAP9 were used for the following analysis of the weather types during the observed events.

For those classifications, the weather type frequency,  $f_{WT}$ , was estimated using the records from September 1957 to December 2011. In order to compare the weather types with the occurrence of rainfall at the field site, daily rainfall data were analysed for the same time period at the weather station in Zermatt. A threshold of 5 mm of cumulative precipitation was set for detection of days with precipitation at this station, i.e. events with a similar magnitude or larger as compared to the events observed in this study. Based on this data set the weather type frequency under rainfall conditions,  $f_{WT,P}$ , was estimated by selecting only days during which a rainfall event was measured.

Because the weather type frequency shows strong seasonal variability (Beck et al., 2007; Weusthoff, 2011), the frequency of the weather types was also analysed on a seasonal basis for the months June to September, which corresponds to the time period of the field experiment. The seasonal weather type frequency is denoted as  $f_{WT,S}$  and the one for rainy days is denoted as  $f_{WT,S,P}$ . In addition, the weather type frequency was estimated for the days during the IOP for which rainfall events were observed ( $f_{WT,E}$ ) in order to test how well it matches the frequency observed on the long term.

**Results** Figures 4.39 to 4.40 show the weather type frequency on an annual time scale,  $f_{WT}$ , on the seasonal time scale,  $f_{WT,S}$ , independent of precipitation occurrence as well as the weather type frequency conditioned on precipitation occurrence for both the annual ( $f_{WT,P}$ ) and the seasonal time scale ( $f_{WT,P,S}$ ). In addition, the frequency of the weather types is shown for the days on which a rainfall event was observed during the field experiment  $f_{WT,E}$ .

The classification GWTWS shows most frequently flow patterns from the west, the southwest and the northwest as well as high and flat pressure systems. The latter are more frequently

observed in summer as compared to the annual time scale (Figure 4.40). Precipitation is associated mainly with flow from the west and the southwest and with flat pressure systems. Events occurred only during the advective weather types, especially in situations with westerly and south-westerly winds. For the latter, the frequency of precipitation occurrence is much higher than the unconditional frequency, which indicates a high probability of rainfall under such conditions. 50% of the days of the observed events fall into this category, and the largest number of event days are categorized as flow from west.

A similar pattern can be observed for the CAP9 classification where the cyclonic W-SW situation with flat pressure distribution is mainly associated with rainfall events on annual as well as seasonal time scales (about 27% and 34% respectively) and also for the observed events (35%) (Figure 4.39).

In summary, based on the analysis of 64 years of rainfall data and corresponding weather types, a strong association between certain weather types and rainfall occurrence is visible, in particular for events with air flow from the southwest and the west and those with cyclonic circulation patterns. The weather type frequency of the observed events shows a good correspondence to the seasonal weather type frequency for rainy days. The weather types observed during those events can therefore be assumed to be representative for the average summer season in this area.

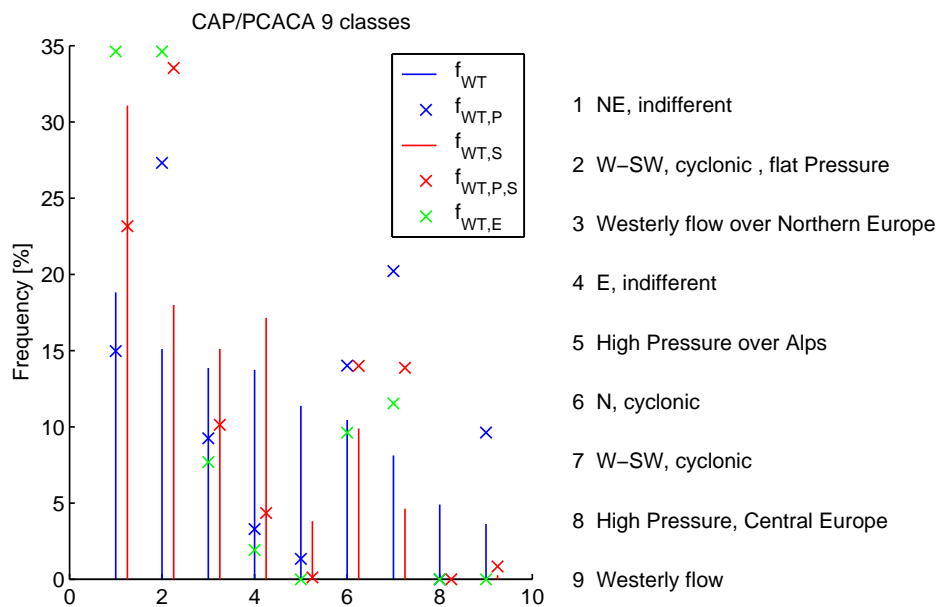


Figure 4.39: CAP9: Occurrence of precipitation and weather type frequency on a seasonal and annual basis within the time period of 1957-2011 and frequency of event occurrence for the field experiments in 2010 and 2011.

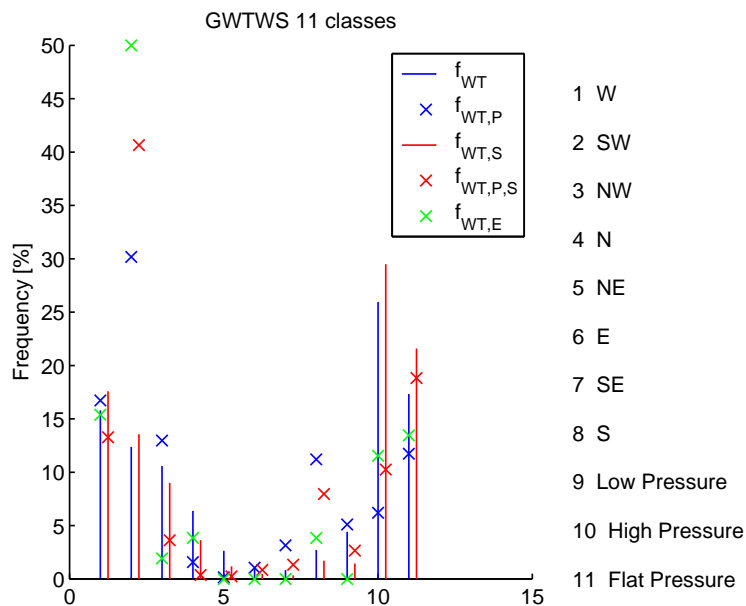


Figure 4.40: GWTWS: Occurrence of precipitation and weather type frequency on a seasonal and annual basis within the time period of 1957-2011 and frequency of event occurrence for the field experiments in 2010 and 2011.

## 4.4 Modelling of orographic precipitation

In the previous section, the meteorological conditions of the different events were investigated based on different observations of the atmospheric processes. In this section, the gradients are compared to the theoretically expected distribution of rainfall based on a simulation of the orographic rainfall process. This comparison between the simulated rainfall amount, generated due to upslope condensation and subsequent fallout, with the observed gradients is expected to highlight the mechanisms relevant for the gradient formation. The aim of the model simulation is not to reproduce the observed gradients accurately, but to provide a reference against which the observations can be compared. Hence, a simple analytical model was chosen, which has only a small set of parameters and can therefore be applied to complex topography. Based on the differences between the simulated and the observed gradients, the presence of additional processes can be highlighted, thereby providing further insight into the driving mechanisms for gradient formation.

### 4.4.1 Model description

In order to estimate the spatial distribution of precipitation due to orography, a linear upslope-time-delay model was applied. It is based on the upslope model, which calculates the condensation rate using wind speed and terrain slope, and it assumes precipitation to be the result of instantaneous fallout of the hydrometeors generated in the condensation process (Smith, 1979). The cloud water,  $S$ , is defined as the sum of background cloud water generation,  $S_\infty$ , and local variation due to terrain forced lifting of the air mass.

$$S(x, y) = S_\infty + C_w \mathbf{U} \nabla \mathbf{h}(\mathbf{x}, \mathbf{y}) \quad (4.19)$$

where  $C_w$  denotes the coefficient relating condensation rate to vertical motion,  $h(x, y)$  denotes the terrain elevation and  $\mathbf{U}$  the wind vector. The term  $\mathbf{U} \nabla \mathbf{h}(\mathbf{x}, \mathbf{y})$  indicates the terrain forced vertical air velocity  $w(x, y)$ . Assuming that only upslope regions are affecting downslope areas,  $S(x, y)$  is set to 0.  $C_w$  is defined as follows:

$$C_w = \rho_{S_{ref}} (\Gamma_m / \gamma) \quad (4.20)$$

where  $\Gamma_m$  and  $\gamma$  denote the moist adiabatic and the environmental lapse rate respectively.  $\rho_{S_{ref}}$  is the reference water vapour density at the reference temperature  $T_{ref}$  under saturated conditions.

$$\rho_{S_{ref}} = e_S(T_{ref}) / R_v T_{ref} \quad (4.21)$$

where  $R_v$  denotes the gas constant for vapour ( $R_v = 461 \text{ J/kgK}$ ). The saturation water vapour pressure,  $e_S$ , is defined by the Clausius-Clapeyron equation:

$$e_S(T) = e_{S_{ref}} e^{L\Delta T/(R_v T_{ref}^2)} \quad (4.22)$$

which is approximated as follows:

$$e_S(T) = 6.112 e^{c_1 T/(c_2 + T)} \quad (4.23)$$

with parameters  $c_1 = 17.67$  and  $c_2 = 243.5^\circ\text{C}$ . Equation 4.19 assumes that the vertical displacement of the air mass is penetrating through the entire moist layer,  $H_w$ , without any decay or dispersion. Its height is defined as follows:

$$H_w = -\frac{R_v T_{ref}^2}{L\gamma} \quad (4.24)$$

where  $L$  denotes the latent heat of vaporization ( $L = 2.25 \cdot 10^6 \text{ J/kg}$ ). Smith (2003b) expanded the model by introducing the concept of characteristic time scales for the conversion of the condensed water into hydrometeors and subsequent fallout as described by Jiang and Smith (2003). In this model the vertically integrated cloud water density  $q_c$  and hydrometeor density  $q_s$  is described as follows:

$$\frac{Dq_c}{Dt} \approx \mathbf{U}\nabla\mathbf{q}_c = \mathbf{S}(\mathbf{x}, \mathbf{y}) - \frac{\mathbf{q}_c}{\tau_c} \quad (4.25)$$

$$\frac{Dq_s}{Dt} \approx \mathbf{U}\nabla\mathbf{q}_s = \frac{\mathbf{q}_c}{\tau_c} - \frac{\mathbf{q}_s}{\tau_f} \quad (4.26)$$

where  $\tau_c$  denotes the time constant for conversion from cloud water to hydrometeors and  $\tau_f$  time constant for hydrometeor fallout. Precipitation on the ground can be estimated from the loss of hydrometeors from the atmosphere as follows:

$$P(x, y) = q_s(x, y)/\tau_f \quad (4.27)$$

In order to apply the model, several parameters need to be estimated. Wind speed and direction need to be defined to determine the magnitude of the upslope flow and the subsequent generation of cloud water. By defining the environmental and moist adiabatic lapse rates,  $\gamma$  and  $\Gamma_m$ , and the reference temperature on the ground, the uplift sensitivity factor  $C_w$  can be determined. Furthermore, the time constants of cloud water generation and hydrometeor fallout,  $\tau_c$  and  $\tau_f$ , need to be defined in order to include advective processes in the model. To apply the model to the observed events, these parameters were estimated based on observations and based on calibration to the observed rainfall amounts at the rain gauges in the surrounding area.



#### 4.4.2 Simulated gradients depending on wind direction

Since in most of the observed events wind directions between south and west were predominant, this model was used to assess the range of gradients that can be expected for different wind directions. In a first step, the model was tested for its ability to reproduce different gradient patterns along the transects investigated in this study by variation of the input parameters. Based on a range of possible model parameter values similar to the one used in Smith and Barstad (2004), different simulations were performed, and the corresponding gradients were estimated. The selected parameters are listed in Table A.21. The simulated gradients at the location of the transects were estimated based on the simulated rainfall intensity observed at the location of the different weather stations, given that at least 3 stations along a transect had a nonzero rainfall intensity. The simulated gradients correspond to an aggregation interval of 1 h. A comparison of the range of the resulting gradients depending on the wind direction is shown in Figure 4.41.

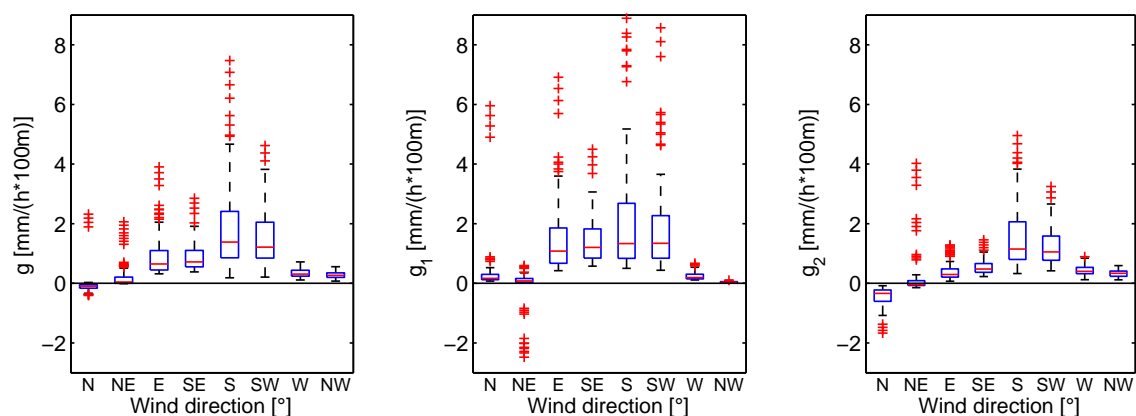


**Figure 4.41:** Comparison of modelled gradient in rainfall intensity along transect T0, T1 and T2 depending on wind direction for different parameter sets.

The results show a strong dependence of the resulting gradient on the wind direction, which highlights the effect of the topography on precipitation enhancement and shielding. The observed variability also indicates that the simulated gradients are very sensitive to the model parameters. The highest median of the simulated gradients is observed for wind directions from the southeast and from the south, i.e. a wind direction perpendicular to the mountain range. The model also suggests that at this particular location the strongest gradients occur when the transect is on the leeside with respect to the prevailing wind direction.

Furthermore, the model is also able to reproduce opposite gradients along T1 and T2, as can be seen from the comparison of the two gradients (Figure 4.42). Even though this model might not give an accurate estimation of the magnitude of the observed gradients, it is capable of reproducing a variety of different gradients that are qualitatively and quantitatively similar

to the observed ones. For the observed gradients, the majority is located in the lower right quadrant, i.e. negative gradients in the upper part and vice versa. Those events are, however, characterized by south-westerly flow rather than winds from the northwest as suggested by the model simulations.

Figure 4.41 illustrates the effect of the input parameters on the resulting gradients along T1 and T2. The lapse rate,  $\Gamma$ , changes the magnitude of the gradients on along T1 and T2, but their ratio remains constant. A change in wind speed,  $U$ , and time constants,  $\tau$ , also tends to increase the gradients, but the relative increase along T1 and T2 is not the same. The wind direction,  $\alpha$ , defines to a large extent the order of magnitude of the resulting gradients, i.e. in situations with wind from the northwest and west only weak gradients are observed on both transects, whereas winds from the south and the southwest cause strong gradients. Also situations with opposite gradients along T1 and T2 are clearly related to a particular wind direction. Negative gradients along T1 correspond to winds from the northeast and negative gradients along T2 occur only when the wind direction is north.

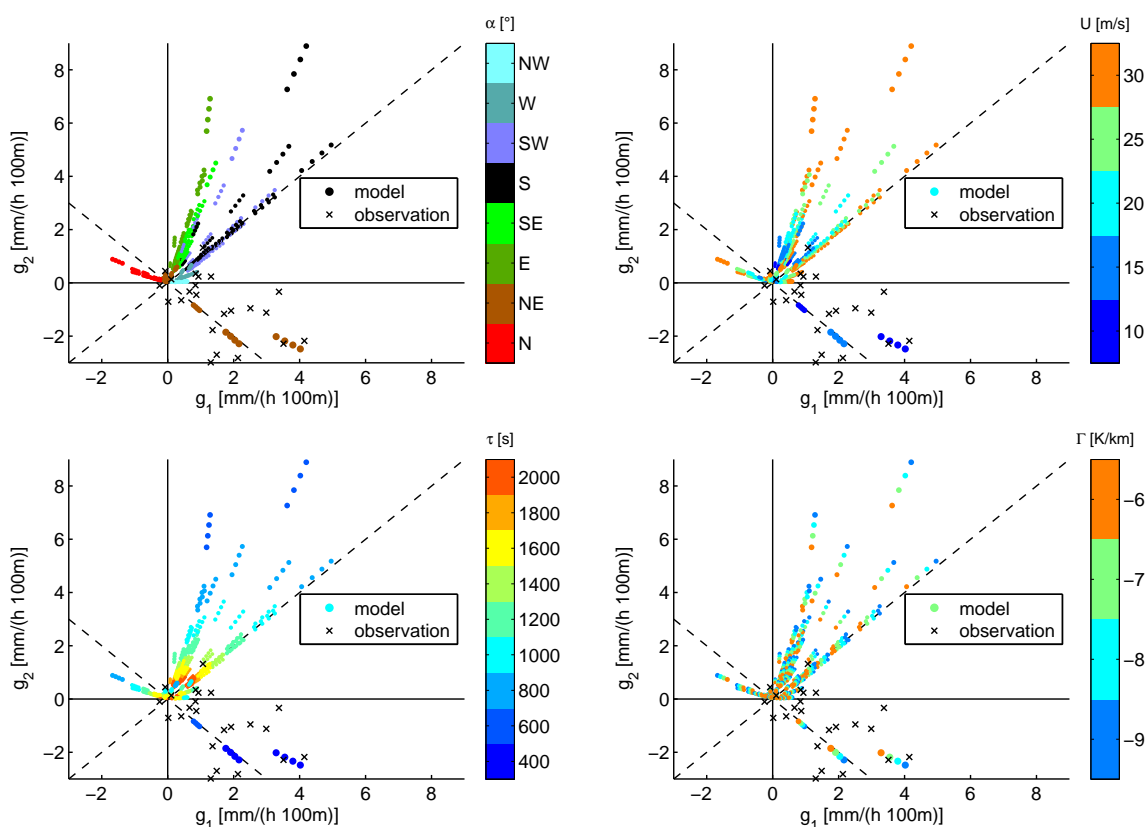


**Figure 4.42:** Gradient on T1 and T2 depending on wind direction,  $\alpha$ , time constants,  $\tau$ , wind speed,  $U$ , and temperature lapse rate,  $\Gamma$ .

In summary, the sensitivity analysis of the gradients with respect to the model parameters shows the strong effect of the wind direction in both the qualitative pattern observed along the two transects as well as the magnitude of the simulated gradients. The local shielding and

enhancement of rainfall due to terrain is strongly related to the wind direction, but it is not in agreement with the observed gradient patterns. This suggests that in reality gradient formation is also influenced by other rainfall generating mechanisms, which are affected differently by the local terrain. Nevertheless, the fact that depending on the wind direction, even under the assumption of steady state atmospheric conditions, the simulations result in variable gradients along a rather short transect, is an indication that at the basin scale an even larger variability can be expected.

### 4.4.3 Model calibration

**Data** In order to select a parameter set which gives a realistic representation of the meteorological conditions during the observed events, the model was calibrated to the data observed at the stations in the surrounding area (Figure 3.1). Especially in the southern and western part, there is a dense network of stations, which provides hourly data of precipitation, but the area in the northwest is not well covered by the network.

The range of altitudes covered by the stations in comparison to the distribution of the terrain elevation is shown in Figure 4.43. There is quite a good correspondence for altitudes below 2000 m a.s.l.. But as in most cases higher altitudes are under-represented by the station network, and the lower areas are over-represented. The mean station altitude is around 1300 m a.s.l. with a standard deviation of about 660 m whereas the mean terrain elevation is at 1800 m with a standard deviation of 850 m.

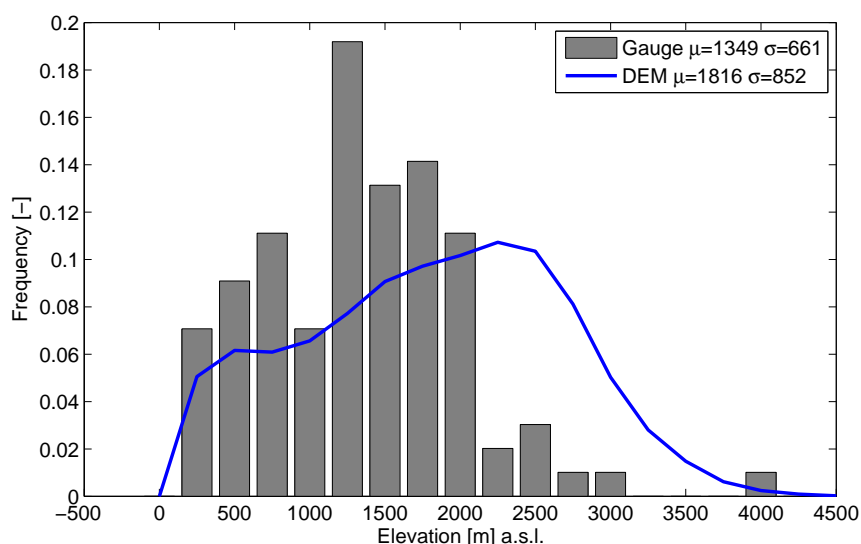


**Figure 4.43:** Elevation distribution of DEM at 100 m resolution and elevation distribution of the raingauges in the surrounding area.

**Table 4.4:** Parameters used for the event calibration: The wind direction was based on the tracking of rain cells using the intensity threshold,  $I_1$ , the environmental lapse rate was estimated by averaging the lapse rates of the individual events and as reference temperature,  $T_{ref}$ , the average for each event was used.

Event	$\alpha$			$\gamma$ [K/100m]	$R^2 > 0.9$	$D_p$ [h]	$T_{ref}$ [°C]
	l1	l2	l3	all			
1	220	250	230	-0.47	-0.47	1.8	10.4
2	230	240	230	-0.53	-0.55	5.4	8.1
3	280	290	290	-0.58	-0.6	5.6	5.0
4	240	240	200	-0.56	-0.56	1.4	10.3
5	240	240	250	-0.56	-0.61	3.2	9.6
6	230	240	200	-0.59	-0.59	2.6	7.5
7	190	170	190	-0.64	-0.64	12.8	5.5
8	260	260	250	-0.46	-0.46	2.1	9.5
9	190	190	-	-0.70	-0.70	10.7	6.8

Nine of the observed events were applied in this model in order to test to which extent it is able to reproduce the observed gradients. As mentioned above, the model is not expected to accurately reproduce the observed gradients due to the strong simplifying assumptions in the model. For example, none of the observed events correspond to a steady state and other rainfall generating mechanisms than upslope condensation are expected to play a role. In addition, none of the model parameters are expected to be constant throughout the event. Nevertheless, the resulting simulations provide a benchmark against which the observations can be compared.

Out of the seven input parameters of the model,  $T_{ref}$  was estimated based on observations, and the remaining parameters were calibrated based on the measured rainfall at the raingauges in the surrounding area. As in the study by Barstad and Smith (2005), the time constants for hydrometeor conversion and fallout,  $\tau_c$  and  $\tau_f$ , were set equal. Table 4.4 shows the parameter values of the events that were applied in the model. The wind direction  $\alpha$  was estimated based on the celltracking of rain cells obtained from radar images using different intensity thresholds (Section 4.3.4).

The event directions obtained by using different intensity thresholds in the rain cell tracking analysis of radar images do not show a strong variability. Especially the directions estimated from the first two intensity thresholds were very similar. Except for event nr. 9, the deviation was never more than  $10^\circ$ . Therefore, the direction estimated based on the lowest intensity threshold is used in the model simulations. The environmental lapse rate,  $\gamma$ , is estimated from the temperature measurements on the ground aggregated on an hourly interval. The median of the hourly lapse rates that had an  $R^2$  larger than 0.9 is used as estimate of the environmental lapse rate of the entire event as shown in Table 4.4. Since the temperature gradient obtained from ground measurements is affected by the local topography and because of the strong

diurnal pattern, an average lapse rate is used in the model ( $\gamma = 0.58 \text{ K}/100\text{m}$ ). The reference temperature on the ground,  $T_{ref}$ , is estimated by averaging of the ground observations. Figure 4.44 shows the cumulative rainfall amount that was recorded at the raingauges in the surrounding area. The temporal resolution of the raingauges ranges between 1 min and 1 h, and the data were aggregated over the entire event rainfall duration. The data of the transect of mobile stations were not used in the calibration. The distribution of cumulative rainfall shows a distinct pattern among the different events. In event 7 and 9 the highest amounts are observed at low level stations in the southeast, whereas the other events generally show largest rainfall amounts in the northern part. The events show large differences not only in the spatial distribution of rainfall but also in terms of cumulative amounts. Especially in short duration

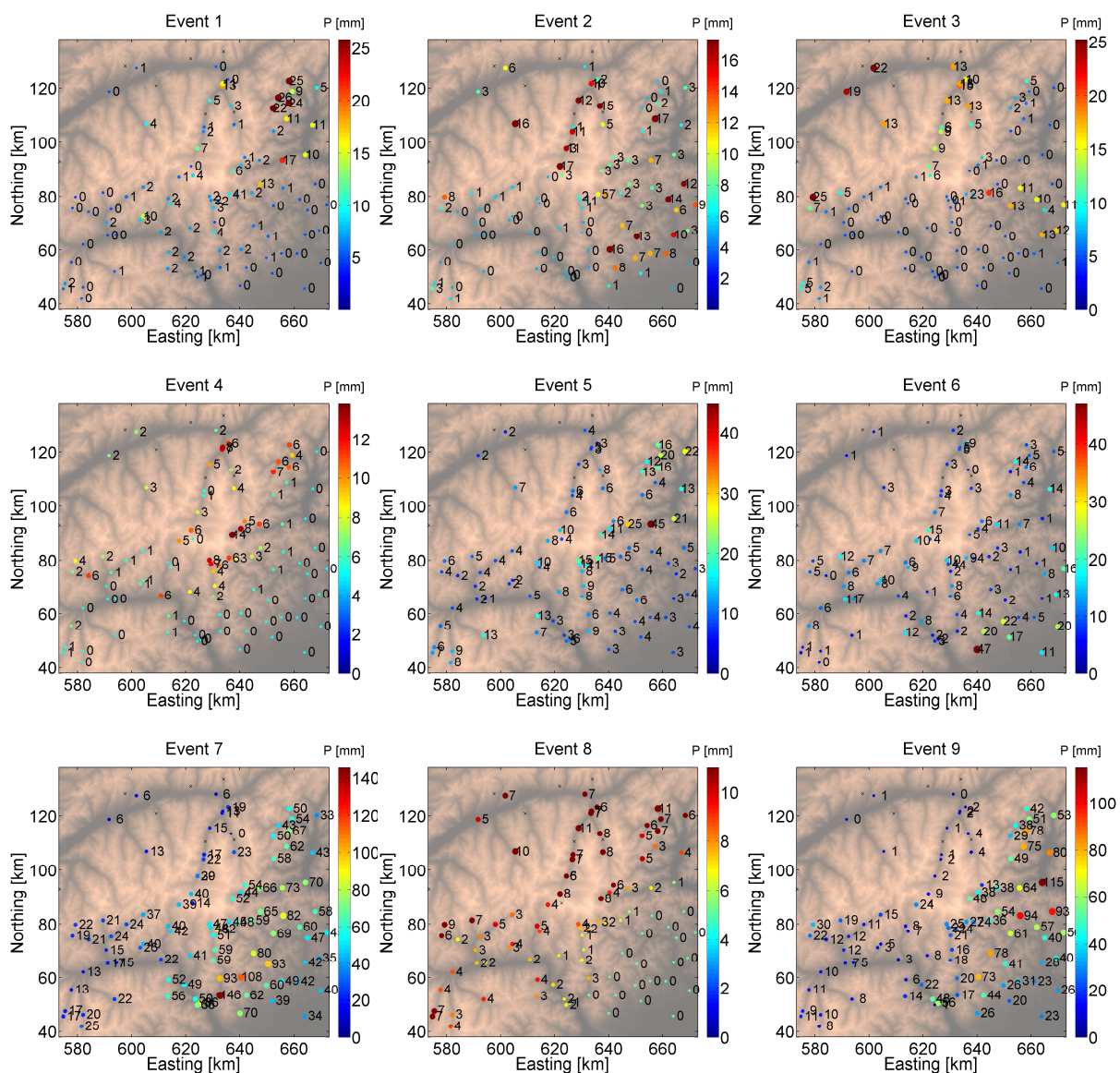


Figure 4.44: Cumulative rainfall amount observed at the raingauges for the 9 events

events, i.e. event 1, 4, 6, and 8, a large number of stations did not record any rainfall.

**Calibration method** In order to evaluate the model's skill in reproducing the observed cumulative rainfall different statistical measures are analysed. The modelled cumulative rainfall,  $P_M$ , is estimated from the modelled intensity,  $I$ , multiplied by the event rainfall duration,  $D_P$ , in the pixels covering the raingauge locations. Three different statistical measures were analysed, the root mean square error (RMSE), the mean absolute error (MAE) and the correlation coefficient as described by Barstad and Smith (2005) and Smith (2003a). Each one was then used independently to find an optimal set of model parameters by minimizing MAE and RMSE and by maximizing the correlation coefficient.

$$MAE = \frac{\sum (|P_M - P_O|)}{N} \quad (4.28)$$

$$RMSE = \sqrt{\frac{\sum (P_M - P_O)^2}{N}} \quad (4.29)$$

The correlation coefficient,  $\rho$ , is estimated as described by Barstad and Smith (2005):

$$\rho = \frac{\sum P_M P_O}{\sqrt{\sum P_M^2 \sum P_O^2}} \quad (4.30)$$

where  $P_M$  denotes the modelled rainfall amount at each station.  $P_O$  denotes the observed rainfall amount at each station and  $N$  denotes the number of stations. The input variables  $U$ ,  $\Gamma_m$  and  $\tau$  are calibrated based on the statistical measures of observed and modelled event rainfall described above. The parameters are selected in a range similar to the one used by Smith and Barstad (2004). The wind speed is varied from 10 to 30 m/s in steps of 5 m/s, the  $\Gamma_m$  values are set between -0.95 and -0.65 K/100m in steps of 0.1 K/100m and the  $\tau$ -values are varied between 1000 and 2000 s in steps of 200 s. Since the estimated direction is affected by uncertainty, the direction is also calibrated using the estimated direction  $\pm 10^\circ$  using steps of  $5^\circ$ . The DEM used in the simulation has a spatial resolution of 100 m.

#### 4.4.4 Results

The model parameters obtained by calibration based on maximization of the correlation coefficient is shown in Figure 4.45. A summary of the results obtained for different statistical measures of model skill are listed in Table A.18. For most events, calibration of the model results in parameter sets with high wind speeds (30 m/s) and high  $\tau$  values (2000 s), indicating strong advective processes. For the two events with southerly wind direction slightly smaller  $\tau$  values are obtained by the calibration. Cumulative event rainfall amounts and rainfall intensity estimated from the calibrated model are listed in Table 4.5. The mean intensity shows some

variation among different events, however also the calibration method can have a strong effect on the resulting intensity. Comparison of the mean observed and modelled rainfall amounts and intensities indicates that the model underestimates the observed rainfall.

**Table 4.5:** Cumulative sum,  $P$ , and mean intensity,  $I$ , obtained from the model and observations. For each event the station average is shown.  $\overline{P_O|P_M > 0}$  indicates the average taken over all observations where the model simulations show a rainfall intensity  $> 0$

P [mm]	$\overline{P_O}$	$\overline{P_O P_M > 0}$			$\overline{P_M}$		
Calibration method		rmse	mae	$\rho$	rmse	mae	$\rho$
Event 1	4.2	5.1	2.9	5.0	1.6	1.2	2.1
Event 2	4.5	4.6	4.6	5.3	3.2	3.2	4.7
Event 3	5.9	5.5	5.3	5.8	3.1	2.7	3.3
Event 4	3.0	3.4	3.4	3.6	1.8	1.8	2.3
Event 5	7.2	8.7	6.9	8.7	5.0	3.7	5.0
Event 6	6.7	6.2	6.1	7.0	2.2	2.4	3.6
Event 7	43.4	51.0	51.1	51.4	17.1	22.5	8.5
Event 8	4.4	4.4	4.4	4.4	2.2	2.2	3.7
Event 9	26.8	34.1	34.3	34.7	16.5	9.7	11.3
I [mm/h]	$\overline{P_O}$	$\overline{P_O P_M > 0}$			$\overline{P_M}$		
Calibration method		rmse	mae	$\rho$	rmse	mae	$\rho$
Event 1	2.3	2.8	1.6	2.8	0.9	0.7	1.2
Event 2	0.8	0.9	0.9	1.0	0.6	0.6	0.9
Event 3	1.1	1.0	0.9	1.0	0.6	0.5	0.6
Event 4	2.2	2.4	2.4	2.5	1.3	1.3	1.6
Event 5	2.2	2.7	2.2	2.7	1.6	1.1	1.6
Event 6	2.6	2.4	2.3	2.7	0.8	0.9	1.4
Event 7	3.4	4.0	4.0	4.0	1.3	1.8	0.7
Event 8	2.1	2.1	2.1	2.1	1.1	1.1	1.8
Event 9	2.5	3.2	3.2	3.2	1.5	0.9	1.1

**Model skills** Comparison of the different model skills shows that there is generally only a small variation among the different calibration methods (Tables A.19 and A.20). The bias estimation shows that the model always underestimates the recorded rainfall amounts mainly because some of the raingauges recorded rainfall at locations where the model did not predict any rainfall. The rather large error in terms of absolute and relative RMSE and MAE indicates that the model is not able to predict rainfall distribution quantitatively. Except for events 1 and 6 the correlation coefficient is larger than 0.5. Interestingly, event 4 shows high correlation coefficients even though the lightning data suggest a strong convective character. Since the model is expected to reproduce the distribution qualitatively rather than quantitatively, the calibration based on the correlation coefficient was used for further analysis.

**Simulated rainfall distribution** For the calibration based on maximization of the correlation coefficient, the contours of the modelled rainfall are shown in Figure 4.45. It shows that the simulated rainfall generally reproduces well the observations on the windward side (Figure 4.45). For example in event 7, which originated from the south, the high rainfall in the southern area is well represented in the model, whereas in event 2 the high observed amounts in the same area cannot be simulated since the wind originated from the west.

Since the majority of the stations are located in the valley, strong advection is required to reproduce the observed rainfall amounts. However, the observed rainfall amounts are not necessarily generated by the process of upslope condensation and subsequent advection, but other rainfall generating mechanisms have an important contribution as well. This explains the underestimation of the rainfall intensity in the model and the dominance of advection in the calibrated model. Even though the calibration cannot reproduce the observed rainfall amounts, it can be assumed that it represents the distribution of rainfall due to the terrain in a qualitative way.

The distribution of the modelled rainfall amounts depends mainly on the wind direction. A clearly distinct pattern can be observed for the events from the south (Events 7 and 9) and the ones with wind directions between southwest and northwest. Furthermore, wind speed and the time constants affect the distribution since they determine the strength of the advection. The moist adiabatic lapse rate affects mainly the rainfall amount as can be seen in the comparison of event 1 and 7 in Figure 4.45.



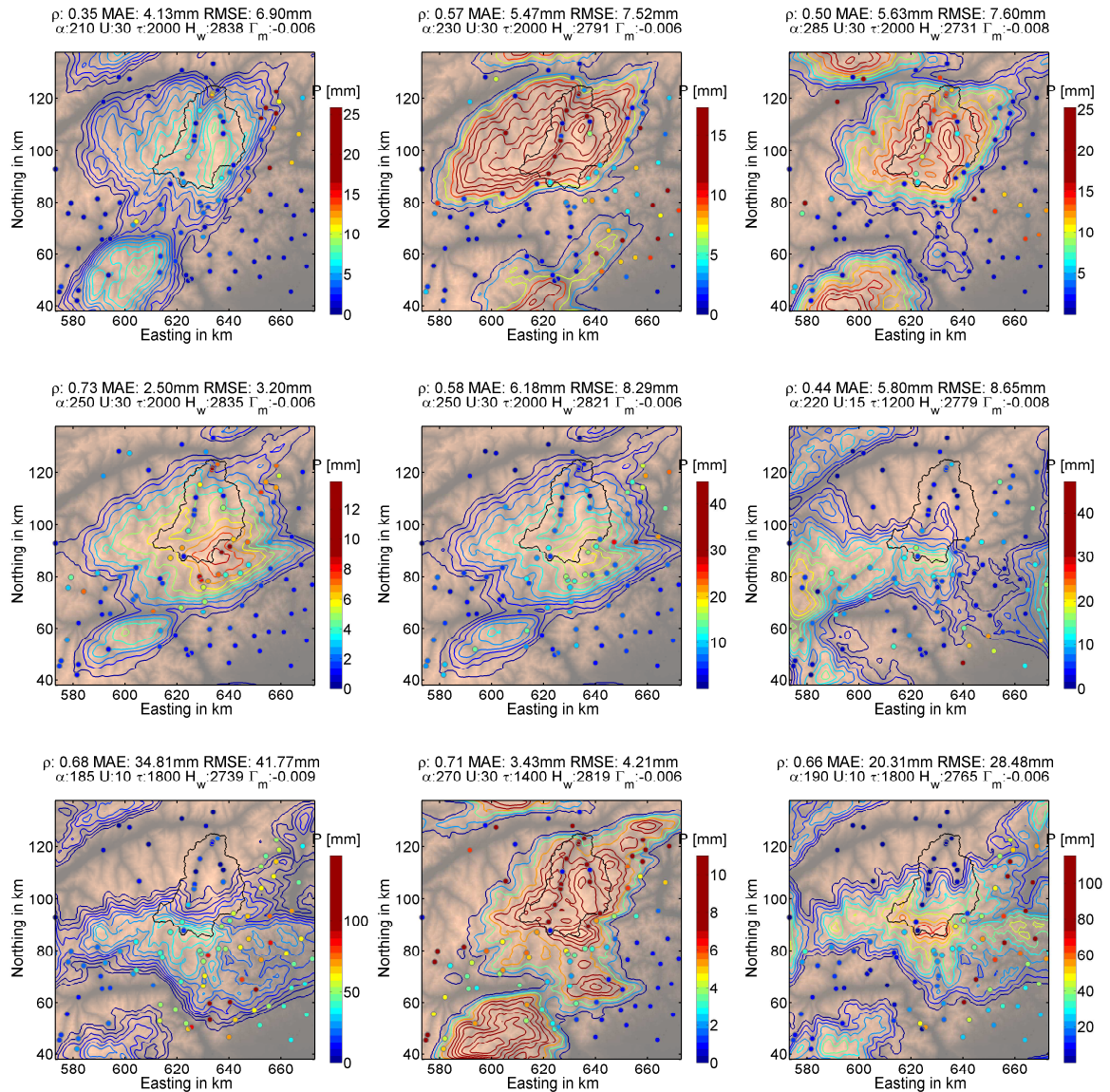


**Figure 4.45:** Contours of the simulated rainfall amount in comparison with the station data used in the calibration of the model for 9 selected events. The model results are based on calibration by maximizing the correlation coefficient.

**Simulated rainfall distribution at the basin scale** The simulated rainfall distribution due to orographic lifting at the watershed scale is shown in Figure 4.46. The model shows strong gradients in terms of cumulative rainfall and also a high variability in those gradients throughout the basin. The wind direction parameter has the strongest influence on the spatial distribution of rainfall. Events with wind from the south (Events 7 and 9) show the strongest gradients along the investigated transects whereas in many other cases the strongest gradients in rainfall occur along the eastern and western slopes. This indicates that the rainfall gradients at the basin scale are likely to be higher than the observed ones since the prevailing wind direction is between west and southwest.

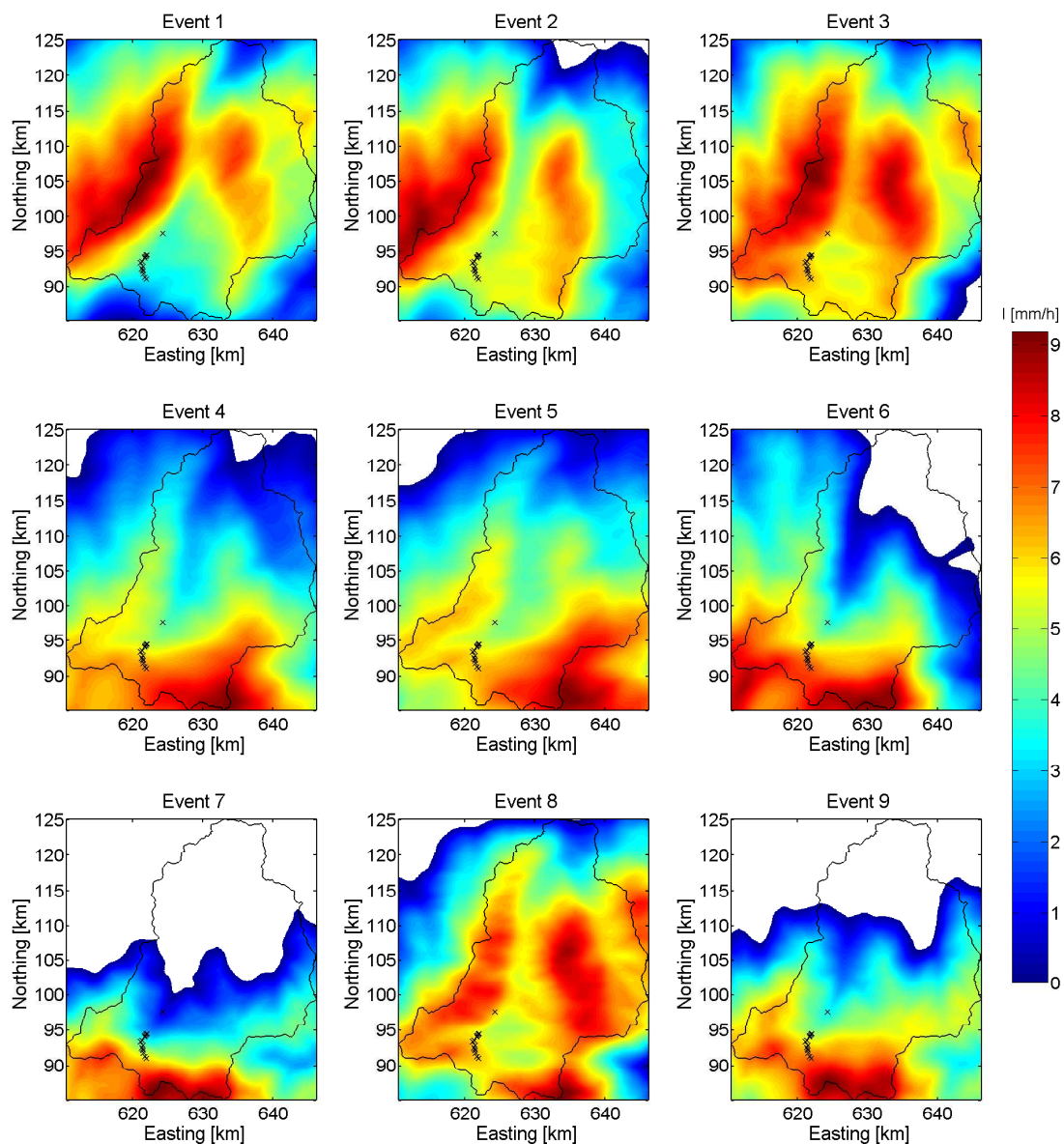


**Figure 4.46:** Comparison of simulated rainfall intensity in basin area for the 9 events.

#### 4.4.5 Comparison of simulated and observed gradients

The gradient along the transect is estimated from the pixels covering the mobile station locations. Figure 4.47 shows the gradients obtained from the calibrated model runs in comparison with the observed ones.

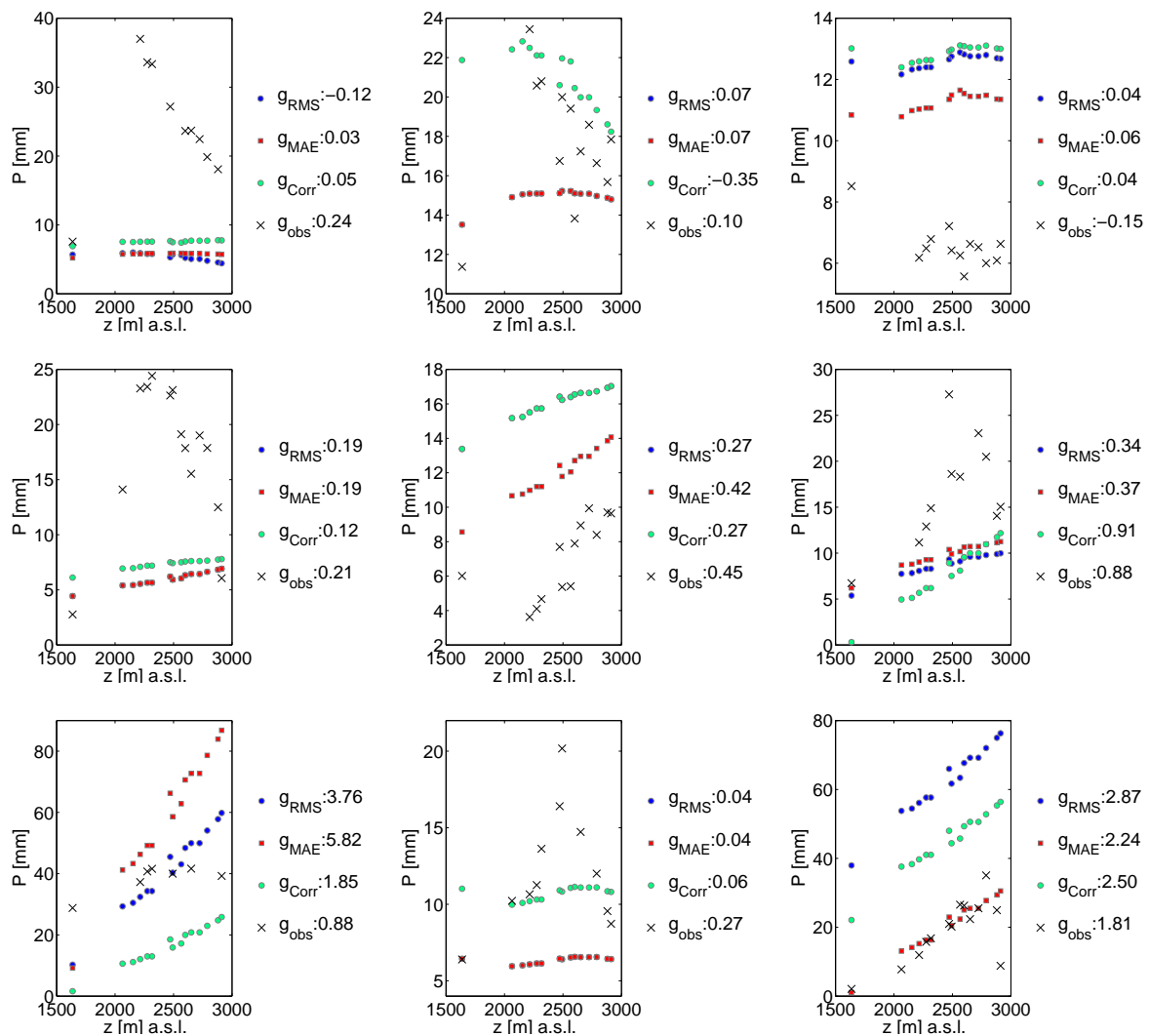


**Figure 4.47:** Comparison of simulated and observed rainfall gradients for the 9 events. The calibration based on the RMSE is shown in blue, the calibration based on the MAE is shown in red and the calibration based on the correlation coefficient is shown in green.

In terms of absolute amounts the simulated and observed rainfall show considerable differences. However, the simulated gradients are often in a similar range as the observed one. There is also a strong variability in the simulated gradient depending on which calibration method is applied. The model is able to reproduce also negative gradients and several simulations show increasing rainfall on the lower transect and a decrease in the upper part (i.e. event 2 and 3

with calibration based on  $\rho$  and Event 3 with MAE and RMSE based calibration). A negative gradient on the entire transect was obtained only for two simulations (Event 1 with RMSE calibration and Event 2 with calibration based on  $\rho$ ).

Events for which the model strongly underpredicts rainfall tend to be associated with lightning activity (Section 4.3.1). This indicates that the model underestimates rainfall if the predominant mechanism is convection rather than terrain forced uplift at this particular location. For most of the other events, simulated rainfall amounts are in the same range or higher than the observed ones. The increase of the simulated rainfall amounts along the transects tends to be more smooth than for the observations. Despite the large differences in the absolute value of the gradient as well as the pattern observed on the upper and the lower transect, the model is able to capture some of the variability observed in the measured gradients. Therefore, it can potentially be used to assess the qualitative distribution of rainfall at the basin scale.

The gradients of simulated rainfall intensity are shown in Figure 4.48. Comparison of the different events shows that at the location of the weather station transects the model produces the strongest gradients in events with wind from south (i.e. event 7 and 9), which corresponds to a storm direction parallel to the transect. In the case of westerly or south-westerly winds, the gradients in rainfall intensity exist as well but they are much weaker. Smith (2003b) mention several cases in which the upslope time delay model is likely to fail. If the atmosphere is unstable, convection is more likely to occur than stratiform rain, and since convection is driven by differential heating of the surface, the resulting distribution of rainfall cannot be captured by the model. Also the model is likely to overestimate rainfall under conditions of high moist static stability, because it assumes unattenuated vertical displacement of the air mass.

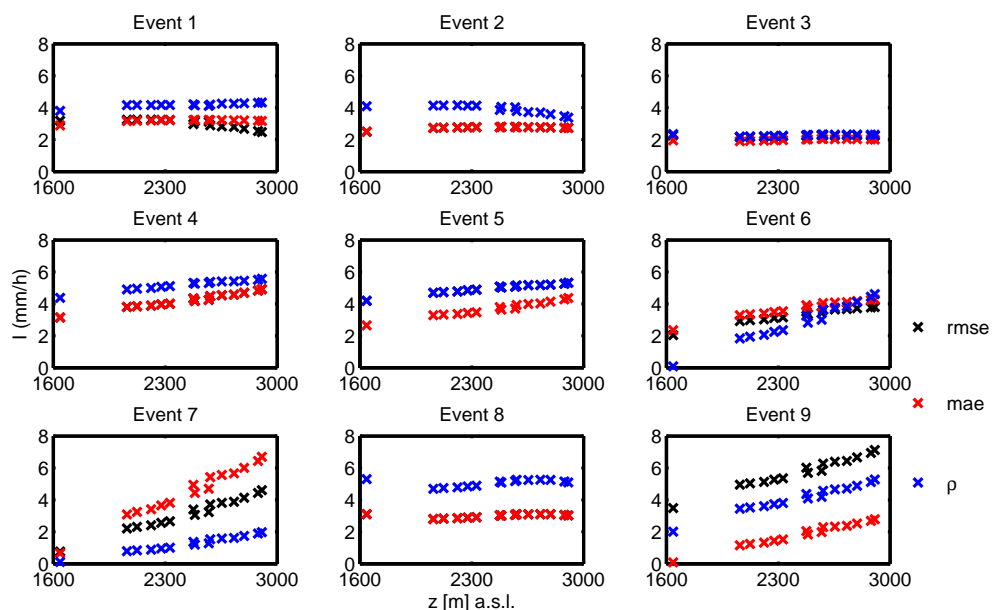


**Figure 4.48:** Comparison of simulated gradient in rainfall intensity along the transects for the 9 events.

However, this assumption is violated if the atmosphere is very stable. Additionally, in areas of strong descent the model will underestimate the effect of evaporation, since the rainfall generated in the upstream area is advected downstream. Since the area of the transects is on the lee side in most observed events, such an overestimation by the model must be expected. Additionally, the indication that many of the observed events have to some extent also convective character explains the deviation from the observed and simulated rainfall distribution. Overall, the model is able to give an indication about the qualitative distribution of rainfall due to orographic lifting and by comparison with observed data the relevance of other rainfall generating mechanisms can be detected. Among the observed events, in particular those with convective character had stronger gradients than simulated by the model. This indicates that in complex terrain also convective rainfall can result in a gradient. Furthermore, the model indicates that due to upslope condensation the strongest gradients can be expected along mountain ranges that are located perpendicular to the prevailing wind direction.

## 4.5 Cluster analysis of gradients

Classification of observed gradient patterns according to similar event characteristics, such as rainfall intensity, depth and duration, can be useful for determining the underlying processes which are relevant for the formation of the gradients. A comparison of the observed gradients and several event characteristics by means of different clustering techniques is presented in this section. The gradient analysis has shown that the gradients are strongly affected by rainfall intensity and duration (Section 4.2), which indicates a strong dependence of the gradient pattern on the rainfall regime. Therefore, the aim of this analysis is to test whether classification of the events according to different rainfall properties corresponds to a specific gradient pattern observed along the hillslope transects. Thereby the event characteristics which are most relevant for the formation of a particular gradient pattern can be identified. Furthermore, the results of the clustering analysis are also compared to the different weather type classifications described in Section 4.3 in order to identify to which extent the event characteristics observed at the local scale are linked to the weather pattern at a larger scale.

At first, the different clustering methods applied in this analysis are presented (Section 4.5.1). The methods applied consist of K-means clustering and agglomerative hierarchical clustering techniques. Next, the data used in the cluster analysis are summarized (Section 4.5.2) and in the last part the results are shown (Section 4.5.3). The resulting clusters are compared to the event characteristics by principal component analysis in order to identify the most important variables in the clustering. Finally, the clusters are compared to the gradients observed along the transects.

### 4.5.1 Clustering methods

Since a cluster analysis strongly depends on which distance measures and linkage criteria are used, the cluster analysis of the observed gradients was approached with different clustering techniques in order to identify a classification that is supported by different methods (Anderberg, 1973).

#### 4.5.1 - i K-means Clustering

In this method, the data are clustered according to the distance between the data points and the cluster centres,  $C_i$ , by minimizing the total within cluster sum of squares:

$$twcss = \sum_{k=1}^{n_k} \sum_{x_j \in C_k} \|x_j - \mu_k\|^2 \quad (4.31)$$

where  $x_j$  denotes the observations,  $n_k$  denotes the number of clusters and  $\mu_k$  denotes the mean of points in cluster  $C_k$ . The cluster number has to be defined a priori. After assigning

all data points to one of the initially defined cluster centres, they are updated and the data are reassigned. This procedure is repeated until none of the data points are reassigned. Since the initial position of the cluster centre is defined randomly, different solutions can be obtained in each run of the program. To circumvent this problem several simulations ( $n=1000$ ) were performed, and the solution that was obtained most frequently was chosen as the final cluster solution.

#### 4.5.1 - ii Agglomerative Hierarchical Clustering

In AHC the number of initial clusters is set equal to the number of data points. Then the clusters are merged successively by grouping the data with the highest similarity. The similarity between each pair of observations is defined in the form of a distance matrix. Furthermore, a criterion has to be defined which defines which elements or clusters of elements are merged in each step. This so called linkage method defines the most similar pair of clusters. By combining different linkage methods and distance measures, the data can be merged into different clusters. The following distance measures between cluster elements  $a$  and  $b$  were used in the definition of the similarity matrix:

- Euclidean distance:

$$d(a, b) = \left( \sum_i (a_i - b_i)^2 \right)^{1/2} \quad (4.32)$$

- Manhattan distance:

$$d(a, b) = \sum_i |a_i - b_i| \quad (4.33)$$

- Minkowski distance:

$$d(a, b) = \left( \sum_i |a_i - b_i|^p \right)^{1/p}, p = 3 \quad (4.34)$$

- Maximum distance:

$$d(a, b) = \max_i |a_i - b_i| \quad (4.35)$$

The Manhattan distance and the Euclidean distance are a special case of the Minkowski distance with  $p=1$  and  $p=2$  respectively. Starting with clusters containing only one entity, the most similar clusters were identified according to the following linkage methods:

- Ward's method: Minimization of the twcss when merging two clusters (Ward, 1963). The sum of squared errors (ss) within cluster  $k$  is defined as follows:

$$ss_k = \sum_{j=1}^{n_e} x_j^2 - \frac{1}{n} \left( \sum_{j=1}^{n_e} x_j \right)^2 \quad (4.36)$$

where  $x_j$  denotes the observations and  $n_e$  denotes the number of elements in the cluster. The twcss is obtained by summing up the ss of all clusters.

$$twcss = \sum_{k=1}^{n_k} ss_k \quad (4.37)$$

- Average linkage: The distance between clusters is defined as the average distance between pairs of observations and those with the smallest distance are merged.

$$\frac{1}{|A||B|} \sum_{a \in A} \sum_{b \in B} d(a, b) \quad (4.38)$$

- Complete linkage: The distance between clusters is defined as the maximum distance between the elements within each cluster and those with the smallest maximum distance are merged in each step of the clustering procedure.

$$\max\{d(a, b) : a \in A, b \in B\} \quad (4.39)$$

where A and B denote separate clusters. Combination of those linkage methods and distance measures results in 12 different hierarchical clustering methods all of which were applied to the following data set. In addition, the data were also clustered according to the K-means clustering method.

## 4.5.2 Summarized event data

For the clustering of the observed gradients, eight variables characterizing the event were chosen, in particular the rainfall intensity, its duration and the cumulative amount. Additionally, the wind speed was included in the cluster analysis. A summary of the event data is shown in Table A.17 and some of the variables are shown in Figure 3.7.

- Mean of cumulative event rainfall observed at each station (P)
- Mean fraction of 1 min timesteps that observed rainfall intensity larger than 1 tip per minute at each station ( $f_I$ )
- Mean of maximum intensity measured within one minute at each station ( $I_{max}$ )
- Mean of event duration as number of wet time steps at each station ( $D_P$ )
- Mean coefficient of variation of rainfall intensity ( $cv$ )
- Mean autocorrelation length of the rainfall time series at each station ( $L_a$ )



- vii. Mean of the mean wind speed at each station ( $U$ )

The gradient data were not used in the clustering process in order to test, whether the resulting clusters have distinct gradient patterns. In this comparison, the gradient of the upper and the lower transect as well as gradient over all stations was used.

### 4.5.3 Results

#### 4.5.3 - i Weather station classification

The data measured at the weather stations were subjected to a cluster analysis in order to identify similarities among the observed events and to test whether such a weather station data classification (WSC) is able to link the observed gradient pattern to distinct event characteristics. Depending on the linkage method and distance measure used in the clustering process, the data are grouped differently. In order to find the optimal grouping of the data, the different cluster solutions were compared. The clustering based on average linkage generally results in few very large groups and the remaining groups consist of only few data points. Since a cluster with only one or two data points is difficult to interpret, the clustering methods which resulted groups with less than 4 events were excluded from the analysis.

The results of the remaining clustering procedures are shown in Table 4.6. Some of the methods resulted in identical clusters, and most of them differ only by the classification of a few events. For further analysis the clustering solution which was obtained most frequently was chosen. The same clustering was obtained for 4 different methods, namely average linkage combined with euclidean distance and manhattan distance, ward linkage in combination with manhattan distance and also complete linkage with euclidean distance.

The last column shows how many of the applied methods assigned a particular event to a different cluster. It can be interpreted as a measure of uncertainty, since a low number indicates that most of the methods assign the data point to the same cluster, whereas a higher number shows that several methods assigned the data point to a different cluster. Comparison of the methods shows quite consistent results. In very few cases more than two methods assigned an event to a different cluster. The classification that was obtained most frequently was then compared to the observed gradients in order to identify the event characteristics which are linked to a certain gradient type.

**Principal component analysis** The resulting clusters were analysed in the space of the principal components of the data set described in Table A.17. Principal component analysis reduces the dimensionality of a data set containing correlated variables by transforming those variables into new ones in such a way that the new artificial variables, called principal components, account for most of the variance in the observed variables. The first principal

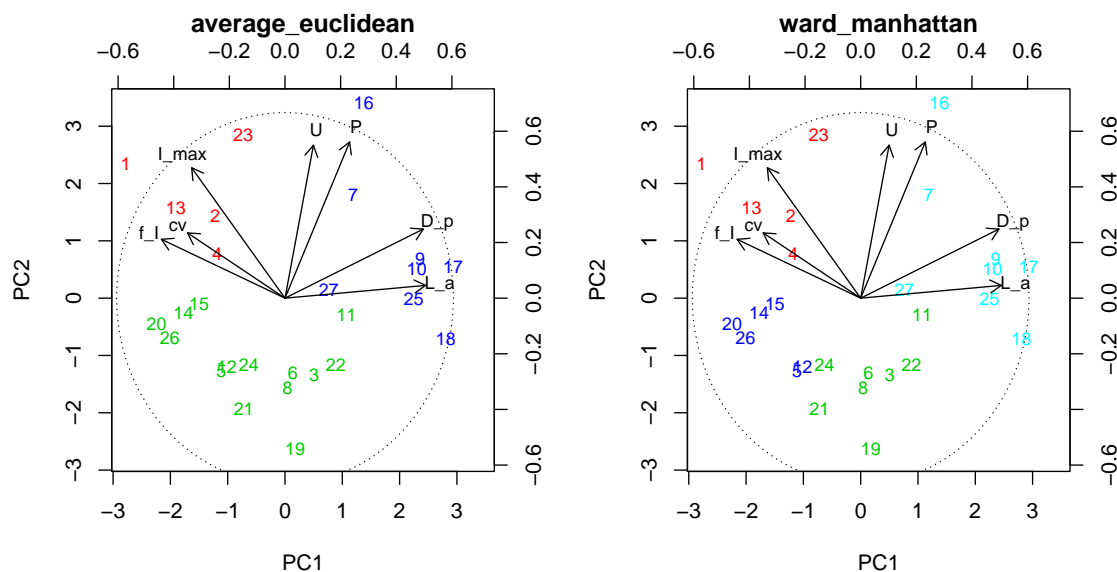
**Table 4.6:** Comparison of cluster analysis with different methods and variability in the cluster assignment by different methods.

Event	ward euclidean	ward maximum / ward minkowski	average euclidean / average manhattan / ward manhattan / complete euclidean	complete manhattan	k-means	Variability
1	1	1	1	1	1	0%
2	1	1	1	1	1	0%
3	2	2	2	2	2	0%
4	1	1	1	1	1	0%
5	3	1	2	2	2	33%
6	3	2	2	2	2	11%
7	1	3	3	1	3	22%
8	3	2	2	2	2	11%
9	2	3	3	3	3	11%
10	2	3	3	3	3	11%
11	2	2	2	2	3	11%
12	3	1	2	2	2	33%
13	1	1	1	1	1	0%
14	3	1	2	2	1	44%
15	3	1	2	2	1	44%
16	1	3	3	1	3	22%
17	2	3	3	3	3	11%
18	2	3	3	3	3	11%
19	3	2	2	2	2	11%
20	3	1	2	2	1	44%
21	3	2	2	2	2	11%
22	2	2	2	2	2	0%
23	1	1	1	1	1	0%
24	3	2	2	2	2	11%
25	2	3	3	3	3	11%
26	3	1	2	2	1	44%
27	2	3	3	3	3	11%

component explains the largest fraction of the total variance in the observed variables.

The results of the event clustering into 3 classes is shown in Figure 4.49(a). The arrows denote the original variables, and the closer they are the higher the correlation between them. High correlations are found between the variables related to rainfall intensity, such as  $f_i$ ,  $cv$  and  $I_{max}$ . Furthermore, the variables describing the event duration are correlated ( $L_a$  and  $D_P$ ) and also the cumulative rainfall and wind speed show some correlation (P and U). The colouring of the data points indicates the WSCs obtained from the analysis described in Section 3.1. The smallest cluster contains only 5 events which are characterized by high rainfall intensities (WSC 1). Another cluster contains events with either long durations or large cumulative rainfall (WSC 3), and the remaining cluster contains events that have short durations and low intensity rainfall (WSC 2).

When the data are clustered into 4 instead of 3 groups the WSC class 2 is splitted into two groups (WSC 2a and WSC 2b) as shown in Figure 4.49(b) when the Ward linkage method is combined with Minkowski or Manhattan distance. Also the K-means clustering procedure results in a very similar result with only event 11 being assigned to WSC 2b instead of WSC 3.



(a) Number of clusters = 3 (WSC 1: red, WSC 2: green, WSC 3: blue) (b) Number of clusters = 4 (WSC 1: red, WSC 2a: blue, WSC 2b: green, WSC 3: turquoise)

**Figure 4.49:** Observations and variables in the coordinate system of the first two principal components. The numbers indicate the events and they are coloured according to the cluster they belong to.

**Comparison of clustering results and gradient** The gradients with  $R^2 > 0.5$  within each of the clusters are shown in Figure 4.50 for 3 and 4 classes respectively. When the data are clustered into three classes the overall gradient,  $g$ , is significant in only one case for cluster 1 (WSC 1), but this cluster is characterized by strong positive gradients on the lower transect and negative ones in the upper part. Comparison with Figure 4.49(a) shows that those gradients are characterized by intense rainfall of short duration.

The second cluster (WSC 2) has generally low gradients on the entire transect and in the lower part. It shows quite strong variability in the gradient of the upper transect,  $g_2$ , with a slightly negative median. The events which belong to this cluster are characterized by short duration and low intensity rainfall. The third cluster (WSC 3) shows strong positive gradients on both the lower and the entire transect. On the upper transect the gradients of cluster 3 are variable but with a higher median than in the other two clusters. In contrast to the other two classes, WSC 3 has also positive gradients on the upper transect. Events which belong to this class are characterized by long durations and large cumulative rainfall. The clustering of the data into 4 classes results in the splitting of the second one into two groups (WSC 2a and WSC 2b). However, they do not show a distinct pattern in the gradients.

The cluster analysis of the weather station data is able to point out distinct gradient patterns along the different transects, and it shows that the main driving factors of gradient

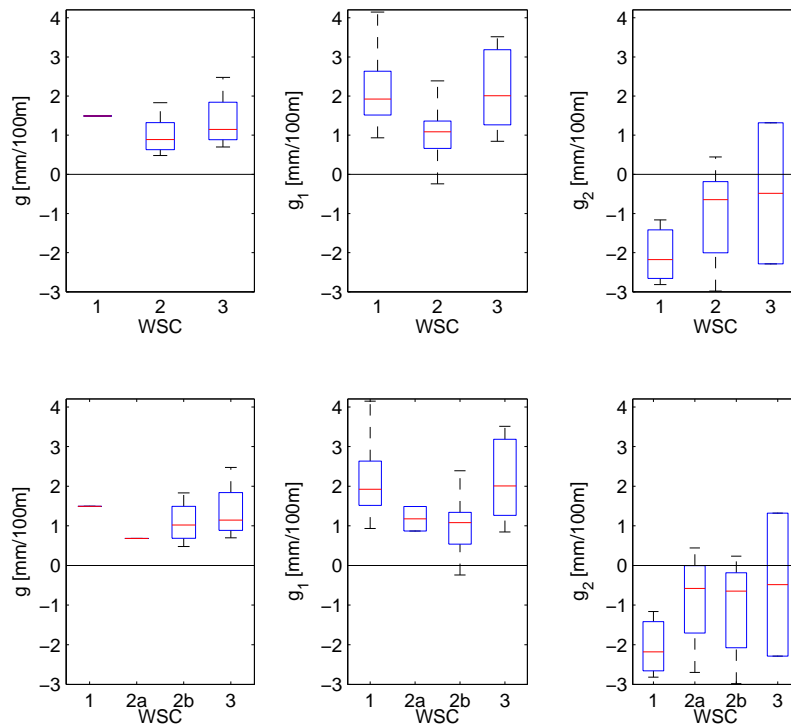


**Figure 4.50:** Gradients with  $R^2 > 0.5$  depending on weather station class (WSC) for 3 and 4 clusters. The red line indicates the location of the median, the blue box denotes the interquartile range and the whiskers have a length of the 1.5 times the interquartile range. The red crosses indicate outliers.

formation are rainfall intensity and duration. This indicates a strong relation to the prevailing weather regime, in particular whether rainfall is of stratiform or convective nature. Therefore, a comparison of this classification of the events with the weather characteristics described in Section 5.1 is performed, in order to relate the observed patterns on the ground to the corresponding atmospheric conditions. This comparison aims at highlighting possible links between similar weather patterns and similarities in the gradient patterns on the ground.



## Chapter 5

# Discussion and conclusions

## 5.1 Discussion

The aim of this work was to challenge simple extrapolation of precipitation with elevation commonly used in practice, by providing experimental evidence that rainfall gradients are event dependent and variable. The discussion is structured with respect to the research questions and working hypotheses stated in Sections 2.1 and 2.2.3 - ii respectively. A particular focus of the discussion is on the different weather type classifications investigated based on different methods and data sets as described in Sections 4.3 and 4.5. They are compared in Section 5.1.5 in order to highlight the similarities and differences in those classifications and in terms of their ability to predict a specific pattern of event rainfall gradients.

### 5.1.1 Effect of elevation on event rainfall variability and cumulative amount

The experimental analysis of rainfall at the hillslope scale showed that gradients in cumulative event rainfall are a very localized phenomenon and that they are highly dependent on the prevailing rainfall regime. Especially the in the upper part, where frequently negative rainfall gradients were observed, there is a strong deviation from the gradient at the seasonal time scale. The magnitude of positive gradients observed within this study was in the order of a few millimetres per 100 m, similar to the ones observed by Loukas and Quick (1993) for rainfall events in a basin in British Columbia. The results of this study also provide evidence that there exists a threshold elevation at about 2600 m, above which rainfall amounts start to decrease with increasing elevation, particularly in the case of convective rainfall events. This finding suggests that in the summer season, when convective processes are predominant, rainfall interpolation based on the assumption of constant rainfall gradients tends to overestimate rainfall amounts at high elevations.

Positive gradients observed in this study were found to be due to either longer rainfall durations or higher intensities at high altitude stations as compared to the lower ones. In most of the events, one of the two factors is predominant. Especially in stratiform rainfall events, formation of the gradients is mainly caused by a difference in rainfall duration between lower and upper stations whereas in events with convective activity the gradients are more often formed due to a difference in terms of rainfall intensity.

The analysis of how rainfall affects the temporal and spatial correlation structure of the events has highlighted the limitations of the rainfall sensors used in this experimental investigation. The inability of the TBRs to resolve low intensity rainfall strongly affects the estimation of the correlation coefficients, and possible effects of altitude cannot be distinguished from the strong artefacts of the rainfall measurement. These results suggest that for future research in this field weighing raingauges should be used preferably.

### **5.1.2 Effects of data post-processing**

In this study, comparison of the gradients obtained from post-processed and original data showed that the corrections result in stronger positive as well as negative gradients. Detailed analysis of the effect of the post-processing of the rainfall data has highlighted the importance of applying those corrections, especially, because some of the errors in the rainfall measurements, such as wind-induced losses and intensity underestimations, can be elevation dependent. Neglecting these effects would therefore result in an underestimation of the gradient in terms of cumulative rainfall amounts.

The estimation of correlation coefficients is strongly affected by the measurement errors and their correction has a strong effect on the results. Even though corrected rainfall data provide a more realistic estimate of the temporal correlation, the applied corrections are not able to fully reconstruct the small scale variability in rainfall intensity in the case of TBRs.

### **5.1.3 Comparison of simulated and observed rainfall distribution**

Rainfall distribution simulated with a steady state model of upslope condensation and downslope advection showed that, despite the simplifying model assumptions, the simulated gradients are of similar magnitude as the observed ones in the case of stratiform rainfall events. This indicates that the simulations can provide qualitative information about the rainfall distribution at the basin scale, which was found to be highly variable and strongly dependent on the prevailing wind direction. This result provides further evidence that the assumption of a constant linear increase of rainfall with elevation is not generally applicable in areas with complex topography.

Furthermore, due to the limited number of observed events, the model was used to assess the

resulting gradient patterns for different wind directions. This analysis highlighted the strong dependence of the rainfall gradients on the prevailing wind direction. This implies that the storm direction can potentially be used as an indicator for selecting an interpolation method that takes into account the specific gradient pattern observed in those conditions.

#### 5.1.4 Influence of terrain scale

The terrain scale resulting in highest correlations between elevation and rainfall amount along the transects was found to be strongly dependent on the method used for the terrain smoothing and on the type of event, and in many cases the strongest correlation was found for the original DEM. This indicates that rainfall at the hillslope scale is affected also by the high resolution terrain features. These results are in contrast to the studies by Sharples et al. (2005) and Hutchinson (1998), who found a better performance of rainfall interpolation at the regional scale when the terrain resolution was lowered.

#### 5.1.5 Influence of meteorological conditions

The cluster analysis of the weather station data on the event timescale (WSC) results in three groups of events, which differ in terms of rainfall intensity, duration and cumulative amount. In this section, the clusters are compared to the predominant atmospheric conditions as described in Section 4.3. The meteorological conditions were analysed based on daily weather type classification (CAP9 and GWTWS), cluster analysis of the low level wind field (LLW classes) and based on the wind direction obtained from ground stations,  $\alpha_S$ , and radar cell tracking,  $\alpha_R$ . In addition, the average and maximum lightning rate,  $R_L$  and  $R_{L,max}$  were used to classify the events according to the predominant rainfall regime. The data are summarized in Table 5.1. The second last column shows the uncertainty of the cluster assignment based on the clustering methods described in Section 4.5.3 - i.

**WSC 1: short duration, high intensity events** The meteorological variables measured at the weather stations show the highest intensities, largest coefficients of variation and rather short durations (Figure 5.1) for this group of events. The gradients tend to be positive in the lower part of the transect and negative in the upper part. The weather type of these events is characterized by strong winds from the southwest and there is a good agreement between the weather type classifications, the low level wind field and the wind direction observed on the ground and in the atmosphere. The LLW classification is available only for two events in this group and shows for both events a wind field with strong winds from the southwest, which is associated with high intensity rainfall. Most of the events are also characterized by strong lightning activity, which indicates strong convective character.



**WSC 2: short duration, low intensity events** This group of events was assigned frequently to other clusters, depending on the clustering method applied, as can be seen from the second to last column in Table 5.1. This indicates high uncertainty in assigning those events to a specific group. The rainfall pattern observed at the weather stations is characterized by low intensities and short durations, which results in mostly weak positive gradients. When the data are clustered into 4 groups, the most frequent cluster solution results in a splitting of those events into two groups (WSC 2a and WSC 2b).

The two subclasses WSC 2a and WSC 2b show some differences in terms of gradients and prevailing meteorological conditions, however, they are less distinct than WSC 1 and 3. WSC 2a is characterized by shorter durations and slightly higher intensities as compared to WSC 2b and it shows therefore gradient patterns more similar to WSC 1. In the LLW field low wind speeds with direction from the southwest are predominant. WSC 2b contains longer events, which show more often significant gradients on the entire transect as compared to WSC 2a. Lightning data show a clear difference, i.e. WSC 2a is associated with convective activity and WSC 2b is of more stratiform character.

**WSC 3: long duration, large cumulative precipitation** The events belonging to this cluster generally have a long durations, large cumulative rainfall amounts and are characterized by strong positive gradients along both transects. In addition, they are not associated with strong lightning activity, which indicates a more stratiform rainfall regime. All wind direction estimates show most frequently winds from the west and the southwest. All the events with southerly wind on the ground or in the atmosphere belong to this group of events.

**Comparison of weather type classifications and observed rainfall gradients** Different meteorological data sets were investigated with respect to their ability to distinguish among different patterns in the observed rainfall gradients that resulted from the cluster analysis of the rainfall data observed at the weather stations. The cluster analysis of the rainfall data observed by the weather stations is successful in characterizing different gradient patterns along the hillslope. Rainfall duration and intensity were identified as main factors in the classification of the events.

The classification of the low level wind field successfully distinguishes between high intensity events of WSC 1, which are assigned to a wind field characterized by strong winds from the southwest (LLW 8), and short duration events of WSC 2a, which are assigned to a similar wind field but with lower wind speeds. These results indicate that for the observed events differences in wind speed rather than wind direction are responsible for different gradient patterns. Generally, large cumulative event precipitation is linked to weather situations with high wind speeds, such as WSC 1 and 3. Previous studies have observed similar patterns, however mostly for the windward side (e.g. Johansson and Chen, 2003), whereas in this study the transects are located on the leeside with respect to the prevailing wind direction in most of

the events.

Due to the small number of events and the high frequency of westerly flow conditions, association of different types of events to a particular daily weather type is highly uncertain. For the same reason, the analysis of the radar based wind direction provides inconclusive results on whether different event directions result in a distinct gradient pattern. The radar data show almost exclusively wind from the southwest, the west and the south. The latter are exclusively assigned to WSC 3, which gives some indication that different gradient patterns are connected to distinct meteorological conditions. Comparison with the wind direction observed on the ground shows considerable differences, which can be explained by local modification of the wind field by the local topography.

Comparison of the WSC classification with observations of lightning strikes supports the clustering of the observed gradient patterns. The short duration events are strongly associated with lightning activity whereas the longer ones tend to be more of stratiform nature.

**Table 5.1:** Comparison of wind direction obtained from radar images at different intensity thresholds ( $I_1$ ,  $I_2$ ,  $I_3$ ), wind direction measured on the ground, low level wind (LLW) classification and weather type (WT) and average and maximum lightning rate,  $R_L$  and ( $R_{L,max}$ ), within a distance of 30 km.

	LLW	CAP9	GWTWS	$\alpha_R$	$\alpha_S$	Gradients ( $R^2 > 0.5$ )			$\sigma^2_{WSC}$	$R_L > 10$
E	10 classes	9 classes	11 classes	8 classes		g	g1	g2	(k=3)	( $R_{L,m} > 120$ )
			WSC 1: high intensity events							
1	-	W-SW, f. P	flat	SW	SW	-	4.15	-2.18	0%	+ (-)
2	-	NE	SW	SW	NE	-	0.93	-	0%	- (-)
4	-	W	W	SW	SW	-	2.13	-2.82	0%	+ (-)
13	8 SW,IP <sub>b</sub>	W-SW, f. P	SW	SW	SW	-	1.71	-1.16	0%	+ (+)
23	8 SW,IP <sub>b</sub>	W-SW, f. P	SW	SW	SW	1.49	1.92	-	0%	+ (+)
			WSC 2a: low intensity short duration events							
5	-	NE	SW	SW	NE	-	-	0.44	33%	- (-)
12	7 SW,P	NE	high P	W	N	0.68	-	-	33%	+ (+)
14	7 SW,P	W	SW	SW	SW	-	0.87	-0.45	44%	+ (+)
15	7 SW,P	NE	SW	SW	SW	-	1.49	-2.70	44%	+ (+)
20	7 SW,P	W	SW	W	SW	-	-	-0.71	44%	+ (+)
26	7 SW,P	W-SW, f. P	SW	SW	SW	-	-	-	44%	+ (+)
			WSC 2b: low intensity short duration events							
3	-	NE	W	W	NE	-	-0.24	-	0%	- (-)
6	-	NE	high P	SW	SW	-	1.31	-2.98	11%	- (-)
8	-	W-SW	W	W	NE	-	1.36	-1.77	11%	- (-)
11	4 N,P	W	W	SW	SW	1.83	2.39	-	11%	- (-)
19	3 NE	NE	flat	N	N	0.89	0.85	-	11%	- (-)
21	3 NE	NE	high P	-	N	-	0.41	-0.65	11%	- (-)
22	7 SW, P	W-SW	SW	W	SW	1.15	1.32	0.23	0%	- (-)
24	5 S	NE	flat	W	SW	0.48	0.66	-0.32	11%	+ (-)
			WSC 3: low intensity long duration events							
7	-	NE	high P	S	S	0.88	1.51	-	22%	-
9	-	W-SW, f. P	SW	S	SW	-	2.51	-	11%	- (-)
10	7 SW,P	W-SW, f. P	SW	W	SW	2.48	3.38	-	11%	- (-)
16	8 SW,IP <sub>b</sub>	W-SW, f. P	SW	W	SW	1.54	2.99	-	22%	+ (+)
17	7 SW,P	W-SW, f. P	flat	W	SW	1.94	3.51	-2.29	11%	- (-)
18	4 N,P	W-SW	S	W	N	0.70	0.84	-	11%	- (-)
25	7 SW,P	W-SW, f. P	flat	S	SW	1.15	1.07	1.32	11%	- (-)
27	3 NE	W-SW, f. P	SW	SW	S	0.91	1.46	-	11%	- (-)

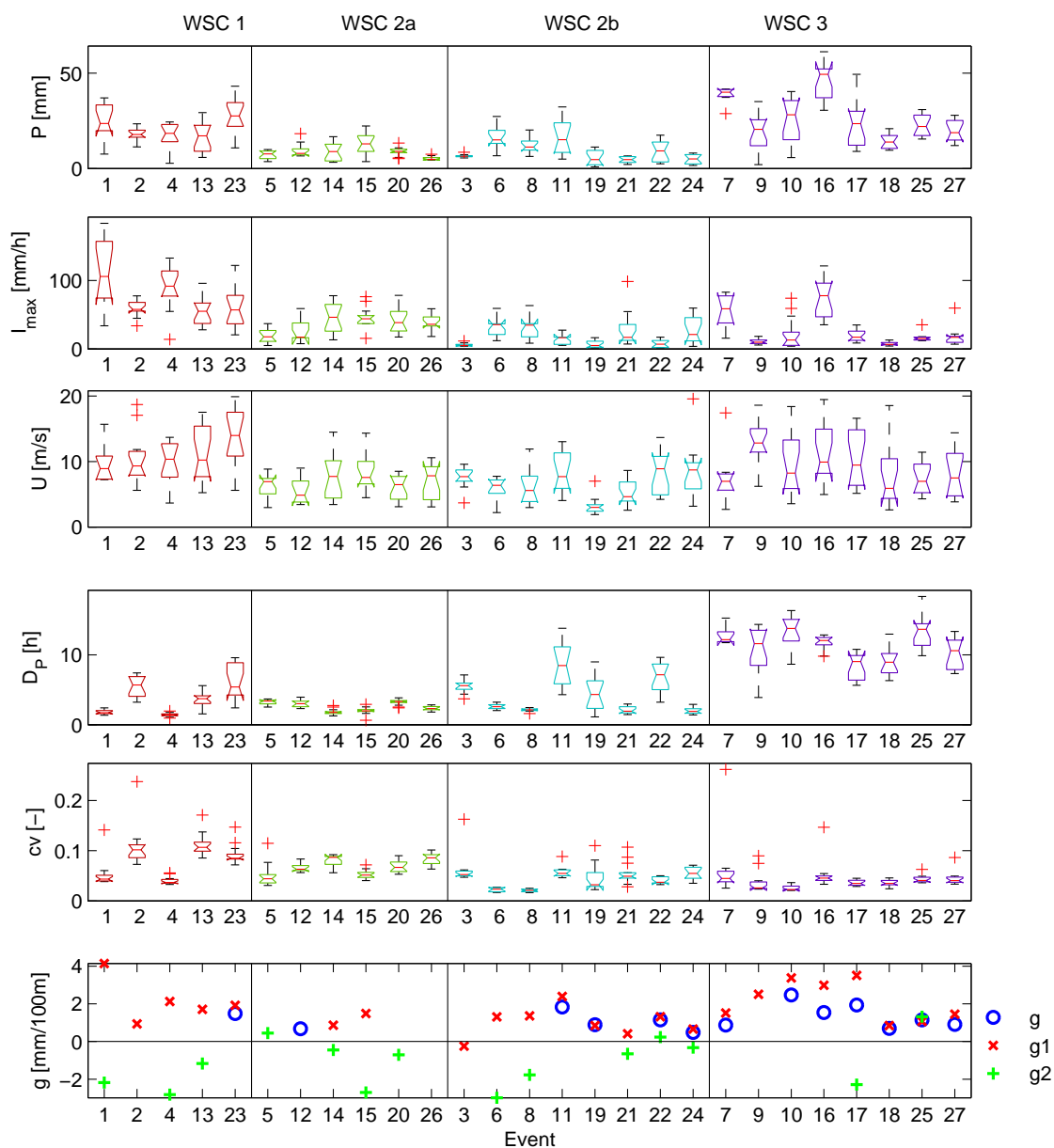


**Figure 5.1:** Boxplot of event data within each WSC. The red line indicates the location of the median, the box denotes the interquartile range and the whiskers have a length of the 1.5 times the interquartile range.

## 5.2 Conclusions

The experimental investigation of rainfall gradients in this study provides a unique data set of event rainfall at the hillslope scale over a horizontal distance of around 7 km and over an elevation range of 1600 - 2900 m a.s.l.. The analysis highlights the variability in the spatial rainfall distribution at the event time scale, where positive, negative or no significant gradients of rainfall with altitude were observed. Comparison of the gradient patterns on the ground with observations of the corresponding atmospheric conditions and simulations of the theoretically expected distribution of rainfall due to upslope condensation and downslope advection shows that the spatial distribution on the ground is primarily controlled by the wind direction and the prevailing rainfall regime, i.e. convective or stratiform precipitation systems. The assumption of a linear increase in rainfall with altitude is generally in good agreement with the observations for stratiform events, but it is frequently violated in the case of events with convective character.

**Post-processing and correlation analysis** Comparison of rainfall data measured by different instruments and investigation of the effects of the data post-processing on different statistical analyses shows the importance of careful analysis of measurement errors and their consideration in the interpretation of the results. The analysis of temporal and spatial correlation of rainfall intensity demonstrates how inadequate resolution of low intensity rainfall can affect the results. Post-processing was successful in reproducing the cumulative precipitation amount and to a certain extent the temporal rainfall structure, but it is not able to reconstruct the spatial correlation structure.

The problem of recording low intensity rainfall with TBRs is demonstrated and the importance of correcting those data is shown by comparison between WR and TBR with respect to the autocorrelation length,  $L_a$ , of the rainfall time series. It decreases very rapidly for the unprocessed TBR data, i.e. 1-2 min, but is in a similar range for both types of gauges, 30-45 min, when the data are corrected for the different errors. Furthermore, in contrast to the uncorrected data set, the post-processed data show the expected difference in the autocorrelation length among different events, depending on whether the rainfall regime is more stratiform ( $L_a=1-4$  h) or convective ( $L_a=15-30$  min).

Analysis of the decrease in spatial correlation with increasing station distance results in a correlation distance of around 5 km and a shape parameter of 1.1, i.e. a slightly slower decrease as compared to the exponential decrease. The parameters were found to be distinct for high intensity rainfall events with convective character as compared to stratiform situations. However, the decrease in spatial correlation is stronger for stratiform rainfall, which contradicts the findings of Krajewski et al. (2003). This behaviour can be explained by the inability of TBR to resolve low intensity rainfall, and the post-processing technique, which simply aver-

ages the rainfall intensity and does not account for the higher variability in rainfall intensity in convective events. This finding shows the limited ability of this post-processing method to reconstruct the spatial structure of the rainfall.

Analysis of the oscillation coefficients at different aggregation levels shows a slight increase in the fluctuations in intensity at higher elevations. However, the correlation with altitude is rather small (0.1 - 0.35 %/100m) and is observed only for some of the events at aggregation intervals of 60-90 min.

The rainfall gradients in absolute terms were found to be around 20% higher for post-processed data. Since at high altitude stations both rainfall intensity and wind speed tend to be higher, correction of the related measurement errors affects those stations more, which results in stronger gradients. Therefore, post-processing affects in particular events in which gradients are formed primarily due to differences in rainfall intensities.

**Gradients** The results of the field investigation of cumulative rainfall along hillslope transects highlight the importance of rainfall measurements at high temporal and spatial resolutions for accurate assessment of the rainfall distribution. The gradients at the event time scale are highly variable not only in terms of magnitude but also in terms of qualitative rainfall patterns. While the cumulative rainfall measured during the entire IOP shows a clear positive gradient (12 mm/100m during 4 months), the pattern at the event time scale can be very different. Out of the 27 events observed during two summer seasons, gradients with an  $R^2 > 0.5$  are observed for 13, 23 and 15 events along the different transects T0, T1 and T2 respectively. Event gradients are in a range of -3 to 4 mm/100m with negative gradients occurring more frequently in the upper part of the transect, which indicates a strong shading effect of the local topography, whereas in the lower part and along the entire transect positive gradients occur more often.

The analysis of the gradient formation at the sub-event time scale shows that in many cases only a small fraction of the event duration is relevant for the gradient formation and that the gradient can be highly variable at low aggregation intervals. This also suggests that the gradients at the event time scale may be highly sensitive to the criteria used for event separation.

Analysis of the effect of the spatial scale on the gradient estimation shows a strong influence of different DEM filtering techniques on the correlation between altitude and cumulative event precipitation and on the magnitude of the gradient itself. For some events, highest correlation was found when terrain features below 3 km were removed from the DEM, which indicates that terrain features at very small spatial scales do not have a strong influence on precipitation generating mechanisms. However, this effect is observed only for some of the events along the entire transect and therefore this finding cannot be generalized.

**Weather type control on gradients** The analysis of the wind directions observed at each station separately shows the strong influence of the local topography, which can substantially alter the general flow direction. A classification of the prevailing wind field patterns on the ground is capable of distinguishing patterns associated with local winds with a strong diurnal cycle and patterns with a less distinct daily cycle, which are more likely linked to large scale winds. The latter can be differentiated into 5 classes which are to some extent linked to other weather characteristics, such as rainfall intensity and cumulative amount.

The dominant south-westerly flow conditions can be detected in both the wind patterns on the ground as well as in the atmospheric wind direction estimated from rain cell tracking in radar images and also in the analysis of daily weather type data. However, there are several events with a strong ground-flow component from the north, which was detected neither in the radar images nor in the weather type classification. This indicates the importance of the local topographic structures in the modification of the general weather conditions. Overall, the analysis of wind direction and weather characteristics shows that in this area events originating from the southwest are predominantly linked to precipitation occurrence and the cluster analysis of the low level wind field shows patterns that are related to distinct rainfall characteristics such as intensity and cumulative amount.

The results obtained by modelling orographic precipitation distribution due to upslope condensation and advection under steady state atmospheric conditions suggest that the magnitude of the gradient shows strong variation across the basin. Strongest gradients were identified at mountain ridges perpendicular to the general wind direction, which in the case of the studied area corresponds to flow from the south. But also comparison of leeward with windward slopes shows considerable differences in the distribution of precipitation. Additionally, this model shows that topographic features can lead to local shading or enhancement of precipitation, which can result in a deviation from the assumption of a constant gradient. Even though the model is based on a strong simplification of the meteorological processes involved and is therefore not able to quantitatively predict the observed gradient patterns, it illustrates the variability of the orographic effects that can be expected at the basin scale. Furthermore, it provides a general idea about the range of gradients that can be expected under different meteorological conditions, in particular storms with wind directions different from the observed ones.

The clustering procedure of event characteristics, such as rainfall duration, intensity and cumulative rainfall amount, is successful in distinguishing three classes of storms according to their driving meteorological processes. Comparison with the observed gradients shows that each of those groups also has distinct gradient patterns. One group is characterized by strong positive gradients on the entire transect caused mainly by long durations, and another group is characterized by strong positive gradients in the lower part of the hillslope and negative ones in the upper part. Those events are related to intense rainfall of short duration, where mainly the differences in intensity are responsible for the observed gradients. The last group exhibits

low gradients, which is common for events with short durations and low variability in intensity among the different stations. Comparison with lightning observations shows that these classes differ in terms of the presence and strength of convective processes. This indicates that differences in the observed gradient patterns are mainly driven by differences in the rainfall regime. The fact that high intensity rainfall events and short duration storms exhibit highly variable and localized gradient patterns indicates that the assumption of a linear increase is frequently violated under those circumstances. Only for long lasting storms, the assumption of a constant gradient is in agreement with the observations.

**Implications for practical applications and future research** This work shows that the high variability in the local gradient patterns is strongly connected to the rainfall regime, which was classified based on lightning data and rainfall observations on the ground. Furthermore, the model simulations show a strong difference in the rainfall distribution at the basin scale depending on the prevailing wind direction. These findings imply that those factors have a crucial influence on the resulting rainfall distribution. Therefore, they have the potential to be used as indicators for selecting a particular interpolation method for spatial rainfall interpolation, which takes into account the peculiarities in the observed rainfall gradient patterns depending on the meteorological conditions.

The high variability in both the observed and simulated event rainfall distribution at the hillslope scale also highlights the need for more detailed measurements at high spatial and temporal resolution. Detailed analysis of the post-processing of the measured rainfall data showed its importance in the assessment of both rainfall amount and temporal autocorrelation structure. However, those corrections were not able to reproduce the spatial correlation structure in the rainfall time series. This illustrates the limitations of the tipping bucket gauges in comparison with weighing raingauges and shows the importance of using a multisensor approach in rainfall measurements in order to detect such shortcomings.

Overall, this experimental investigation highlights that the assumption of a constant gradient in cumulative event rainfall with elevation is not generally valid in areas of complex topography due to local shading and enhancement effects, especially for events with a convective rainfall regime. For those events, a threshold elevation was observed above which rainfall tends to decrease with elevation. Further research is needed in order to test whether this threshold is constant across the entire basin or whether it is location dependent.



### 5.2.1 Summary of conclusions

- Experimental investigation of the effect of altitude on the spatial distribution of cumulative event rainfall by deployment of weather stations provides a unique data set of the small scale rainfall variability for 27 rainfall events in an area with complex orography. It provides experimental evidence of how rainfall gradients are formed and how they are controlled by differences in rainfall intensity and duration among the different weather stations.
- Estimation of rainfall gradients based on linear regression with altitude shows that the assumption of a constant gradient is not valid in general but depends on several event characteristics, in particular on the rainfall regime. Among the events that show a rainfall gradient, stratiform events are more often associated with positive gradients, while storms with a strong convective character frequently show strong variability in the gradients, which can also be negative.
- Cluster analysis of the events based on the ground observations of rainfall (WSC) is successful in highlighting events with similar gradient patterns. It also provides evidence that depending on the rainfall regime either a difference in rainfall intensity or duration is the predominant mechanism in gradient formation.
- Weather type analysis shows that rainfall occurrence is strongly associated with westerly and south-westerly flow situations. Comparison of wind direction estimates based on different methods and data sets illustrates the strong influence of topography on the local wind field.
  - Comparison of the wind field observed on the ground (LLW) and in the atmosphere highlights the strong modification of the wind patterns due to the local terrain. The wind direction estimated from weather radar observations and weather type classifications shows that events originate primarily from the southwest, but they are not able to distinguish among different types of events. On the other hand, the LLW classification shows a distinct wind field for short intense rainfall events, which are characterized by stronger wind speeds.
  - Lightning data were analysed for their ability to distinguish between convective and stratiform events and the results are in good agreement with the event classification based on ground data (WSC).
- Application of the linear steady state model of orographic precipitation due to upslope condensation and downslope advection illustrates the complexity in the rainfall pattern that can be expected at the basin scale and its strong dependence on the wind direction. It shows that at the field site, maximum gradients can be expected for southerly flow

conditions whereas for the more frequent westerly and south-westerly winds maximum gradients occur at different locations in the basin.

- A detailed analysis of the errors in raingauge measurements and their correction shows that the error increases with altitude due to higher wind speeds and rainfall intensities. Therefore, uncorrected data tend to underestimate the gradients. Furthermore, the analysis of the autocorrelation length in the rainfall time series at the event time scale shows that only the corrected data provide a realistic estimate of the temporal correlation structure. These findings emphasize the limitations of tipping bucket raingauges in resolving the small scale rainfall structure and the importance of applying an appropriate correction.



# Bibliography

- Anderberg, M. R. (1973). *Cluster analysis for applications*. Probability and mathematical statistics, 19. Academic Press, New York,.
- Arnaud, P., Bouvier, C., Cisneros, L., and Dominguez, R. (2002). Influence of rainfall spatial variability on flood prediction. *Journal of Hydrology*, 260(1-4):216–230.
- Bardossy, A. and Filiz, F. (2005). Identification of flood producing atmospheric circulation patterns. *Journal of Hydrology*, 313(1-2):48–57.
- Barry, R. G. (2008). *Mountain Weather and Climate*. Cambridge University Press.
- Barstad, I. and Smith, R. B. (2005). Evaluation of an orographic precipitation model. *Journal of Hydrometeorology*, 6(1):85–99.
- Basist, A., Bell, G. D., and Meentemeyer, V. (1994). Statistical relationships between topography and precipitation patterns. *Journal of Climate*, 7(9):1305–1315.
- Beck, C. (2000). *Variability of circulation dynamics in the area of Northatlantic-Europe since 1780 (in german)*. Geographische Gesellschaft Würzburg.
- Beck, C., Jacobeit, J., and Jones, P. D. (2007). Frequency and within-type variations of large-scale circulation types and their effects on low-frequency climate variability in central europe since 1780. *International Journal of Climatology*, 27(4):473–491.
- Blumer, F. (1994). *Die Höhenabhängigkeit des Niederschlags im Alpenraum*. PhD thesis, ETH Zürich.
- Boni, G., Parodi, A., and Siccardi, F. (2008). A new parsimonious methodology of mapping the spatial variability of annual maximum rainfall in mountainous environments. *Journal of Hydrometeorology*, 9(3):492–506.
- Briggs, P. R. and Cogley, J. G. (1996). Topographic bias in mesoscale precipitation networks. *Journal of Climate*, 9(1):205–218.

- Bronstert, A. and Bardossy, A. (2003). Uncertainty of runoff modelling at the hillslope scale due to temporal variations of rainfall intensity. *Physics and Chemistry of the Earth*, 28(6-7):283–288.
- Carsteanu, A. and Foufoula-Georgiou, E. (1996). Assessing dependence among weights in a multiplicative cascade model of temporal rainfall. *Journal of Geophysical Research-Atmospheres*, 101(D21):26363–26370.
- Ciach, G. J. (2003). Local random errors in tipping-bucket rain gauge measurements. *Journal of Atmospheric and Oceanic Technology*, 20(5):752–759.
- Ciach, G. J. and Krajewski, W. F. (1999a). On the estimation of radar rainfall error variance. *Advances in Water Resources*, 22(6):585–595.
- Ciach, G. J. and Krajewski, W. F. (1999b). Radar-rain gauge comparisons under observational uncertainties. *Journal of Applied Meteorology*, 38(10):1519–1525.
- Clark, M. P. and Slater, A. G. (2006). Probabilistic quantitative precipitation estimation in complex terrain. *Journal of Hydrometeorology*, 7(1):3–22.
- Colle, B. A., Mass, C. F., and Westrick, K. J. (2000). Mm5 precipitation verification over the pacific northwest during the 1997-99 cool seasons. *Weather and Forecasting*, 15(6):730–744.
- Cosma, S., Richard, E., and Miniscloux, F. (2002). The role of small-scale orographic features in the spatial distribution of precipitation. *Quarterly Journal of the Royal Meteorological Society*, 128(579):75–92.
- Daly, C., Neilson, R. P., and Phillips, D. L. (1994). A statistical topographic model for mapping climatological precipitation over mountainous terrain. *Journal of Applied Meteorology*, 33(2):140–158.
- Daly, C., Smith, J. W., Smith, J. I., and McKane, R. B. (2007). High-resolution spatial modeling of daily weather elements for a catchment in the oregon cascade mountains, united states. *Journal of Applied Meteorology and Climatology*, 46(10):1565–1586.
- Dinku, T., Anagnostou, E. N., and Borga, M. (2002). Improving radar-based estimation of rainfall over complex terrain. *Journal of Applied Meteorology*, 41(12):1163–1178.
- Dinku, T., Chidzambwa, S., Ceccato, P., Connor, S. J., and Ropelewski, C. F. (2008). Validation of high-resolution satellite rainfall products over complex terrain. *International Journal of Remote Sensing*, 29(14):4097–4110.
- D’Odorico, P., Fagherazzi, S., and Rigon, R. (2005). Potential for landsliding: Dependence on hyetograph characteristics. *Journal of Geophysical Research-Earth Surface*, 110(F1).

- Duchon, C. E. and Essenberg, G. R. (2001). Comparative rainfall observations from pit and aboveground rain gauges with and without wind shields. *Water Resources Research*, 37(12):3253–3263.
- Fankhauser, R. (1998). Influence of systematic errors from tipping bucket rain gauges on recorded rainfall data. *Water Science and Technology*, 37(11):121–129.
- Fekete, B. M., Vorosmarty, C. J., Roads, J. O., and Willmott, C. J. (2004). Uncertainties in precipitation and their impacts on runoff estimates. *Journal of Climate*, 17(2):294–304.
- Fiener, P. and Auerswald, K. (2009). Spatial variability of rainfall on a sub-kilometre scale. *Earth Surface Processes and Landforms*, 34(6):848–859.
- Finger, D., Pellicciotti, F., Konz, M., Rimkus, S., and Burlando, P. (2011). The value of glacier mass balance, satellite snow cover images, and hourly discharge for improving the performance of a physically based distributed hydrological model. *Water Resources Research*, 47.
- Fiser, O. and Wilfert, O. (2009). Novel processing of tipping-bucket rain gauge records. *Atmospheric Research*, 92(3):283–288.
- Germann, U., Galli, G., Boscacci, M., and Bolliger, M. (2006). Radar precipitation measurement in a mountainous region. *Quarterly Journal of the Royal Meteorological Society*, 132(618):1669–1692.
- Glazirin, G. E. (1997). Precipitation distribution with altitude. *Theoretical and Applied Climatology*, 58(3-4):141–145.
- Guzzetti, F., Peruccacci, S., Rossi, M., and Stark, C. P. (2008). The rainfall intensity-duration control of shallow landslides and debris flows: an update. *Landslides*, 5(1):3–17.
- Habib, E., Krajewski, W. F., and Kruger, A. (2001). Sampling errors of tipping-bucket rain gauge measurements. *Journal of Hydrologic Engineering*, 6(2):159–166.
- Habib, E., Krajewski, W. F., Nesper, V., and Kruger, A. (1999). Numerical simulation studies of rain gage data correction due to wind effect. *Journal of Geophysical Research-Atmospheres*, 104(D16):19723–19733.
- Habib, E. H., Meselhe, E. A., and Aduvala, A. V. (2008). Effect of local errors of tipping-bucket rain gauges on rainfall-runoff simulations. *Journal of Hydrologic Engineering*, 13(6):488–496.
- Harris, D., Menabde, M., Seed, A., and Austin, G. (1996). Multifractal characterization of rain fields with a strong orographic influence. *Journal of Geophysical Research-Atmospheres*, 101(D21):26405–26414.

- Havlik, D. (1969). Altitude levels of maximum cumulative precipitation in the western alps (in german). *Freiburger Geographische Hefte*, 7.
- Hegg, C., Schmid, F., and Frick, E. (2002). Floods 2002, event analysis and case studies - reports of the (fowg) (in german). Technical Report Nr. 2, Federal Office for Water and Geology (FOWG).
- Hess, P. and Brezowsky, H. (1977). Catalogue of gross weather types in europe (1881 - 1976) (in german). Technical Report 113, Reports of the German weather service, Offebach a. M.
- Hevesi, J. A., Flint, A. L., and Istok, J. D. (1992). Precipitation estimation in mountainous terrain using multivariate geostatistics .2. isohyetal maps. *Journal of Applied Meteorology*, 31(7):677–688.
- Hill, F. F. (1983). The use of average annual rainfall to derive estimates of orographic enhancement of frontal rain over england and wales for different wind directions. *Journal of Climatology*, 3(2):113–129.
- Hutchinson, M. F. (1995). Interpolating mean rainfall using thin-plate smoothing splines. *International Journal of Geographical Information Systems*, 9(4):385–403.
- Hutchinson, M. F. (1998). Interpolation of rainfall data with thin-plate smoothing splines ii: Analysis of topographic dependence. *Journal of Geographic Information and Decision Analysis*, 2(2):152 –167.
- Ingelrest, F., Barrenetxea, G., Schaefer, G., Vetterli, M., Couach, O., and Parlange, M. (2010). Sensorscope: Application-specific sensor network for environmental monitoring. *Acm Transactions on Sensor Networks*, 6(2).
- Jiang, Q. F. and Smith, R. B. (2003). Cloud timescales and orographic precipitation. *Journal of the Atmospheric Sciences*, 60(13):1543–1559.
- Johansson, B. and Chen, D. L. (2003). The influence of wind and topography on precipitation distribution in sweden: Statistical analysis and modelling. *International Journal of Climatology*, 23(12):1523–1535.
- Joss, J. and Germann, U. (2000). Solutions and problems when applying qualitative and quantitative information from weather radar. *Physics and Chemistry of the Earth Part B-Hydrology Oceans and Atmosphere*, 25(10-12):837–841.
- Joss, J. and Lee, R. (1995). The application of radar-gauge comparisons to operational precipitation profile corrections. *Journal of Applied Meteorology*, 34(12):2612–2630.
- Kaufmann, P. and Weber, R. O. (1994). Cluster analysis of wind fields in complex terrain. *Air Pollution li, Vol 2: Pollution Control and Monitoring*, pages 253–260.

- Kaufmann, P. and Whiteman, C. D. (1999). Cluster-analysis classification of wintertime wind patterns in the grand canyon region. *Journal of Applied Meteorology*, 38(8):1131–1147.
- Krajewski, W. F. (1987). Cokriging radar-rainfall and rain-gauge data. *Journal of Geophysical Research-Atmospheres*, 92(D8):9571–9580.
- Krajewski, W. F., Ciach, G. J., and Habib, E. (2003). An analysis of small-scale rainfall variability in different climatic regimes. *Hydrological Sciences Journal-Journal Des Sciences Hydrologiques*, 48(2):151–162.
- Kyriakidis, P. C., Kim, J., and Miller, N. L. (2001). Geostatistical mapping of precipitation from rain gauge data using atmospheric and terrain characteristics. *Journal of Applied Meteorology*, 40(11):1855–1877.
- La Barbera, P., Lanza, L. G., and Stagi, L. (2002). Tipping bucket mechanical errors and their influence on rainfall statistics and extremes. *Water Science and Technology*, 45(2):1–10.
- Loukas, A. and Quick, M. C. (1993). Rain distribution in a mountainous watershed. *Nordic Hydrology*, 24(4):225–242.
- Loukas, A. and Quick, M. C. (1996). Spatial and temporal distribution of storm precipitation in southwestern british columbia. *Journal of Hydrology*, 174(1-2):37–56.
- Mandapaka, P. V., Krajewski, W. F., Mantilla, R., and Gupta, V. K. (2009). Dissecting the effect of rainfall variability on the statistical structure of peak flows. *Advances in Water Resources*, 32(10):1508–1525.
- Marsalek, J. (1981). Calibration of the tipping-bucket raingage. *Journal of Hydrology*, 53(3-4):343–354.
- Minder, J. R., Durran, D. R., Roe, G. H., and Anders, A. M. (2008). The climatology of small-scale orographic precipitation over the olympic mountains: Patterns and processes. *Quarterly Journal of the Royal Meteorological Society*, 134(633):817–839.
- Molini, A., Lanza, L. G., and La Barbera, P. (2005). Improving the accuracy of tipping-bucket rain records using disaggregation techniques. *Atmospheric Research*, 77(1-4):203–217.
- Neiman, P. J., Ralph, F. M., White, A. B., Kingsmill, D. E., and Persson, P. O. G. (2002). The statistical relationship between upslope flow and rainfall in california's coastal mountains: Observations during caljet. *Monthly Weather Review*, 130(6):1468–1492.
- Nespor, V. and Sevruk, B. (1999). Estimation of wind-induced error of rainfall gauge measurements using a numerical simulation. *Journal of Atmospheric and Oceanic Technology*, 16(4):450–464.



- Niemczynowicz, J. (1986). The dynamic calibration of tipping-bucket rain-gages. *Nordic Hydrology*, 17(3):203–214. E8372 Times Cited:28 Cited References Count:0.
- Nykanen, D. K. and Harris, D. (2003). Orographic influences on the multiscale statistical properties of precipitation. *Journal of Geophysical Research-Atmospheres*, 108(D8).
- Obled, C., Wendling, J., and Beven, K. (1994). The sensitivity of hydrological models to spatial rainfall patterns - an evaluation using observed data. *Journal of Hydrology*, 159(1-4):305–333.
- Paschalis, A., Molnar, P., and Burlando, P. (2012). Temporal dependence structure in weights in a multiplicative cascade model for precipitation. *Water Resources Research*, 48.
- Petersen, W. A. and Rutledge, S. A. (1998). On the relationship between cloud-to-ground lightning and convective rainfall. *Journal of Geophysical Research-Atmospheres*, 103(D12):14025–14040.
- Pierce, C. E., Ebert, E., Seed, A. W., Sleigh, M., Collier, C. G., Fox, N. I., Donaldson, N., Wilson, J. W., Roberts, R., and Mueller, C. K. (2004). The nowcasting of precipitation during sydney 2000: An appraisal of the qpf algorithms. *Weather and Forecasting*, 19(1):7–21.
- Rigo, T., Pineda, N., and Bech, J. (2010). Analysis of warm season thunderstorms using an object-oriented tracking method based on radar and total lightning data. *Natural Hazards and Earth System Sciences*, 10(9):1881–1893.
- Roe, G. H. (2005). Orographic precipitation. *Annual Review of Earth and Planetary Sciences*, 33:645–671.
- Rotunno, R. and Ferretti, R. (2001). Mechanisms of intense alpine rainfall. *Journal of the Atmospheric Sciences*, 58(13):1732–1749.
- Röthlisberger, G. (1988). Weather damages in switzerland in 1987 (in german). Technical Report Nr. 1/2, Water, Energy, Air - Swiss water management association.
- Savina, M., Molnar, P., and Burlando, P. (2011). Seasonal long-term persistence in radar precipitation in complex terrain. *Water Resources Research*, 47.
- Savina, M., Schappi, B., Molnar, P., Burlando, P., and Sevruk, B. (2012). Comparison of a tipping-bucket and electronic weighing precipitation gage for snowfall. *Atmospheric Research*, 103:45–51.
- Schiemann, R. and Frei, C. (2010). How to quantify the resolution of surface climate by circulation types: An example for alpine precipitation. *Physics and Chemistry of the Earth*, 35(9-12):403–410.

- Sevruk, B. (1982). Methods of correction for systematic error in point precipitation measurement. Technical Report Operational Hydrology, Report No. 21, Secretariat of the World Meteorological Organization, Geneva, Switzerland.
- Sevruk, B. (1997). Regional dependency of precipitation-altitude relationship in the swiss alps. *Climatic Change*, 36(3-4):355–369.
- Sevruk, B. and Mieglietz, K. (2002). The effect of topography, season and weather situation on daily precipitation gradients in 60 swiss valleys. *Water Science and Technology*, 45(2):41–48.
- Sharples, J. J., Hutchinson, M. F., and Jellett, D. R. (2005). On the horizontal scale of elevation dependence of australian monthly precipitation. *Journal of Applied Meteorology*, 44(12):1850–1865.
- Sieck, L. C., Burges, S. J., and Steiner, M. (2007). Challenges in obtaining reliable measurements of point rainfall. *Water Resources Research*, 43(1).
- Simoni, S., Padoan, S., Nadeau, D. F., Diebold, M., Porporato, A., Barrenetxea, G., Ingelrest, F., Vetterli, M., and Parlange, M. B. (2011). Hydrologic response of an alpine watershed: Application of a meteorological wireless sensor network to understand streamflow generation. *Water Resources Research*, 47.
- Sinclair, M. R., Wratt, D. S., Henderson, R. D., and Gray, W. R. (1997). Factors affecting the distribution and spillover of precipitation in the southern alps of new zealand - a case study. *Journal of Applied Meteorology*, 36(5):428–442.
- Singh, P. and Kumar, N. (1997). Effect of orography on precipitation in the western himalayan region. *Journal of Hydrology*, 199(1-2):183–206.
- Smith, R. B. (1979). The influence of mountains on the atmosphere. In Saltzman, B., editor, "", volume 21 of *Advances in Geophysics*, pages 87 – 230. Elsevier.
- Smith, R. B. (2003a). Advection, diffusion, and deposition from distributed sources. *Boundary-Layer Meteorology*, 107(2):273–287.
- Smith, R. B. (2003b). A linear upslope-time-delay model for orographic precipitation. *Journal of Hydrology*, 282(1-4):2–9.
- Smith, R. B. and Barstad, I. (2004). A linear theory of orographic precipitation. *Journal of the Atmospheric Sciences*, 61(12):1377–1391.
- Soriano, L. R., de Pablo, F., and Diez, E. G. (2001). Relationship between convective precipitation and cloud-to-ground lightning in the iberian peninsula. *Monthly Weather Review*, 129(12):2998–3003.

- Steiner, M., Bousquet, O., Houze, R. A., Smull, B. F., and Mancin, M. (2003). Airflow within major alpine river valleys under heavy rainfall. *Quarterly Journal of the Royal Meteorological Society*, 129(588):411–431.
- Tapia, A., Smith, J. A., and Dixon, M. (1998). Estimation of convective rainfall from lightning observations. *Journal of Applied Meteorology*, 37(11):1497–1509.
- Taylor, J. R. (1997). *An Introduction to Error Analysis: The Study of Uncertainties in Physical Measurements*. University Science Books, 2nd edition.
- Tobin, C., Nicotina, L., Parlange, M. B., Berne, A., and Rinaldo, A. (2011). Improved interpolation of meteorological forcings for hydrologic applications in a swiss alpine region. *Journal of Hydrology*, 401(1-2):77–89.
- Trubilowicz, J., Cai, K., and Weiler, M. (2009). Viability of motes for hydrological measurement. *Water Resources Research*, 45.
- Vasvari, V. (2005). Calibration of tipping bucket rain gauges in the graz urban research area. *Atmospheric Research*, 77(1-4):18–28.
- Villarini, G., Mandapaka, P. V., Krajewski, W. F., and Moore, R. J. (2008). Rainfall and sampling uncertainties: A rain gauge perspective. *Journal of Geophysical Research-Atmospheres*, 113(D11).
- Vuerich, E., Monesi, C., Lanza, L. G., Stagi, L., and Lanzinger, E. (2009). Wmo field inter-comparison of rainfall intensity gauges, instruments and observing methods, report no. 99. Technical Report WMO/TD-No. 1504, WMO.
- Wang, J. X., Fisher, B. L., and Wolff, D. B. (2008). Estimating rain rates from tipping-bucket rain gauge measurements. *Journal of Atmospheric and Oceanic Technology*, 25(1):43–56.
- Ward, J. H. (1963). Hierarchical grouping to optimize an objective function. *Journal of the American Statistical Association*, 58(301):236–244.
- Wastl, C. and Zangl, G. (2010). Mountain-valley precipitation differences in the northern alps: an exemplary high-resolution modeling study. *Meteorology and Atmospheric Physics*, 108(1-2):29–42.
- Weber, R. O. and Furger, M. (2001). Climatology of near-surface wind patterns over switzerland. *International Journal of Climatology*, 21(7):809–827.
- Weingartner, R. and Pearson, C. (2001). A comparison of the hydrology of the swiss alps and the southern alps of new zealand. *Mountain Research and Development*, 21(4):370–381.

- Weisse, A. K. and Bois, P. (2001). Topographic effects on statistical characteristics of heavy rainfall and mapping in the french alps. *Journal of Applied Meteorology*, 40(4):720–740.
- Weusthoff, T. (2011). Weather type classification at meteoswiss - introduction of new automatic classifications schemes, arbeitsberichte der meteoschweiz. Technical Report 235, 46 pp., MeteoSwiss.
- Whiteman, C. D. and Doran, J. C. (1993). The relationship between overlying synoptic-scale flows and winds within a valley. *Journal of Applied Meteorology*, 32(11):1669–1682.
- Zangl, G. (2007). Small-scale variability of orographic precipitation in the alps: Case studies and semi-idealized numerical simulations. *Quarterly Journal of the Royal Meteorological Society*, 133(628):1701–1716.
- Zeller, J. and Röthlisberger, G. (1994). Weather damages in switzerland in 1993 (in german). Technical Report Nr. 1/2, Water, Energy, Air - Swiss water management association.



## Appendix A

# Appendix

## A.1 Sensors

**Table A.1:** *Wind sensors deployed at mobile and reference stations*

<b>Wind</b>	<b>Davis</b>	<b>Vaisala</b>	<b>Unit</b>
Name	Davis Anemometer	Vaisala WINDCAP Ultrasonic Wind Sensor WMT52	
Measurement technique	Anemometer	Ultrasonic wind sensor	
<b>Wind Direction</b>			
Resolution	22.5	1	°
Accuracy	± 7	±3	°
<b>Wind Speed</b>			
Resolution		0.1	m/s
Range	0.9÷78	0÷60	m/s
Accuracy	± 5	0÷35 m/s ±0.3 m/s or ±3 % whichever is greater 35÷60m/s ±5 %	%
Technical details	<a href="http://www.davisnet.com">www.davisnet.com</a>	<a href="http://www.vaisala.com">www.vaisala.com</a>	
Deployment	mobile station	reference station	

**Table A.2:** *Rainfall sensors deployed at mobile and reference stations*

<b>Rainfall</b>	<b>Davis raingauge</b>	<b>MPS weighing raingauge</b>	<b>Unit</b>
Name	Rain Collector II	TrWS 200E	-
Measurement technique	Tipping bucket with magnetic reed switch	Total rain weighing sensor	-
Diameter	16.5	16.0	cm
Sampling area	213.7	200	cm <sup>2</sup>
Measuring element		strain-gauge bridge	-
Temporal resolution	1	1	min
Resolution of rainfall amount	0.254	0.001	mm
Maximum rain intensity		60	mm/min
Accuracy	±4%, ±1 rainfall count between 0.01" and 2.00" per hour (0.2 mm and 50.0 mm per hour); ±5%, ±1 rainfall count between 2.00" and 4.00" per hour (50.0 mm and 100.0 mm per hour)	0.10%	-
Operating temperature range		-35 ÷ +70	°C
Operating humidity range		0 ÷ 100	%
Technical details	www.davisnet.com	www.mps-system.sk	-
Deployment	mobile station	reference station	

**Table A.3:** *Temperature sensors deployed at mobile and reference stations*

<b>Temperature &amp; Relative humidity</b>	<b>Sensirion</b>	<b>MPS</b>	<b>Unit</b>
Name	SHT75		
Range	-40 ÷ 123.8	-35 ÷ +70	°C
Resolution	0.01		°C
Accuracy	±0.3	±0.5	°C
Resolution	0.05		%
Accuracy	1.8		%
Technical details	www.sensirion.com	www.mps-system.sk	-
Deployment	mobile station	reference station	



**Figure A.1:** Reference Stations: from left to right, top to bottom: Zermatt, Trockener Steg, St. Niklaus, Saas Balen, Randa, Stalden

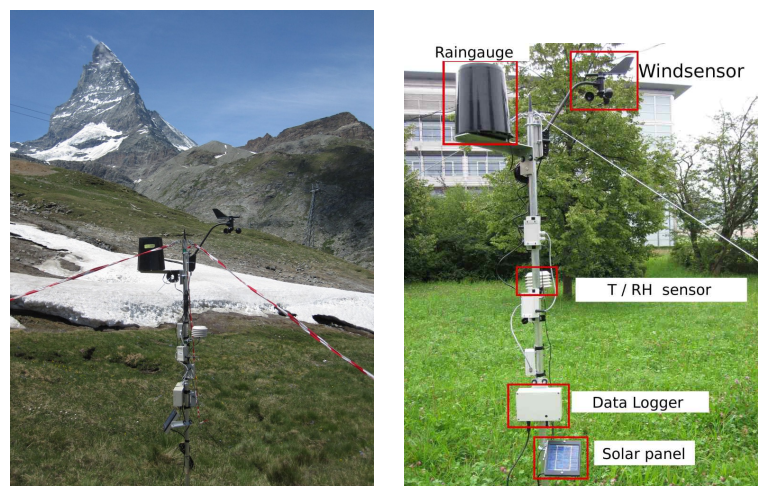


**Figure A.2:** Setup of mobile stations



## A.2 Maps and station setup

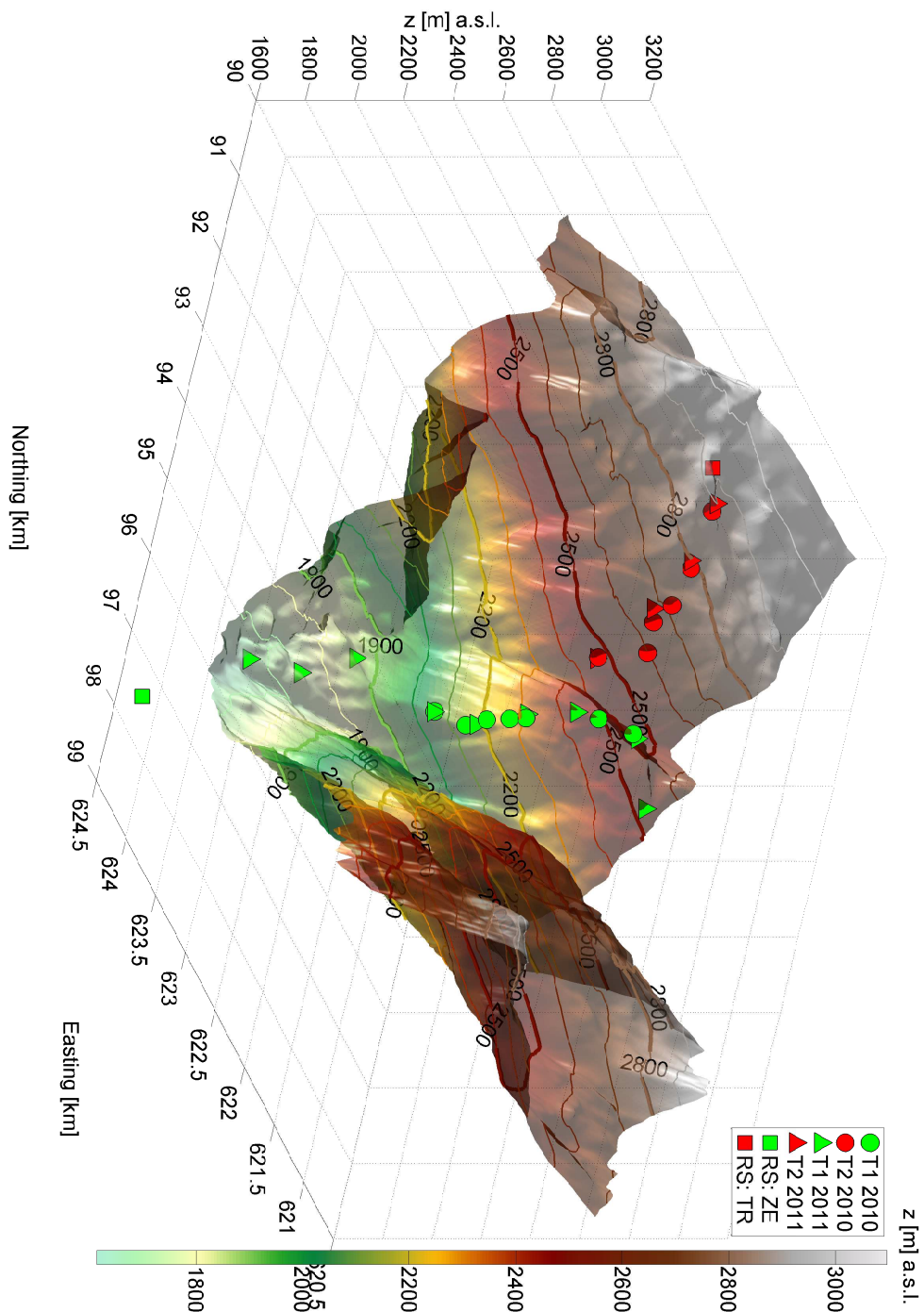


**Figure A.3:** Topography of the hillslopes. DEM ©2011 swisstopo (JD100042). Source: Bundesamt für Landestopografie swisstopo (Art. 30 GeoIV): 5704 000 000

**Table A.4:** *Coordinates and id of mobile stations 2010: the letters in the last column indicate the stations that were at the same location in 2011*

Station number	Index	x [m]	y [m]	z [m]	Time period	d [m]	$\delta z$ [m]	
1	1029	622094	94433	2064	7/7 - 10/2	155	89	a
2	1024	621945	94389	2153	8/8 - 10/2	157	62	
3	1025	621894	94240	2215	7/7 - 10/2	170	60	
4	1026	621806	94094	2275	7/7 - 10/2	150	41	
5	1018	621728	93966	2316	7/7 - 10/2	602	176	b
6	1027	621392	93467	2492	7/7 - 10/2	280	73	
7	1028	621159	93312	2566	7/7 - 10/2	597	-95	c
8	1023	621505	92825	2471	7/7 - 10/2	401	129	d
9	1020	621312	92473	2600	7/7 - 10/2	230	51	
10	1017	621471	92307	2651	7/7 - 10/2	165	72	e
11	1021	621511	92147	2723	7/7 - 10/2	397	65	
12	1022	621574	91755	2788	7/7 - 10/2	523	92	f
13	1019	621747	91261	2880	7/7 - 10/2			
<b>min abs</b>						<b>150</b>	<b>41</b>	
<b>max abs</b>						<b>602</b>	<b>176</b>	
<b>mean abs</b>						<b>319</b>	<b>84</b>	

**Table A.5:** *Coordinates and id of mobile stations 2011: the letters in the last column indicate the stations that were at the same location in 2010*

Station number	Index	x [m]	y [m]	z [m]	Time period	d [m]	$\delta z$ [m]	
1	1021	623230	95465	1659	6/12-9/31	508	96	
2	1024	622873	95104	1756	6/12-9/31	675	111	
3	1020	622595	94489	1866	6/12-9/31	496	195	
4	1029	622101	94448	2062	6/12-9/31	223	121	a
5	1025	621912	94329	2183	6/12-9/31	439	134	
6	1018	621736	93927	2317	6/12-9/31	385	131	b
7	1027	621537	93598	2447	6/12-9/31	507	123	
8	1028	621118	93313	2571	6/12-9/31	512	-42	c
9	1026	620715	93629	2528	6/12-9/31	1114	-63	
10	1023	621510	92848	2465	6/12-9/31	575	207	d
11	1017	621568	92276	2672	6/12-9/31	547	124	e
12	1022	621628	91732	2796	6/12-9/31	560	100	f
13	1019	621767	91190	2896	6/12-9/31			
<b>min abs</b>						<b>223</b>	<b>42</b>	
<b>max abs</b>						<b>1114</b>	<b>207</b>	
<b>mean abs</b>						<b>545</b>	<b>103</b>	





Figure A.4: Map of weather stations in 2010 and 2011. ©2011 swisstopo (JD100042). Source: Bundesamt für Landestopografie swisstopo (Art. 30 GeoIV): 5704 000 000

### A.3 Post-processing

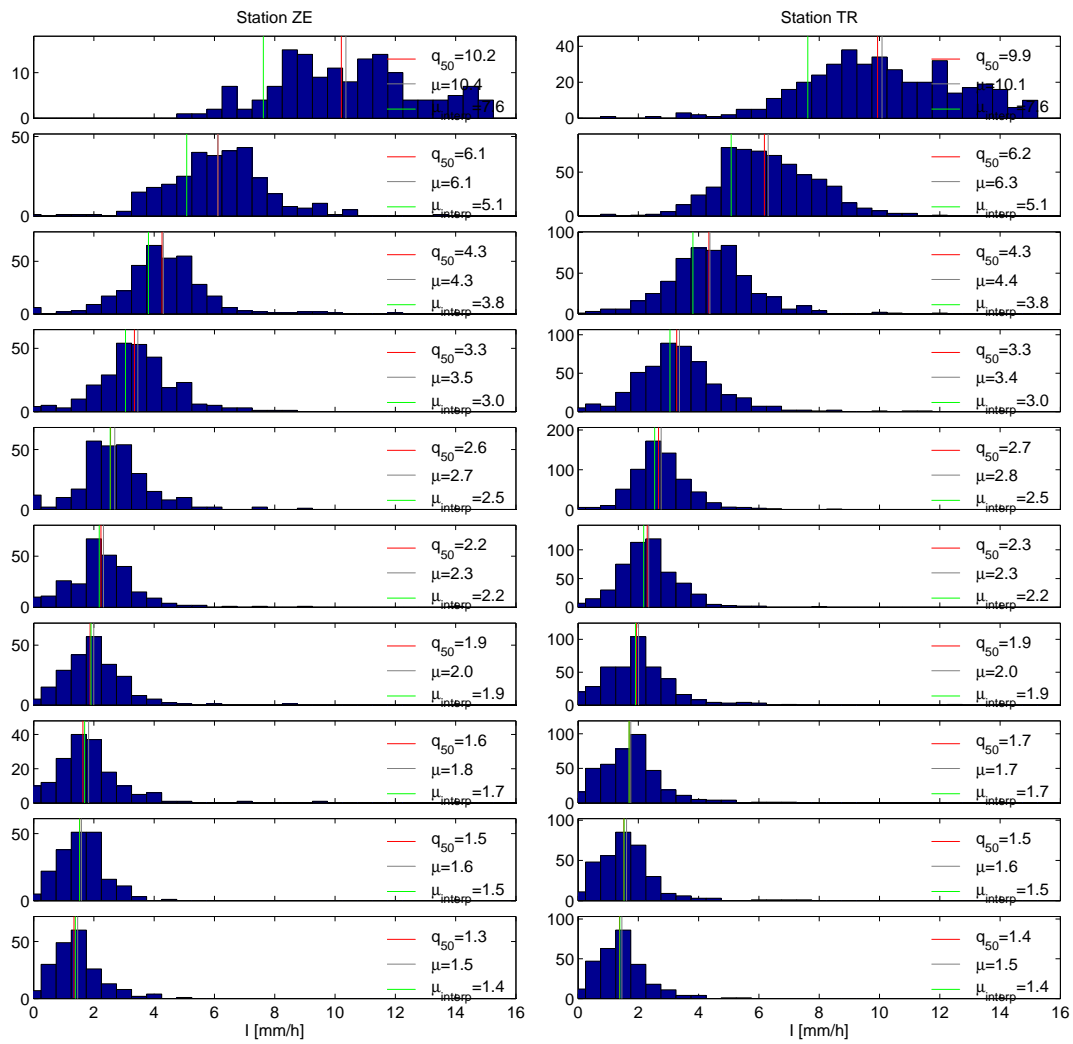


Figure A.5: Distribution of intensities at MPS station for different tip durations.

**Table A.6:** Stations used in the analysis. 0 indicates a station which was not used in the event analysis due to gaps in the time series.

id	date	ZE	1	2	3	4	5	6	7	8	9	10	11	12	13	TR
1	2010-07-12	1	0	0	1	1	1	0	0	1	1	1	1	1	1	0
2	2010-07-22	1	0	0	1	1	1	1	1	1	1	1	1	1	1	1
3	2010-07-28	1	0	0	1	1	1	1	1	1	1	1	1	1	1	1
4	2010-08-01	1	1	0	1	1	1	1	1	1	1	1	1	1	1	1
5	2010-08-02	1	0	0	1	1	1	1	1	1	1	1	1	1	1	1
6	2010-08-11	1	0	0	1	1	1	1	1	1	0	0	1	1	1	1
7	2010-08-13	1	0	0	1	1	1	1	0	0	0	1	0	0	0	1
8	2010-08-27	1	1	0	1	1	1	1	0	1	0	1	0	1	1	1
9	2010-09-07	1	1	0	1	1	1	1	1	1	1	1	1	1	1	1
10	2011-06-17	1	1	1	1	1	1	1	1	0	1	1	1	1	0	1
11	2011-06-21	1	1	1	1	1	1	1	1	0	1	0	0	1	0	1
12	2011-06-29	1	1	1	1	1	1	1	1	0	1	0	0	0	0	1
13	2011-07-07	1	1	1	1	1	1	1	1	1	1	0	1	1	1	1
14	2011-07-09	1	1	1	1	1	1	1	1	1	1	0	1	1	1	1
15	2011-07-10	1	1	1	1	1	1	1	1	1	1	0	1	0	1	1
16	2011-07-12	1	1	1	1	1	1	1	1	1	1	0	1	0	1	1
17	2011-07-16	1	1	1	1	1	1	1	1	1	1	0	1	0	1	1
18	2011-07-19	1	1	1	1	1	1	1	1	0	1	0	1	0	1	1
19	2011-07-28	1	1	1	1	1	1	1	1	1	1	1	1	0	0	1
20	2011-08-03	1	1	1	1	1	1	1	1	1	1	1	1	0	1	1
21	2011-08-05	1	1	1	1	1	1	1	1	1	1	1	1	0	1	1
22	2011-08-06	1	1	1	1	1	1	1	1	1	1	1	1	0	1	1
23	2011-08-25	1	1	1	1	1	1	1	1	1	1	1	1	0	1	1
24	2011-08-31	1	1	1	1	1	1	1	1	0	1	1	0	0	1	1
25	2011-09-03	1	1	1	1	1	1	1	1	1	1	1	0	1	1	1
26	2011-09-11	1	1	1	1	1	1	0	1	1	1	1	0	1	1	1
27	2011-09-17	1	1	1	1	1	1	0	1	1	1	0	0	0	1	1

Table A.7: Uncertainty [%]

id	date	ZE	1	2	3	4	5	6	7	8	9	10	11	12	13	TR
1	2010-07-12	8.4	-	-	23.8	22.9	22.4	-	-	21.3	21.3	20.8	21.1	20.4	20.6	-
2	2010-07-22	6.6	-	-	19.6	18.8	19.3	21.2	19.7	19.3	20.2	18.5	21.0	20.8	21.2	7.7
3	2010-07-28	6.0	-	-	18.1	17.1	17.4	18.5	17.1	16.7	17.5	17.4	17.9	17.9	18.6	5.6
4	2010-08-01	6.6	19.8	-	23.0	20.0	22.6	25.1	22.4	22.6	22.5	19.8	23.0	22.5	22.2	9.0
5	2010-08-02	7.3	-	-	17.9	17.5	17.5	19.1	17.5	17.4	18.6	17.6	19.6	18.5	19.1	6.8
6	2010-08-11	6.3	-	-	19.4	18.8	19.6	20.8	19.0	19.5	-	-	19.8	19.5	19.4	7.0
7	2010-08-13	6.1	-	-	19.2	18.5	18.8	19.9	-	-	-	17.7	-	-	-	6.4
8	2010-08-27	6.5	17.9	-	18.8	18.1	17.6	21.0	-	18.6	-	17.8	-	19.3	20.0	7.4
9	2010-09-07	5.4	16.5	-	18.3	17.7	17.8	19.3	17.8	17.2	18.4	17.9	19.0	18.7	19.1	6.0
10	2011-06-17	5.6	18.2	17.0	17.7	16.6	17.9	18.0	19.1	-	17.6	17.7	18.7	19.2	-	6.5
11	2011-06-21	5.8	18.2	16.9	18.3	16.4	18.3	17.9	19.6	-	17.8	-	-	18.9	-	6.5
12	2011-06-29	7.4	19.3	17.7	18.3	16.3	18.2	17.9	20.2	-	17.8	-	-	-	-	8.2
13	2011-07-07	7.2	20.0	19.7	21.0	18.9	21.0	20.6	21.9	20.5	20.1	-	19.1	20.0	20.3	7.9
14	2011-07-09	7.0	21.0	20.0	20.1	20.3	22.0	21.8	23.5	20.3	20.6	-	19.2	19.0	18.9	7.0
15	2011-07-10	7.5	20.3	19.2	20.1	19.2	21.0	20.6	22.3	21.2	20.3	-	20.3	-	19.9	8.0
16	2011-07-12	6.9	19.1	18.2	19.2	18.3	18.8	19.4	20.9	19.1	18.8	-	18.9	-	20.9	7.9
17	2011-07-16	6.2	18.4	17.4	18.0	16.8	18.4	17.8	19.3	18.3	18.2	-	18.4	-	19.6	6.6
18	2011-07-19	5.8	18.5	17.4	17.9	16.7	17.7	17.6	18.7	-	17.5	-	17.7	-	18.3	5.9
19	2011-07-28	5.6	18.3	16.7	17.3	16.7	18.3	17.2	18.5	17.4	17.0	16.9	17.7	17.6	19.0	5.9
20	2011-08-03	8.1	20.8	19.4	19.4	17.7	19.1	19.5	22.2	18.6	17.9	18.9	18.7	-	18.6	6.8
21	2011-08-05	5.8	18.9	18.3	18.6	19.0	21.3	18.2	19.5	18.5	19.0	17.3	17.9	-	19.4	6.2
22	2011-08-06	5.3	17.7	17.1	18.3	16.5	18.0	17.6	19.0	18.1	17.5	17.0	18.2	-	18.7	6.2
23	2011-08-25	7.2	19.2	18.9	19.6	18.5	20.3	19.9	21.0	20.7	19.7	20.0	22.7	-	20.0	8.7
24	2011-08-31	5.7	18.4	17.5	18.1	17.6	19.0	19.1	21.6	-	19.7	19.7	-	-	19.3	7.0
25	2011-09-03	5.9	18.3	17.5	18.0	16.9	17.9	17.8	19.0	17.4	17.3	17.3	-	18.3	19.2	6.1
26	2011-09-11	7.4	19.5	18.7	19.1	18.6	20.9	-	20.8	18.3	18.8	17.8	-	18.3	18.4	7.3
27	2011-09-17	7.2	18.2	17.3	17.9	16.6	18.3	-	19.2	18.0	17.3	17.1	-	-	18.2	6.8



Table A.8: Uncorrected event rainfall amounts [mm]

id	date	ZE	1	2	3	4	5	6	7	8	9	10	11	12	13	TR
1	2010-07-12	7.1	-	-	29.7	27.2	27.9	-	-	22.9	20.3	20.3	19.6	17.5	15.5	-
2	2010-07-22	11.4	-	-	21.3	20.1	19.9	17.8	18.3	16.1	14.5	16.0	16.5	15.0	14.0	17.3
3	2010-07-28	8.7	-	-	5.8	7.0	7.2	6.5	6.7	7.9	5.8	7.1	6.7	6.2	6.2	6.9
4	2010-08-01	2.8	12.2	-	18.5	19.4	19.9	18.5	16.5	19.6	15.2	13.5	15.7	15.1	10.7	5.6
5	2010-08-02	5.9	-	-	3.8	4.4	4.8	5.3	5.7	8.0	7.7	8.9	9.3	8.1	9.3	9.6
6	2010-08-11	6.9	-	-	10.3	12.2	13.8	16.0	17.1	25.3	-	-	20.3	18.7	13.1	14.8
7	2010-08-13	29.7	-	-	35.4	39.8	40.5	36.8	-	-	-	41.1	-	-	-	39.7
8	2010-08-27	6.4	10.4	-	9.1	10.9	12.4	15.5	-	15.4	-	13.7	-	11.0	8.6	8.3
9	2010-09-07	2.3	8.5	-	11.8	15.5	16.0	19.2	26.0	21.2	24.8	21.8	23.9	29.7	23.5	8.9
10	2011-06-17	6.1	10.7	13.1	17.1	18.4	23.4	29.1	33.5	-	40.9	33.1	36.4	34.8	-	29.2
11	2011-06-21	5.1	7.4	8.3	11.4	12.4	15.4	18.9	29.8	-	23.4	-	-	25.9	-	24.0
12	2011-06-29	9.6	6.9	7.5	7.2	6.9	7.4	8.4	12.6	-	10.2	-	-	-	-	17.5
13	2011-07-07	7.1	11.3	15.2	16.1	18.8	21.2	20.3	19.1	24.0	26.8	-	8.6	8.3	6.7	5.6
14	2011-07-09	4.0	8.6	8.5	7.0	11.2	11.4	11.8	10.0	11.7	15.1	-	4.2	3.3	3.2	3.2
15	2011-07-10	3.5	7.5	7.7	8.8	11.3	12.4	13.7	15.7	19.8	15.5	-	15.9	-	8.3	12.2
16	2011-07-12	30.2	31.6	36.3	35.6	44.3	46.9	47.6	50.4	52.3	57.9	-	46.7	-	36.4	48.0
17	2011-07-16	8.9	11.4	12.8	12.2	18.0	20.6	23.6	28.2	41.1	47.5	-	29.2	-	22.7	24.7
18	2011-07-19	11.1	10.7	11.2	10.0	13.8	14.0	15.7	17.0	-	18.5	-	19.1	-	14.5	20.2
19	2011-07-28	0.9	1.1	1.9	2.3	4.8	4.6	5.1	6.0	10.4	10.2	9.8	11.7	-	-	11.2
20	2011-08-03	10.4	9.3	8.9	8.4	8.6	8.9	9.8	11.7	9.0	8.4	8.8	5.7	-	5.1	5.6
21	2011-08-05	2.3	2.9	3.8	3.3	5.0	5.7	5.1	5.5	6.6	6.2	6.6	4.6	-	3.4	3.2
22	2011-08-06	2.8	3.6	3.6	3.7	5.1	6.7	7.5	12.4	17.9	14.0	14.4	13.8	-	13.7	15.1
23	2011-08-25	10.5	17.4	21.0	20.3	23.2	27.6	27.3	30.2	21.0	36.3	39.9	19.6	-	31.7	30.7
24	2011-08-31	1.8	2.3	2.3	2.7	4.2	4.8	4.7	6.5	-	7.4	7.7	-	-	6.7	6.2
25	2011-09-03	18.2	16.4	17.9	15.6	20.7	21.8	17.1	22.1	28.3	29.5	25.8	-	31.0	28.6	31.7
26	2011-09-11	4.4	4.4	5.2	4.7	6.9	6.9	-	5.2	4.8	6.1	4.6	-	4.6	5.3	4.4
27	2011-09-17	16.6	12.3	15.1	14.9	18.2	19.6	-	22.9	26.9	28.4	-	-	-	18.3	24.5

## A.4 Gradient analysis of cumulative event rainfall

**Table A.9:** Gradients of post-processed data with  $0.5 < R^2 < 1$  and standard deviation

Processed	T0			T1			T2		
	$g$	$\sigma$	$R^2$	$g_1$	$\sigma$	$R^2$	$g_2$	$\sigma$	$R^2$
	mm/100m	%	-	mm/100m	%	-	mm/100m	%	-
Event 1				4.15	9.85	0.94	-2.18	38.30	0.97
Event 2				0.93	19.52	0.56			
Event 3				-0.24	23.80	0.81			
Event 4				2.13	10.63	0.70	-2.82	19.94	0.69
Event 5							0.44	47.22	0.58
Event 6				1.31	12.22	0.90	-2.98	25.20	0.89
Event 7	0.88	21.84	0.60	1.51	25.97	0.88			
Event 8				1.36	14.15	0.76	-1.77	23.40	0.96
Event 9				2.51	7.61	0.92			
Event 10	2.48	6.48	0.83	3.38	9.04	0.95			
Event 11	1.83	6.28	0.80	2.39	8.59	0.84			
Event 12	0.68	10.08	0.58						
Event 13				1.71	12.99	0.86	-1.16	39.40	0.69
Event 14				0.87	14.23	0.74	-0.45	45.96	0.90
Event 15				1.49	10.96	0.90	-2.70	34.18	0.76
Event 16	1.54	16.61	0.51	2.99	16.01	0.97			
Event 17	1.94	7.06	0.51	3.51	8.09	0.83	-2.29	65.67	0.99
Event 18	0.70	11.15	0.77	0.84	17.11	0.90			
Event 19	0.89	4.13	0.91	0.85	6.77	0.90			
Event 20							-0.71	30.11	0.81
Event 21				0.41	11.32	0.87	-0.65	21.29	0.96
Event 22	1.15	4.71	0.86	1.32	7.50	0.83	0.23	148.39	0.73
Event 23	1.49	11.25	0.53	1.92	14.48	0.71			
Event 24	0.48	6.92	0.78	0.66	9.70	0.96	-0.32	69.34	0.78
Event 25	1.15	11.56	0.83	1.07	18.59	0.66	1.32	50.24	0.96
Event 26									
Event 27	0.91	12.05	0.61	1.46	14.23	0.88			
min	0.48	4.20	0.51	-0.24	6.67	0.56	-2.98	20.22	0.58
max	2.48	22.33	0.91	4.15	25.84	0.97	1.32	144.56	0.99
mean	1.24	10.00	0.70	1.67	13.20	0.84	-1.15	46.73	0.83



**Table A.10:** Gradients of observed data with  $0.5 < R^2 < 1$  and standard deviation

Observed	T0			T1			T2		
	g	$\sigma$	$R^2$	$g_1$	$\sigma$	$R^2$	$g_2$	$\sigma$	$R^2$
	mm/100m	%	-	mm/100m	%	-	mm/100m	%	-
Event 1				3.25	1.21	0.95	-1.72	5.14	0.96
Event 2				0.76	3.44	0.51			
Event 3				-0.23	7.07	0.58			
Event 4				1.71	1.20	0.73	-2.40	2.35	0.73
Event 5							0.34	9.74	0.53
Event 6				1.10	1.94	0.90	-2.63	3.44	0.92
Event 7	0.82	6.21	0.65	1.10	6.49	0.68			
Event 8				0.95	2.32	0.82	-1.68	3.15	0.96
Event 9				2.37	1.10	0.92			
Event 10	2.30	1.04	0.81	3.28	1.28	0.96			
Event 11	1.72	1.17	0.84	2.25	1.22	0.88			
Event 12	0.62	2.33	0.60						
Event 13				1.47	1.70	0.82	-1.15	4.95	0.81
Event 14				0.69	1.94	0.66	-0.40	7.07	0.85
Event 15				1.29	1.38	0.93	-2.33	4.63	0.67
Event 16				2.54	2.33	0.95			
Event 17				3.32	1.17	0.83	-2.31	8.86	0.87
Event 18	0.66	2.12	0.75	0.86	2.57	0.91			
Event 19	0.93	0.83	0.90	0.90	0.97	0.88			
Event 20							-0.71	4.14	0.80
Event 21				0.39	1.65	0.90	-0.72	2.98	0.98
Event 22	1.12	0.83	0.83	1.34	1.06	0.84			
Event 23				1.56	2.03	0.60			
Event 24	0.43	1.13	0.80	0.57	1.36	0.95	-0.30	9.98	0.89
Event 25	1.17	1.92	0.80	1.06	2.89	0.63	1.05	10.46	0.67
Event 26									
Event 27	0.83	2.25	0.55	1.41	2.11	0.88			
min	0.43	0.81	0.55	-0.23	0.98	0.51	-2.63	2.25	0.53
max	2.30	6.45	0.90	3.32	6.87	0.96	1.05	10.69	0.98
mean	1.06	2.00	0.75	1.48	2.20	0.81	-1.15	5.92	0.82

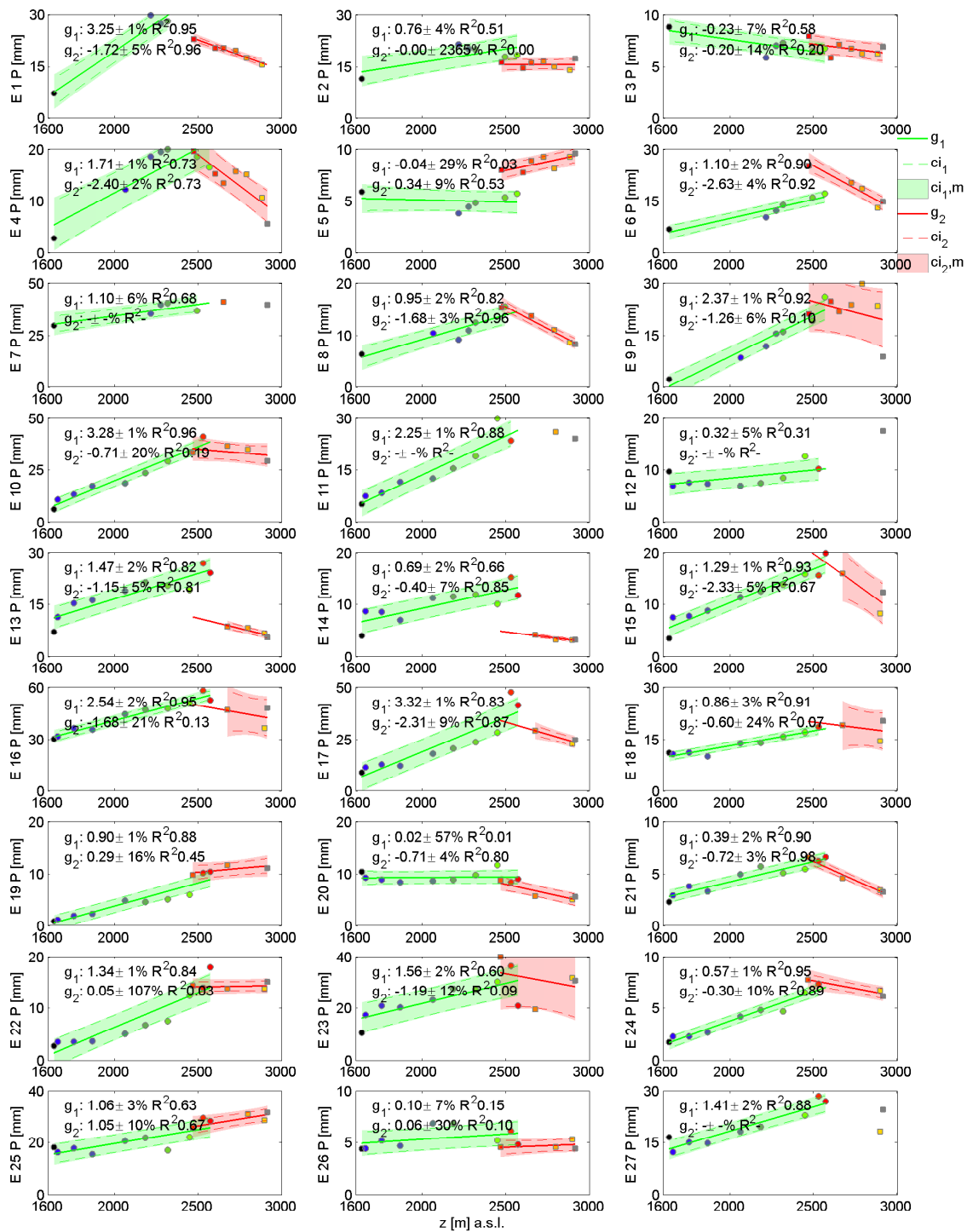
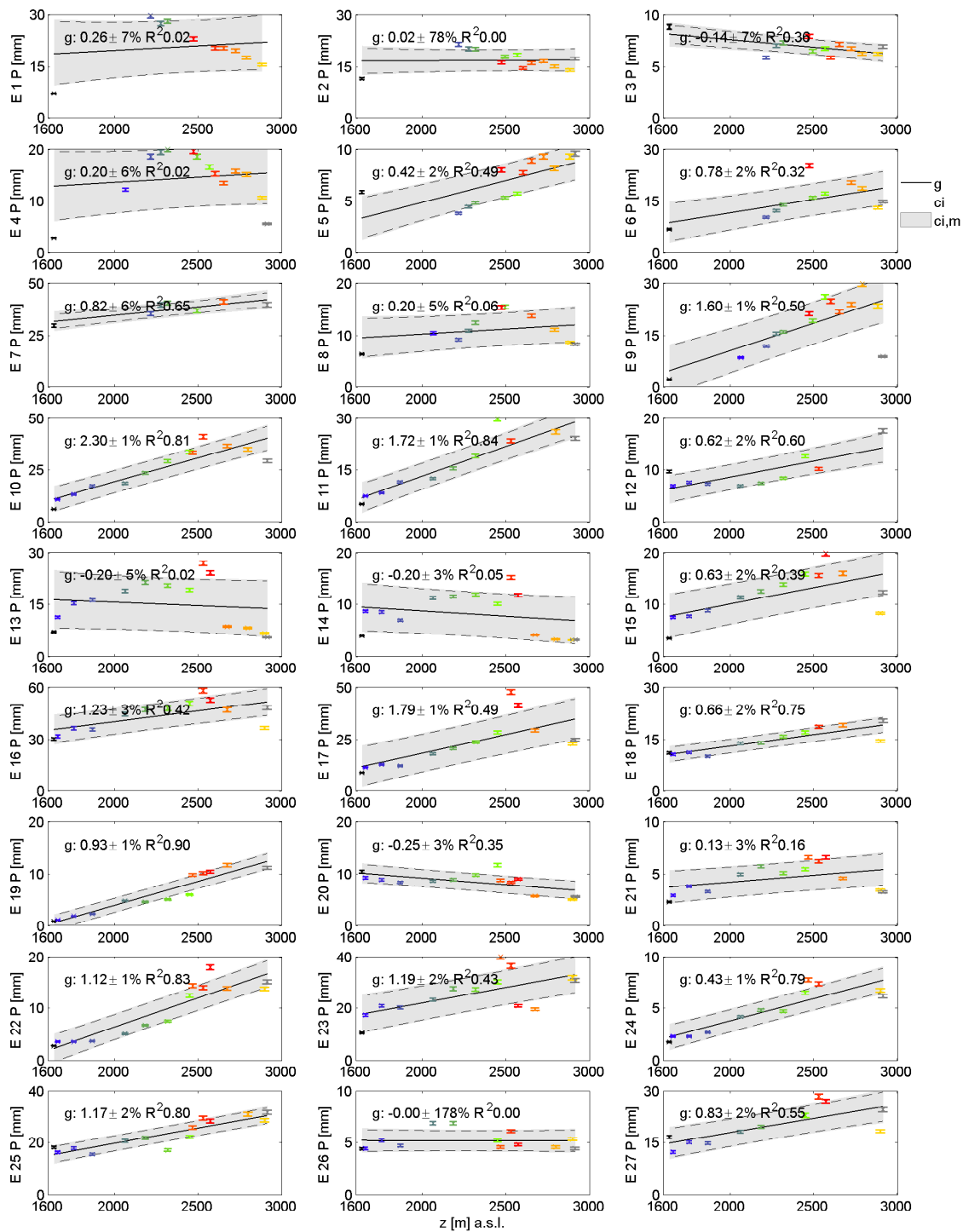


Figure A.6: Gradients on T1 and T2 based on the original data. The confidence interval of the regression is indicated by ci<sub>1</sub> and ci<sub>2</sub> for T1 and T2 respectively. The confidence interval based on the combined uncertainty in the data and the fitting method is indicated by ci<sub>1,m</sub> and ci<sub>2,m</sub> for T1 and T2 respectively.



**Figure A.7:** Gradients on  $T_0$  based on the **original** data. The confidence interval of the regression is indicated by  $ci$ . The confidence interval based on the combined uncertainty in the data and the fitting method is indicated by  $ci_m$ .

**Table A.11:** Explained variance of DEMs filtered in the fourier domain at different frequencies  $w$  and resulting length scale.  $N=1000, f_s=0.01m^{-1}$

explained variance [%]	w	$f_w [m^{-1}]$	length scale [km]
0.8126	10	0.00010	10.00
0.8334	11	0.00011	9.09
0.8507	12	0.00012	8.33
0.8652	13	0.00013	7.69
0.8773	14	0.00014	7.14
0.8876	15	0.00015	6.67
0.8964	16	0.00016	6.25
0.9042	17	0.00017	5.88
0.9111	18	0.00018	5.56
0.9174	19	0.00019	5.26
0.9231	20	0.00020	5.00
0.9375	23	0.00023	4.35
0.9485	26	0.00026	3.85
0.9568	29	0.00029	3.45
0.9634	32	0.00032	3.13
0.9685	35	0.00035	2.86
0.9725	38	0.00038	2.63
0.9758	41	0.00041	2.44
0.9785	44	0.00044	2.27
0.9807	47	0.00047	2.13
0.9826	50	0.00050	2.00
0.9887	65	0.00065	1.54
0.9920	80	0.00080	1.25
0.9939	95	0.00095	1.05

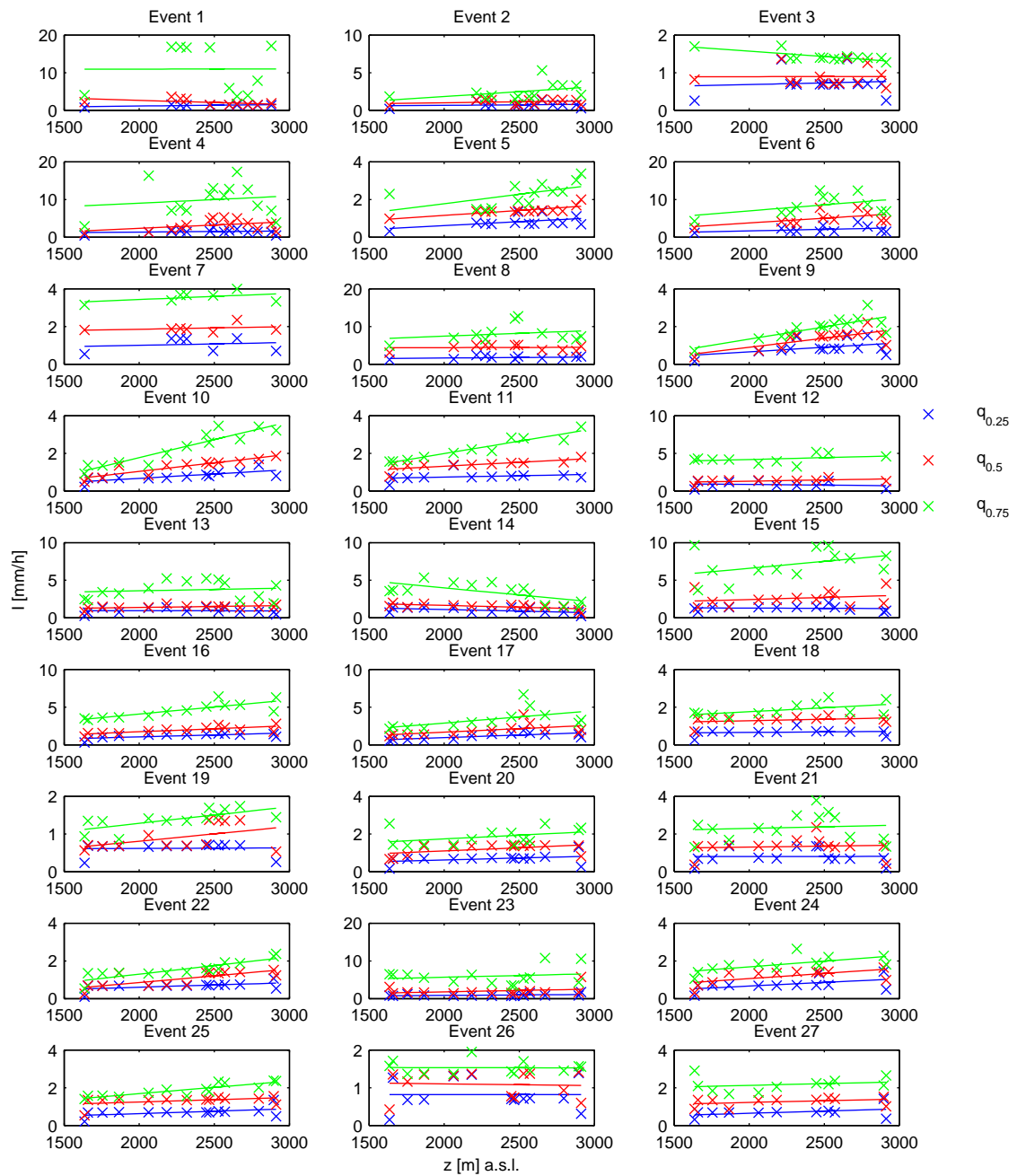


**Figure A.8:** 25, 50 and 75 % quantiles of rainfall intensity depending on the station altitude for the observed events.

## A.5 Weather type

**Table A.12:** Frequency of weather types with and without conditioning on rainfall occurrence ( $f_{WT}$  and  $f_{WT,P}$  respectively) on the annual time scale and on a seasonal time scale ( $f_{WT,S}$  and  $f_{WT,P,S}$  respectively) and frequency of weather types associated with observed events during the field experiment,  $f_{WT,E}$ .

[%]	1	2	3	4	5	6	7	8	9	10	11
	GWTWS										
$f_{WT}$	15.8	12.4	10.6	6.4	2.6	1.0	0.8	2.7	4.4	26.0	17.3
$f_{WT,P}$	16.7	30.2	13.0	1.6	0.1	1.0	3.1	11.2	5.1	6.2	11.7
$f_{WT,S}$	17.6	13.6	9.0	3.6	1.2	0.5	0.3	1.7	1.4	29.5	21.6
$f_{WT,P,S}$	13.3	40.7	3.6	0.4	0.2	0.8	1.3	8.0	2.7	10.3	18.8
$f_{WT,E}$	15.4	50.0	1.9	3.8	0.0	0.0	0.0	3.8	0.0	11.5	13.5
	CAP9										
$f_{WT}$	18.8	15.1	13.9	13.7	11.4	10.5	8.1	4.9	3.6		
$f_{WT,P}$	15.0	27.3	9.2	3.3	1.3	14.0	20.2	0.0	9.6		
$f_{WT,S}$	31.1	18.0	15.1	17.1	3.8	9.9	4.6	0.1	0.3		
$f_{WT,P,S}$	23.2	33.5	10.1	4.3	0.1	14.0	13.9	0.0	0.8		
$f_{WT,E}$	34.6	34.6	7.7	1.9	0.0	9.6	11.5	0.0	0.0		

**Table A.13:** Cluster reassignment from agglomerative hierarchical clustering to K-means clustering

AHC / K-means	LLW1	LLW2	LLW3	LLW4	LLW5	LLW6	LLW7	LLW8	LLW9	sum	Fraction [%]
LLW1	4	5	0	1	0	22	59	3	0	94	5.3
LLW2	22	10	0	0	0	41	37	16	0	126	7.0
LLW3	0	0	166	14	0	0	0	0	144	324	18.1
LLW4	0	0	46	98	0	0	0	0	70	214	12.0
LLW5	0	0	0	30	0	0	0	0	0	30	1.7
LLW6	0	0	4	30	0	0	3	0	13	50	2.8
LLW7	0	1	0	4	0	0	16	0	0	21	1.2
LLW8	162	129	0	2	4	147	277	150	0	871	48.7
LLW9	1	0	0	0	38	20	0	0	0	59	3.3
sum	189	145	216	179	42	230	392	169	227	1789	
Fraction [%]	10.6	8.1	12.1	10.0	2.3	12.9	21.9	9.4	12.7		

**Table A.14:** Meteorological conditions in different wind field clusters based on hourly averages of weather station data. The abbreviation shows the prevailing wind direction and its association with rainfall intensity I or cumulative amount P. Classes with identical properties are distinguished with letters.

Abbreviation	LLW1	LLW2	LLW3	LLW4	LLW5	LLW6	LLW7	LLW8	LLW9
	SW	SW,I	NE	N,P	S	SW,IP <sub>a</sub>	SW,P	SW,IP <sub>b</sub>	NNE
diurnal pattern	Night SW	Night SW	Midday O	Morning/Afternoon SO	Afternoon SO-W	Night SW	Night (day) SW	Night SW	Midday O
$\alpha$	-	++	-	-	-	++	-	++	-
I	-	+	-	+	-	++	++	++	-
P	-	+	-	+	-	++	++	++	-
<b>Mean</b>									
T	9.8	10.8	11.8	10.6	11.7	9.3	9.3	10.4	13.2
I	1.1	1.4	0.9	0.9	1.0	1.6	0.8	1.6	1.1
U	1.7	1.8	1.2	0.8	1.8	1.5	1.0	2.1	1.1
$\alpha$	221	217	51	100	276	233	203	227	63
$S_R$	28	94	588	276	295	58	107	30	645
T gradient	-0.42	-0.48	-0.78	-0.62	-0.65	-0.47	-0.52	-0.45	-0.75
<b>Std</b>									
T	4.4	5.0	5.0	5.8	5.8	5.1	5.1	4.0	5.1
I	1.3	1.8	1.1	1.4	0.9	2.0	1.0	2.1	1.0
U	1.6	1.7	0.9	0.9	1.8	1.7	1.3	2.0	0.6
$\alpha$	36	38	41	61	65	46	51	34	39
$S_R$	97	190	279	263	302	142	211	98	223
T gradient	0.20	0.24	0.18	0.24	0.30	0.23	0.23	0.20	0.21
<b>max</b>									
T	28.7	28.8	30.7	30.6	29.0	25.4	29.4	25.9	30.0
I	5.9	9.4	6.6	8.9	3.9	12.2	8.6	15.5	5.1
U	10.6	11.0	6.6	7.5	8.9	10.9	9.9	9.7	5.8
$\alpha$	359	353	360	359	359	359	357	352	360
$S_R$	822	830	1008	1018	992	764	982	750	993
T gradient	0.03	0.01	-0.11	0.18	0.32	0.09	0.19	-0.02	0.05



Table A.15: Wind class occurrence during observed events in 2011.

Event	10	11	12	13	14	15	16	17	18	19	20	21	22	23	24	25	26	27	
Class	Number of hours																		
1	1	4	0	6	2	1	2	1	1	0	0	0	3	5	1	4	0	0	
2	0	5	1	5	0	3	5	1	0	0	0	0	1	0	0	2	1	0	
3	2	1	1	0	0	0	0	1	0	9	0	0	0	4	0	4	0	3	
4	7	13	3	1	1	0	2	6	17	4	4	5	5	4	0	3	2	1	
5	0	4	0	0	0	0	0	0	4	0	0	1	1	0	0	0	0	1	
6	8	6	1	5	1	1	1	4	4	0	3	0	7	12	3	6	3	1	
7	8	12	11	4	8	3	6	10	1	1	4	2	8	3	0	9	6	1	
8	1	6	0	11	1	0	8	2	0	0	0	0	3	17	4	6	0	1	
9	0	0	3	0	0	0	0	1	0	1	2	0	0	2	0	0	0	0	
Class	Percentage of event duration																		
1	3.7	7.8	0.0	18.8	15.4	12.5	8.3	3.9	3.7	0.0	0.0	0.0	10.7	10.6	12.5	11.8	0.0	0.0	
2	0.0	9.8	5.0	15.6	0.0	37.5	20.8	3.9	0.0	0.0	0.0	0.0	3.6	0.0	0.0	5.9	8.3	0.0	
3	7.4	2.0	5.0	0.0	0.0	0.0	0.0	3.9	0.0	60.0	0.0	0.0	0.0	8.5	0.0	11.8	0.0	37.5	
4	25.9	25.5	15.0	3.1	7.7	0.0	8.3	23.1	63.0	26.7	30.8	62.5	17.9	8.5	0.0	8.8	16.7	12.5	
5	0.0	7.8	0.0	0.0	0.0	0.0	0.0	0.0	14.8	0.0	0.0	12.5	3.6	0.0	0.0	0.0	0.0	12.5	
6	29.6	11.8	5.0	15.6	7.7	12.5	4.2	15.4	14.8	0.0	23.1	0.0	25.0	37.5	17.7	25.0	12.5		
7	29.6	23.5	55.0	12.5	61.5	37.5	25.0	38.5	3.7	6.7	30.8	25.0	28.6	6.4	0.0	26.5	50.0	12.5	
8	3.7	11.8	0.0	34.4	7.7	0.0	33.3	7.7	0.0	0.0	0.0	0.0	10.7	36.2	50.0	17.7	0.0	12.5	
9	0.0	0.0	15.0	0.0	0.0	0.0	0.0	3.9	0.0	6.7	15.4	0.0	0.0	4.3	0.0	0.0	0.0	0.0	

**Table A.16:** *Weather classification on days with events during the field experiment in 2010 and 2011*

event	CAP9	GWTWS
1	2	11
2	2, 1, 1	2, 2, 4
3	1, 6, 6	1, 1, 4
4	3	1
5	1	2
6	1, 2	10, 2
7	1, 1	10, 8
8	7	1
9	2, 7	2, 2
10	2, 2	2, 2
11	3, 2, 1, 4	1, 2, 2, 1
12	1, 1	10, 1
13	2, 2	2, 2
14	3	2
15	1	2
16	2, 6	2, 2
17	2, 7	11, 2
18	7, 6	8, 3
19	1, 1	11, 10
20	3	2
21	1	10
22	7, 6	2, 2
23	2, 2, 1	2, 2, 1
24	1, 1	1, 11
25	2, 2, 1	11, 11, 2
26	2, 2	2, 10
27	2, 7	2, 2

Table A.17: Event data used in cluster analysis and corresponding gradients. The unit of the gradients is mm/100m.

Event	P	$f_t$	$l_{max}$	$D_p$	U	$\alpha_S$	$L_a$	CV	$g$	$g_1$	$g_2$	$g_S$	$g_{1S}$	$g_{2S}$
	mm	mm/h	mm/h	h	m/s	°	min	-						
1	24.64	0.71	111.30	1.82	9.62	4.76	0.24	3.17	0.24	4.15	-2.18	1.93	32.98	-17.33
2	17.86	0.14	58.97	5.43	10.41	1.06	0.50	6.51	0.10	0.93	0.24	0.07	0.66	0.17
3	6.56	0.00	5.90	5.56	7.61	1.46	1.19	3.66	-0.15	-0.24	-0.10	-0.08	-0.13	-0.06
4	17.26	0.08	89.94	1.42	9.68	5.09	0.22	2.39	0.21	2.13	-2.82	2.02	20.31	-26.87
5	7.03	0.38	19.34	3.22	6.26	2.41	0.46	3.01	0.45	-0.07	0.44	0.95	-0.15	0.93
6	16.59	0.00	32.94	2.60	5.85	4.83	0.54	1.36	0.88	1.31	-2.98	5.26	7.81	-17.82
7	38.47	0.02	57.04	12.76	7.74	4.70	0.78	3.72	0.88	1.51	-0.82	0.84	1.45	-0.88
8	12.16	0.00	29.77	2.11	6.23	2.25	0.52	1.25	0.27	1.36	-1.77	2.14	10.84	-14.09
9	18.93	0.00	10.89	10.73	12.54	5.22	1.88	2.16	1.81	2.51	-0.95	1.44	2.00	-0.76
10	24.94	0.00	20.91	13.27	9.48	4.50	1.21	1.56	2.48	3.38	-0.33	2.28	3.11	-0.31
11	16.67	0.00	14.07	8.52	8.42	4.51	1.18	3.46	1.83	2.39	-0.82	0.73	0.96	-1.05
12	9.63	0.28	24.36	3.04	5.31	3.22	0.77	4.02	0.68	0.37	-0.82	0.76	0.41	0.70
13	16.38	0.32	57.23	3.69	11.07	4.43	0.41	6.67	-0.18	1.71	-1.16	-0.12	1.14	-0.78
14	8.89	0.29	45.06	1.82	7.70	4.86	0.46	4.85	-0.19	0.87	-0.45	-0.40	1.81	-0.94
15	12.81	0.39	45.21	1.99	8.24	4.79	0.35	3.15	0.72	1.49	-2.70	2.45	5.09	-9.23
16	46.06	0.17	74.96	11.80	11.37	4.38	1.41	3.10	1.54	2.99	-1.12	1.32	2.56	-0.96
17	23.62	0.00	18.89	8.47	10.47	4.55	3.42	2.13	1.94	3.51	-2.29	1.86	3.37	-2.19
18	14.21	0.00	7.72	9.09	7.93	3.85	3.39	2.13	0.70	0.84	-0.09	0.54	0.65	-0.07
19	5.78	0.00	6.80	4.51	3.21	1.64	0.80	2.64	0.89	0.85	0.34	1.52	1.46	0.59
20	8.80	0.60	40.80	3.24	6.03	4.03	0.23	4.14	-0.28	0.02	-0.71	-0.52	0.04	-1.31
21	4.60	0.00	28.12	2.08	5.11	3.37	0.45	3.33	0.13	0.41	-0.65	0.46	1.41	-2.22
22	9.24	0.00	7.80	6.75	8.18	4.71	0.96	2.40	1.15	1.32	0.23	0.97	1.11	0.20
23	28.10	0.31	59.61	5.95	13.71	4.25	0.82	5.54	1.49	1.92	-1.05	0.74	0.96	-0.52
24	4.95	0.00	27.25	2.02	8.53	4.98	0.33	3.32	0.48	0.66	-0.32	1.64	2.27	-1.11
25	22.50	0.01	16.47	13.24	7.28	4.70	1.76	2.57	1.15	1.07	1.32	0.57	0.54	0.66
26	5.30	0.34	38.80	2.33	6.74	3.85	0.25	5.03	-0.00	0.11	0.13	-0.01	0.23	0.28
27	19.67	0.27	18.70	10.20	8.16	3.72	1.00	2.69	0.91	1.45	-0.82	0.61	0.97	28.82

## A.6 Modelling of orographic precipitation

**Table A.18:** Calibrated parameters of linear orographic model and resulting gradients along the transects in 2010. A: Calibration based on RMSE, B: Calibration based on MAE, C: Calibration based on correlation coefficient

	$\alpha$ °	u m/s	$\tau_c$ s	$\tau_f$ s	$\Gamma$ K/m	$g_{24h}$ 2010 mm/100m
Event 1 A	225	30	2000	2000	-0.6	-1.609
Event 1 B	220	30	2000	2000	-0.7	0.362
Event 1 C	210	30	2000	2000	-0.6	0.665
Event 2 A	220	30	2000	2000	-0.7	0.297
Event 2 B	220	30	2000	2000	-0.7	0.297
Event 2 C	230	30	2000	2000	-0.6	-1.546
Event 3 A	285	30	2000	2000	-0.9	0.172
Event 3 B	285	25	2000	2000	-0.9	0.275
Event 3 C	285	30	2000	2000	-0.8	0.168
Event 4 A	250	30	2000	2000	-0.7	3.232
Event 4 B	250	30	2000	2000	-0.7	3.232
Event 4 C	250	30	2000	2000	-0.6	2.098
Event 5 A	250	30	2000	2000	-0.6	1.997
Event 5 B	250	30	2000	2000	-0.8	3.132
Event 5 C	250	30	2000	2000	-0.6	1.997
Event 6 A	240	20	2000	2000	-0.7	3.152
Event 6 B	240	25	1800	1800	-0.9	3.457
Event 6 C	220	15	1200	1200	-0.8	8.364
Event 7 A	190	15	1200	1200	-0.9	7.052
Event 7 B	190	15	1000	1000	-0.7	10.917
Event 7 C	185	10	1800	1800	-0.9	3.465
Event 8 A	270	25	2000	2000	-0.6	0.408
Event 8 B	270	25	2000	2000	-0.6	0.408
Event 8 C	270	30	1400	1400	-0.6	0.683
Event 9 A	190	20	1200	1200	-0.8	6.427
Event 9 B	195	10	1600	1600	-0.7	5.019
Event 9 C	190	10	1800	1800	-0.6	5.611

**Table A.19:** Error statistics of the calibrated model of orographic precipitation. The relative error is estimated by dividing the error by the mean of the observed rainfall amounts.

Calibration	minimizing rmse		minimizing mae		maximizing $\rho$	
	mm	%	mm	%	mm	%
rmse						
Event 1	6.8	164	7.1	170	6.9	166
Event 2	6.0	132	6.0	132	7.5	166
Event 3	7.6	127	7.6	128	7.6	128
Event 4	3.1	103	3.1	103	3.2	106
Event 5	8.3	115	8.3	116	8.3	115
Event 6	8.3	125	8.3	125	8.7	130
Event 7	37.7	87	37.8	87	41.8	96
Event 8	3.6	82	3.6	82	4.2	95
Event 9	28.0	104	30.1	112	28.5	106
bias						
Event 1	-2.4	-57.1	-2.8	-67.5	-1.6	-39.4
Event 2	-1.2	-26.0	-1.2	-26.0	0.3	6.0
Event 3	-2.1	-35.4	-2.7	-45.1	-1.8	-31.2
Event 4	-0.6	-18.8	-0.6	-18.8	0.1	3.7
Event 5	-2.0	-28.3	-3.4	-47.5	-2.0	-28.3
Event 6	-4.4	-66.7	-4.2	-62.5	-3.0	-45.6
Event 7	-25.0	-57.8	-19.3	-44.5	-34.2	-78.9
Event 8	-1.8	-40.0	-1.8	-40.0	-0.1	-1.7
Event 9	-10.4	-38.7	-17.0	-63.3	-15.7	-58.5
mae						
Event 1	3.9	93	3.8	92	4.1	99
Event 2	4.4	96	4.4	96	5.5	121
Event 3	5.5	93	5.3	89	5.6	95
Event 4	2.3	77	2.3	77	2.5	83
Event 5	6.2	86	5.7	79	6.2	86
Event 6	5.1	76	5.0	76	5.8	87
Event 7	29.0	67	28.6	66	34.8	80
Event 8	2.7	62	2.7	62	3.4	78
Event 9	20.8	77	19.8	74	20.3	76

**Table A.20:** Correlation between modelled and observed precipitation for the selected events based on different calibration methods

$\rho$ [-]	minimizing rmse	minimizing mae	maximizing correlation
Event 1	0.34	0.23	0.35
Event 2	0.55	0.55	0.57
Event 3	0.50	0.47	0.50
Event 4	0.68	0.68	0.73
Event 5	0.58	0.50	0.58
Event 6	0.44	0.44	0.44
Event 7	0.66	0.66	0.68
Event 8	0.71	0.71	0.71
Event 9	0.65	0.60	0.66

**Table A.21:** Parameter values used in model simulations

parameter	unit	min	step size	max
$\tau$	s	400	200	2000
U	m/s	10	5	30
$\Gamma$	K/100m	-0.9	0.1	-0.6
$\alpha$	°	0	45	360



# Acronyms

**ACH** Agglomerative Hierarchical Clustering. 95–97, 127, 174

**bw** Butterworth. 82–85, 87

**CAP** cluster analysis of principal components. 107–109, 135

**DC** dynamic calibration. 36, 39–41

**DEM** Digital Elevation Model. 10, 82–85, 87–89, 118, 135

**GPRS** General Packet Radio Service. 13, 20, 21

**GWT** Gross Weather Type. 107, 108, 135

**IFS** Integrated Forecast System. 107

**ilp** ideal low pass. 82, 83, 87

**IOP** intensive observation period. 19–21, 23, 24, 39, 44, 68, 69, 92, 93, 95, 108, 141

**LLW** low level wind. 97, 98, 104, 135

**MAE** mean absolute error. 118, 119

**MS** mobile station. 84

**P1** first set of tipping bucket raingauges. 22, 29, 30, 64

**P2** second set of tipping bucket raingauges. 22, 29, 30, 64

**RMSE** root mean square error. 118, 119

**SC** static Calibration. 29



**ss** sum of squared errors. 127, 128

**T0** entire transect. 21, 69, 71, 87–89, 141

**T1** lower transect. 21, 23, 61, 69, 71, 84, 89, 113, 114, 141

**T2** upper transect. 21, 69, 71, 84, 89, 113, 114, 141

**TBR** tipping bucket raingauge. 7, 8, 14, 23, 31, 36, 44, 45, 49, 58, 64, 134, 140

**TR** reference station Trockener Steg. 19, 20, 22, 23, 37, 64, 95

**twcss** total within cluster sum of squared error. 96, 126–128

**WC** wind correction. 37, 40

**WMO** World Meteorological Organization. 8

**WR** weighing raingauge. 31, 140

**WSC** weather station data classification. 129–131, 135, 137, 144

**WT** weather type. 108

**ZE** reference station Zermatt. 19, 23, 41, 64, 84, 93

## Curriculum Vitae

Name: Bettina Schäppi  
Address: Lägernstrasse 21  
8037 Zürich  
Switzerland  
Date of birth: May 6, 1982  
Place of birth: Frauenfeld, Switzerland

## Work experience

October 2008 - February 2013 Ph.D. student in the group of Hydrology and Water Resources Management at the Institute of Environmental Engineering of ETH Zurich

October 2007 - September 2008 Natural hazard mapping and land use planning projects at the engineering company Frey + Gnehm, Olten AG

## Education

September 2001 - September 2007 Studies in Environmental Sciences at ETH Zurich, Switzerland  
Thesis: Integrating river bed topography and DEM data for a reach of the river Thur and related flow modelling

September 2005 - March 2006 Exchange semester in Lausanne at the Institute of Environmental Engineering at EPFL (Ecole polytechnique fédérale de Lausanne, Switzerland)

## **Publications**

Schaeppli, B., Perona, P., Schneider, P., Burlando, P.; Integrating river cross section measurements with digital terrain models for improved flow modelling applications; *COMPUTERS & GEOSCIENCES*; Volume: 36; Issue: 6; Pages: 707-716; DOI: 10.1016/j.cageo.2009.12.004; Published: JUN 2010

Savina, M., Schaeppli, B., Molnar, P., Burlando, P. and B. Sevruk; Comparison of recording precipitation gauges: tipping-bucket ANETZ and electronic weighing system MPS; *Atmospheric Research*; Volume 103; Pages: 45-51; DOI: 10.1016/j.atmosres.2011.06.010; Published: JAN 2012

## **Presentations at conferences**

Schaeppli, B., Molnar, P., Burlando, P.; Orographic effect on cumulative rainfall at the event time scale and its relation to meteorological conditions; (ZHydro Hydrology seminar, Zürich 2012)

Schaeppli, B., Molnar, P., Burlando, P.; Precipitation gradients along hillslopes estimated from rain gauge transects; (European Geosciences Union, General Assembly 2011)

Schaeppli, B., Molnar, P., Perona, P., Tockner, K., Burlando, P.; Hydrogeomorphological variability and ecological impacts in straight and restored river reaches; (European Geosciences Union, General Assembly 2009)

Schaeppli, B., Perona P., Schneider, P., Burlando, P.; Integrating river bathymetry data with digital terrain models for improved river flow simulations; (European Geosciences Union, General Assembly 2008)